UNIVERSITÀ DEGLI STUDI FIRENZE

DOTTORATO DI RICERCA
INTERNATIONAL DOCTORATE IN STRUCTURAL BIOLOGY

CICLO XXIX

COORDINATORE Prof. Claudio Luchinat

Human ferritin nanocages: from iron oxidation to drug delivery

Settore Scientifico Disciplinare CHIM/03

Dottorando
Dott. *Silvia Ciambellotti*

Tutore
Prof. *Paola Turano*

Coordinatore
Prof. Claudio Luchinat

Novembre 2013 – 2016

This thesis has been approved by the University of Florence, the University of Frankfurt and the Utrecht University

Universiteit Utrecht

CERM Firenze

FRANKFURT AM MAIN

Table of contents

Chapter 1

Introduction

Life on earth is dependent on the catalytic activity of a number of different metal ions in their polypeptide scaffold. Among these metals, iron is widely used for catalysis of many reactions by living organisms. Iron is an essential element for cellular survival (1). In mammals, its participation in heme and iron-sulfur cluster (ISC)-containing proteins allows the involvement of iron in a variety of vital functions, including oxygen transport (hemoglobins), DNA synthesis (ribonucleotide reductase), oxygen metabolism (catalases and peroxidases) and cellular respiration electron transfer (cytochromes) (2). Using iron in an oxygenic environment requires organisms to precisely control intracellular availability of free Fe(II) and Fe(III), which are the two most common oxidation states of iron. Free Fe(II) will donate an electron to molecular oxygen, and as a result superoxide radical, which is a reactive oxygen species (ROS), and free Fe(III) will form, as a result of iron participation in the Fenton reaction, (equation **1**).

$$Fe^{2+} + H_2O_2 \rightarrow Fe^{3+} + OH^- + OH^{\bullet} \quad (\mathbf{1})$$

Fe(III) is insoluble under physiological conditions (solubility 10^{-18} M) (3) and precipitates as Fe(III) oxide species. Instead, ROS trigger oxidative stress, lipid peroxidation, and DNA damage, which can lead to genomic instability and DNA repair defects that ultimately compromise cell viability and promote programmed cell death (4). These deleterious effects are prevented by regulatory mechanisms that maintain systemic and cellular iron homeostasis (5) through: the cooperation of functional compartments (erythroid and proliferating cells), uptake and recycling systems (enterocytes and splenic macrophages), storage elements (hepatocytes), and mobilization processes that allow iron trafficking through polarized cells and their corresponding organs (6).

1.1 Systemic iron metabolism

In healthy individuals, the amount of body iron is maintained within a range of ∼3−5 g of iron (7) by a strict control of its absorption, mobilization, storage, and recycling. The majority is present as heme in hemoglobin of erythroid cells (>2 g) or myoglobin of muscles (∼300 mg). Macrophages in the spleen, liver, and bone marrow maintain a transient fraction of iron (∼600 mg), while excess iron is stored in the liver within ferritin (∼1000 mg). All other cellular iron-containing proteins and enzymes are estimated to bind a total of ∼8 mg of iron (8). Iron is delivered to erythroblasts and to most tissues via circulating transferrin (Tf),

which carries ~3 mg of the metal. Plasma iron is predominantly recycled by macrophages and to a small extent (~1−2 mg/day) by absorption from the diet, mediated by duodenal enterocytes. The macrophages acquire iron primarily via erythrophagocytosis and the enterocytes by internalization of heme or inorganic iron from the intestinal lumen (9). The absorption of inorganic iron involves: reduction of Fe^{3+} to Fe^{2+} by ascorbate and/or membrane-associated ferrireductases such as duodenal cytochrome b (DcytB), coupled to transport of Fe^{2+} across the apical membrane by divalent metal transporter 1 (DMT1) (7). The mechanism of heme internalization remains poorly defined and may involve either direct transport of heme or receptor-mediated endocytosis (10). Macrophages and enterocytes catabolize heme in a reaction catalyzed by heme oxygenase-1 and -2 (HO-1 and HO-2, respectively), which liberate inorganic iron. Both cell types export Fe^{2+} to plasma via the transmembrane transporter, ferroportin (Fpn) in a process coupled to the oxidation of Fe^{2+} to Fe^{3+}. This is mediated by the circulating ferroxidase ceruloplasmin or its homologue, hephaestin, which is expressed on the basolateral membrane of duodenal enterocytes and physically interacts with Fpn. Exported iron is scavenged by plasma Tf, which maintains it in a redox inert state and delivers it to tissues. Systemic Fe homeostasis is ensured by a body sensor, hepcidin, a peptide hormone produced by the liver in response to iron and inflammation (Fig. 1). Upregulation of hepcidin prevents duodenal iron uptake and entry into circulation, recycling from red blood cells heme-iron and release from iron stores. This hormone binds to Fpn on the plasma membrane of enterocytes, macrophages, hepatocytes, and other cells, promoting its internalization that leads to its lysosomal degradation (11). Since Fpn is the only exporter of inorganic iron in mammalian cells, its inactivation causes intracellular iron retention. Additionally, hepcidin has also been shown to promote proteasomal degradation of DMT1 (11).

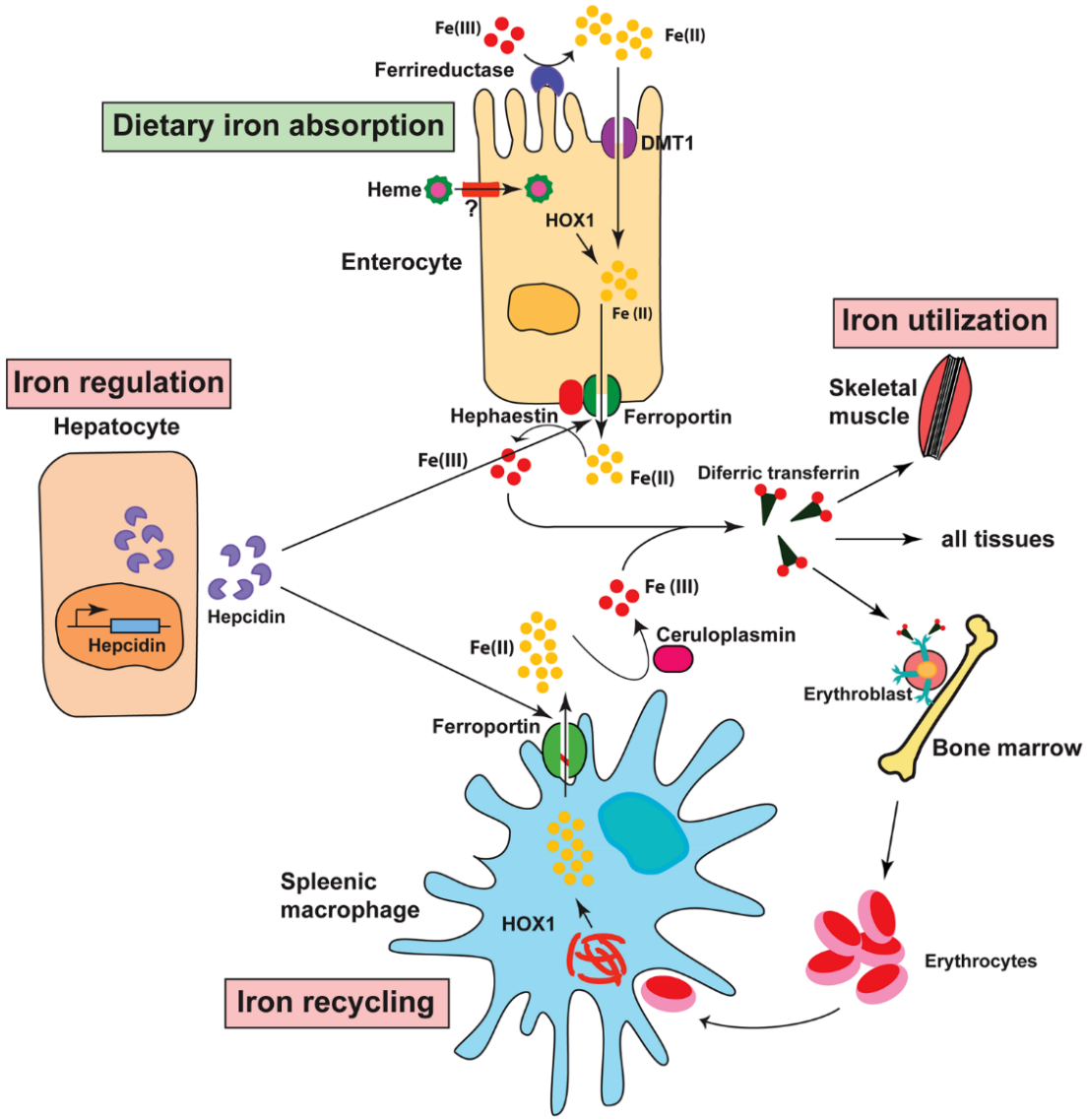

Figure 1 - Regulation of systemic iron metabolism. Reprinted from Biochemistry 2012, 51, 5705−5724. Duodenal enterocytes absorb dietary iron via DMT1 located on the apical surface upon reduction of Fe^{3+} to Fe^{2+} by DcytB. Spleenic reticuloendothelial macrophages recycle iron from senescent red blood cells. Both cell types release iron via ferroportin with the aid of hephaestin, which oxidizes Fe^{2+} to Fe^{3+}. Iron is also oxidized by ceruloplasmin in the circulation. Plasma Tf captures and circulates iron in the body. Hepatic hormone hepcidin regulates the efflux of iron from these cells by regulating the stability of ferroportin. Iron levels in the body, as well as conditions that affect iron metabolism indirectly such as inflammation, ER stress, erythropoiesis, and hypoxia influence the synthesis and secretion of hepcidin by hepatocytes.

1.2 Cellular iron metabolism

Cells have evolved metabolic strategies for safely managing iron. Regulation of iron uptake, intracellular trafficking, storage and utilization is critical for the maintenance of cellular iron homeostasis (Fig. 2).

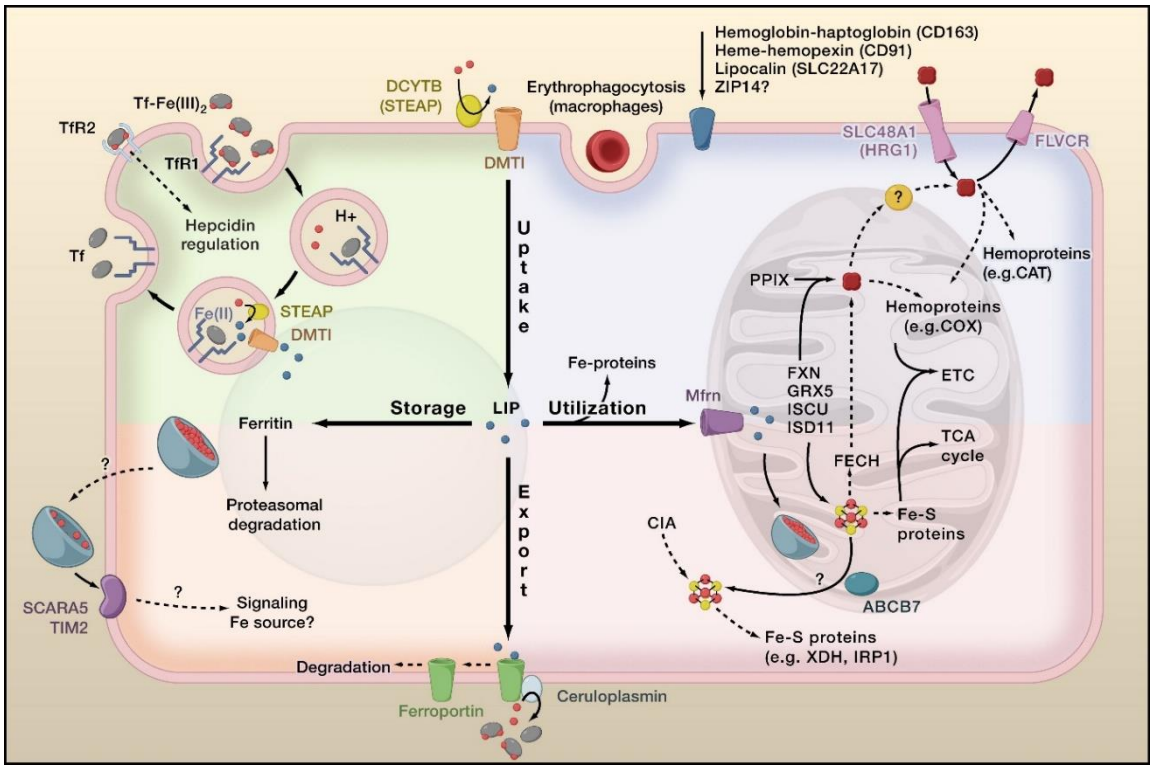

Figure 2. Cellular iron metabolism. Reprinted from Cell, 2010, 142(1), 24-38. A generic cell is depicted. Most cells acquire plasma iron via transferrin receptor 1 (TfR1)-mediated endocytosis of transferrin-bound iron. In endosomes, iron is freed from transferrin and reduced to Fe(II) by STEAP metalloreductases prior its release into cytosol via divalent metal transporter 1 (DMT1); transferrin and TfR1 return to the plasma membrane to be used for further cycles. DMT1 also functions in the apical absorption of dietary iron after reduction by DCYTB and possibly other ferrireductases. Other iron acquisition pathways are symbolized (e.g., acquisition of heme iron from red blood cells by macrophages). Iron uptake systems feed the so-called labile iron pool (LIP). The LIP is utilized for direct incorporation into iron proteins or iron transport to mitochondria via mitoferrin (Mfrn), where the metal is inserted into heme and Fe/S cluster prosthetic groups. The fraction of the LIP that is not utilized for metalation reactions can be exported via ferroportin, which works together with ferroxidases for iron loading onto transferrin, or stored in a nontoxic form in ferritin shells. Ferritin can be released into the extracellular milieu by unknown mechanisms and interact with specific receptors on the cell surface.

1.2.1 Iron uptake

Cell membranes and tight junctions between cells prevent the free flow of iron. Cells therefore have transporters, chaperones, and chelators, which allow iron crossing through membranes and facilitate intracellular trafficking. Most mammalian cells acquire iron from circulating Tf, upon binding to transferrin receptor 1 (TfR1). Tf, an 80 kDa glycoprotein, is synthesized and secreted mainly by the liver. Tf binds iron in plasma and extracellular fluids such as lymph and cerebrospinal fluid. It is equally distributed between plasma and extracellular fluids. Tf is a homodimeric β-globulin, which binds two molecules of ferric iron with high affinity ($K_d = 10^{-23}$ M). TfR1 provides the physiological route for entry of Tf-bound

iron into cells. It is expressed by most nucleated mammalian cells, and its levels correlate with cellular iron requirements. TfR1 is a disulfide-linked transmembrane glycoprotein that forms a homodimer with a molecular mass of 180 kDa, where each subunit binds one Tf molecule (12). Iron is released from Tf within endocytic vesicles due to acidification through the action of a v-ATPase proton pump. In a cooperative manner, Tf and TfR1 undergo conformational changes in the acidified endosome leading to iron release (13).

The released Fe^{3+} is then reduced to Fe^{2+} by STEAP 3 (six- transmembrane epithelial antigen of prostate-3), a member of the metalloreductase family (14). Fe^{2+} is transported across the endosomal membrane into the cytosol by DMT1 in most cells or by its homologue Nramp 1 (natural resistance-associated macrophage protein-1) in macrophages. In this regard, DMT1 is a dual-function protein, which regulates both systemic and cellular iron homeostasis. DMT1 inactivation in mice and humans leads to iron deficiency anemia (15). Newly assimilated cytosolic iron is transported to intracellular sites either for local use or for storage in ferritin. Hepatocytes may take up Tf-bound iron via both TfR1 and TfR2. However, while TfR1 is almost ubiquitously expressed, the expression of TfR2 is restricted to liver hepatocytes and to differentiated erythroblasts. Additionally, there is the portion of non transferrin bound iron (NTBI) that comprises all forms of plasma iron that are bound to ligands other than Tf. Cells can also acquire iron that is in complexes with other proteins or small molecules. For instance, internalization of ferritin via ferritin-specific receptors such as Scavenger receptor family class A member 5 (Scara5) facilitates iron import (16). Heme ingested from the diet also serves as an important source of iron. The importance of this route of iron uptake is exemplified by the enhanced heme uptake observed in iron deficiency. Cells are thought to internalize heme via a receptor-dependent process or indirectly with the aid of a heme carrier protein-1 (HCP-1), also known as proton-coupled folate transporter (PCFT) (17).

1.2.2 Iron trafficking

Iron taken up by Tf-dependent or -independent routes presumably enters into a labile intermediary pool or labile iron pool (LIP). The LIP is also termed as the “exchangeable”, “regulatory”, or “chelatable” iron pool, because its presence has been documented by using metal chelators (18). It is defined as a low molecular weight pool of weakly chelated iron, including both Fe^{2+} and Fe^{3+} and represents a minor fraction of the total amount of cellular iron (~3−5%). The LIP links cellular iron uptake with iron utilization, storage, or export. The

other source of iron for this pool is the degradation of non-heme and heme iron-containing proteins. Iron within the LIP is thought to be in steady state equilibrium and is proposed to bind diverse low-molecular weight chelates, such as organic anions (phosphates, citrates, and carboxylates) and polyfunctional ligands such as polypeptides and siderophores. Mitochondria are central for the regulation of cellular iron metabolism, and the majority of iron imported into the cell is utilized within this organelle for the synthesis of heme and ISCs (19). Mitoferrin-1 (Mfrn1) and Mitoferrin-2 (Mfrn2) are crucial for the import of mitochondrial iron into erythroid and non-erythroid cells, respectively (20). Heme synthesis begins and ends in mitochondria, but intermediate steps occur in the cytoplasm (21). As regarding the synthesis of ISCs, these cofactors consist of iron cations and sulfide anions. They are assembled on scaffold proteins and then targeted to specific proteins via sulfur of cysteine residues. In mammals, the scaffold protein is "ISC assembly protein U" (IscU) (22). Loading of iron onto IscU is very likely mediated by mitochondrial frataxin (23), which thereby plays an important role in mitochondrial iron metabolism. Besides the biosynthesis of heme and ISCs, iron in excess in mitochondria is stored in the mitochondrion-specific iron storage protein mitochondrial ferritin or mitoferritin (FtMt) (see below).

1.2.3 Iron regulation

While systemic iron metabolism is mainly regulated at the transcriptional level, cellular iron balance is largely controlled by post-transcriptional mechanisms. Inside the cell, a machinery involving the Iron Regulatory Proteins (IRPs) and the Iron Responsive Elements (IREs) controls the iron levels. The IREs structural motifs are within untranslated regions (UTRs) of several mRNAs. The mRNAs encoding TfR1 and ferritin are typical examples of coordinate post-transcriptional regulation by IRE-IRP interactions (24). IREs are evolutionarily conserved stem loop structures of 25−30 nucleotides. In iron deficiency, IRPs bind with high affinity (K_d ~10^{-12} M) to target IREs. This results in stabilization of TfR1 mRNA and steric inhibition of ferritin mRNA translation. Under these conditions, accumulation of TfR1 promotes the uptake of cellular iron from plasma Tf, while inhibition of ferritin biosynthesis prevents storage of iron, allowing its metabolic utilization. Conversely, in response to excess cellular iron, IRPs are inactivated, which leads to TfR1 mRNA degradation and ferritin mRNA translation. This minimizes further internalization of iron via TfR1 and promotes the storage of excessive intracellular iron into ferritin. Interestingly, mutations in the

L-ferritin IRE that prevent IRP binding are causatively linked to hereditary hyperferritinemia-cataract syndrome (HHCS), an autosomal dominant disorder characterized by overexpression of serum ferritin (without iron overload) and early onset cataract (25). IRP1 and IRP2 are homologous to mitochondrial aconitase and other members of the ISC isomerase family, which possess a cubane ISC in their active site. In iron starvation, IRP1 assembles an ISC and functions as cytosolic aconitase (catalyzing the conversion of citrate to iso-citrate via a cis-aconitate intermediate). The ISC keeps IRP1 in a closed conformation, which precludes access of IREs. Iron deficiency promotes the loss of the ISC and a resulting structural rearrangement of the protein that acquires IRE binding activity. Thus, IRP1 is a bifunctional protein that is regulated by an ISC switch. Despite its extensive homology with IRP1, IRP2 does not assemble an ISC and is regulated by a distinct mechanism. It remains stable in iron-starved or hypoxic cells and undergoes ubiquitination and proteasomal degradation in response to iron and oxygen.

1.2.4 Iron export

Cellular iron export occurs in specialized cells such as enterocytes and macrophages that are involved in iron absorption and recycling, respectively. The main purpose of iron export is to maintain adequate plasma iron levels and to meet systemic needs. Iron export involves coordination between many enzymes and proteins. First, iron is reduced in endosomes prior to being released into the cytoplasm. Thus, Fpn exports Fe^{2+}, which has to be oxidized to Fe^{3+} upon its release into plasma for binding to Tf (26). This is mediated by the blue copper ferroxidases ceruloplasmin (soluble in serum or plasma membrane-associated in some cell types) and hephaestin (expressed on the plasma membrane of enterocytes and other cell types). These enzymes thus work in concert with Fpn to coordinate iron export and oxidation. As copper is essential for ferroxidase activity, adequate levels of this metal are required for proper iron balance. Cells may also export iron bound to ferritin or to heme. Feline leukemia virus subgroup C receptor 1 (FLVCR1) facilitates the efflux of heme from hematopoietic cells. In addition to the list of heme exporters, an ATP binding cassette family member, ABCG2, has also been implicated in cellular heme export.

1.2.5 Iron storage

Cellular iron storage is carried out by ferritin, ubiquitous nanocage protein that can accommodate up to thousands of iron atoms inside its cavity. Twenty-four subunits assemble to make a hollow spherical protein with octahedral symmetry. Ferritin binds and oxidizes Fe(II) and subsequently stores the Fe(III) product inside its cavity as a ferrihydrite-like mineral core. In mammals, ferritin is a heteropolymer of 24 subunits of two different polypeptides: heavy chain (H) and light chain (L) (see below for detailed description).

1.3 The superfamily of ferritin

The ferritin family consists of three sub-families, the classical ferritins (Ftn), the bacterioferritins (Bfr) and the 'DNA-binding protein from starved cells' (Dps proteins) (27). Besides the above-cited proteins, the ferritin superfamily encompasses proteins that have a four α-helix bundle structure such as soluble methane monooxygenase, ribonucleotide reductase, rubrerythrin, Dps-like proteins and the recently identified archaeoferritin (28). Ftn's are found in all three domains of life. They are composed of 24 subunits that form a rhombic dodecahedron. Instead, Bfr proteins are restricted to the bacterial and archaeal domains of life even if they possess the same quaternary structure as Ftn. Both Bfr and Ftn proteins can be composed of more than one (homologous) subunit type. The main difference between the Ftn and Bfr proteins is the presence of b-type heme within the Bfr shell. Up to 12 hemes are located between pairs of subunits, within a binding pocket positioned towards the inner protein surface. Dps and Dps-like proteins have a spherical-shape structure composed of 12 identical subunits that form a smaller molecule (9.5 nm rather than 12 nm outer diameter) with a lower iron-storage capacity (500 rather than 4500 iron atoms) than the Ftn and Bfr proteins.

1.3.1 Structure and biological role of human ferritins

Twentyfour-mers ferritins (called maxi-ferritins) are spherical nanocaged proteins of ~480 kDa of around 12 nm in external diameter with an internal cavity of 8 nm able to host up to 4500 iron atoms (Fig. 3 A and B). The extraordinary compact architecture confers to the protein the ability to resist at extreme pH conditions (3<pH<9), high temperatures (at least up

to 80°C) and high concentrations of denaturant agents (for example 6 M urea or guanidine) (29). Each subunit shares a 4-helix bundle conformation characterized by four antiparallel α-helices (I-IV) and a smaller fifth α-helix(V) tilted by 60° with respect to the bundle axis. Helices I and III are solvent-exposed together with a long loop that connects helices II and III, while II and IV are buried inside the protein. The subunit ends with helix V at the C-terminal.

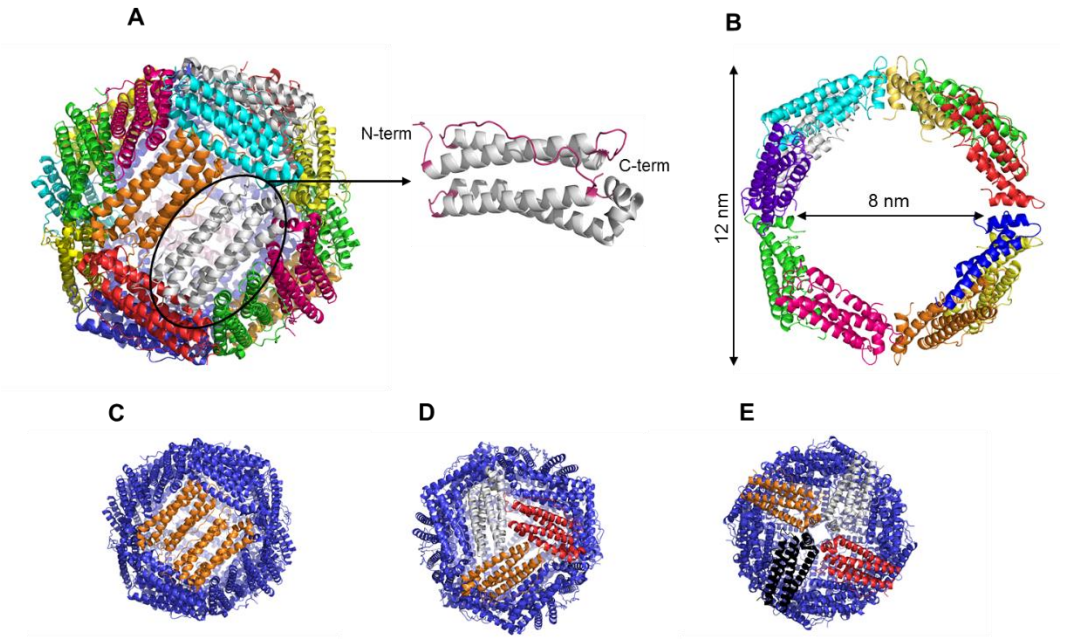

Figure 3. Overview on ferritin structural features. A) 24-mer polymer and the four-helix bundle conformation of each subunits, characterized by four antiparallel helices (I-IV) with a fifth smaller helix (V) placed at the C-terminal. **B**) The cavity of 8 nm can host up to thousands of iron atoms. **C**) A dimer of antiparallel monomers along the 2-fold symmetry axis; **D**) the C3 channel and **E**) the C4 channels.

This system is highly symmetric with a 4,3,2 (octahedral) symmetry (Fig. 3 C,D,E). Along the twelve 2-fold symmetry axes (C2), two subunits come in contact giving rise to dimers that assemble to form the cage structure. Along 3-fold (C3) and 4-fold (C4) symmetry axes, where three or four subunits are in contact, the so-called C3 and C4 channels are placed. The former are mainly hydrophilic and characterized by the presence in their bottom end of prevalently negatively charged amino acid side chains belonging to helices I and III. The electrostatic gradient created by this charge distribution along the channels is the basis for their role as iron entry channels. The C4 channels are more hydrophobic and neutral, with a still unclear function and delimited by the C-terminal portion of 4 helices V (30).

In humans, as in vertebrates in general, ferritin are heteropolymers constituted by two highly homologous subunits: L “light” (20 kDa) and H “heavy” (22.8 kDa) subunits (31) that

share 53% of sequence identity. A third subunit M “middle” (21 kDa) has been found in bullfrog ferritin (32). Hereafter, only human ferritins will be discussed. They are the products of the assembly of 24 H- and/or L-subunits, in different ratios depending on the tissues. The H-subunit contains a binuclear ferroxidase center that catalyzes Fe(II) oxidation. This antioxidant activity consumes Fe(II) and dioxygen or hydrogen peroxide (the overall and intermediate reactions are shown in equations **2-5**) (33, 34), the reagents that produce toxic free radicals in the Fenton reaction.

$$2Fe^{2+} + O_2 \rightarrow [Fe(III)\text{-}O\text{-}O\text{-}Fe(III)] \quad (\mathbf{2})$$

$$[Fe(III)\text{-}O\text{-}O\text{-}Fe(III)] + H_2O \rightarrow H_2O_2 + [Fe(III)\text{-}O\text{-}Fe(III)] \quad (\mathbf{3})$$

$$[Fe(III)\text{-}O\text{-}Fe(III)] + (H_2O)_{x+2} \rightarrow Fe_2O_3(H_2O)_x + 4H^+ \quad (\mathbf{4})$$

$$2Fe^{2+} + O_2 + (H_2O)_{x+3} \rightarrow Fe_2O_3(H_2O)_x + 4H^+ + H_2O_2 \quad (\mathbf{5})$$

In the first step (equation **2**) two ferrous ions are oxidized and coupled to form a diferric-peroxo (DFP) species at the binuclear ferroxidase center. DFP is a transient intermediate that decays to form diferric-oxo complexes (equation **3**). The ferric products that form at the catalytic site are precursors of the ferric hydrated biomineral that grows at the cavity level, while the second product H_2O_2 goes into solution (where catalases disproportionate H_2O_2 to harmless water and oxygen) or is recycled by the ferritin nanocage for further iron oxidation steps. On the contrary, the L-subunit lacks enzymatic activity; yet they are still able to store iron as a caged ferric biomineral, although biomineralization proceeds at a much slower rate. The L-subunit contains a high number of carboxyl groups lining the ferritin cavity, which have been proposed to serve as iron nucleation sites, although the identification of this site was still lacking before this thesis work. Thus, H-richer ferritins are preferentially expressed in tissues requiring fast iron metabolism (heart, muscle and brain) while L-richer ferritins are found in tissues involved in long-term storage of iron (liver and spleen).

The mechanism by which iron is delivered to ferritin remains elusive. Experimental evidence suggests the involvement of the cytosolic iron chaperone poly(rC)-binding protein 1 (PCBP1) (35).

The mechanism of iron release from ferritin is also unclear. However, it is known that degradation of ferritin is coupled to the supply of available metabolic iron under iron-starvation. In fact, treatment with iron chelators or expression of Fpn accelerates ferritin degradation (36). Changes in iron availability regulate ferritin gene expression mainly at the post-transcriptional level via the IRE−IRP system. Additionally, ferritin expression is

regulated transcriptionally, which determines the tissue distribution of H and L chains. Ferritin is transcriptionally activated under oxidative stress via an upstream antioxidant response element (ARE) in the promoter region of the ferritin genes. In contrast, extracellular H_2O_2 inhibits ferritin mRNA translation by activating the IRE−IRP regulatory system (7). By sequestering redox-active iron, ferritin plays an important antioxidant role and promotes cell survival. Thus, overexpression of ferritin decreases the LIP, impedes the generation of ROS, and confers resistance to oxidative damage. Conversely, H-ferritin depletion caused by genetic deletion of Fth1 gene (encoding H-ferritin), results in embryonic lethality suggesting that its ferroxidase activity is critical (37). Mutations in L-ferritin are associated with an autosomal dominant neurological disorder (neuroferritinopathy), characterized by brain iron overload and entrapment of iron in mutant ferritin shells, which causes functional iron deficiency (38).

1.3.2 Human ferritin distribution

Ferritins is mainly cytosolic but it is also present in i) serum, ii) mitochondrion and iii) nucleus.

i) A glycosylated, primarily composed by L-subunits ferritin circulates in serum and exhibits a low iron loading capacity. Serum ferritin does not contain a signal peptide for secretion; some studies proposed hepatocytes, macrophages and Kupffer cells as sources able to secrete ferritin (39). The levels of serum ferritin increase in response to systemic iron load or infection (7). Ferritin secretion might function limiting iron storage after a shift from high to low iron concentrations, and before the activation of IRPs (31).

ii) The mitochondrial subunit is encoded by a different mRNA, which lacks the IRE sequence for the iron-dependent translation control. The 242 amino acid FtMt precursor includes a long N-terminal targeting signal peptide (around 60 residues) which is cleaved after the import in the mitochondrion. It shares 79% of sequence identity with H-ferritin and complete conservation of the ferroxidase centers (31, 40). Differently to cytosolic ferritin, it has restricted tissue expression (in testis and brain) and it is found as a homopolymer. More importantly, FtMt has been found to incorporate iron more efficiently than H-ferritin and its over-expression caused iron deficiency (41). Thus, FtMt serves as a molecular sink to prevent accumulation of iron in mitochondria protecting the organelle against iron’s toxicity. It has

been postulated that FtMt is important to protect mitochondria with high metabolic activity and ROS production, while it may be harmful in the less active mitochondria. Moreover, the unique distribution and the overexpression during oxidative stress strongly correlate it with numerous neurological pathologies, indicating that this protein could be involved in the pathogenesis of a series of diseases (42).

iii) Several studies over the last two decades have reported also the presence of ferritin in nuclei, specifically H-ferritin, in developing neurons, hepatocytes, corneal epithelial cells and some cancer cells (43). Analysis of the H-ferritin sequence does not reveal a typical nuclear localization signal peptide. Analysis of H-ferritin sequence showed several putative *O*-glycosylation sites, whereas only one is present in L-ferritin. In light of the evidence suggesting that H-ferritin is the preferred subunit for nuclear translocation, it has been hypothesized the involvement of *O*-glycosylation in this process. Deletion and truncation studies are underway to evaluate the importance of several *O*-glycosylation sites in the nuclear translocation of ferritin (44). Even phosphorylation of serine residues is another possible modification that can mediate the nuclear translocation (45). Others propose the existence of a specific nuclear chaperone for ferritin delivery into the nucleus, called ferritoid (46). Despite of what it is known about the involvement of *O*-glycosylation and phosphorylation in nuclear translocation of ferritin, the specifics of this mechanism are still unclear. As concerning the ferritoid chaperone, its specificity to the corneal epithelium cells limits the possibility to be considered a candidate for ferritin nuclear transport. All these observations encouraged a new role for ferritin beyond its classical iron storage function, such as the regulation of iron accessibility to nuclear components, DNA protection from iron-induced oxidative damage, and transcriptional regulation.

1.4 Ferritin in biomedicine

In recent years, the interest in nanoscale systems in biomedicine has grown up. Nanotechnology applied to the diagnosis and treatment of diseases, such as cancer, is a recently born technology that deals with the development of new delivery systems able to target specific sites using nanoparticles (nanocarriers). Basically a good nanocarrier increases the bioavailability of drugs or diagnostic probes in specific organs or cells and over a period of time, lowering side-effects and the amount of needed doses.

Nanoparticle-based delivery systems provide a high cargo-loading capacity for delivery and a versatile surface that can be used to add functional groups that improve the aqueous solubility of desired cargoes, as well as to attach targeting ligands (47). Various types of chemical ligands, short peptides, and antibodies have been used as targeting moieties of nanoparticle-based delivery systems to enhance their efficiency of delivery. For the localized release of therapeutics and target-specific early diagnosis, nanocarriers have been designed to release encapsulated drugs and to exhibit diagnostic signals upon changes, for example, in pH, light, proteolysis and temperature (48-50).

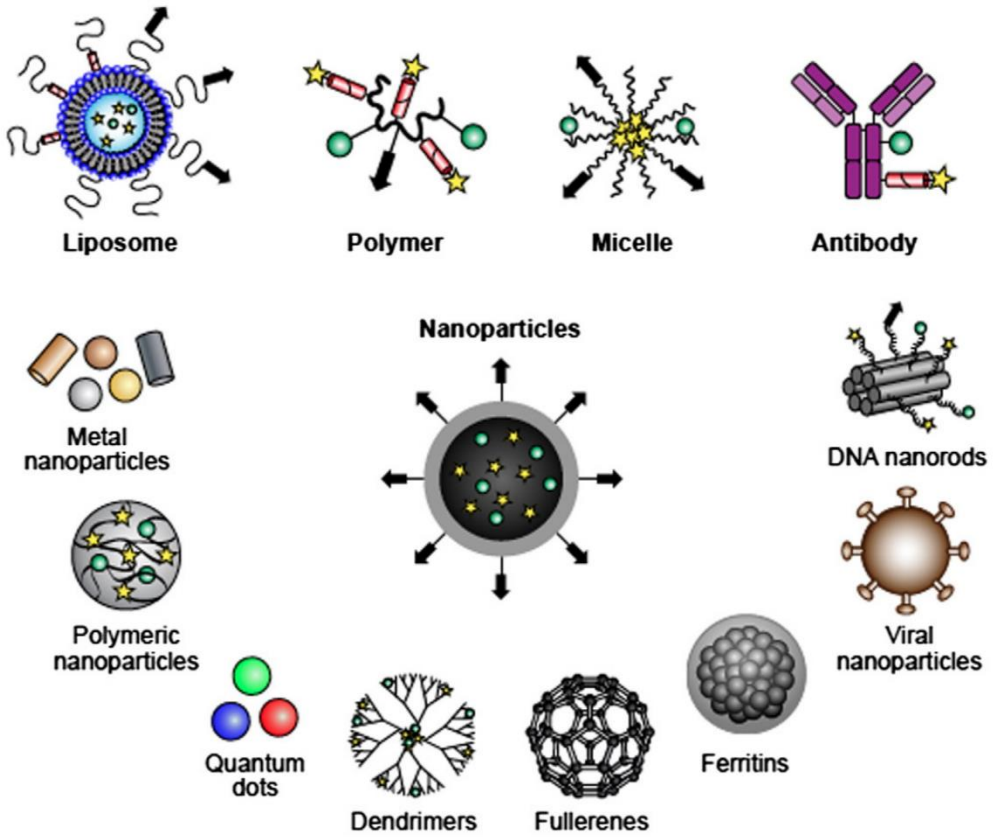

Figure 4. Examples of nanoparticle-based delivery systems. Reprinted from Advanced Drug Delivery Reviews 79–80 (2014) 107–118. Multi-valent, multi-functional and stimuli-responsive nanocarrier delivery systems for tumor targeting. Examples of nanocarrier delivery vehicles include (left to right) liposomes, polymers, micelles, engineered antibodies and nanoparticles decorated with stimuli-responsive cleavable stealth coatings (blue rectangles), targeting moieties (arrows), and anti-cancer drugs or imaging agents (stars and suns).

Nanoparticle-based delivery systems are generally prepared from synthetic polymers, inorganic nanomaterials and biomaterials derived from various types of biological sources (Fig. 4).

Among biomaterials, there are the natural protein cages that have well-defined hollow spherical architectures. Protein cages, including ferritins, viral capsids, and heat shock proteins, are precisely self-assembled from multiple copies of a limited number of subunits, thus resulting in highly symmetric and uniformly sized architectures.

Ferritin is a promising nano-vehicle thanks to its intrinsic features: i) a large cavity that once depleted of iron can encapsulate and protect the cargo during the delivery; ii) an endogenous origin that prevents immunological responses; iii) a versatile surface composition that allows various type of functionalization to target specifically different types of cells; iv) the presence of receptor-mediated endocytosis mechanism by TfR1 (Transferrin receptor 1) for H-rich cages and SCARA5 (Scavenger receptor class A type 5) for L-rich cages that allows the accumulation of ferritin in particular tissues or cells.

So far, plenty of molecules have been encapsulated inside ferritin: doxorubicin (51), curcumin (52), cisplatin (53) and desferrioxamine B (54) are only few examples. Approaches to encapsulate bulky molecules and ionic species in the interior of ferritin, once depleted of iron, followed the observation of Webb that apoferritin can be reversible disassociated and reassociated by simple adjustment of the pH to pH 2 or above pH 7, respectively (55). Once trapped, molecules were sequestered in the protein cage if they are too large to escape. Otherwise, if the species to be internalized are small enough to pass across channels, as in the case of metal ions, inclusion occurs by simple diffusion.

Unfortunately, so far none of these drug-ferritin carrier system has been approved for clinical use owing to the complexity of designing particles that can meet all of the design criteria of targeted drug delivery (56). Only one protein-based nanoparticle has entered the clinic so far: albumin-nanoparticle-bound paclitaxel (nab-paclitaxel; Abraxane®). It is used for the therapy of breast cancer, non-small-cell lung cancer and pancreatic cancer. Paclitaxel is a cytotoxic compound isolated from the bark of the pacific yew tree (Taxus brevifolia).

1.5 Aims and topics of the research

During the three years of my PhD program, I was involved in the structural and functional characterization of the family of ferritins, with a special focus on those of human

origin. Through the development of heterologous expression in engineered *E. coli* strains, recombinant ferritins were prepared and purified to be available for biochemical studies.

There is an intense ongoing debate in the literature about the mechanisms by which the different ferritins operate. Identifying the pathway of iron from the uptake to the ferroxidase site of ferritin is a challenging task. When I started my PhD program, none iron-loaded structures in maxiferritins had been solved by X-ray crystallography, with few exceptions (see Section 3.1). Other metal ions were loaded inside human ferritin to mimic the behavior of the natural iron substrate. The identification of iron-binding sites was more difficult owing to the quite rapid reaction turnover. For this reason, part of my research addressed the clarification of the mechanisms adopted by H/H'- and L- homopolymeric ferritins for iron "handling", mainly by X-ray crystallography and electronic spectroscopy with the help of site-directed mutagenesis to identify the role of specific amino acids.

In the frame of PRIN 2012 "Innovative chemical tools for improved molecular approaches in biomedicine", we established collaborations with research groups involved in the investigation of different aspect of ferritin chemistry.

Besides its iron storage function, new roles have been proposed for this protein. The interaction study with HoSF (horse spleen ferritin) with a pool of lipids, was performed with ligand-based NMR experiments accompanied by mineralization assays through UV/visible measurements, aimed at verifying whether a functional coupling between mineralization and ferritin/lipid interactions do exist.

Only in 2001, a mitochondrial ferritin subunit has been discovered. Thanks to a signal peptide, it is specifically imported in mitochondria where its maturation ends with the signal cleavage. The mitochondrial isoform is a crucial player in the cellular iron homeostasis. Since, an electron transfer (ET) between ferritin and cytochrome c has been reported, we decided to investigate deeply by NMR, the inter-protein ET process trying to see whether it occurs via specific protein-protein interactions.

Additionally, ferritin represents a good scaffold to develop successful drug delivery nano-systems. The stable architecture with its endogenous origin and the ability to be recognized by specific cellular receptors, make ferritin a good candidate nanocarrier.

In this view, encapsulation of the antimetastatic Ru-based drug inside human H- and L-ferritin has been investigated with the goal to prepare a drug-ferritin adduct with improved

pharmacokinetic properties. It is well known that PEGylation of biological drugs, such as proteins, provides reduced renal clearance, increased stability to degradation, and a reduced immunogenic response. PEGylation unfortunately prevents crystallization of protein for X-ray analysis. A new methodology, based on solid state NMR of PEG-protein in a pelleted state, has been developed in order to confirm that PEGylation does not compromise the native structure/function of proteins. PEG-ferritin has been chosen as a case study to build this new approach.

Finally, an iron-loaded ferritin was proposed as a therapeutic agent. The administration of iron-loaded H-Ferritin (100% H chain) and Horse Spleen Ferritin (15% H chains and 85% L chains) as a novel nanotherapy in cancer has been investigated in HeLa cells. The capacity of these proteins to deliver high amounts of iron was exploited with the scope to trigger mechanisms of cell damage and death associated with a persistent LIP increase.

Reference List

1. Crichton, R. R. (2001) *Inorganic biochemistry of iron metabolism: from molecular mechanism to clinical consequences* (John Wiley & Sons.

2. Zhang C (2014) Essential functions of iron-requiring proteins in DNA replication, repair and cell cycle control. *Protein Cell* **5**:750-760.

3. Theil EC, Goss DJ (2009) Living with iron (and oxygen): questions and answers about iron homeostasis. *Chem. Rev.* **109**:4568-4579.

4. Gozzelino R, Arosio P (2016) Iron Homeostasis in Health and Disease. *Int. J. Mol. Sci.* **17**.

5. Andrews NC, Schmidt PJ (2007) Iron homeostasis. *Annu. Rev. Physiol* **69**:69-85.

6. Philpott CC, Ryu MS (2014) Special delivery: distributing iron in the cytosol of mammalian cells. *Front Pharmacol.* **5**:173.

7. Wang J, Pantopoulos K (2011) Regulation of cellular iron metabolism. *Biochem. J.* **434**:365-381.

8. Hentze MW, Muckenthaler MU, Galy B, Camaschella C (2010) Two to tango: regulation of Mammalian iron metabolism. *Cell* **142**:24-38.

9. Knutson M, Wessling-Resnick M (2003) Iron metabolism in the reticuloendothelial system. *Crit Rev. Biochem. Mol. Biol.* **38**:61-88.

10. West AR, Oates PS (2008) Mechanisms of heme iron absorption: current questions and controversies. *World J. Gastroenterol.* **14**:4101-4110.

11. Nemeth E *et al.* (2004) Hepcidin regulates cellular iron efflux by binding to ferroportin and inducing its internalization. *Science* **306**:2090-2093.

12. Aisen P (2004) Transferrin receptor 1. *Int. J. Biochem. Cell Biol.* **36**:2137-2143.

13. Dautry-Varsat A, Ciechanover A, Lodish HF (1983) pH and the recycling of transferrin during receptor-mediated endocytosis. *Proc. Natl. Acad. Sci. U. S. A* **80**:2258-2262.

14. Ohgami RS, Campagna DR, McDonald A, Fleming MD (2006) The Steap proteins are metalloreductases. *Blood* **108**:1388-1394.

15. Mims MP *et al.* (2005) Identification of a human mutation of DMT1 in a patient with microcytic anemia and iron overload. *Blood* **105**:1337-1342.

16. Li JY *et al.* (2009) Scara5 is a ferritin receptor mediating non-transferrin iron delivery. *Dev. Cell* **16**:35-46.

17. Shayeghi M *et al.* (2005) Identification of an intestinal heme transporter. *Cell* **122**:789-801.

18. Kakhlon O, Cabantchik ZI (2002) The labile iron pool: characterization, measurement, and participation in cellular processes(1). *Free Radic. Biol. Med.* **33**:1037-1046.

19. Richardson DR *et al.* (2010) Mitochondrial iron trafficking and the integration of iron metabolism between the mitochondrion and cytosol. *Proc. Natl. Acad. Sci. U. S. A* **107**:10775-10782.

20. Shaw GC *et al.* (2006) Mitoferrin is essential for erythroid iron assimilation. *Nature* **440**:96-100.

21. Ajioka RS, Phillips JD, Kushner JP (2006) Biosynthesis of heme in mammals. *Biochim. Biophys. Acta* **1763**:723-736.

22. Tong WH, Rouault TA (2006) Functions of mitochondrial ISCU and cytosolic ISCU in mammalian iron-sulfur cluster biogenesis and iron homeostasis. *Cell Metab* **3**:199-210.

23. Stemmler TL, Lesuisse E, Pain D, Dancis A (2010) Frataxin and mitochondrial FeS cluster biogenesis. *J. Biol. Chem.* **285**:26737-26743.

24. Wang J, Pantopoulos K (2011) Regulation of cellular iron metabolism. *Biochem. J.* **434**:365-381.

25. Roetto A *et al.* (2002) Pathogenesis of hyperferritinemia cataract syndrome. *Blood Cells Mol. Dis.* **29**:532-535.

26. Ganz T (2005) Cellular iron: ferroportin is the only way out. *Cell Metab* **1**:155-157.

27. Andrews SC (2010) The Ferritin-like superfamily: Evolution of the biological iron storeman from a rubrerythrin-like ancestor. *Biochim. Biophys. Acta* **1800**:691-705.

28. Ebrahimi KH *et al.* (2012) A novel mechanism of iron-core formation by Pyrococcus furiosus archaeoferritin, a member of an uncharacterized branch of the ferritin-like superfamily. *J. Biol. Inorg. Chem.* **17**:975-985.

29. Listowsky I, Blauer G, Enlard S, Betheil JJ (1972) Denaturation of horse spleen ferritin in aqueous guanidinium chloride solutions. *Biochemistry* **11**:2176-2182.

30. Theil EC *et al.* (2014) Coordinating Subdomains of Ferritin Protein Cages with Catalysis and Biomineralization viewed from the C4 Cage Axes. *J. Biol. Inorg. Chem.* **19**:615-622.

31. Arosio P, Ingrassia R, Cavadini P (2009) Ferritins: a family of molecules for iron storage, antioxidation and more. *Biochim. Biophys. Acta - Gen. Subj.* **1790**:589-599.

32. Dickey LF *et al.* (1987) Differences in the regulation of messenger RNA for housekeeping and specialized-cell ferritin. A comparison of three distinct ferritin complementary DNAs, the corresponding subunits, and identification of the first processed in amphibia. *J. Biol. Chem.* **262**:7901-7907.

33. Hwang J *et al.* (2000) A short Fe-Fe distance in peroxodiferric ferritin: control of Fe substrate versus cofactor decay? *Science* **287**:122-125.

34. Schwartz JK *et al.* (2008) Spectroscopic definition of the ferroxidase site in M ferritin: comparison of binuclear substrate vs cofactor active sites. *J. Am. Chem. Soc.* **130**:9441-9450.

35. Shi H, Bencze KZ, Stemmler TL, Philpott CC (2008) A cytosolic iron chaperone that delivers iron to ferritin. *Science* **320**:1207-1210.

36. De D, I *et al.* (2006) Ferroportin-mediated mobilization of ferritin iron precedes ferritin degradation by the proteasome. *EMBO J.* **25**:5396-5404.

37. Arosio P, Levi S (2010) Cytosolic and mitochondrial ferritins in the regulation of cellular iron homeostasis and oxidative damage. *Biochim. Biophys. Acta* **1800**:783-792.

38. Muhoberac B, Vidal R Abnormal iron homeostasis and neurodegeneration.

39. Wang W *et al.* (2010) Serum ferritin: Past, present and future. *Biochim. Biophys. Acta* **1800**:760-769.

40. Levi S, Arosio P (2004) Mitochondrial ferritin. *Int. J. Biochem. Cell Biol.* **36**:1887-1889.

41. Corsi B *et al.* (2002) Human mitochondrial ferritin expressed in HeLa cells incorporates iron and affects cellular iron metabolism. *J. Biol. Chem.* **277**:22430-22437.

42. Yang H *et al.* (2013) Mitochondrial ferritin in neurodegenerative diseases. *Neurosci. Res.* **77**:1-7.

43. Alkhateeb AA, Connor JR (2010) Nuclear ferritin: A new role for ferritin in cell biology. *Biochim. Biophys. Acta* **1800**:793-797.

44. Surguladze N *et al.* (2005) Characterization of nuclear ferritin and mechanism of translocation. *Biochem. J.* **388**:731-740.

45. Li R *et al.* (2006) Chemokine CXCL12 induces binding of ferritin heavy chain to the chemokine receptor CXCR4, alters CXCR4 signaling, and induces phosphorylation and nuclear translocation of ferritin heavy chain. *J. Biol. Chem.* **281**:37616-37627.

46. Millholland JM *et al.* (2003) Ferritoid, a tissue-specific nuclear transport protein for ferritin in corneal epithelial cells. *J. Biol. Chem.* **278**:23963-23970.

47. Petros RA, DeSimone JM (2010) Strategies in the design of nanoparticles for therapeutic applications. *Nat. Rev. Drug Discov.* **9**:615-627.

48. Petros RA, DeSimone JM (2010) Strategies in the design of nanoparticles for therapeutic applications. *Nat. Rev. Drug Discov.* **9**:615-627.

49. Law B, Tung CH (2009) Proteolysis: a biological process adapted in drug delivery, therapy, and imaging. *Bioconjug. Chem.* **20**:1683-1695.

50. Gao W, Chan JM, Farokhzad OC (2010) pH-Responsive nanoparticles for drug delivery. *Mol. Pharm.* **7**:1913-1920.

51. Liang M *et al.* (2014) H-ferritin-nanocaged doxorubicin nanoparticles specifically target and kill tumors with a single-dose injection. *Proc. Natl. Acad. Sci. U. S. A* **111**:14900-14905.

52. Cutrin JC *et al.* (2013) Curcumin/Gd loaded apoferritin: a novel "theranostic" agent to prevent hepatocellular damage in toxic induced acute hepatitis. *Mol. Pharm.* **10**:2079-2085.

53. Pontillo N *et al.* (2016) Cisplatin encapsulation within a ferritin nanocage: a high-resolution crystallographic study. *Chem. Commun. (Camb.)* **52**:4136-4139.

54. Dominguez-Vera JM (2004) Iron(III) complexation of Desferrioxamine B encapsulated in apoferritin. *J. Inorg. Biochem.* **98**:469-472.

55. Webb B *et al.* (1994) Molecular entrapment of small molecules within the interior of horse spleen ferritin. *Arch. Biochem. Biophys.* **309**:178-183.

56. Shi J, Xiao Z, Kamaly N, Farokhzad OC (2011) Self-assembled targeted nanoparticles: evolution of technologies and bench to bedside translation. *Acc. Chem. Res.* **44**:1123-1134.

Chapter 2

Proteins production

During my PhD, I mainly worked on the structural and functional characterization of the family of human ferritins. All the ferritin variants studied during my doctorate activities were produced according to home-made protocols that I developed. Tables 1 and 2 list all the protein samples I prepared. Table 1, reports: i) the nomenclature with the complete names and their abbreviations used throughout the text; ii) the eventual mutations introduced by site-directed mutagenesis; iii) the isotopic labelling, if present; iv) the publications (or draft manuscripts) resulting from the production and characterization of these proteins.

Source	Protein	Mutations	Name abbreviation	Isotopic labelling	Publications
Bullfrog	H'(M) ferritin	H54A	H54A	/	**1**
Human	H-chain ferritin	WT	HuHf	/	**2,5,6,7**
Human	H-chain ferritin	WT	HuHf	^{15}N, ^{13}C	**3**
Human	H-chain ferritin	W94G, E95K, ins96I, ins93G, ins99FEE	EF hand-HuHf	/	/
Human	L-chain ferritin	WT	HuLf	/	**4,6,7**
Human	L-chain ferritin	E60A, E61A, E64A	E60AE61AE64A	/	**4**
Human	Mitochondrial ferritin	WT	FtMt	/	/

Table 1. Overview of all recombinant proteins produced and purified for the doctorate's projects.

1. Bernacchioni C., Ciambellotti S., Theil E.C. and Turano P. *Biochim Biophys Acta.* **2015**. 1854(9):1118-22.
2. Pozzi C., Di Pisa F., Bernacchioni C., Ciambellotti S., Turano P. and Mangani S. *Acta Crystallogr D* **2015**. D71, 1909–1920.
3. Ravera E., Ciambellotti S., Cerofolini L., Martelli T., Kozyreva T., Bernacchioni C., Giuntini S., Fragai M., Turano P. and Luchinat C. *Angew Chem Int Ed Engl.* **2016**, 55(7), 2446-9.
4. Pozzi C., Ciambellotti S., Bernacchioni C., Di Pisa F., Mangani S. and Turano P. Chemistry at the protein-mineral interface in L-ferritin: assisted assembly of a functional (μ^3-oxo)tris[(μ^2-peroxo)] triiron cluster ***Submitted***
5. Interaction studies of ferritin with lipids. ***In preparation***
6. "Ferritinoxis": a route to induce cancer cell death by the administration of ferritins. ***In preparation***
7. Spectral Investigation of the NAMI A/ferritin system. ***In preparation***

In Table 2, I added further details on the samples cited above. In particular, I summarized the optimal expression and purification conditions developed for each protein.

Source	Name	Strain	Isotopic labeling	Induction conditions T(°C), t(h), IPTG (mM)	Purification*	Yield (mg/L)
Bullfrog	H54A	BL21(DE3)pLysS	/	37°C, 4h, 1 mM	65°C, AE, SE	100
Human	HuHf	BL21(DE3)pLysS	/	37°C, 4h, 1 mM	65°C, AE, SE	110
Human	HuHf	BL21(DE3)pLysS	^{15}N, ^{13}C	37°C, O/N, 1 mM	65°C, AE, SE	70
Human	EF hand-HuHf	BL21(DE3)pLysS	/	17°C, 48h, 0.2 mM	65°C, AE, SE	100
Human	HuLf	BL21(DE3)pLysS	/	17°C, 48h, 0.2 mM	65°C, 70% AmS, AE, SE	45
Human	E60AE61AE64A	BL21(DE3)pLysS	/	17°C, 48h, 0.2 mM	65°C, 70% AmS, AE, SE	35
Human	FtMt	BL21(DE3)pLysS	/	37°C, 4h, 1 mM	65°C, AE, SE	60

Table 2. Expression and purification conditions with related protein yields.

* 65°C = after lysis of cell by sonication, the crude lysate is treated at 65°C for 15 minutes;
AE= anionic exchange chromatography;
SE= size exclusion chromatography;
70% AmS= precipitation in ammonium sulfate at 70 % of saturation.

Proteins listed in these tables were all produced as recombinants through the heterologous expression in *E. coli*. Essentially, after several expression trials, the best expression conditions in terms of *E. coli* competent cellular strain, temperature of incubation, time of induction and concentration of inductor were selected. Mutants were prepared with site-directed mutagenesis consisting in a PCR reaction with mutations-containing primers elongated by a high-fidelity DNA polymerase performed with a temperature cycler. QuikChange® Site-Directed Mutagenesis kit was used and the reactions performed according to the related protocol.

As regarding the detailed descriptions of each expression and purification procedure, they are available in the “Materials and Methods” sections of corresponding publications or draft manuscripts in the “Annexes” section.

Besides the *in cell* expression approach with *E. coli* bacteria, I produced HuHf also through the *cell-free* methodology with the RTS 100 *E. coli* HY Kit purchased from Eppendorf. This methods consists in protein synthesis *in vitro* through a coupled

transcription/translation reaction. An expression plasmid carrying the gene of interest is added to the reaction compartment to induce the synthesis. The DNA is first transcribed from the template vector into mRNA by T7 RNA polymerase, followed by translation by the ribosomal machinery present in the *E. coli* lysate. Expressed protein accumulates in the reaction compartment and is harvested after few hours. This kit allowed us to express functionally active HuHf in a 50 µl reaction from circular pET-9a plasmid carrying the H-ferritin gene within 6 hours. To evaluate the efficiency of protein expression, the kit provided the DNA template for GFP expression as a control. After the reaction, an SDS-PAGE analysis (Fig. 1) was performed to confirm the presence of the protein.

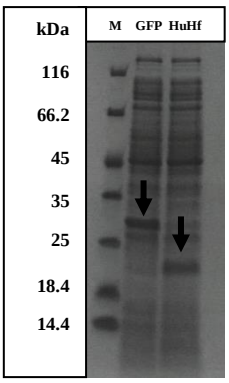

Figure 1. SDS-PAGE analysis of cell-free HuHf expression. In parallel the results of GFP and HuHf expressions. Black arrows indicate the bands corresponding to the molecular weights of the two proteins (30 kDa GFP, 20 kDa HuHf).

After the purification, the final protein yield was of 5 µg as measured by Bradford assay. The biomineralization capacity was verified by TEM analysis, showing the formation of the characteristic ferric core with a diameter size around 5nm (Fig. 2), and thus demonstrating that under cell-free expression the subunits self-assemble to produce the 24-mer cage.

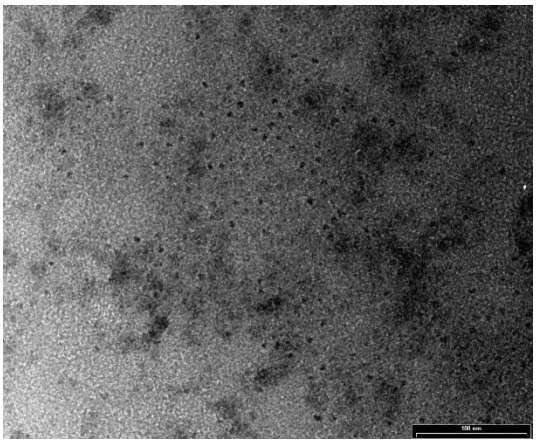

Figure 2. TEM analysis of HuHf expressed with the cell-free approach. Reconstituted HuHf with 960 Fe^{2+} per cage in Tris 20 mM pH 7.5 buffer. This buffer condition is not ideal to mineralize the protein but due to the very low quantity of available protein, a buffer exchange was not feasible.

Chapter 3

Iron pathways in ferritin nanocages

3.1 Ferritin: a peculiar diiron catalytic site

As already mentioned, each subunit of 24-mers ferritins is enzymatically active (H-type) except in animal ferritins, which coproduce a catalytically inactive subunit (L-type) that is responsible for the nucleation of the growing biomineral (1, 2). Amphibians have a further catalytically active type of subunits, called H′ (or M). Homopolymeric animal ferritins composed by catalytically active subunits have been extensively studied as model systems for the ferroxidase-driven iron biomineralization reaction.

Iron-binding sites in maxi-ferritins have been identified by conventional X-ray crystallography only for those from the extremophilic archaeon *Pyrococcus furiosus* (3), the prokaryote *Escherichia coli* (4) and the eukaryotic pennate diatom *Pseudo-nitzschia* (5). No iron-bound crystal structure was available until few years ago for ferritins from higher eukaryotes, but only structures with non-functional divalent cations as redox-stable alternative for Fe(II), namely, Zn(II) in human H ferritin and Mg(II) in H′ frog ferritin (RcMf) (6, 7). Those structures showed a dimetal center in the internal central position of the four-helix bundle with different number and nature of the metal ligands with respect to the ferroxidase sites in bacterial ferritins and bacterioferritins and in the catalytic sites of nonheme di-iron enzymes. Binuclear nonheme iron enzymes catalyze a variety of reactions using a largely conserved ligand set at the active site. Among the most studied there are ribonucleotide reductase (R2), which converts ribonucleotide into deoxyribonucleotides, and methane monooxygenase (MMO), which catalyzes the oxidation of methane to methanol. Spectroscopic and crystallographic studies of these proteins have shown that the catalytic sites contain two Fe(II) atoms that are weakly coupled through two bridging carboxylate ligands, and act as cofactors that are retained at the active site after the catalytic cycle. Dioxygen reacts with Fe(II) in the catalytic sites to form diferric peroxo intermediates, and in MMO and R2; these convert to high-valent intermediates (8). Instead, the ferritins with binuclear active sites accommodate two Fe(II) atoms as substrates. The substrate ions catalytically react with dioxygen to form diferric oxo/hydroxo products (9-11). The difficulty in detecting iron at the ferroxidase site in eukaryotic ferritins has been ascribed to the transient nature of this site where, at variance with R2 and MMO metalloenzymes, iron is not a cofactor at the catalytic center, but is a substrate that, after oxidation, has to be released to migrate toward the nanocavity to form the biomineral.

3.2 The structure of the ferroxidase site and the discovery of accessory iron binding sites in the catalytic cavity

Mangani *et al.* have developed a new crystallographic method that consists on flash-freezing ferritin crystals at different time intervals after exposure of apoferritin crystals to a crystalline ferrous salt. This approach lead for the first time to the identification of the two iron sites (called Fe1 and Fe2) in the dinuclear ferroxidase center of a vertebrate ferritin, RcMf (12, 13). The iron-coordinating residues in RcMf are Glu58, which bridges the two iron ions Fe1 and Fe2, monodentate Glu23 and His61 as Fe1 ligands and bidentate Glu103 as Fe2 ligand. Furthermore, multiple binding sites were identified in close proximity of the ferroxidase center and proposed to define the iron path from the entry ion channels to the oxidoreductase sites. Among these amino acid side chains, His54 was found to be differently populated at different times of free diffusion of Fe(II) through the ferritin crystals. The imidazole ring of His54 faces the inner cavity of ferritin and upon binding metal ions swings between two main conformations, named distal and proximal. This movement could be important to capture iron from the inner cavity and drag it into the 4-helix bundle channel. On the other hand, it could also constitute an exit strategy for the ferric products produced at the ferroxidase site and migrating into the inner cage cavity. To clarify the role of His54, we produced the H54A variant of RcMf to remove any possibility of binding metal ions at this position and evaluated the effect of this substitution on the ferritin activity (**Annex I**). In the H54A variant of RcMf, where the coordination imidazole ring is substituted by a non-coordinating aliphatic side chain, we observed a speeding up of the reaction, which becomes more evident at high turnover numbers (Fig. 1).

From this study, His54 appears to control the access of iron to the active site avoiding overloading before the catalytic reaction has been completed and the ferric-oxy/hydroxo products have been released towards the inner cavity. His54 could also have a defense role by trapping non-natural divalent cations, thus keeping them far from the dinuclear iron site, where they compete with iron inhibiting the reaction. Consistently, His54 has been observed to stably bind other transition metal cations such as Co(II) and Cu(II), trapping them out from the metal binding site (12, 14). His54 in RcMf corresponds to Gln58 in HuHf. Since the residues at the catalytic sites of RcMf and HuHf are highly conserved, the H54Q mutant of RcMf was studied to mimic the behavior of human ferritin. H54Q did not show any significant difference with wild type RcMf, neither in terms of activity nor in terms of ability

to transiently bind iron in crystals, indicating that the human and amphibian proteins do not differ for the function of the residue at this position.

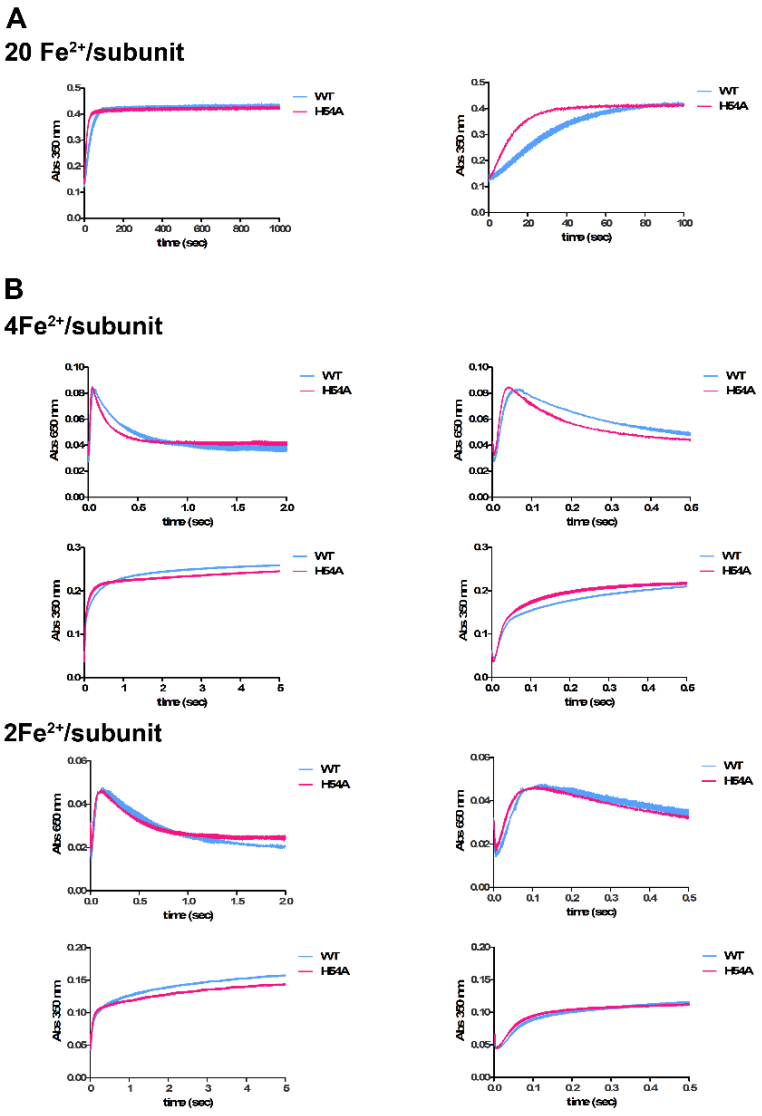

C

Initial rates of formation (fold-increase over WT values)

Protein	$(Fe^{3+}O)_x$ ($20Fe^{2+}$/subunit) ($\Delta A_{350\ nm}/s$)	DFP ($4Fe^{2+}$/subunit) ($\Delta A_{650\ nm}/s$)	$(Fe^{3+}O)_x$ ($4Fe^{2+}$/subunit) ($\Delta A_{350\ nm}/s$)	DFP ($2Fe^{2+}$/subunit) ($\Delta A_{650\ nm}/s$)	$(Fe^{3+}O)_x$ ($2Fe^{2+}$/subunit) ($\Delta A_{350\ nm}/s$)
H54A	2.4*	1.2*	1.2*	1.2*	1.2*

Figure 1. Kinetics of products formation in WT and H54A by rapid-mixing, UV–vis spectroscopy. A) Reaction progress at high iron:protein ratio (20 Fe^{2+}/subunit; 480 Fe^{2+}/cage) monitored as $(Fe^{3+}O)_x$ products ($A_{350\ nm}$) formation; the right panel shows an enlargement of the first 100 s. **B**) Formation and decay of DFP intermediate ($A_{650\ nm}$) (left) and formation of $(Fe^{3+}O)_x$ products ($A_{350\ nm}$) (right)measured after the addition of 4 Fe^{2+}/subunit (upper panels) or 2 Fe^{2+}/subunit (lower panels); the right panels show enlargements of the first 0.5 s to highlight the differences in the initial rates. Each graph shows a set of curves (mean±SEM) of a representative experiment of at least three. **C**) Table reporting the fold change over WT (set as 1) of the initial rates of formation of the various species. calculated from three independent analyses. *Significantly different from the corresponding value in wild type; $P < 0.05$. WT: blue curves, H54A: pink curves.

The wide ferritin panorama still lacked the identification of the iron-binding sites in a mammalian ferritin. To fill this gap, the crystallographic determination of iron adducts of HuHf was obtained (**Annex II**) by applying the same experimental method as used for previous study of RcMf.

A comparative analysis of the iron sites in RcMf and HuHf identified the same ferroxidase site but underlined clear differences in the pattern of ligands that defined the additional iron sites that precede the oxidoreductase binding sites along this path (Fig. 2).

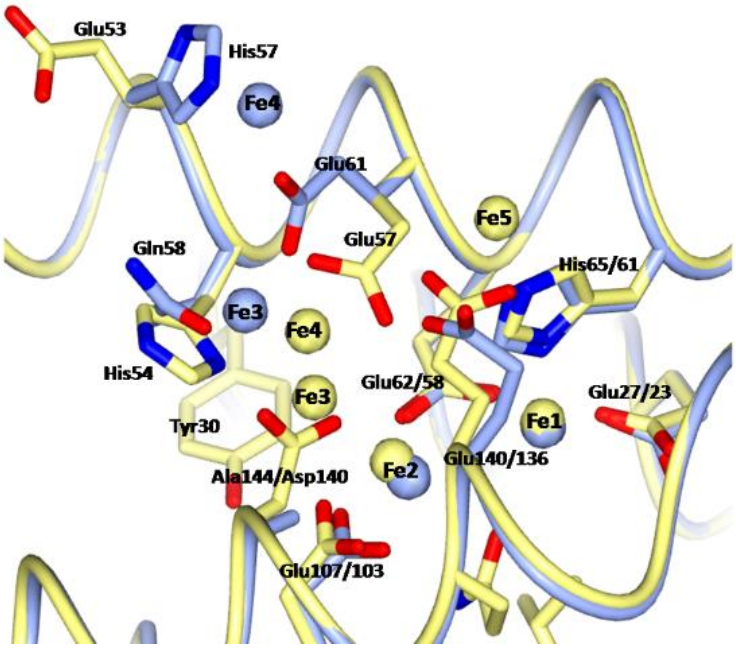

Figure 2. Superimposition of the Oxidoreductase Site (OS) of HuHf (pale blue ribbon) and RcMf (pale yellow ribbon). The different locations and ligands of the Fe3, Fe4 and Fe5 iron-binding sites are evident. The amino acids are represented as sticks coloured following the colour of the parent protein backbone.

Stopped-flow kinetics assays revealed that HuHf has different levels of activity compared with RcMf counterpart, which were attributed to the different nature of these accessory binding sites. Time-lapse anomalous data allowed us to follow the progressive population of a series of iron binding sites. Taken together, the time-lapse pictures from the present study delineate a pathway for the incoming Fe(II) ions that starts with the electrostatic attraction and hydrogen-bonding interactions of the Fe(II) hexa-aqua ions with the Asp131 and Glu134 residues in the threefold channel and continues with Glu140, Glu61, His57 and Gln58 to reach the Fe1 and Fe2 sites. The residues identified as active-site ligands in HuHf (i.e. Glu107, Glu62, His65 and Glu27) are all conserved in RcMf (the RcMf sequence

numbering is shifted by -4 with respect to HuHf) (Fig. 2). Glu62/Glu58 acts as a bridging ligand between the two metals Fe1 and Fe2; the metal at Fe1 is also bound to His65/His61 and monodentate Glu27/Glu23 while the metal at Fe2 binds bidentate Glu107/Glu103 (HuHf/RcMf numbering, respectively).

Accessories transient metal sites (Fe3, Fe4 and, in some cases, Fe5) have been also identified. There are meaningful differences in the amino-acid composition of the oxidoreductase site residues proposed to be additional transient iron-binding sites between the two ferritins. In RcMf Fe3 is bound only to His54; Fe4 is bound to Glu57 and to Asp140. A further binding site Fe5 is bound to Glu136. In HuHf Fe3 is bound to Gln58 and Glu61 and occupies a different location with respect the RcMf Fe3; Asp140 (RcMf) is substituted by the non-coordinating Ala144 (HuHf). The crystal structure of HuHf confirmed that Gln58 is involved in controlling the access of iron into the Fe1 and Fe2 iron binding sites in a dynamic process, as shown by the structural disorder present in this portion of the cavity. The fourth iron ion is bound to His57 in HuHf, which replaces Glu53 in RcMf. In HuHf there are no evidences of a Fe5 site. The replacement of RcMf residues Glu53, His54 and Asp140 with HuHf His57, Gln58 and Ala144, respectively, results in the net loss of two negative charges and in different ligand strengths towards iron ions in the HuHf oxidoreductase site. Consequently, it is not surprising that the kinetic data show different reaction rates for the same iron loading of the two enzymes and markedly different decay rates of the DFP intermediate (Fig. 3 A and B). Nevertheless, for both RcMf and HuHf, stopped-flow kinetic measurements reveal that the same intermediate species form during the reaction, although with different kinetics. In both cases, at least a stoichiometry of two Fe(II) ions per subunit is needed for the activity at the OS to clearly observe the formation of the DFP intermediate, its rapid decay (through a monoexponential process) as well as the formation of the ferric oxo species. As demonstrated in the structures solved in collaboration with Mangani *et al.*, a distinguishing feature of the ferritin diiron substrate catalytic centers is the weaker Fe(II) ligands in the Fe2 site that contrast with diiron cofactor catalytic centers. Ferritin diiron substrate centers lack one of the two carboxylate ligands of the diiron cofactor sites of R2 and MMO, which, like iron in the ferritin substrate sites, react with O_2 to form a DFP intermediate. Only four of the six iron ligands at the ferroxidase catalytic centers of ferritins are present in diiron enzyme cofactor centers (Fig. 4 A-C).

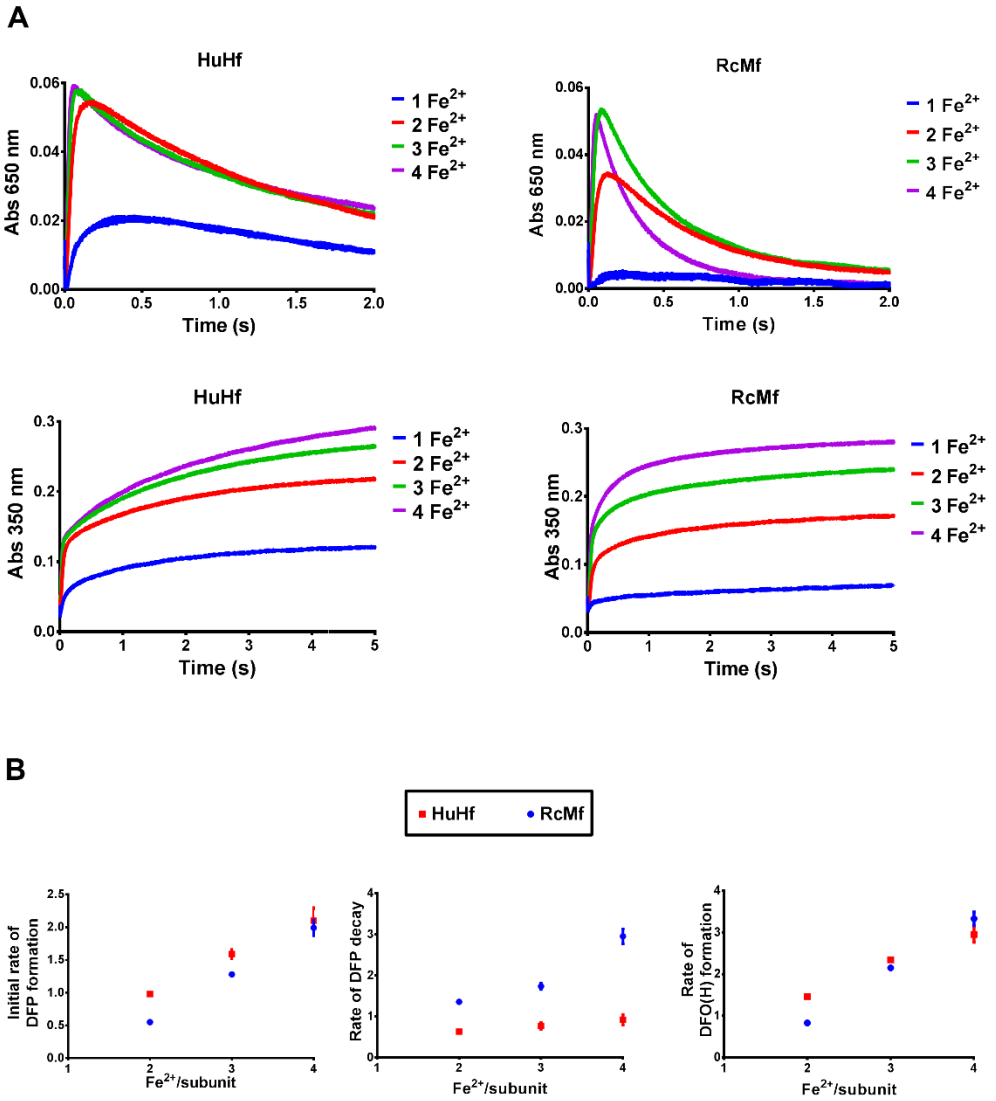

Figure 3. A) The catalytic reaction rates in HuHf and RcMf are differently modulated by the Fe^{2+}:subunit ratio. Comparison of the reaction kinetics of the formation of (upper panels) the intermediate DFP ($A_{650\ nm}$) and (lower panels) the products DFO(H) ($A_{350\ nm}$) after the addition of one, two, three and four Fe^{2+} ions per subunit to HuHf (left) and RcMf (right). **B**) The panels show the dependency on the Fe^{2+}:subunit ratio of the initial rates of the formation of DFP (left), the decay of DFP (middle) and the formation of DFO(H) (right).

The two divergent residues in the ferritin catalytic centers are both in the Fe2 site, namely, a conserved glutamine at position 141 in ferritins against glutamate in the cofactor sites (where it acts as a second metal bridge) and a variable residue at position 144 (HuHf numbering) such as alanine, aspartate or serine instead of conserved histidine in the cofactor sites. These differences in the ferritin catalytic centers residues are associated with a weaker Fe(II) binding environment and a more open structure with a single carboxylate bridge between the two Fe atoms in structures of ferritin diiron substrate sites compared with the

stronger binding environment and more closed structures in the R2 and MMO diiron cofactor sites.

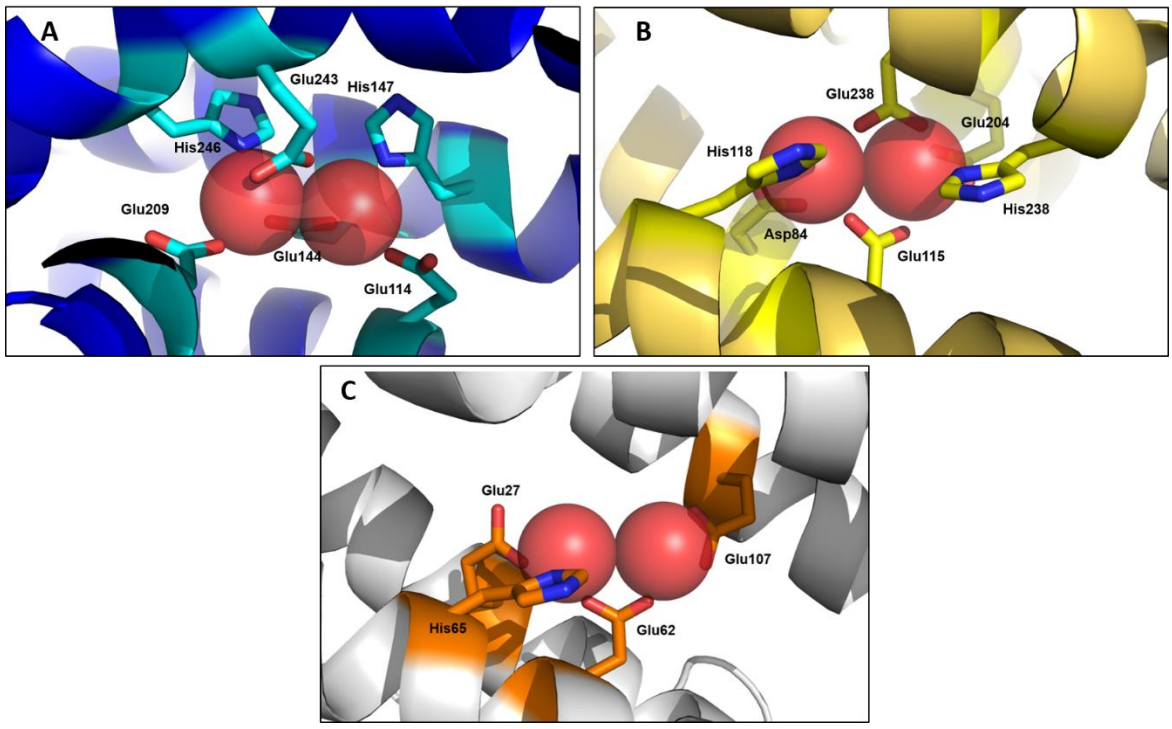

Figure 4. Diiron catalytic sites: iron cofactor Vs iron substrate. A) View of the catalytic site of MMO with iron coordinating residues represented in cyan sticks (PDB id 1FYZ. **B**) R2 catalytic site and iron coordinating residues in yellow sticks (PDB id 1PFR). **C**) HuHf catalytic sites with iron coordinating residues represented in orange sticks (PDB id 4OYN).

In all bacterioferritins' structures, two metal ions have been found in the ferroxidase center just like in Ftns; however, the coordination environment of sites Fe1 and Fe2 is different. In fact two glutamate residues act as bridging ligand for the metal ions in sites Fe1 and Fe2; while in Ftns one of the glutamate residues is replaced by a glutamine. The second difference is in one of the residues of site Fe2 that is highly variable in organisms as *Pyrococcus furiosus* Ftn (Glu130) or in HuHf (Ala141), while this residue in bacterioferritin appears to always be a histidine. The coordinating amino acid residues to the iron in the ferroxidase center of bacterioferritins are identical to those of the diiron catalytic site in dioxygen-activating enzymes.

In summary, the X-ray data on HuHf helped defining some key structure/function relationships:

1. The binuclear ferroxidase site is maintained in different vertebrates' ferritins, with common ligands for Fe1 and Fe2.

2. Metal ions at the ferroxidase site are loosely bound when compared to those of diferric metalloenzymes.

3. The ability to release reaction products from the ferroxidase site, as required by the ferroxidase reaction turnover, is realized through the presence of accessory iron binding sites that, shuttle new incoming irons towards the ferroxidase site.

4. The accessory sites are provided by iron ligands that are different between H and M ferritins and this influence the ferroxidase reaction rates.

3.3 Biomineralization

As already stressed, the multistep biomineralization process in ferritin remains largely elusive. The entire process is governed by a number of specific, but weak, interactions between the protein shell and the iron species moving across the cage. This situation constituted the major problem for crystallography; the approach of solid-to-solid iron diffusion followed by flash freezing allowed us to detect the iron in its path through the C3-channels and in the ferroxidase cavity.

We also tried to obtain information of the events occurring after iron oxidation at the ferroxidase site that lead to the formation of the iron oxide caged biomineral. Understanding the chemical structure of the ferritin core may also help, for example, to elucidate the alteration or dysfunction of ferritin and its role in the development of degenerative diseases.

The existing knowledge on the biomineralization process was very limited. The only low-resolution structural data on the biomineral precursor in ferroxidase-active ferritins originated from NMR. Here at CERM an original NMR approach was designed and used to characterize the interaction with iron of the 480 kDa RcMf ferritin cage. NMR analysis of ferritin represented a challenge for two main reasons: spectral crowding and signal broadening. Large molecular assemblies generally imply a signal crowding; the RcMf nanocage represents a favorable case of high molecular weight assembly because of its homopolymeric composition in a highly symmetric arrangement; in practice, the number of observed signals equals that expected for a single subunit. Nevertheless, the resolution of ^{1}H experiments is compromised by signal line width broadened beyond detection. Neither producing perdeuterated sample (up to 90% of deuteration) is sufficient to use solution ^{1}H

detection NMR. Starting from those considerations, Turano *et al.* developed an original combination of solution and solid state experiments on the model homopolymeric RcMf enriched with ^{2}H, ^{13}C, ^{15}N isotopes based on ^{13}C-detection NMR (15). Briefly, the sequential assignment obtained for 59 over 176 residues with ^{13}C-^{13}C DARR at the solid state was transferred to solution ^{13}C-^{13}C NOESY, since the spectra were essentially superimposable. To study the reaction of ferritin with iron, they used the assigned residues as probes to locate paramagnetic ferric species in the protein cage following the increasing line broadening on the resonances of nearby residues. Increasing the equivalents of Fe(II) added in ferritin solution the broadening even beyond detection suggested that:

The ferric products that form at the first catalytic turnover remain bound at the ferroxidase site, which therefore is always occupied in the non-apo protein. This finding is fully consistent with our X-ray data (see Section 3.2). The ferric products that form in subsequent turnovers move from the catalytic site in the middle of the four-helix bundle toward the short fifth helix at the C-terminus of each subunit. Moreover, magnetic susceptibility measurements suggested that the species emerging from the OS formation iron clusters of increasing nuclearity (dimers, tetramers and octamers of iron), as derived from bulk susceptibility measurements.

These two findings together with the presented X-ray data confirm a push-pull mechanism as the driving force of the successive turnovers that is driven by the nature of the residues in the accessory iron binding sites (as discussed in Section 3.2). They also propose the formation of multimeric iron clusters as mineral precursors. The existence of such clusters has been also proposed by Mossbauer (16). Nevertheless, X-ray crystallography is unable to observe both biomineral precursor clusters and the biomineral itself.

Here, the formation of the iron-oxo core has been monitored by transmission electron microscopy (TEM) using unstained iron-loaded protein. A mineral of 4.74 ± 0.26 nm for HuHf versus 5.37 ± 0.29 nm for RcMf was observable for iron:cage ratio of 1920:cage (Fig. 5).

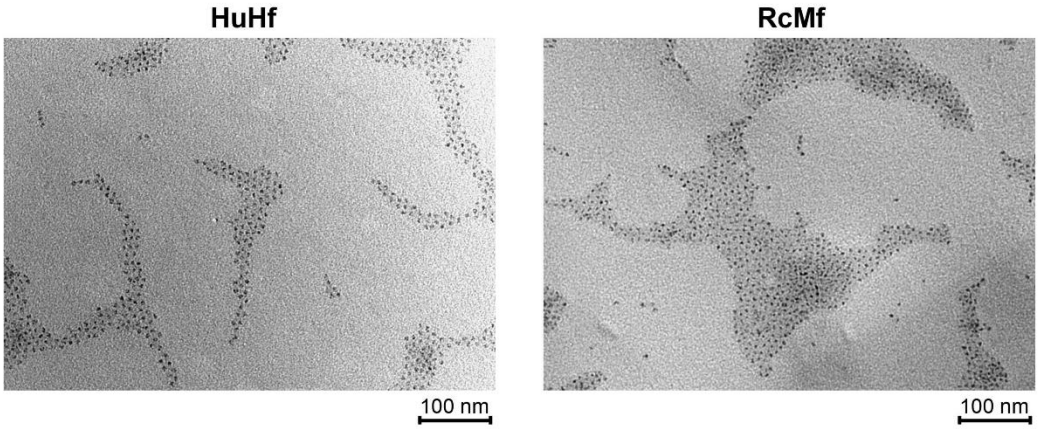

Figure 5. Biomineral core characterization. Representative TEM micrographs of HuHf and RcMf caged biominerals obtained from 3.0 μM solutions of each protein mineralized with ferrous sulfate (80 Fe^{2+} ions per subunit). Bright-field TEM let us to observe the formation of an iron-oxo core without contrast dying of the protein, thanks to the high electron density of the ferric biomineral. The proteins, both HuHf and RcMf, were reconstituted with 80 Fe^{2+} ions per subunit. The TEM micrographs showed a quite regular shape with comparable size in spite of the different rates of the catalytic reactions descripted above.

The same protein samples analyzed via X-ray crystallography did not show any trace of biomineralized iron. X-ray crystallography can only locate biomineral precursors or biomineralized iron if they show architectural consistency arranged over the crystal lattice; apparently, this is not our case. On the other, TEM only detects the final stages of the biomineralization, when the iron oxide particles have a measurable size.

AADF-STEM has been used by López-Castro *et al* (17) to show that the fine structure of the biomineral is slightly different between H- and L-cages. In the latter it seems that the iron core grows starting from nucleation sites at the inner cage surface giving rise to a fine structure of the biomineral under the form of discrete electron-dense cores. Although the ferritin mineral core was traditionally described as ferrihydrite (18), other studies based on TEM, SAXS and XANES on L-ferritin, have revealed a polyphasic structure, consisting of ferrihydrite and other phases, including a magnetite-like phase (19, 20). The different phases do not coexist within a single core; magnetite appears to form along the inner surface of the protein shell, while hematite and ferrihydrite are more prevalent closer to the center of the mineral (Fig. 6). These two studies can be reconciled assuming that the magnetite (i.e. Fe_3O_4) forms in correspondence of the nucleation sites of L subunits.

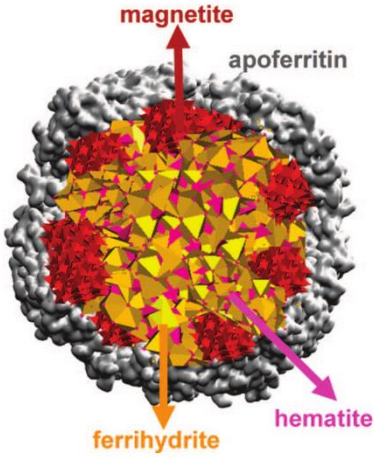

Figure 6. Composition of the ferritin mineral core. Reprinted from J. Am. Chem. Soc. 130 (2008) 8062–8068. A schematic core-shelled ferritin iron core structure.

3.4 Nucleation site of human L-ferritin

It is generally accepted that in ferritin cages lacking (like the human L ferritin) or containing a low number of ferroxidase-active subunits (like the heteropolymer found in horse spleen), the core biomineral formation proceeds via oxidation of Fe^{2+} at specific, yet unobserved, nucleation sites that facilitate the subsequent growth of the biomineral. L-subunits lack the ferroxidase site, whereas a number of other residues are conserved with respect to the H-subunit (homology 53% between human L- and H-chains; Fig. 7) (21). Consequently, iron incorporation in nanocages rich in L-subunits is much slower. Nevertheless, even homopolymeric L-ferritins are able to biomineralize iron.

```
           1         10        20        30        40        50        60        70
FRIH_HUMAN TTASTSQVRQNYHQDSEAAINRQINLELYASYVYLSMSYYFDRDDVALKNFAKYFLHQSHEEREHAEKLM
FRIL_HUMAN ----SSQIRQNYSTDVEAAVNSLVNLYLQASYTYLSLGFYFDRDDVALEGVSHFFRELAEEKREGYERLL

           71        80        90        100       110       120       130       140
FRIH_HUMAN KLQNQRGGRIFLQDIKKPDCDDWESGLNAMECALHLEKNVNQSLLELHKLATDKNDPHLCDFIETHYLNE
FRIL_HUMAN KMQNQRGGRALFQDIKKPAEDEWGKTPDAMKAAMALEKKLNQALLDLHALGSARTDPHLCDFLETHFLDE

           141       150       160       170       180
FRIH_HUMAN QVKAIKELGDHVTNLRKMGAPESGLAEYLFDKHTLGDSDNES
FRIL_HUMAN EVKLIKKMGDHLTNLHRLGGPEAGLGEYLFERLTLKHD----
```

Figure 7. Alignment of amino acid sequences of HuHf and HuLf (FRIH_HUMAN and FRIL_HUMAN respectively), performed by Clustal Omega. All sequences are depleted of the initiator methionine. In light blue, the residues binding the metal cluster in L-ferritin. In orange, the iron-binding amino acids in the ferroxidase site of the catalytically active H-subunit and the corresponding amino acids in HuLf (lacking the ferroxidase site). In magenta, the amino acids in the conserved pore responsible of iron entry.

With a similar X-ray method as introduced above for HuHf, we solved the crystal structure (1.98 Å resolution) of the iron-loaded recombinant homopolymeric L-human ferritin (HuLf) and detected for the first time iron bound at inner cage sites of L-subunits in the form of a triiron(III) triperoxo cluster (Fig. 8 A and B) (see **Annex III**). The protein acts as a template for the anchoring of the metal cluster providing glutamic acid side chains of Glu60 (bridging Fe1 and Fe3), Glu61 (bridging Fe2 and Fe3) and Glu64 (bridging Fe1 and Fe2). Glu57 acts as a monodentate ligand to Fe3 and seems to shuttle towards the cluster incoming iron under the form of ferrous aqua ions (human H-chain aligned numbering, see Fig. 7).

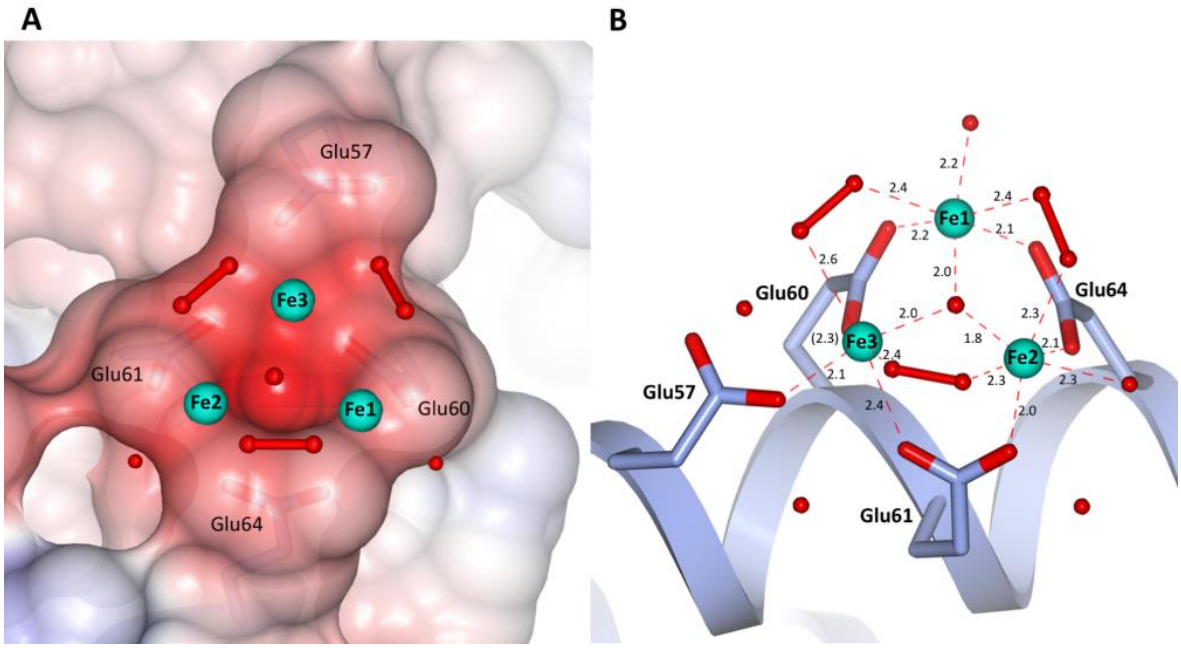

Figure 8. Different views of the trinuclear iron binding site in HuLf. A) Electrostatic surface representation of the trinuclear cluster binding site. Iron ions and water molecules are represented as cyan and red spheres, respectively. Peroxide molecules are shown as red ball-and-stick models. **B**) Structure of the oxo-centered trinuclear iron cluster. Coordinating glutamates are highlighted as sticks. Iron ions, water and peroxide molecules are represented as in "A". Coordination bonds to iron ions are shown as dashed red lines; coordination distances (Å) are also displayed. Two different orientations are proposed in panels A and B to better appreciate the structural features of the protein site and metal cluster.

A similar metallocluster was observed in the lower resolution (2.22 Å) structure of horse spleen ferritin, a natural heteropolymer where more than 85% of subunits are L-type, suggesting that it represents a common feature of mammalian ferritins.

More in details, three iron ions are coordinated to the above carboxylate side chains, generating a μ^3-oxo centered trinuclear cluster. The carboxylate groups of Glu60, Glu61 and Glu64 symmetrically bridge the three Fe couples on the same side of the cluster. On the

opposite side, each pair of iron ions results connected by an elongated electron density compatible with a diatomic molecule. The observed densities have been interpreted as due to three peroxide anions generating a second series of bridges. A likely explanation of the described arrangement of the iron ions in this site, is that we have detected a (μ^3-oxo)tris[(μ^2-peroxo)(μ^2-glutamato-κ*O*:κ*O*')](glutamato-κ*O*)(diaquo)triiron(III) anion. The comparison with the iron-free HuLf structure reveals that the formation of the oxo-centered trinuclear iron cluster occurs without modification of the protein fold, but with a rearrangement of the glutamate side chains involved in iron coordination. The cluster structure is unprecedented in biological systems although it shows striking structural similarities to a synthetic hexanuclear iron cluster (Fig. 9), proposed about 20 years ago as a possible model of ferritin biomineral (22).

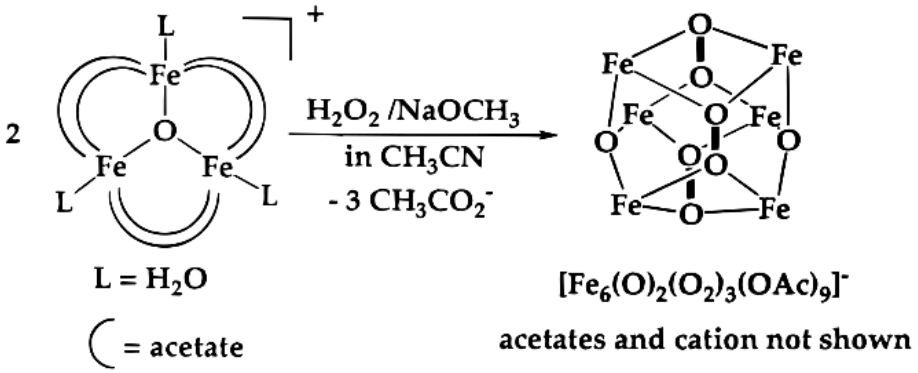

Figure 9. Synthetic hexanuclear iron cluster proposed as a possible model for ferritin biomineral. Reprinted from J. Am. Chem. Soc. 1997, 119, 1037-1042.

The structural similarity between the two cluster supports:

i) our interpretation of the elongated electron densities as due to peroxide species, which could form as a consequence of iron oxidation at the nucleation site;

ii) the presence of iron ions in the ferric state resulting in an overall trinegative charge of the assembly in HuLf, which can provide the driving force to attract new iron(II) ions to promote oxidation and biomineralization, as exemplified by the observed fourth iron ion approaching the cluster via Glu57.

To corroborate X-ray data and establish a functional significance for the observed patch of carboxylate side chains and the resulting cluster, site-directed mutagenesis was

applied to produce E60AE61AE64A mutant in order to prevent iron coordination at these sites. The comparison of the iron oxidation kinetics in the wild type and E60AE61AE64A variant of HuLf nanocage showed a significantly lower reaction rate for the mutant especially at low iron content (Fig. 10). For comparison purposes, we report also the oxidation kinetic of Fe(II) in the absence of ferritin to show the fundamental role of the protein cage, that maintains soluble the Fe(III) species that otherwise precipitate at physiological pH. The latter process is shown by the blue curves, where the absorbance at 350 nm falls down with time due to precipitation of the ferric oxo species (Fig. 10 A-D).

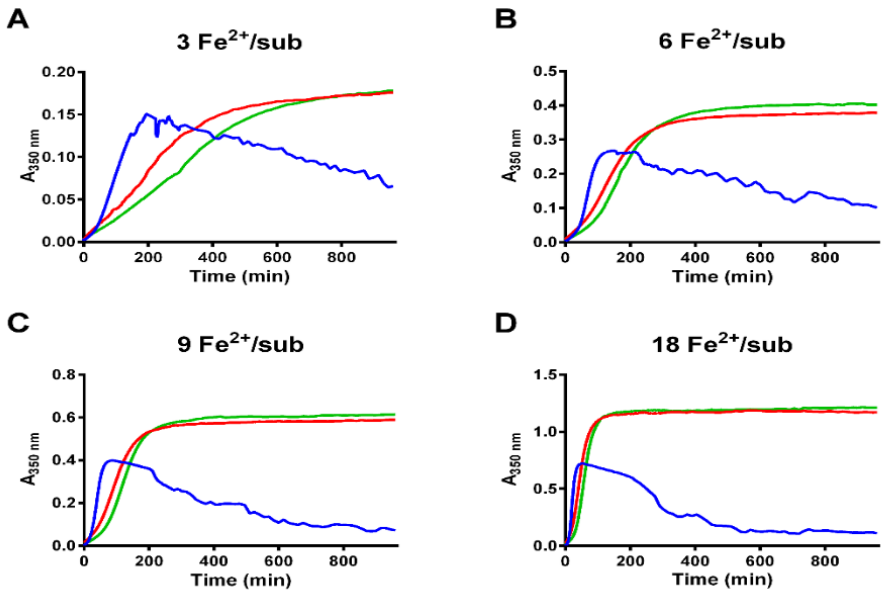

Figure 10. Kinetic measurements in WT and E60AE61AE64A HuLf variant. Kinetics of oxo-ferric species formation followed spectrophotometrically as the change in absorbance at 350 nm over 16 hours (960'). Different concentrations of Fe^{2+} were incubated, at room temperature, in 200 mM MOPS 200 mM NaCl pH 7 buffer with 25 µM protein subunits of WT HuLf (red curves) and triple mutant E60AE61AE64A (green curves) or without protein (blank, blue curves). Addition of: A) 3 Fe^{2+} ions per subunit; B) 6 Fe^{2+} ions per subunit; C) 9 Fe^{2+} ions per subunit; D) 18 Fe^{2+} ions per subunit.

We therefore proposed that the observed metal cluster corresponds to the suggested (23, 24) nucleation site of animal L-ferritins.

As a perspective work, we plan to investigate deeply the proposed role of Glu57 in iron shuttling; a further mutant has been designed, called E57AE60AE61AE64A. The tetra-mutant will be subjected to the same functional analysis as the wild type and its triple-mutant.

3.5 Highlights

In summary, our studies on H nanocages have led to the definition of the ferroxidase diiron centers where Fe1 and Fe2 sites contain iron ions that are more loosely bound that in dicarboxylate diferric sites due to the lower number of protein ligands and where the flexibility of the amino acid ligands allows to modulate the distance between the two metal ions as a function of their oxidation state. In H ferritin, we might have been able to trap dioxygen bound to the diferrous center.

In L cages, we have identified a novel trinuclear iron cluster, which is unprecedented in bioinorganic chemistry and might represent the nucleation site in ferroxidase-inactive subunits.

Beside shedding light on the mechanism of ferritin reactions, these results contribute to expand the ensemble of metal cofactors in metalloproteins.

Reference List

1. Arosio P, Ingrassia R, Cavadini P (2009) Ferritins: a family of molecules for iron storage, antioxidation and more. *Biochim. Biophys. Acta - Gen. Subj.* **1790**:589-599.

2. Torti FM, Torti SV (2002) Regulation of ferritin genes and protein. *Blood.* **99**:3505-3516.

3. Tatur J, Hagen WR, Matias PM (2007) Crystal structure of the ferritin from the hyperthermophilic archaeal anaerobe Pyrococcus furiosus. *J. Biol. Inorg. Chem.* **12**:615-630.

4. Stillman TJ *et al.* (2001) The high-resolution X-ray crystallographic structure of the ferritin (EcFtnA) of Escherichia coli; comparison with human H ferritin (HuHF) and the structures of the Fe(3+) and Zn(2+) derivatives. *J. Mol. Biol.* **307**:587-603.

5. Marchetti A *et al.* (2009) Ferritin is used for iron storage in bloom-forming marine pennate diatoms. *Nature* **457**:467-470.

6. Ha Y *et al.* (1999) Crystal structure of bullfrog M ferritin at 2.8 Å resolution: analysis of subunit interactions and the binuclear metal center. *J. Biol. Inorg. Chem.* **4**:243-256.

7. Toussaint L *et al.* (2007) High-resolution X-ray structures of human apoferritin H-chain mutants correlated with their activity and metal-binding sites. *J Mol Biol* **365**:440-452.

8. Schwartz JK *et al.* (2008) Spectroscopic definition of the ferroxidase site in M ferritin: comparison of binuclear substrate vs cofactor active sites. *J. Am. Chem. Soc.* **130**:9441-9450.

9. Logan DT *et al.* (1996) Crystal structure of reduced protein R2 of ribonucleotide reductase: The structural basis for oxygen activation at a dinuclear iron site. *Structure* **4**:1053-1064.

10. Rosenzweig AC *et al.* (1995) Geometry of the soluble methane monooxygenase catalytic diiron center in two oxidation states. *Chem Biol* **2**:409-418.

11. Lee SK, Nesheim JC, Lipscomb JD (1993) Transient intermediates of the methane monooxygenase catalytic cycle. *J. Biol. Chem.* **268**:21569-21577.

12. Bertini I *et al.* (2012) Structural insights into the ferroxidase site of ferritins from higher eukaryotes. *J. Am. Chem. Soc.* **134**:6169-6176.

13. Pozzi C *et al.* (2015) Time lapse, anomalous X-ray diffraction shows how Fe2+ substrate ions move throgh ferritin protein nanocages to oxidoreductase sites. *Acta Cryst. D* **D71**:941-953.

14. Tosha T *et al.* (2010) Moving metal ions through ferritin-protein nanocages from three-fold pores to catalytic sites. *J. Am. Chem. Soc.* **132**:14562-14569.

15. Turano P *et al.* (2010) NMR reveals a pathway for iron mineral precursors to the central cavity of ferritin. *Proc. Natl. Acad. Sci. USA* **107**:545-550.

16. Bauminger ER *et al.* (1993) Iron (II) oxidation and early intermediates of iron-core formation in recombinant human H-chain ferritin. *Biochem. J.* **296**:709-719.

17. Lopez-Castro JD *et al.* (2012) A new approach to the ferritin iron core growth: influence of the H/L ratio on the core shape. *Dalton Trans.* **41**:1320-1324.

18. Chasteen ND, Harrison PM (1999) Mineralization in ferritin: an efficient means of iron storage. *J Struct Biol* **126**:182-194.

19. Quintana C, Cowley JM, Marhic C (2004) Electron nanodiffraction and high-resolution electron microscopy studies of the structure and composition of physiological and pathological ferritin. *J. Struct. Biol.* **147**:166-178.

20. Quintana C (2007) Contribution of analytical microscopies to human neurodegenerative diseases research (PSP and AD). *Mini. Rev. Med. Chem.* **7**:961-975.

21. Andrews SC *et al.* (1992) Structure, function, and evolution of ferritins. *J Inorg Biochem* **47**:161-174.

22. Shweky I *et al.* (1997) A Hexairon(III) Complex with Three Non-Planar h2-m4-Peroxo Ligands Bridging Two Basic Iron Acetate Units. *J. Am. Chem. Soc.* **119**:1037-1042.

23. Behera RK, Theil EC (2014) Moving Fe^{2+} from ferritin ion channels to catalytic OH centers depends on conserved protein cage carboxylates. *Proc. Natl. Acad. Sci. U. S. A* **11**:7925-7930.

24. Haldar S, Bevers LE, Tosha T, Theil EC (2011) Moving Iron through ferritin protein nanocages depends on residues throughout each four a-helix bundle subunit. *J. Biol. Chem.* **286**:25620-25627.

Chapter 4

Ferritin-based nanocarriers

Ferritin and its structural and biochemical features have been widely exploited in bionanotechnology applications ranging from the production of metal nanoparticles to templated production of semi-conductors as well as scaffold nanocage for vaccine design and drug delivery. In this thesis section, I will describe experiments related to the use of human ferritins as a drug delivery system, especially for cancer therapy. The ability of ferritin cages to disassemble and reassemble under pH control has allowed for the loading of a number of potentially therapeutic compounds (see Section 1.4). The combination of modifiable interior and exterior surfaces, and the presence of hydrophobic and hydrophilic channels across the cage, allows the inclusion or attachment (chemical cross-linking) of both water-insoluble and soluble drugs for delivery.

4.1 Nanocarriers in cancer therapy

Nanotechnology offers opportunities in disease prevention, diagnosis and therapy (1). Among the various approaches for biomedical applications, nanocarriers offer some unique advantages as delivery, sensing and imaging agents (2). Many drugs used for pharmacotherapy, while have a beneficial action, can also exhibit side effects that may limit their clinical application. For example, cytotoxic compounds used in cancer therapy can kill target cells, but also normal cells in the body. In order to achieve better therapeutic application, nanocarriers are considered for target-specific delivery of drugs and gene to various sites in the body in order to improve the therapeutic efficacy, while minimizing undesirable side effects. Loading of drugs into nanocarriers can increase their *in vivo* stability, extend compound's blood circulation time and allow for controlled drug release and accumulation preferably at the tumor site. This phenomenon is known as enhanced permeability and retention effect (EPR). Summarizing there are five advantages to use nanocarriers to vehicle drugs instead of administering drugs alone. First, nanoparticles may help to overcome problems of solubility and chemical stability of anti-cancer drugs. Second, they can protect anti-cancer compounds from biodegradation or excretion and thus influence the pharmacokinetic profile of a compound. Third, nanosystems can help to improve distribution and targeting of anti-tumor therapy. Distribution of anti-cancer drugs is defined by their physico-chemical properties and is limited by drug penetration into tumor tissue. Both passive and active targeting strategies are used to redirect anti-cancer drugs (see below). Fourth, nanocarriers can be designed to release their payload upon a trigger resulting in

stimuli-sensitive nanomedicine therapeutics. Finally, targeted nanomedicine therapeutics may decrease resistance of tumors against anti-cancer drugs. Generally, specific uptake reduces the probability for unspecific efflux pump-driven elimination.

As mentioned above, there are essentially two kind of specific delivery: passive and active targeted delivery (Fig. 1).

The majority of tumour-targeted nanomedicines systems utilize the so-called ‘passive targeting’ concept. By designing the systems such that a long circulation time is achieved, significant accumulation in tumours is obtained, especially in those tumour areas with active angiogenesis. Passive targeting refers to the extravasation of the nanomedicine-associated drug into the interstitial fluid at the tumour site, exploiting the locally increased vascular permeability. In addition, solid tumours tend to lack functional lymphatics, and extravasated (nano)materials are retained within the tumour site for prolonged periods of time. The exploitation of this so-called ‘enhanced permeability and retention’ (EPR) effect is currently the most important strategy for improving the delivery of low-molecular-weight (chemo)therapeutic agents to tumours (3-5).

The active-targeting concept utilizes the specific binding affinities of targeting ligands that are bound to the drug or drug-carrier systems used to selectively target site receptor structures. This approach also takes advantage of the EPR effect for accumulation of the drug-carrier system into the interstitial fluid of the tumor. Some delivery systems has been developed in order to bind to specific surface receptors that are endocytosis prone (5, 6), such as the folate receptor that is upregulated and numerous in many cancers, while has low access in normal cells (7), the transferrin receptor that internalizes continuously even if the ligand is not bound (8) and the epidermal growth factor receptor (EGRF).

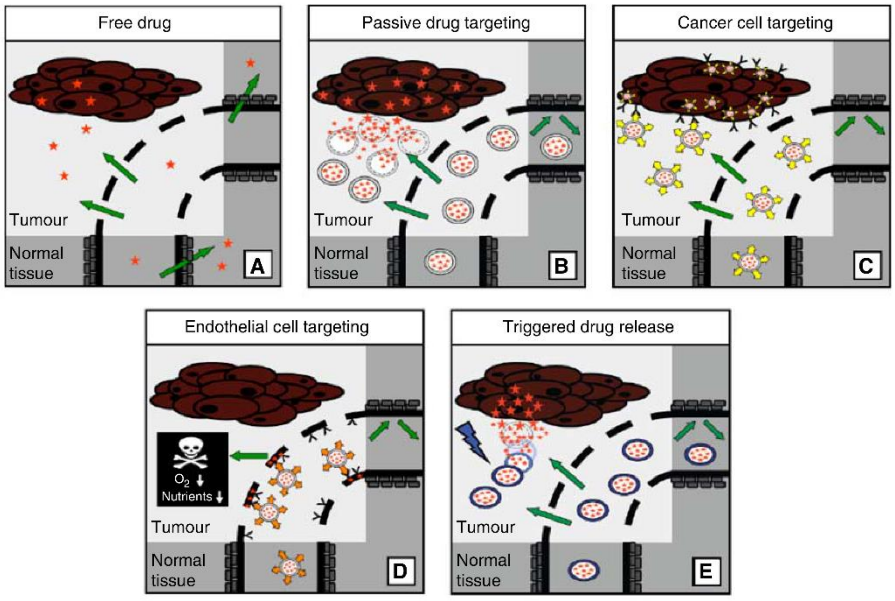

Figure 1. Overview of the clinically most relevant drug targeting strategies. Reprinted from British Journal of Cancer (2008) 99, 392–397. A) Upon the intravenous injection of a low-molecular-weight (chemo)therapeutic agent, which is often rapidly cleared from blood, only low levels of the drug accumulate in tumours and in tumour cells, whereas their localization to certain healthy organs and tissues can be relatively high. **B**) Upon the implementation of a passively targeted drug delivery system, by virtue of the enhanced permeability and retention (EPR) effect, the accumulation of the active agent in tumours and in tumour cells can be increased substantially. **C**) Active drug targeting to internalization-prone cell surface receptors (over)expressed by cancer cells generally intends to improve the cellular uptake of the nanomedicine systems, and can be particularly useful for the intracellular delivery of macromolecular drugs, such as DNA, siRNA and proteins. **D**) Active drug targeting to receptors (over)expressed by angiogenic endothelial cells aims to reduce blood supply to tumours, thereby depriving tumour cells from oxygen and nutrients. **E**) Stimuli-sensitive nanomedicines can be activated (i.e., induced to release their contents) by externally applied physical triggers, such as hyperthermia, ultrasound, magnetic fields and light.

In addition to targeted delivery, a number of studies, especially in cancer therapy, have shown that stimuli-responsive nanocarriers can provide significant advantages. The use of stimuli-responsive nanocarriers offers an interesting opportunity for drug delivery where the delivery system becomes an active participant, rather than passive vehicle, in the optimization of therapy. The benefit of stimuli responsive nanocarriers is especially important when the stimuli are unique to disease pathology, allowing the nanocarrier to respond specifically to the pathological "triggers". Select examples of biological stimuli that can be exploited for targeted drug delivery include pH, temperature and redox microenvironment (2). Besides the classical structural ferritin characterization, my PhD activities regarded also the development of different ferritin nanocarriers of different types, as described in Sections 4.2-4.4/5). This part of my research project has been supported by PRIN 2012 namely "Innovative chemical tools for improved molecular approaches in biomedicine".

In Section 4.2, functionalized ferritin at the surface are introduced describing the possible advantages of PEGylation in nanomedicine especially for drug-delivery. In Sections 4.4 and 4.5, ferritins loaded with two different metal-based antitumor molecules are proposed. Due to the fact that ferritin cages are recognized by specific cellular receptors (see Section 1.4), in principle, they can be all exploited for active targeting any time those receptors are overexpressed at the target site allowing specific receptor-mediated endocytosis. Nevertheless, in case of ferritins, SCARA 5 and TfR1 for L and H cages respectively are expressed in several types of cells, making more difficult to obtain a localized internalization. To increase this probability and to prevent accumulation in undesired sites, a further functionalization of ferritin surface can be applied, as in case of PEGylated HuHf. This particular modification causes the protein to become stealth even for TfRs increasing its life-time circulation and the possibility to reach in a passive targeting way the tumour site exploiting the EPR effect.

4.2 PEGylated ferritin

Biological drugs (biologics) are the fastest-growing category of approved therapeutics. Most biologics are proteins that are the closest proxy of a “natural” help against disease. Unfortunately, proteins have poor pharmacokinetic and safety profiles. Protein solubility, route of administration, distribution and stability are all factors that can hinder the successful application of a protein therapy (9). Proteins are large molecules with both hydrophilic and hydrophobic properties that can make entry into cells and other compartments of the body difficult. The half-life of a therapeutic protein can be drastically affected by proteases, protein-modifying chemicals or other clearance mechanisms. Another important challenge is that the body may cause an immune response against the therapeutic protein (10).

In order for a protein or a protein-based nanocarrier to achieve the desired benefits, it must be present in the bloodstream long enough to reach or recognize their target site of action, as described in five points in Section 4.1. Opsonization and phagocytosis are two common mechanisms considered the major obstacles to the realization of these goals. The macrophages of the mononuclear phagocytic system (MPS), also known as the reticuloendothelial system (RES), have the ability to remove unprotected nanoparticles from the bloodstream within seconds of intravenous administration, rendering them ineffective as site-specific drug delivery devices (11). These macrophages, which are typically Kupffer

cells, or macrophages of the liver, cannot directly identify the nanoparticles themselves, but rather recognize specific opsonin proteins bound to the surface of the particles (12). Several methods of camouflaging or masking nanoparticles have been developed, which allow them to temporarily bypass recognition by the MPS and increase their blood circulation half-life (11, 13, 14). Many of these systems make use of surface treatments that interfere with the binding of opsonin proteins to the particle surface as a means of imparting stealth characteristics to nanoparticles. Such limitations can be addressed, for example, through the production of PEGylated versions of therapeutic proteins. PEG coating provides reduced renal clearance, increased solubility and stability to degradation and a reduced immunogenic response, improving the pharmacokinetic and pharmacodynamics properties of polypeptide drugs (15). For protein nanocarriers, PEGylation is even more important. PEG coating makes them larger so they are cleared more slowly and their life-times become longer protecting them from the activity of the reticuloendothelial system. The purpose of these PEG chains is to create a barrier layer to block the adhesion of opsonins present in the blood serum, so that the particles can remain invisible to phagocytic cells. PEGylated HuHf has been proposed by Tsukamoto *et al*. (16) aiming at masking the protein from its physiological receptors (Transferrin receptor 1) and at decreasing the uptake by the reticuloendothelial and mononuclear phagocytic systems thus resulting in an increased blood circulation time (17). Obviously, preservation of the three dimensional structure and activity of the PEGylated protein is mandatory for human use. While activity can be easily measured *in vitro*, structural characterization at atomic resolution of PEGylated proteins and protein-based nanocarriers is almost impossible. PEG coating prevents crystallization for X-ray crystallography and causes an increase in protein mass that makes in unsuitable for solution NMR studies. Conversely, solid-state NMR (ssNMR) is a valid alternative to study proteins because it does not suffer from molecular-weight limitations and high resolution spectra can be obtained for multimeric assemblies, but the best resolution is usually obtained for crystalline materials, which are exactly what cannot be achieved for PEGylated proteins.

In 2011, the so-called SedNMR (solid state NMR on sedimented sample) was implemented for the first time on ferritin sample (18). Relatively large proteins in solution, spun in NMR rotors for solid samples at typical ultracentrifugation speeds, sediment at the rotor wall. The sedimented proteins provide high-quality solid-state-like NMR spectra suitable for structural investigation. Sedimentation is a transient phase since the proteins fully revert to the native solution state when spinning is stopped. NMR of transiently sedimented

molecules under fast magic angle spinning has the advantage of overcoming protein size limitations of solution NMR without the need of sample crystallization/precipitation required by solid-state NMR. Inspired by SedNMR, we showed here that highly resolved ssNMR spectra can be obtained also for PEGylated proteins in the pelleted state (**Annex IV**). It was shown that the simple comparison of a standard two-dimensional ssNMR spectrum of the pelleted PEGylated protein with that of the crystalline state of the native protein can reveal whether the three-dimensional structure is maintained in the PEGylated form. The applicability of the approach was demonstrated in the PEGylated forms of three proteins of increasing size: human CuII-ZnII-Superoxide Dismutase (SOD), *E.coli* L-asparaginase II (ANSII) and human H ferritin (HuHf). In particular, I worked directly on the characterization of HuHf that has been chosen as a case study being a huge molecular assembly and due to its relevance in the family of protein-based nanocarrier. SDS-PAGE analysis showed that each monomer was functionalized with 3–4 PEG chains, thereby increasing the size of the tetramer from 504 kDa up to 600–650 kDa. On the other hand, stopped-flow kinetic measurements confirmed the maintained biological activity upon PEG-functionalization. PEGylated HuHf was still able to sediment easily and the SedNMR spectra of the pelleted PEGylated protein and the crystalline native protein were largely superimposable (Fig. 2), thus demonstrating for the first time a negligible effect of PEG coating on ferritin structure and assembly.

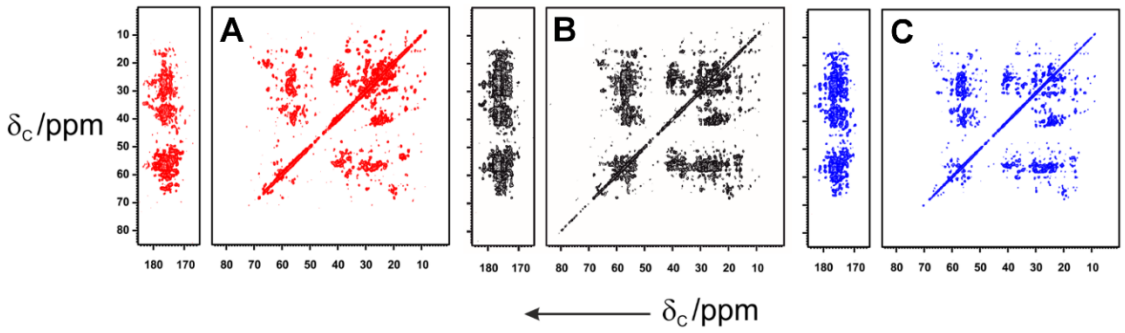

Figure 2. Comparison of native or PEGylated ferritin spectra. 2D ^{13}C-^{13}C correlation spectra of **A**) native crystalline (red spectrum), **B**) native pelleted (black spectrum) and **C**) PEGylated (blue spectrum) HuHf.

4.3 Design of a responsive HuHf mutant

In order to make the targeting more specific, the design and production of a HuHf variant able to load/release molecules under specific conditions, were performed. We produced an engineered HuHf with EF-hand domains (called EF hand-HuHf). This domain is typically present in calmodulin and consists of two alpha helices, E and F, linked by a short loop region of 12 amino acids that bind calcium ions. When the calcium ion binds, helix F moves from a closed to an opened conformation. Our working hypothesis was to insert a motif able to change conformation in presence of calcium and make the cage more prone to uptake/release molecules. According to the consensus sequence of the 12 amino acids-loop region, we designed the opportune mutations or insertions on the long loop connecting helices II and III in HuHf (seven mutations: insertion G93, W94G, E95K, insertion I96, insertions FEE99) that according to our structural analysis might affect the viability of the pores at the C4 axes. This HuHf variant resulted in seven mutations: We tried to verify our hypothesis applying X-ray crystallography to determine whether in the presence and in the absence of Ca(II) ions, some conformational changes could be induced changing the structure of the C4 pores. Until now, our crystallization trails failed. Attempts to crystallize EF hand-HuHf in conditions similar to those of WT protein were unsuccessful. This was not completely unexpected as suggested from previous X-ray studies on ferritins mutated in the solvent-exposed loop region (19). Even modifying only one residue, as in the case of D80K in M ferritin from bullfrog (19), it could compromise solubility and stability protein properties. Furthermore, modifications of the surface charge distribution not only affect the physical properties of the protein but may also contribute to differences in crystal packing. NMR could represent an alternative approach for solving the structure of our mutant. Nevertheless, the residue assignment of human ferritins is not available yet. The main limitation in approaching NMR ferritin-structure determination is the elevated cost of isotopic labeling for protein preparation that is needed to afford specific residue assignment in a so huge system.

4.4 Ru-based metal drug loaded into human ferritins

Due to its natural tendency to bind metal ions, ferritin readily encapsulates metal containing drugs (for example cisplatin and the iron chelator desferrioxamine B). With this in mind, we chose a Ru-based drug called NAMI A, that corresponds to the acronym of Novel

anticancer metastasis inhibitor of class A (20). Why NAMI A? Ruthenium drugs have been developed to overcome the limitations of the platinum containing drugs. Even if cisplatin and its analogues carboplatin and oxaliplatin have been approved by FDA and became the most widely used compounds for cancer therapy (at least as part of patients' treatment), they are not effective against many common type of cancer, drug resistance is frequent and they cause several side effects (21). Ru-compounds tend to cause fewer and less severe side effects compared to platinum drugs (22). NAMI A is active against secondary tumour cells (the metastases which form after cells from the primary tumour and move to a different organ, e.g. via the bloodstream). Currently there are very few treatment options for metastatic cancers. To date, NAMI A is being evaluated in phase II clinical trials (23). In spite of flexibility in ruthenium oxidation states, ruthenium complexes display relatively slow ligand exchange rates in water, with kinetics on the timescale of cellular reproduction (mitosis), meaning that if a ruthenium ion does bind to something in the cell, it is likely to remain bound for the remainder of the cell's lifetime. Furthermore, ruthenium tends to form octahedral complexes, which gives the chemist two more ligands to exploit compared with Pt(II) complexes, which adopt a square planar geometry. Ruthenium can also form strong chemical bonds with a range of different elements of varying chemical 'hardness' and electronegativity, meaning that ruthenium can bind to a range of biomolecules, not just DNA. The chemical structure of NAMI A consists of a hexacoordinated Ru(III) center linked to four chlorides as equatorial ligands and to DMSO and imidazole as axial ligands (Fig. 3).

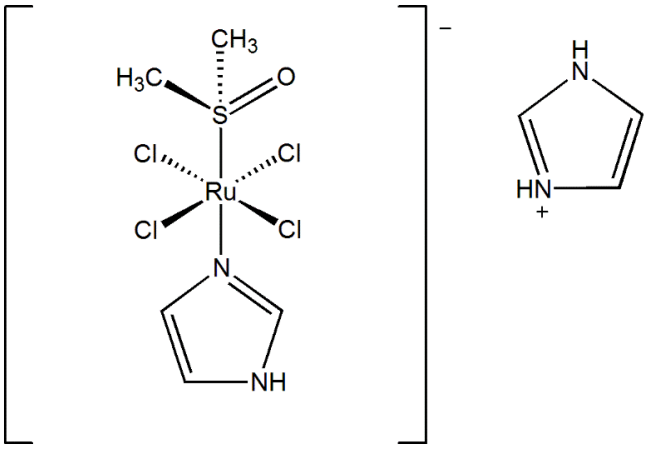

Figure 3. Chemical structure of NAMI A.

However, a major limitation in ruthenium drug discovery is the unknown mode of action of its compounds. Very recent findings suggest that NAMI A is not internalized easily

into cells and consequently, it acts at an extracellular level. Likely, interactions with actin-type proteins on the cell surface or with collagens of the extracellular matrix occur, which lead to reduced mobility of invasive cancer cells.

The fact that iron and ruthenium are in the same chemical group (Group 8) has led to hypothesize that it is capable of taking iron's place in some proteins, most notably in the chaperone and uptake protein transferrin (24). Owing to the analogy of ruthenium to iron, we wondered whether NAMI A might interact also with ferritin (**Annex V**). We therefore analyzed the direct reaction of NAMI A with human homopolymeric H- and L-ferritins. When NAMI A is added in buffer solution the classical spectral evolution is noticed where the band centered at 390 nm is assigned, this bands disappears progressively being replaced by an absorption at 345 nm. This spectral change have been assigned to the replacement of the first chloride ligand by a water molecule (20). Replacement of a second chloride by water was also described, again accompanied by characteristic spectral changes, namely the disappearance of the absorption at 340 nm. Further aquation and/or oligomerization process take place afterward. Thanks to these characteristic time dependent changes of spectral profile in the UV-visible region, we could detect differences in the NAMI A hydrolysis process attributable to the presence of HuHf and HuLf. The rate of hydrolysis appears to be much faster with both proteins (Fig. 4).

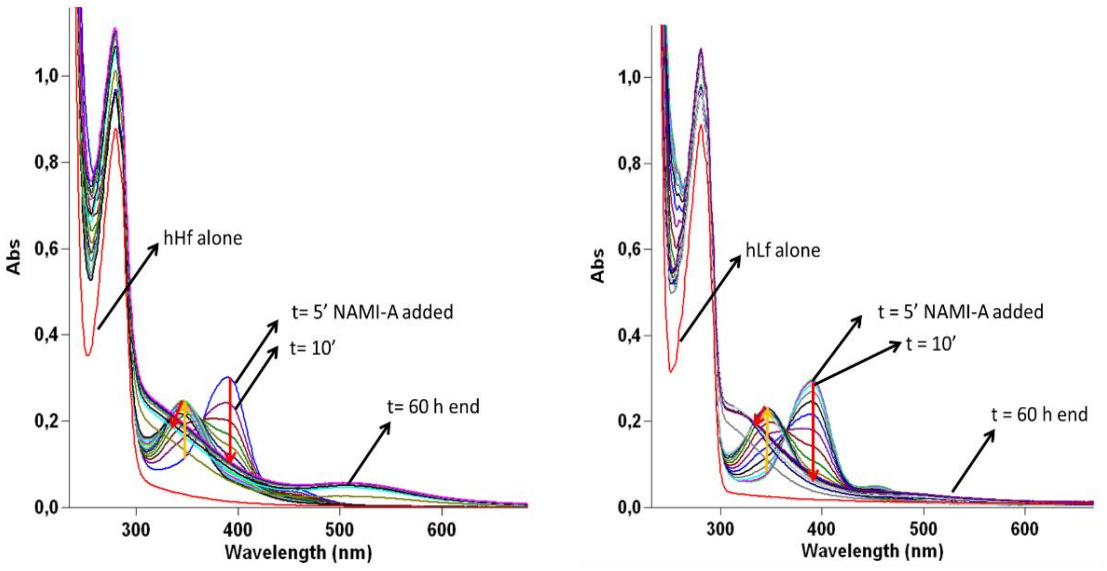

Figure 4. Hydrolysis of NAMI A in presence of HuHf (left) and HuLf (right). Molar ratio protein: NAMI A 1:2 (protein 5* 10-5 M in subunits).

The formation of a Ru-adduct with HuHf was established by UV-visible and circular dichroism (CD) spectroscopy. The appearance of a characteristic band around 500 nm in HuHf was observed, which is responsible of the observed pink color of this adduct.

In addition, kinetics measurements showed inhibition of the ferroxidase activity of HuHf. Nevertheless, the observed inhibition of the ferroxidase activity in HuHf could be explained by Ru-binding at the ferroxidase center. The different spectroscopic properties of HuHf and HuLf suggesting Ru binding at different sites. It is well known the preference of Ru(III) NAMI A for histidine residues in other proteins, such as albumin and transferrin. A possible high-affinity binding site for ruthenium in HuHf could be provided by the 4-symmetry related His173 imidazole rings in C4 channels. In HuLf, the corresponding site is absent because His173 is substituted by Leu173. These hypotheses need a structural confirmation. Unfortunately, until now our crystallization trials failed preventing the exact localization of ruthenium binding site(s) inside the two ferritin cages.

4.5 Fe-loaded ferritins as a nanotherapeutic against cancer

Although iron is an essential nutrient for cellular growth and homeostasis, its redox active form, namely free Fe^{2+}, may become a threat for cells due to its ability to trigger reactive oxygen species based on the Fenton reaction, whereas the Fe^{3+} form is highly insoluble at physiological pH (25). Therefore, in order to prevent or attenuate oxidative damage and cell death and to provide a bioavailable Fe^{3+} form iron is cautiously transported and stored, in a non-redox active form, by transferrin and ferritin, respectively.

In collaboration with the group of Prof. Aime in Turin, we investigated the administration of iron-loaded H-Ferritin (100% H chain) and Horse Spleen Ferritin (15% H chains and 85% L chains) (26) as a novel nanotherapy in cancer, by exploiting the capacity of these proteins to deliver high amounts of iron with the scope to trigger mechanisms of cell damage and death associated with a persistent LIP (labile iron pool) increase (**Annex VI**).

To this purpose, HeLa cells were treated for 24 hours with different concentrations of human recombinant H-Ferritin or horse spleen Ferritin, in the L-rich natural heteropolymeric composition (Fig. 5).

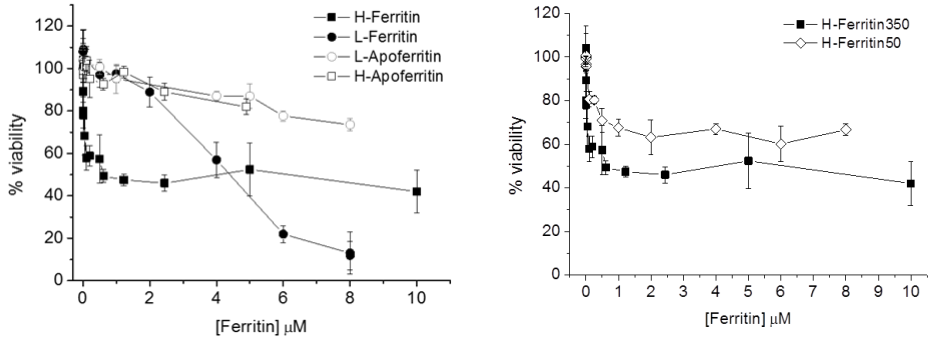

Figure 5. On the left, dose-dependent L- and H- Ferritin effects on HeLa cell viability measured by MTT assay. On the right, dose-dependent H-Ferritin50 and H-Ferritin350 effects on HeLa cell viability measured by MTT assay. In all experiments, cell viability was expressed as percentage relative to untreated cells. Data are presented as mean and SD of at least three independent experiments.

Each ferritin is up-taken trough specific receptor mediated endocytosis. Internalized iron was significantly different on the basis of the different receptor uptake capacity. TfR-1 mediated cellular uptake of human H-ferritin loaded with 50 or 350 iron ions, without any additional modifications, results in a high cytotoxicity on HeLa cells (Fig. 5). At variance, L-ferritin, which is internalized through the SCARA5 receptor is significantly less toxic, even when loaded with 1000 iron ions. Confocal microscopy studies revealed that L-ferritin co-localized with the lysosomal compartment, whereas only a small fraction of rhodamine labeled H-Ferritin undergoes to lysosomal degradation. Exploiting the endosomal-lysosomal compartment iron overload, Fe-loaded HuHf was found to be more toxic than the Fe-loaded L-ferritin. We were able to attribute that toxicity to the mobile iron pool associated to the presence of the ferroxidase center. This mobile iron pool is readily released during the endosomal-mediated H-ferritin internalization and is more prone to redox reactions with consequent ROS production causing toxicity. The iron-loaded HuHf was therefore proposed as a novel nanotherapeutic agent, named Ferritinoxis, able to put under stress critical pathways for cell survival.

4.6 Highlights

The results of this chapter can be summarized in three points:

i) PEGylation of human H Ferritin has been performed and solid state NMR of sedimented PEG-protein has been proposed as a feasible method to evaluate the 3D structure maintenance upon functionalization. This approach represents a valid alternative for those systems that are too big for solution NMR or prevent crystallization like PEGylation.

ii) Ferritin has been proposed as a drug delivery system for Ru-based drug, NAMI A. Since the antimetastatic properties of this molecule that put it in clinical phase II trials, we investigated its interaction with human ferritins. So far, we established that both HuHf and HuLf influence the NAMI A hydrolysis. Evidences of a NAMI A-ferritin adduct has been detected spectrophotometrically for HuHf. Nevertheless, we did not obtain crystals that diffract properly to show whether Ru-species are bound to ferritin. Other crystallization trials have been planned together with mass spectrometry approaches. The advantages to use ferritin as a container for NAMI A could be the ability to protect this molecule upon its release in the target area maximizing its efficacy and increasing its life-time before clearance.

iii) We address the issue of stimulated cell death by supplementing the tumour cells with large iron loadings, in order to stress critical pathways for cell survival, through the administration of Fe-loaded ferritins. The administration of H-Ferritin or Horse Spleen Ferritin is proposed as a novel nanotherapy of cancer, named Ferritinoxis.

Reference List

1. Couvreur P, Vauthier C (2006) Nanotechnology: intelligent design to treat complex disease. *Pharm. Res.* **23**:1417-1450.

2. Torchilin VP (2007) Targeted pharmaceutical nanocarriers for cancer therapy and imaging. *AAPS. J.* **9**:E128-E147.

3. Maeda H *et al.* (2000) Tumor vascular permeability and the EPR effect in macromolecular therapeutics: a review. *J. Control Release* **65**:271-284.

4. Torchilin VP (2005) Recent advances with liposomes as pharmaceutical carriers. *Nat. Rev. Drug Discov.* **4**:145-160.

5. Duncan R (2006) Polymer conjugates as anticancer nanomedicines. *Nat. Rev. Cancer* **6**:688-701.

6. Allen TM (2002) Ligand-targeted therapeutics in anticancer therapy. *Nat. Rev. Cancer* **2**:750-763.

7. Lu Y, Low PS (2002) Folate-mediated delivery of macromolecular anticancer therapeutic agents. *Adv. Drug Deliv. Rev.* **54**:675-693.

8. Qian ZM, Li H, Sun H, Ho K (2002) Targeted drug delivery via the transferrin receptor-mediated endocytosis pathway. *Pharmacol. Rev.* **54**:561-587.

9. Putney SD, Burke PA (1998) Improving protein therapeutics with sustained-release formulations. *Nat. Biotechnol.* **16**:153-157.

10. Schellekens H (2002) Bioequivalence and the immunogenicity of biopharmaceuticals. *Nat. Rev. Drug Discov.* **1**:457-462.

11. Gref R *et al.* (1994) Biodegradable long-circulating polymeric nanospheres. *Science* **263**:1600-1603.

12. Frank MM, Fries LF (1991) The role of complement in inflammation and phagocytosis. *Immunol. Today* **12**:322-326.

13. Illum L, Davis SS (1984) The organ uptake of intravenously administered colloidal particles can be altered using a non-ionic surfactant (Poloxamer 338). *FEBS Lett.* **167**:79-82.

14. Kaul G, Amiji M (2002) Long-circulating poly(ethylene glycol)-modified gelatin nanoparticles for intracellular delivery. *Pharm. Res.* **19**:1061-1067.

15. Harris JM, Chess RB (2003) Effect of pegylation on pharmaceuticals. *Nat. Rev. Drug Discov.* **2**:214-221.

16. Tsukamoto R *et al.* (2013) Effect of PEGylation on controllably spaced adsorption of ferritin molecules. *Langmuir* **29**:12737-12743.

17. Barreto JA *et al.* (2011) Nanomaterials: applications in cancer imaging and therapy. *Adv. Mater.* **23**:H18-H40.

18. Ravera E *et al.* (2016) Solid-state NMR of PEGylated proteins. *Angew. Chem. Int. Ed* **55**:1-5.

19. Bernacchioni C *et al.* (2014) Loop Electrostatics Modulates the Intersubunit and Intercage Interactions in Ferritin. *ACS Chem. Biol.* **9**:2517-2525.

20. Sava G, Pacor S, Mestroni G, Alessio E (1992) Na[trans-RuCl4(DMSO)Im], a metal complex of ruthenium with antimetastatic properties. *Clin. Exp. Metastasis* **10**:273-280.

21. Cvitkovic E (1998) Cumulative toxicities from cisplatin therapy and current cytoprotective measures. *Cancer Treat. Rev.* **24**:265-281.

22. Sava G, Bergamo A (2000) Ruthenium-based compounds and tumour growth control (review). *Int. J. Oncol.* **17**:353-365.

23. Leijen S *et al.* (2015) Phase I/II study with ruthenium compound NAMI-A and gemcitabine in patients with non-small cell lung cancer after first line therapy. *Invest New Drugs* **33**:201-214.

24. Vincent JB, Love S (2012) The binding and transport of alternative metals by transferrin. *Biochim. Biophys. Acta* **1820**:362-378.

25. Linder MC (2013) Mobilization of stored iron in mammals: a review. *Nutrients.* **5**:4022-4050.

26. Proudhon D, Wei J, Briat J-F, Theil EC Ferritin gene organization: Differences between plants and animals suggest possible kingdom-specific selective constraints.

Chapter 5

New redox activity for ferritin

5.1 Ferritin as new lipid-binding protein.

Fatty acids are involved in several physiological functions, including structural, signaling, and metabolic functions, and are therefore tightly regulated and transported via a series of both intracellular and extracellular fatty acid-binding proteins. These proteins also maintain free fatty acid concentration in the low micromolar range to reduce their toxicity and potential oxidative injury (1). Under conditions of tissue stress, such as ischemia and reperfusion, free fatty acids released by the action of calcium-activated phospholipases serve primarily signaling and substrate roles (2). Because of the unsaturation of many released fatty acids (e.g., oleic and arachidonic acids), they can be oxidized and facilitate peroxidation chain reactions. Hydrogen peroxide, which in the presence of free iron participate in the harmful Fenton chemistry, is one of the intermediates formed in these reactions. The radical products maintain the peroxidation cycle, further damaging lipids, proteins, nucleic acids, and ultimately activating apoptosis or cell death (3). A functional coupling between iron and fatty acid metabolism has been previously demonstrated (4). It has been suggested that ferritin plays a role in lipid metabolism. For example, application of free fatty acids to cells in culture causes an upregulation in ferritin expression, interpreted as part of a generalized stress response (5). Additionally, downregulation of L-ferritin in melanoma cell's culture produced an enhanced response to oxidative stress and the resulting apoptosis, whereas the most resistant cells displayed the highest ferritin expression (6). The ability of lipids to directly bind to ferritin has been demonstrated through ITC and crystallography (4, 7); horse spleen ferritin has revealed that the pockets at the 2-fold intersubunit contacts are suitable to bind organic molecules such as arachidonic acid and sodium dodecyl sulfate. The crystal structure of the horse spleen ferritin (HoSf)-arachidonate complex has been solved (4), revealing that the bound ligand has a U-shaped conformation and the long tail of arachidonate accommodates close to the nucleation sites (Fig. 1). Interestingly, arachidonate bound to ferritin caused faster biomineralization accelerating iron uptake.

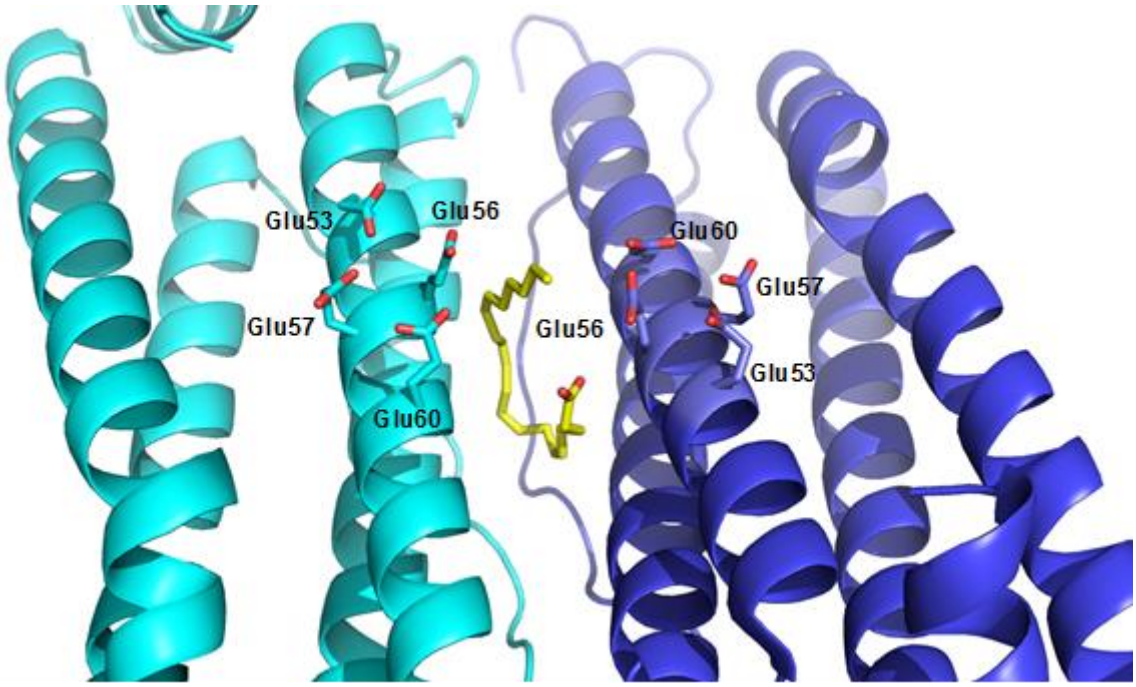

Figure 1. Location of the arachidonate binding site in HoSf, a sight from the inner cage. Arachidonic acid in U-shaped conformation represented as yellow sticks at the interface of two subunits (cyan and blue cartoons). One arachidonate molecule was observed at each of the 12 intersubunit 2-fold pockets, very close to the carboxylate groups of nucleation sites (represented in sticks). (PDB id 4DE6).

In collaboration with the group of Prof. Molinari (CNR, Milano and University of Verona), the interaction of apo HoSf with a pool of lipids has been investigated through NMR ligand-based experiments (**Annex VII**). DOSY and STD NMR experiments established a stronger interaction of ferritin with unsaturated fatty acids (arachidonate, ARA and oleate, OLA) with respect to saturated fatty acids (lauric acid, LAU), detergents (sodium dodecyl sulfate, SDS) and bile acids (chenodeoxycholic acid, CDA). These studies have been accompanied by mineralization assays through UV/visible spectroscopy aimed at verifying the existence of a functional role between ferritin/lipid binding and iron mineralization (Fig. 2).

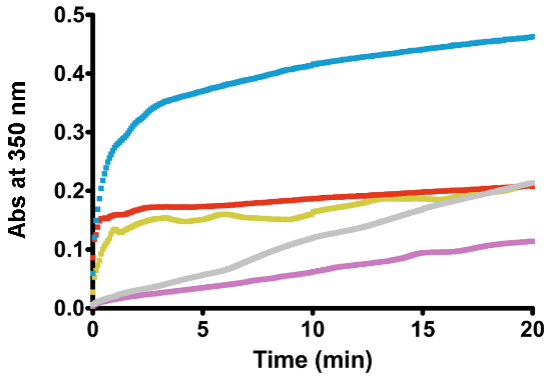

Figure 2. Mineralization kinetics of ferritin in presence of different lipids. Kinetics of mineralization for HoSf alone (gray trace), incubated with 700 µM of OLA (blue), ARA (red), LAU (gold) and SDS (purple). The kinetics of biomineral formation was followed as the change of $A_{350\ nm}$ after addition of 480 Fe^{2+} per cage.

Oleate caused the highest increase in the initial rate of iron oxidation and the highest formation of ferric species as shown in the kinetic analysis following the peculiar absorbance at 350 nm over the time.

Previous X-ray data showed that SDS binds HoSf at the two-fold intersubunit pocket in the same site as ARA even though with a weaker affinity (K_D of 24±9 µM for OLA against 60 µM for ARA) (4, 7) In order to confirm that OLA occupies the same site at the dimer interface in ferritin, NMR competition binding experiments were performed. OLA was added to HoSf:SDS complex to obtain a sample with HoSf:SDS:OLA ratio of 1:1:1. OLA could displace SDS and free SDS resonances emerged in the spectrum.

The lipid binding pocket is located at a largely hydrophobic interface between two subunits. Open questions remain about the mechanism through which the lipidic molecules can reach this pocket and about the factors that induce a faster biomineralization. As far as the latter aspect is concerned, two main hypotheses can be formulated:

i) the presence of OLA opens a new iron entry channel;

ii) the terminal carboxylate of the lipid, which clearly points towards the inner cavity surface in the ARA X-ray structure, facilitates the reaction at the nucleation site (see Section 3.4).

It is not clear how the fatty acid gains access to the intersubunit pocket. Anyway, it seems that ferritin could protect unsaturated fatty acids from oxidation, limiting their

participation in lipid peroxidation chain reaction, thus reducing their inflammatory effects. We tried to analyze the structure of ferritins from different families and we found that bacterioferritin hosts a heme group at the interface between two subunits along the 2-fold symmetry axes. The b-type heme group is placed exactly in the same hydrophobic 2-fold pocket with a similar orientation like ARA in the horse spleen ferritin cited above. The two carboxylate groups of propionates on heme b faces on the inner cavity in analogy with the carboxylic head of the lipid. In bacteria ferritin-bound heme seems to facilitate iron core mineralization via an electron transfer mechanism whose details remain unknown (8). Besides this structural analogy, it could be interesting to verify any functional similarity involving an electron transfer among lipids and the mineral iron core.

To further exploit the role of the lipid on the ferritin reaction mechanism we have initiate an analogous characterization on the H-ferritin. Preliminary data have shown that OLA can still bind with high affinity but does not influence the reaction at the ferroxidase site. We still need to check whether it has any role on the overall biomineralization process.

5.2 NMR study of the interaction between mitochondrial ferritin and cytochrome c

Cytochrome c (cyt c) is small soluble heme protein loosely associated with the inner membrane of the mitochondrion. It plays as an electron carrier protein that is responsible for accepting an electron from cytochrome c reductase and for transferring an electron to cytochrome c oxidase (9). In addition to functioning as an electron carrier, cyt c promotes the assembly of a caspase-activating complex to induce cell apoptosis (10). These diverse functions of cyt c are associated with the protein–protein interactions between cytochrome c and its interacting proteins.

Human cyt c form an electron transfer (ET) pair with ferritin depending on the redox state of the two systems, as reported in electronic spectroscopy studies (11, 12). The reaction was proposed to be of particular interest because it demonstrated that Fe^{2+} in the ferritin interior is readily oxidized to Fe^{3+} by a molecule too large to enter the protein interior. This reaction was demonstrated with horse spleen ferritin that is a cytosolic protein. Since cyt c is found in mitochondria, their different distribution let to conclude that they could not be physiological partners. After a decade, in 2001 the mitochondrial catalytically active ferritin (FtMt) was

described for the first time. Human mitochondrial cyt c is a well-characterized protein in our lab. Thus, we hypothesized that an interaction between FtMt and cyt c.

We therefore decided to investigate deeply the inter-protein ET process, trying to see whether it occurs via specific protein-protein interactions. The work was conducted by

NMR. We expressed and purified unlabelled FtMt depleted of the signal peptide. ^{15}N-labelled human cyt c was produced according to an already developed protocol (13) and used to monitor ^{1}H 1D and 2D HSQC spectral changes upon addition of increasing amounts of FtMt. Both reduced and oxidized-states of cyt c were investigated. We clearly observed the occurrence of an ET process when mixing reduced cyt c with iron-loaded FtMt: in one dimensional ^{1}H NMR spectra the diamagnetic iron(II) cyt c and the paramagnetic (S=172) iron(III) cyt c have clearly different signals patterns; appearance of paramagnetic signals unequivocally indicated heme iron oxidation induced by iron-loaded ferritin. The same phenomenon was observed with the HuHf. 2D ^{1}H-^{15}N NOESY spectra of ^{15}N-enriched cyt c recorded in the absence and in the presence of iron loaded ferritin did not show any significant chemical shift perturbations. While chemical shift perturbations are extremely tiny, if any, significant signal broadening (in both 1D and 2D spectra) was observed (Fig. 3 and 4).

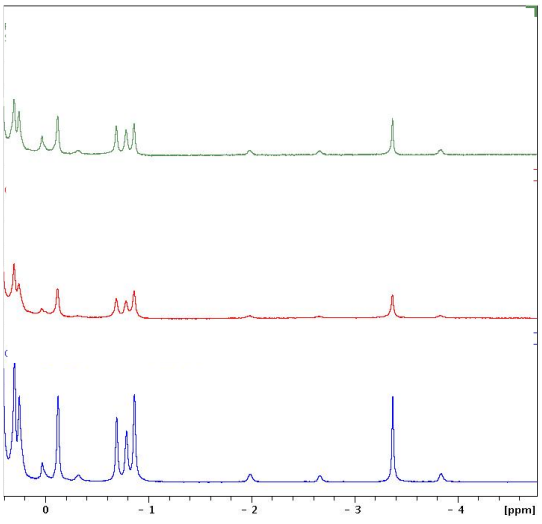

Figure 3. 1D NMR spectra acquired at 700 MHz spectrometer at 298 K. In blue the reference spectrum of reduced cyt c (400 µM protein in 50 mM NaPi pH 6.8; in red, cyt c in presence of 5 equivalents of apo HuHf (without iron); in green, cyt c in presence of 5 equivalents of apo FtMt.

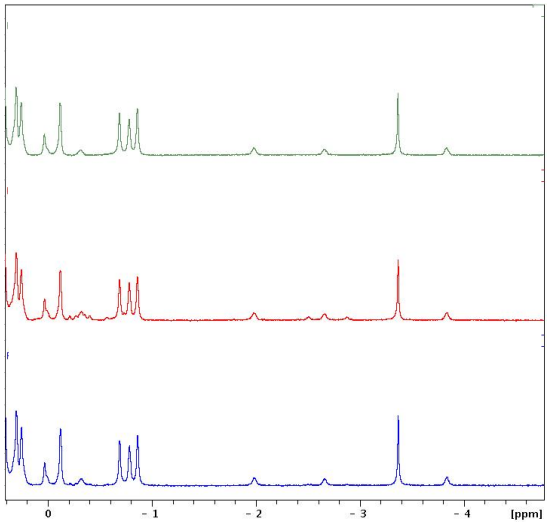

Figure 4. 1D NMR spectra acquired at 700 MHz spectrometer at 298 K. In blue the reference spectrum of reduced cyt c (400 µM) in 50 mM NaPi pH 6.8; in red, cyt c in presence of 0.1 equivalents of holo FtMt (with iron); in green, DTT addition to revert cyt c at the reduced redox state.

In order to understand if the ET occurred through the iron mineralized in the core or through the iron mobile pool (see Section 4.5) available at the catalytic site, we repeated the cyt c titration with holo L-ferritin that lacks the catalytic site and no ET occurred (see Scheme 1). This indicated that only mobile iron ions at the catalytic site are able to participate in the redox exchange.

Fe^{3+}(holo FtMt/H ferritin) + Fe^{2+}- (Red cyt c) ⟶ Fe^{2+}(holo FtMt/H ferrritin) + Fe^{3+}- (Ox cyt c)

Fe^{3+}(holo L ferritin) + Fe^{2+}-(Red cyt c) ✖⟶ Fe^{2+}(holo L ferrritin) + Fe^{3+}-(Ox cyt c)

Scheme 1. Schematic ET reaction between holo ferritins and reduced cyt c.

This finding seems to contradict former observations of an ET between cyt c and horse spleen ferritin (11). In practice, horse spleen ferritin contains about 10% of H-type subunits which might be at the origin of the observed ET.

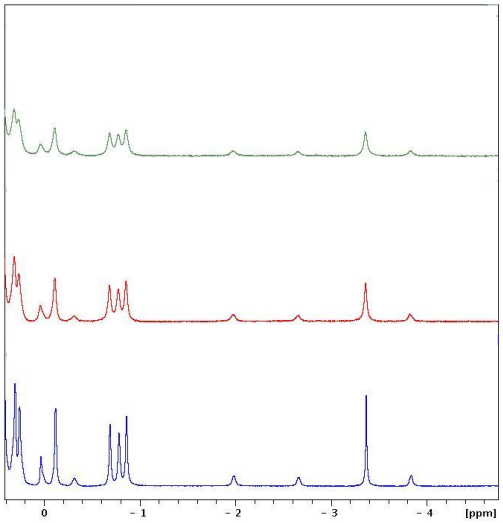

Figure 5. 1D NMR spectra acquired at 700 MHz spectrometer at 298 K. In blue the reference spectrum of reduced cyt c (400 µM) in 50 mM NaPi pH 6.8; in red, cyt c in presence of 2 equivalents of holo HuLf (with iron); in green, add of other 2 equivalents of holo HuLf. Line broadening suggests interaction between the two proteins even though in absence of ET.

While our data constitute a further proof of the presence of a redox accessible pool of iron in H-subunits, as proposed in Section 4.5, the structural interpretation of our NMR data is not straightforward. The lack of residue-specific chemical shift perturbations supports an

unspecific interaction between the two proteins. The observed line broadening effects could be compatible with a general increase in solution viscosity due to the addition of the large ferritin nanocage, although we cannot rule out the presence of interaction equilibria on the quasi-fast chemical shift NMR time scale involving a small molar fraction of complexed cyt c.

5.3 Highlights

Besides its iron-biomineralization and storage function, ferritin has been proposed to exhibit other redox activities different from the iron oxidation in presence of dioxygen.

Intrigued by ferritin as a new lipid-binding protein, we studied by NMR the interaction of HoSf with a variety of fatty acids. Ligand-based NMR experiments demonstrated that the stronger binders are unsaturated lipids such as oleate and arachidonate. Combining competition binding NMR experiments with previous crystallographic data, allowed us to conclude that oleate binds ferritin at the 2-fold intersubunit pocket, as already seen for ARA and SDS. The presence of oleate speeds up the biomineralization reaction, possibly contributing to a more efficient reaction at the nucleation site, which is located just below the fatty acid binding pocket.

The lack of specific protein-protein interactions between cyt c and ferritins probably rules out a functional significance to this redox reaction. On the other hand, it provides a further evidence of the different redox activity of the biomineralized iron and iron at the ferroxidase sites.

Reference List

1. Zimmerman AW, van Moerkerk HT, Veerkamp JH (2001) Ligand specificity and conformational stability of human fatty acid-binding proteins. *Int. J. Biochem. Cell Biol.* **33**:865-876.

2. Burke JE, Dennis EA (2009) Phospholipase A2 structure/function, mechanism, and signaling. *J. Lipid Res.* **50** Suppl:S237-S242.

3. Kell DB (2010) Towards a unifying, systems biology understanding of large-scale cellular death and destruction caused by poorly liganded iron: Parkinson's, Huntington's, Alzheimer's, prions, bactericides, chemical toxicology and others as examples. *Arch. Toxicol.* **84**:825-889.

4. Bu W *et al.* (2012) Ferritin couples iron and fatty acid metabolism. *FASEB J.* **26**:2394-2400.

5. Elia G, Polla B, Rossi A, Santoro MG (1999) Induction of ferritin and heat shock proteins by prostaglandin A1 in human monocytes. Evidence for transcriptional and post-transcriptional regulation. *Eur. J. Biochem.* **264**:736-745.

6. Baldi A *et al.* (2005) Ferritin contributes to melanoma progression by modulating cell growth and sensitivity to oxidative stress. *Clin. Cancer Res.* **11**:3175-3183.

7. Liu R *et al.* (2012) Beyond the detergent effect: a binding site for sodium dodecyl sulfate (SDS) in mammalian apoferritin. *Acta Crystallogr. D. Biol. Crystallogr.* **68**:497-504.

8. Wong SG *et al.* (2012) Fe-haem bound to Escherichia coli bacterioferritin accelerates iron core formation by an electron transfer mechanism. *Biochem. J.* **444**:553-560.

9. Scott, R. A. & Mauk, A. G. (1996) *Cytochrome c. A multidisciplinary approach* (University Science Books, Sausalito, California).

10. Li P *et al.* (1997) Cytochrome c and dATP-dependent formation of Apaf-1/caspase-9 complex initiates an apoptotic protease cascade. *Cell* **91**:479-489.

11. Watt GD, Jacobs D, Frankel RB (1988) Redox reactivity of bacterial and mammalian ferritin: is reductant entry into the ferritin interior a necessary step for iron release? *Proc. Natl. Acad. Sci. U. S. A* **85**:7457-7461.

12. Kadir FH *et al.* (1991) Electron transfer between horse ferritin and ferrihaemoproteins. *Biochem. J.* **278**:817-820.

13. Bertini I *et al.* (2011) The anti-apoptotic Bcl-xL protein, a new piece in the puzzle of cytochrome c interactome. *Plos ONE* **6**:18329.

Chapter 6

Conclusions and perspectives

My thesis project has been developed in the frame of the PRIN 2012 project, “Innovative chemical tools for improved molecular approaches in biomedicine”. In this project, human ferritins have been selected as the reference proteins to be structurally and functionally characterized, for a deeper knowledge of the mechanisms that regulate iron handling and storage. The long-term goal is that of rational design a novel ferritin-based cage able to efficiently encapsulate drug, imaging probe or theranostic agents and to modulate their release in response to specific chemical properties of the microenvironment typical of different pathological states.

The results of my PhD activities contributes to the achievement of these goals. First of all, the development of efficient expression and purification methods for the high yield production of HuHf, HuLf and FtMt ferritins (Chapter 2) is crucial for focusing research on human proteins that, have clear advantages because it should not activate inflammatory or immunological response when administered to patients. Historically, most studies on mammalian ferritins instead had been obtained on the commercially available horse spleen protein. High-resolution time-lapse anomalous X-ray diffraction data on H-ferritin have led to the definition of the ferroxidase site and accessory binding site in the catalytic cavity (Section 3.2). The ferroxidase site, where the substrate Fe(II) is oxidized by dioxygen, is unique among the diferric iron centers because of the low number of protein ligands and a single bridging carboxylate. The coordinating amino acids are conserved across the vertebrates H-type ferritins. The functional requirement of reaction turnover at this site explains the relatively loose coordination of the metal ions to the protein matrix. Each of the accessory sites that drive Fe(II) into the catalytic site consist of one/two ligands (His or Asp/Glu); these residues are generally not conserved across different species but their presence is needed to sustain the catalytic reaction cycles. Stopped-flow kinetic measurements on different wilt-type ferritins and newly designed variants have been crucial for the functional interpretation of the crystallographic results. With a similar approach that combines time-lapse diffraction and reaction kinetic measurements as well as the production of protein mutants, we identified a novel cluster that defines the nucleation site of L-ferritins (Section 3.4). Further details about the mineral growth are planned and will require the production and functional characterization of novel mutants. From this study, we derived a picture of the ferritin as a cage that controls specific iron trafficking pathways. The C3 channels are designed to assist the import of ferrous hexa-aquaions via an attractive electrostatic potential. In H-ferritins, the delivery of Fe(II) towards the ferroxidase sites under the form of partially hydrated ferrous ions is mainly

controlled by Asp/Glu accessory sites that design a path from the inner cage to the interior of the 4-helix bundle. In L-type ferritins, a cluster of three glutamates blocks the iron at the inner cage surface and acts as a template for the formation of a novel (μ^3-oxo)tris[(μ^2-peroxo)(μ^2-glutamato-κO:κO')](glutamato-κO)(diaquo)triiron(III) anionic cluster.

The presence of a "mobile" iron pool in the catalytic site of H-ferritins, which has no counterpart in L-ferritin, is here proposed as the main source of redox active iron species. This observation has led us to suggest the use of iron-loaded H-ferritin cages as toxic agents for cancer cells overexpressing the TfR-1 receptor, which is involved in the selective import of H-cages with respect to L-cages (Section 4.5). This species causing the here named "Ferritinoxis", are our first example of encapsulated inorganic materials with potential anticancer activity. Encapsulation of different metal derivatives, like the here proposed NAMI-A (Section 4.4), is another promising area that would require future deeper structural and *in vitro*/*in cell* functional characterization. The demonstrated interaction with fatty acids (Section 5.1) is encouraging to exploit ferritin-binding lipids conjugated with contrast agent or drugs as a further strategy.

Last but not least, the demonstrated feasibility of ss-NMR of pelleted protein in PEGylated ferritin provides an important tool to monitor structural integrity in surface functionalized cages (Section 4.1). It could constitute a valuable means to analyze other human ferritins that are naturally glycosylated or artificially conjugated with different molecules.

Annex I

Publication

"Is His54 a gating residue for the ferritin ferroxidase site?"

C. Bernacchioni[a,b], S. Ciambellotti[a,b], E. C. Theil[c,d] and P. Turano[a,b]

[a] Department of Chemistry, University of Florence, via della Lastruccia 3, Sesto Fiorentino, (FI) – Italy.
[b] Center for Magnetic Resonance, University of Florence, Via L. Sacconi 6, Sesto Fiorentino, (FI) – Italy
[c] Children's Hospital Oakland Research Institute, 5700 Martin Luther King, Jr. Way, Oakland, CA 94609, USA
[d] Department of Molecular and Structural Biochemistry, North Carolina State University, Raleigh, NC 29695-7622, USA

Biochimica et Biophysica Acta 1854 (2015) 1118–1122

Contents lists available at ScienceDirect

Biochimica et Biophysica Acta

journal homepage: www.elsevier.com/locate/bbapap

Is His54 a gating residue for the ferritin ferroxidase site?☆

Caterina Bernacchioni [a,b], Silvia Ciambellotti [a,b], Elizabeth C. Theil [c,d], Paola Turano [a,b,*]

[a] Magnetic Resonance Center CERM, University of Florence, Via Luigi Sacconi 6, 50019, Sesto Fiorentino, Florence, Italy
[b] Department of Chemistry, University of Florence, Via della Lastruccia 3, 50019, Sesto Fiorentino, Florence, Italy
[c] Children's Hospital Oakland Research Institute, 5700 Martin Luther King, Jr. Way, Oakland, CA 94609, USA
[d] Department of Molecular and Structural Biochemistry, North Carolina State University, Raleigh, NC 29695-7622, USA

ARTICLE INFO

Article history:
Received 3 November 2014
Received in revised form 17 February 2015
Accepted 18 February 2015
Available online 26 February 2015

Keywords:
Ferritin
Ferroxidase site
Reaction kinetics
Mutagenesis

ABSTRACT

Ferritin is a ubiquitous iron concentrating nanocage protein that functions through the enzymatic oxidation of ferrous iron and the reversible synthesis of a caged ferric-oxo biomineral. Among vertebrate ferritins, the bullfrog M homopolymer ferritin is a frequent model for analyzing the role of specific amino acids in the enzymatic reaction and translocation of iron species within the protein cage. X-ray crystal structures of ferritin in the presence of metal ions have revealed His54 binding to iron(II) and other divalent cations, with its imidazole ring proposed as "gate" that influences iron movement to/from the active site. To investigate its role, His54 was mutated to Ala. The H54A ferritin variant was expressed and its reactivity studied via UV–vis stopped-flow kinetics. The H54A variant exhibited a 20% increase in the initial reaction rate of formation of ferric products with 2 or 4 Fe^{2+}/subunit and higher than 200% with 20 Fe^{2+}/subunit. The possible meaning of the increased efficiency of the ferritin reaction induced by this mutation is proposed taking advantage of the comparative sequence analysis of other ferritins. The data here reported are consistent with a role for His54 as a metal ion trap that maintains the correct levels of access of iron to the active site. This article is part of a Special Issue entitled: Cofactor-dependent proteins: evolution, chemical diversity and bio-applications.

1. Introduction

Maxiferritins (hereafter simply called ferritins) are iron storage proteins characterized by a highly symmetric overall structure, conserved in eukaryotes and prokaryotes [1–3]. The ferritin nanocage self-assembles from twenty-four 4-helix bundle subunits to provide an almost spherical protein shell with 432 point symmetry (Fig. 1A). Each ferritin subunit is enzymatically active (H-type) except in animal ferritins, which coproduce a catalytically inactive subunit (L type) that co-assembles with active subunits in H:L ratios that are tissue specific [4,5]. Amphibians have a further catalytically active type of subunits, called M (or H′). Homopolymeric animal ferritins composed by M or H subunits have been extensively studied as model systems for the iron biomineralization reaction [6,7]:

$$2Fe^{2+} + O_2 \rightarrow \left[Fe^{3+}\text{-}O\text{-}O\text{-}Fe^{3+}\right]$$
$$\left[Fe^{3+}\text{-}O\text{-}O\text{-}Fe^{3+}\right] + H_2O \rightarrow H_2O_2 + \left[Fe^{3+}\text{-}O\text{-}Fe^{3+}\right]$$
$$\left[Fe^{3+}\text{-}O\text{-}Fe^{3+}\right] + (H_2O)_{x+2} \rightarrow Fe_2O_3(H_2O)_x + 4H^+$$
$$2Fe^{2+} + O_2 + (H_2O)_{x+3} \rightarrow Fe_2O_3(H_2O)_x + 4H^+ + H_2O_2.$$

The first two steps of the reactions occur at the catalytic site (named ferroxidase or oxidoreductase site), hosted within the central part of the 4-helix bundle of the active subunits.

The exact definition of the residues binding iron during the catalytic reaction has been hampered for several years by the transient nature of the ferric species that form at the ferroxidase centers. The analysis of the available X-ray structures of animal ferritins with non-native divalent cations (Cu^{2+}, Co^{2+}, Zn^{2+}, Mg^{2+}) has revealed the presence of several amino acid side chains that can potentially act as metal ion ligands [8–10]; their number is larger than what needed to bind the pre-oxidation diferrous species and the diferric-peroxo (DFP, hereafter) and ferric-oxo/hydroxo products. The several potential metal binding amino acids in the same area have been proposed to play a role in regulating the access of the iron substrate to the reaction center [8–11].

The amino acid ligands of the dinuclear ferric-oxo/hydroxo species formed by the catalytic reaction have been identified in bullfrog M ferritin crystal structures at 2.7 Å resolution (Fig. 1B); they are Glu58, which bridges the two iron ions Fe1 and Fe2, monodentate Glu23 and His61 as Fe1 ligands and bidentate Glu103 as Fe2 ligand [8]. His54 was initially proposed as a possible ligand for ferrous ion entering the Fe2 site [8]. Recently, the ligands of the pre-oxidation diferrous species have been found to be the same as for the ferric form (PDB: 4MY7 and 4LQV) [12].

The same structures have revealed additional metal ions interacting with side chains other than those in the ferroxidase center, including

☆ This article is part of a Special Issue entitled: Cofactor-dependent proteins: evolution, chemical diversity and bio-applications.

* Corresponding author at: Magnetic Resonance Center CERM, University of Florence, Via Luigi Sacconi 6, 50019 Sesto Fiorentino, Florence, Italy. Tel.: +39 055 4574266.
E-mail address: turano@cerm.unifi.it (P. Turano).

http://dx.doi.org/10.1016/j.bbapap.2015.02.011
1570-9639/

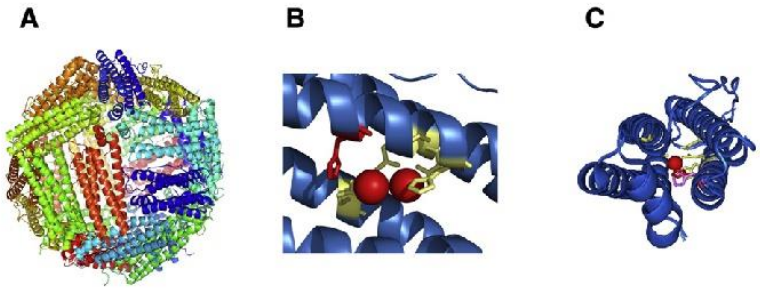

Fig. 1. The nanocage structure of bullfrog ferritin assembled from M subunits. Cartoon representation of the nanocage structure (A). Front (B) and side (C) close-up views of the ferritin monomer with the residues in the enzymatic ferroxidase site shown as yellow sticks. The swinging of the His54 ring from the distal (pink) to the proximal (red) conformation upon iron (red sphere) binding is highlighted in panel C. Drawn using PyMOL (PDB: 3RBC and 3RGD).

His54, that is differently populated at different times of free diffusion of iron(II) through ferritin crystals (PDB: 4LPJ, 4LQJ, 4LYX, 4LYU, 4LQV, 4LQN, 3RGD) [8,12].

The imidazole ring of His54 faces the inner cavity of ferritin and upon binding metal ions swings between two main conformations, named distal and proximal (Fig. 1C). This movement could be important to capture iron from the inner cavity and drag it inside the 4-helix bundle channel. On the other hand, it could also constitute an exit strategy for the ferric products migrating into the inner cavity.

Additionally, His54 has been observed to stably bind other transition metal cations such as Co(II) and Cu(II), [8,9], trapping them out from the metal binding site.

Here we have produced the H54A variant of M ferritin to remove any possibility of binding metal ions at this position and evaluated the effect of this substitution on the ferritin activity.

2. Materials and methods

2.1. Mutagenesis

Site directed amino acid substitution in bullfrog-M ferritin protein cages was generated by PCR, with expression plasmid pET-3a bullfrog-M ferritin DNA as template, using the QuikChange II site-directed mutagenesis kit (Stratagene). The DNA in the coding regions in all the protein expression vectors was analyzed for sequence confirmation (Primm srl, Milan, Italy).

2.2. Protein expression

pET-3a constructs encoding WT and H54A ferritins from the American bullfrog were transformed into *Escherichia coli* BL21(DE3) pLysS cells which were subsequently cultured in LB medium containing ampicillin (0.1 mg/ml) and chloramphenicol (34 μg/ml). Cells were grown at 37 °C, until $A_{600\ nm}$ reached 0.6–0.8 and subsequently induced with isopropyl 1-thio-β-D-galactopyranoside (IPTG, 1 mM final concentration) for 4 h. Recombinant ferritins were purified from the harvested cells, as described previously [13,14]. Briefly, cells were sonicated and the cell free extract obtained after centrifugation (40 min, 40,000 rpm, 4 °C) was incubated for 15 min at 65 °C as the first purification step. After removal of the aggregated proteins (15 min, 40,000 rpm, 4 °C), the supernatant solution was dialyzed against Tris–HCl 20 mM pH 7.5; applied to a Q-Sepharose column in the same buffer and eluted with a linear NaCl gradient of 0–1 M in Tris 20 mM, pH 7.5. Fractions containing ferritin, identified by Coomassie staining of SDS-PAGE gels, were combined and further purified by size exclusion chromatography using a Superdex 200 HiLoad 16/60 column.

2.3. Stopped-flow kinetics

Addition of 2 Fe^{2+} ions per subunit [15] or 4 Fe^{2+} ions per subunit in frog M ferritin, WT or H54A, was monitored as the change in $A_{650\ nm}$ (diferric peroxo; DFP) or $A_{350\ nm}$ ($(Fe^{3+}O)_x$) after rapid mixing (less than 10 ms) of equal volumes of 100 μM protein subunits (4.16 μM protein cages) in 200 mM 3-(N-morpholino)propanesulfonic acid (MOPS), 200 mM NaCl, pH 7.0, with freshly prepared solutions of 200 μM ferrous sulfate or 400 μM ferrous sulfate in 1 mM HCl in a UV/visible stopped-flow spectrophotometer (SX.18MV stopped-flow reaction analyzer, Applied Photophysics, Leatherhead, UK). Routinely, 4000 data points were collected during the first 5 s. Initial rates of DFP and $Fe^{3+}O$ species formation were determined from the linear fitting of the initial phases of the 650- and 350-nm traces (0.01–0.03 s). The reaction progress at high iron:protein ratio was followed after addition of 20 Fe^{2+} ions per subunit as the change of $A_{350\ nm}$ using rapid mixing (less than 10 ms) of 50 μM protein subunits (2.08 μM protein cages) in 200 mM MOPS, 200 mM NaCl, pH 7.0, with an equal volume of freshly prepared 1 mM ferrous sulfate in 1 mM HCl; the same UV/visible stopped-flow spectrophotometer was used, and 4000 data points were routinely collected in 1000 s [14]. Rates of $Fe^{3+}O$ mineralization were calculated from the linear fitting of the initial phases of the 350-nm traces.

2.4. $Fe^{3+}O$ mineral dissolution/chelation

Recombinant ferritin protein cages were mineralized with ferrous sulfate (20 Fe^{2+} ions per subunit) in 100 mM MOPS, 100 mM NaCl, pH 7.0 [14]. After mixing, the solutions were incubated for 2 h at room temperature and then overnight at 4 °C to complete the iron mineralization reaction. Fe^{2+} exit from caged ferritin minerals was initiated by reducing the ferritin mineral with added NADH (2.5 mM) and FMN (2.5 mM) and trapping the reduced and dissolved Fe^{2+} as the $[Fe(2,2'\text{-bipyridyl})_3]^{2+}$ complex outside the protein cage. Fe^{2+} release from the protein cage was measured as the absorbance of $[Fe(2,2'\text{-bipyridyl})_3]^{2+}$ at the maximum of $A_{522\ nm}$. The experiments were performed at two different iron and protein concentrations, 2.08 μM cages and 1.0 mM iron, and 1.04 μM cages and 0.5 mM iron respectively, with similar results. Initial rates were calculated using the molar extinction coefficient of $[Fe(2,2'\text{-bipyridyl})_3]^{2+}$ (8430 $M^{-1}\ cm^{-1}$) obtained from the slope of the linear plot ($R^2 =$ 0.98–0.99) of the data related to the initial linear phase.

2.5. Sequence alignment

Sequence similarities with bullfrog M ferritin were analyzed to identify the nature of the amino acid present at positions corresponding to His54 using 500 sequences of vertebrate ferritins (identity range 100–55%) [16]. Search for ferritin from vertebrate sequences in

UniProtKB database was performed using BLAST and multiple sequence alignment was obtained by ClustalW.

2.6. Statistical analysis

The data were analyzed by Student's *t* test, and $P < 0.05$ was considered significant.

3. Results

The diferric-oxo-species and the ferric oxide $(Fe^{3+}O)_x$ that form at the second and third steps of the biomineralization reaction (see Introduction) are both characterized by an absorbance at 350 nm, although with different extinction coefficients; the short-lived DFP product of the first reaction steps has a characteristic absorbance at 650 nm. Stopped-flow electronic absorption kinetics allows monitoring the formation of these ferric species, after addition of iron(II) to apoferritin solutions [14,15,17]. Comparative kinetics data for the wild type and the H54A variant were used to monitor possible differences in the reaction efficiency using different Fe^{2+}/protein ratios.

Upon addition of 20 Fe^{2+}/subunit, i.e. with a stoichiometry that theoretically corresponds to 10 subsequent turnovers [14], we observed the behavior reported in Fig. 2A. The total amount of ferric-oxo species at plateau is the same for both wild type and H54A, but the initial rate is more than two times faster for the latter variant, as quantified in Fig. 2C, first column.

The biomineralization reaction is a complex phenomenon. After the catalytic oxidation of the ferrous species, under the effect of new incoming ferrous ions [8,18], the ferric products are released from the ferroxidase site and migrate towards the inner cavity, where they grow to provide a mineral of nanometer dimension [16]. NMR data have suggested that the migration process might involve ferric-oxo cluster of high nuclearity, but confirmatory high-resolution data are still missing [3,19]. Paramagnetic broadening of the NMR signals induced by ferric species formed in subsequent turnovers, has suggested that the path of ferric products from the catalytic site to the cavity involves the subunit area from the ferroxidase center to the short H5 helix, where also H54 is located [3,19]. To factorize out the possible contribution of His54 to Fe^{2+} entry into the ferroxidase site from its potential role in assisting ferric-product replacement with new ferrous ions, we have analyzed the kinetics at a lower number of turnovers. With 4 Fe^{2+}/subunit (Fig. 2B and C), the initial reaction rates of the DFP and ferric-oxo species formation in H54A ferritin variant, monitored at 650 nm and 350 nm respectively, are about 20% faster than the corresponding rates in wild type ferritin. In particular, at 650 nm the mean ± SD values of the initial rates obtained from three independent experiments are 1.75 ± 0.23 for the WT vs. 2.10 ± 0.19 for H54A; at 350 nm, 3.20 ± 0.50 for the WT vs. 3.93 ± 0.44 for H54A. Again, the total maximum absorbance does not change significantly for the two cage proteins. The situation is exactly the same when stopped-flow kinetics data are acquired with 2 Fe^{2+}/subunit (Fig. 2B and C), with the following mean ± SD values of the initial rates obtained from three independent experiments: at 650 nm, 0.50 ± 0.03 for the WT vs. 0.61 ± 0.08 for H54A; at 350 nm, 0.82 ± 0.14 for the WT vs. 1.02 ± 0.12 for H54A. Although the differences with respect to the wild type protein are statistically significant ($P < 0.05$), the effects with 4 and 2 Fe^{2+}/subunit are much attenuated compared to the stoichiometry of 20 Fe^{2+}/subunit. Consistently with the increased rate of formation of the ferric-oxo species, the decay of DFP is also faster in H54A than in wild type for both stoichiometries.

In summary, with low Fe^{2+}/subunit ratios, the observed speeding up of the reaction induced by the H54A mutation is meaningful but relatively weak (20% increase). Much stronger, instead, is the increase in initial rate of $(Fe^{3+}O)_x$ formation with 20 Fe^{2+}/subunit, suggesting a role for His54 in the release of ferric products from the catalytic site rather than in the uptake of ferrous ion from the inner cavity. Very importantly, for any stoichiometry the H54A substitution always results in an increased rate of product formation.

Exhaustive characterization of ferritin variants includes also the analysis of the caged biomineral dissolution induced by reducing and chelating agents [14,20–22]. In H54A the amount of iron released from the caged biomineral is unaffected by the mutation (Fig. 3). This result is not unexpected, as His54 is far from channels that have been proposed to control this process [14,20–22].

4. Discussion

Fe^{2+}-aqua ions enter the ferritin cage through the eight 3-fold symmetry channels that form where three subunits come in contact; the uptake of the metal ion is driven by an electrostatic gradient (or electric field gradient) generated by carboxylate protein residues located in the inner bottom part of these channels [8,9,14,23–25]. As proposed based on potential energy profile calculations and observed by X-ray crystallography, these residues can attract up to three Fe^{2+} ions into the inner bottom edge of the channels [8,12,25]. Once in, the inner cavity ferrous ions are imported into the catalytic reaction centers, located in the central inner part of the 4-helix bundle subunits. According to the X-ray data (PDB: 4LPJ, 4LQJ, 4LYX, 4LYU, 4LQV, 4LQN, 3RGD) [8,12], the permeability to iron of the ferroxidase site arises from a set of amino acids (E136, E57, H54) located in the close proximity of the catalytic center and facing the inner cavity of the cage. Substitution of conserved cage carboxylates E136 and/or E57 with Ala, slows down the catalytic reaction in bullfrog M ferritin, as recently demonstrated [11], supporting the idea that the translocation of cations from the inner cavity to the bundle interior is again driven by electrostatic attractions exerted by clusters of negatively charged residues.

Contrarily to what happens for E136A, E57A and E57AE136A, in H54A we observed a speeding up of the reaction, which becomes more evident at high turnover numbers. Obtaining an activation of an enzymatic reaction upon substitution of a natural amino acid with an Ala is quite a surprising result, whose interpretation is not obvious.

The presence of a residue potentially able to act as a metal ion ligand in positions structurally analogous to His54 of M ferritin is a common feature of catalytically active ferritin subunits.

In vertebrates H ferritins, the position corresponding to His54 is generally occupied by an Asn or a Gln (Q58 according the human H numbering) and in a few cases by a Tyr; those residues can play a role similar to His. Indeed, iron trapped at this site has been observed in crystal structures of the bullfrog M ferritin variant H54Q under iron free diffusion (PDB: 4ML5, 4MN9, 4MJY) [12]. An exception is represented by the ferritin from marine pennate diatom *Pesudonitzschia multiseries*, which is largely divergent from the other eukaryotic sequences [26], where the corresponding amino acid is an Asp, i.e. again a residue able to bind iron and other cations. The well-characterized archeal ferritin [18,27–29] from *Pyrococcus furiosus* also contains a Gln at this position.

In bacterioferritin from *Pseudomonas aeruginosa* a structurally similar position is occupied by His130, and the reorientation of its imidazole ring has been proposed to create a path for the translocation of iron from the ferroxidase center to the inner cavity [30]. This does not seem to be the case of His54 in bullfrog M ferritin, because in this hypothesis its substitution with a non-coordinating residue should lead to a decreased rate of biomineral formation, whereas we observed the opposite behavior (Fig. 2A).

Contrarily to the above cases, non-active subunits like the human L ferritin contain a Leu.

Paradoxically, in M ferritin the substitution of a coordinating hydrophilic residue by a hydrophobic non-coordinating one, like in non-active subunits, produces a variant that results to be an activator of the reaction. It should be noted, however, that in the fish *Gillichthys mirabilis* an Ala is naturally occurring in a ferritin subunit reported as active [31].

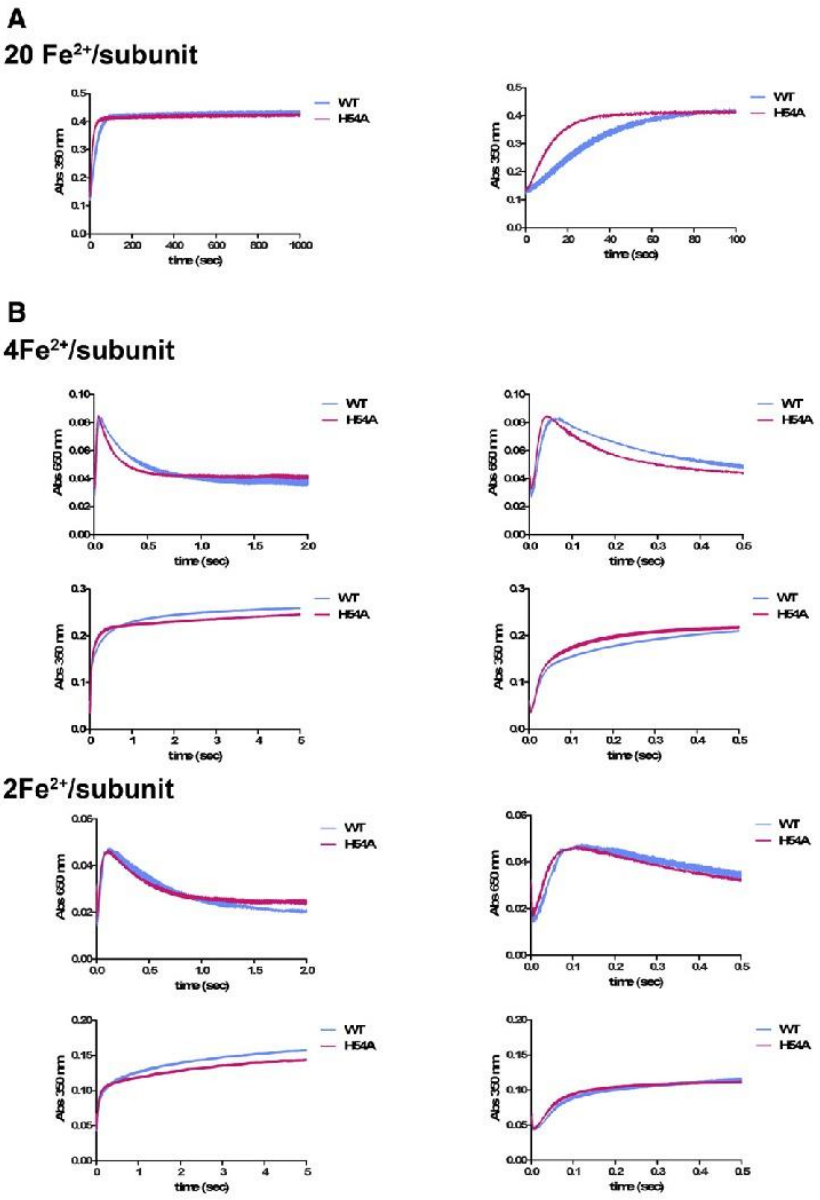

C

Initial rates of formation (fold-increase over WT values)

Protein	$(Fe^{3+}O)_x$ ($20Fe^{2+}$/subunit) ($\Delta A_{350\ nm}$/s)	DFP ($4Fe^{2+}$/subunit) ($\Delta A_{650\ nm}$/s)	$(Fe^{3+}O)_x$ ($4Fe^{2+}$/subunit) ($\Delta A_{350\ nm}$/s)	DFP ($2Fe^{2+}$/subunit) ($\Delta A_{650\ nm}$/s)	$(Fe^{3+}O)_x$ ($2Fe^{2+}$/subunit) ($\Delta A_{350\ nm}$/s)
H54A	2.4*	1.2*	1.2*	1.2*	1.2*

Fig. 2. Kinetics of products formation in WT and H54A by rapid-mixing, UV–vis spectroscopy. (A) Reaction progress at high iron:protein ratio (20 Fe^{2+}/subunit; 480 Fe^{2+}/cage) monitored as $(Fe^{3+}O)_x$ products ($A_{350\ nm}$) formation; the right panel shows an enlargement of the first 100 s. (B) Formation and decay of DFP intermediate ($A_{650\ nm}$) (left) and formation of $(Fe^{3+}O)_x$ products ($A_{350\ nm}$) (right) measured after the addition of 4 Fe^{2+}/subunit (upper panels) or 2 Fe^{2+}/subunit (lower panels); the right panels show enlargements of the first 0.5 s to highlight the differences in the initial rates. Each graph shows a set of curves (mean ± SEM) of a representative experiment of at least three. (C) Table reporting the fold change over WT (set as 1) of the initial rates of formation of the various species, calculated as described in Materials and methods section from three independent analyses. *Significantly different from the corresponding value in wild type; $P < 0.05$. WT: blue curves, H54A: pink curves.

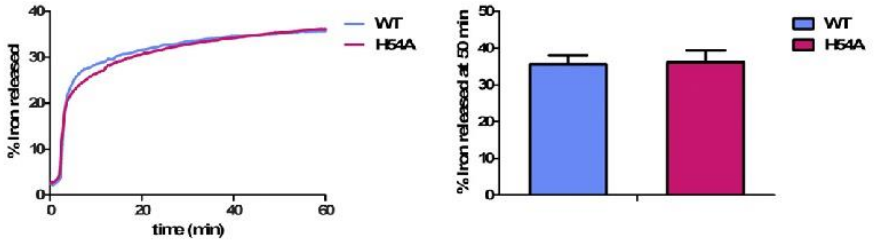

Fig. 3. Dissolution/chelation of iron from the ferritin biomineral formed in WT and H54A cages. Iron was recovered from caged hydrated ferric oxide mineral, synthesized by and inside ferritin protein cages, by adding reductant (NADH and FMN) in the presence of a chelator (2,2′-bipyridyl) and measuring the rate of formation of $[Fe(2,2'\text{-bipyridyl})_3]^{2+}$ outside the protein cage as described in Materials and methods section. One representative curve from three independent experiments is reported for both WT (blue) and H54A (pink) (left panel); the percentage of Fe^{2+} released at 60 min, calculated from three independent experiments performed with WT (blue) and H54A (pink), is shown in bar plot (right panel).

The present results highlight the importance of site directed mutagenesis and activity measurements to interpret correctly the results obtained via X-rays crystallography when unraveling the role of single amino acids in the mechanism of iron handling in the complex ferritin nanocages and their contribution to mechanistic variations among ferritins [32]. We showed that metal ions bound in wild type M ferritin crystals do not represent productive states for the ferritin reactions. From this study His54 seems to control the access of iron to the active site avoiding overloading, before the catalytic reaction has been completed and the ferric-oxy/hydroxo products have been released towards the inner cavity. His54 could also have a defense role by trapping non-natural divalent cations, thus keeping them far from the dinuclear iron site, where they compete with iron inhibiting the reaction [8,9]. It should be noted that the available structural data have been acquired under iron free diffusion and the largest effect on kinetics is again observed under excess iron in solution. The functional meaning of the present data for the *in vivo* function of ferritin is not clear at the present stage and would require in cell studies.

Transparency documents

The Transparency documents associated with this article can be found, in online version.

Acknowledgments

We acknowledge the financial support of MIUR PRIN 2012 (contract number 2012SK7ASN) and Ente Cassa di Risparmio di Firenze (contract number 2013.0494).

References

[1] E.C. Theil, R.K. Behera, T. Tosha, Ferritins for chemistry and for life, Coord. Chem. Rev. 257 (2013) 579–586.
[2] R.R. Crichton, J.P. Declercq, X-ray structures of ferritins and related proteins, Biochim. Biophys. Acta 1800 (2010) 706–718.
[3] D. Lalli, P. Turano, Solution and solid state NMR approaches to draw iron pathways in the ferritin nanocage, Acc. Chem. Res. 46 (2013) 2676–2685.
[4] F.M. Torti, S.V. Torti, Regulation of ferritin genes and protein, Blood 99 (2002) 3505–3516.
[5] P. Arosio, R. Ingrassia, P. Cavadini, Ferritins: a family of molecules for iron storage, antioxidation and more, Biochim. Biophys. Acta 1790 (2009) 589–599.
[6] J.K. Schwartz, X.S. Liu, T. Tosha, E.C. Theil, E.I. Solomon, Spectroscopic definition of the ferroxidase site in M ferritin: comparison of binuclear substrate vs cofactor active sites, J. Am. Chem. Soc. 130 (2008) 9441–9450.
[7] J. Hwang, C. Krebs, B.H. Huynh, D.E. Edmondson, E.C. Theil, J.E. Penner-Hahn, A short Fe–Fe distance in peroxodiferric ferritin: control of Fe substrate versus cofactor decay? Science 287 (2000) 122–125.
[8] I. Bertini, D. Lalli, S. Mangani, C. Pozzi, C. Rosa, E.C. Theil, P. Turano, Structural insights into the ferroxidase site of ferritins from higher eukaryotes, J. Am. Chem. Soc. 134 (2012) 6169–6176.
[9] T. Tosha, H.L. Ng, O. Bhattasali, T. Alber, E.C. Theil, Moving metal ions through ferritin-protein nanocages from three-fold pores to catalytic sites, J. Am. Chem. Soc. 132 (2010) 14562–14569.
[10] L. Toussaint, L. Bertrand, L. Hue, R.R. Crichton, J.P. Declercq, High-resolution structures of human apoferritin H-chain mutants correlated with their activity and metal-binding sites X-ray, J. Mol. Biol. 365 (2007) 440–452.
[11] R.K. Behera, E.C. Theil, Moving Fe^{2+} from ferritin ion channels to catalytic OH centers depends on conserved protein cage carboxylates, Proc. Natl. Acad. Sci. U. S. A. 111 (2014) 7925–7930.
[12] C. Pozzi, F. Di Pisa, D. Lalli, C. Rosa, E.C. Theil, P. Turano, S. Mangani, Time lapse, anomalous X-ray diffraction shows how Fe^{2+} substrate ions move through ferritin protein nanocages to oxidoreductase sites, Acta Crystallogr. D (2015) http://dx.doi.org/10.1107/S1399004715002333 (in press).
[13] M. Matzapetakis, P. Turano, E.C. Theil, I. Bertini, ^{13}C–^{13}C NOESY spectra of a 480 kDa protein: solution NMR of ferritin, J. Biomol. NMR 38 (2007) 237–242.
[14] E.C. Theil, P. Turano, V. Ghini, M. Allegrozzi, C. Bernacchioni, Coordinating subdomains of ferritin protein cages with catalysis and biomineralization viewed from the C4 cage axes, J. Biol. Inorg. Chem. 19 (2014) 615–622.
[15] T. Tosha, R.K. Behera, E.C. Theil, Ferritin ion channel disorder inhibits $Fe(II)/O_2$ reactivity at distant sites, Inorg. Chem. 51 (2012) 11406–11411.
[16] C. Bernacchioni, V. Ghini, C. Pozzi, F. Di Pisa, E.C. Theil, P. Turano, Loop electrostatics modulates the intersubunit interactions in ferritin, ACS Chem. Biol. 21 (2014) 2517–2525.
[17] X. Liu, E.C. Theil, Ferritin reactions: direct identification of the site for the diferric peroxide reaction intermediate, Proc. Natl. Acad. Sci. U. S. A. 101 (2004) 8557–8562.
[18] K.H. Ebrahimi, E. Bill, P.L. Hagedoorn, W.R. Hagen, The catalytic center of ferritin regulates iron storage via Fe(II)–Fe(III) displacement, Nat. Chem. Biol. 8 (2012) 941–948.
[19] P. Turano, D. Lalli, I.C. Felli, E.C. Theil, I. Bertini, NMR reveals pathway for ferric mineral precursors to the central cavity of ferritin, Proc. Natl. Acad. Sci. U. S. A. 107 (2010) 545–550.
[20] X. Liu, W. Jin, E.C. Theil, Opening protein pores with chaotropes enhances Fe reduction and chelation of Fe from the ferritin biomineral, Proc. Natl. Acad. Sci. U. S. A. 100 (2003) 3653–3658.
[21] W. Jin, H. Takagi, B. Pancorbo, E.C. Theil, "Opening" the ferritin pore for iron release by mutation of conserved amino acids at interhelix and loop sites, Biochemistry 40 (2001) 7525–7532.
[22] M.R. Hasan, T. Tosha, E.C. Theil, Ferritin contains less iron (^{59}Fe) in cells when the protein pores are unfolded by mutation, J. Biol. Chem. 283 (2008) 31394–31400.
[23] S. Levi, A. Luzzago, F. Franceschinelli, P. Santambrogio, G. Cesareni, P. Arosio, Mutational analysis of the channel and loop sequences of human ferritin H-chain, Biochem. J. 264 (1989) 381–388.
[24] A. Treffry, E.R. Bauminger, D. Hechel, N.W. Hodson, I. Nowik, S.J. Yewdall, P.M. Harrison, Defining the roles of the threefold channels in iron uptake, iron oxidation and iron-core formation in ferritin: a study aided by site-directed mutagenesis, Biochem. J. 296 (1993) 721–728.
[25] T. Takahashi, S. Kuyucaky, Functional properties of threefold and fourfold channels in ferritin deduced from electrostatic calculations, Biophys. J. 84 (2003) 2256–2263.
[26] A. Marchetti, M.S. Parker, L.P. Moccia, E.O. Lin, A.L. Arrieta, F. Ribalet, M.E. Murphy, M.T. Maldonado, E.V. Armbrust, Ferritin is used for iron storage in bloom-forming marine pennate diatoms, Nature 457 (2009) 467–470.
[27] K.H. Ebrahimi, E. Bill, P.L. Hagedoorn, W.R. Hagen, The catalytic center of ferritin regulates iron storage via Fe(II)–Fe(III) displacement, Nat. Chem. Biol. 8 (2012) 941–948.
[28] K.H. Ebrahimi, P.L. Hagedoorn, J.A. Jongejan, W.R. Hagen, Catalysis of iron core formation in *Pyrococcus furiosus* ferritin, J. Biol. Inorg. Chem. 14 (2009) 1265–1274.
[29] J. Tatur, W.R. Hagen, P.M. Matias, Crystal structure of the ferritin from the hyperthermophilic archaeal anaerobe *Pyrococcus furiosus*, J. Biol. Inorg. Chem. 12 (2007) 615–630.
[30] S.K. Weeratunga, S. Lovell, H. Yao, K.P. Battaile, C.J. Fischer, C.E. Gee, M. Rivera, Structural studies of bacterioferritin B from *Pseudomonas aeruginosa* suggest a gating mechanism for iron uptake via the ferroxidase center, Biochemistry 49 (2010) 1160–1175.
[31] A.Y. Gracey, J.V. Troll, G.N. Somero, Hypoxia-induced gene expression profiling in the euryoxic fish *Gillichthys mirabilis*, Proc. Natl. Acad. Sci. U. S. A. 98 (2001) 1993–1998.
[32] J.M. Bradley, G.R. Moore, N.E. Le Brun, Mechanisms of iron mineralization in ferritins: one size does not fit all, J. Biol. Inorg. Chem. 19 (2014) 775–785.

Annex II

Publication

“Iron binding to human heavy-chain ferritin”

C. Pozzi[a], F. Di Pisa[a], C. Bernacchioni[b,c], S. Ciambellotti[b,c], P. Turano[b,c] and S. Mangani[a,c]

[a] Dipartimento di Biotecnologie, Chimica e Farmacia, Universita` di Siena, Via Aldo Moro 2, 53100 Siena, Italy,
[b] CERM, Universita` di Firenze, Via L. Sacconi 6, Sesto Fiorentino, 50019 Firenze, Italy.
[c] Dipartimento di Chimica, Universita` di Firenze, Via Della Lastruccia 3, Sesto Fiorentino, 50019 Firenze, Italy,

BIOLOGICAL CRYSTALLOGRAPHY
ISSN 1399-0047

Iron binding to human heavy-chain ferritin

Cecilia Pozzi,[a] Flavio Di Pisa,[a] Caterina Bernacchioni,[b,c] Silvia Ciambellotti,[b,c] Paola Turano[b,c] and Stefano Mangani[a,c]*

[a]Dipartimento di Biotecnologie, Chimica e Farmacia, Università di Siena, Via Aldo Moro 2, 53100 Siena, Italy, [b]Dipartimento di Chimica, Università di Firenze, Via Della Lastruccia 3, Sesto Fiorentino, 50019 Firenze, Italy, and [c]CERM, Università di Firenze, Via L. Sacconi 6, Sesto Fiorentino, 50019 Firenze, Italy. *Correspondence e-mail: stefano.mangani@unisi.it

Received 20 May 2015
Accepted 7 July 2015

Edited by Z. S. Derewenda, University of Virginia, USA

Keywords: ferritin; human heavy chain; iron; mechanism.

PDB references: human H-chain ferritin loaded with iron ions for 1 min, 4p03; for 5 min, 4zjk; for 15 min, 4oyn; for 30 min, 4ykh

Supporting information: this article has supporting information at journals.iucr.org/d

Maxi-ferritins are ubiquitous iron-storage proteins with a common cage architecture made up of 24 identical subunits of five α-helices that drive iron biomineralization through catalytic iron(II) oxidation occurring at oxido-reductase sites (OS). Structures of iron-bound human H ferritin were solved at high resolution by freezing ferritin crystals at different time intervals after exposure to a ferrous salt. Multiple binding sites were identified that define the iron path from the entry ion channels to the oxidoreductase sites. Similar data are available for another vertebrate ferritin: the M protein from *Rana catesbeiana*. A comparative analysis of the iron sites in the two proteins identifies new reaction intermediates and underlines clear differences in the pattern of ligands that define the additional iron sites that precede the oxidoreductase binding sites along this path. Stopped-flow kinetics assays revealed that human H ferritin has different levels of activity compared with its *R. catesbeiana* counterpart. The role of the different pattern of transient iron-binding sites in the OS is discussed with respect to the observed differences in activity across the species.

1. Introduction

Ferritins are ubiquitous chemical reactors that control the biosynthesis and dissolution of caged hydrated ferric minerals (EC 1.16.3.1). They also function as antioxidants by retrieving iron ions released from degraded iron proteins, preventing the occurrence of Fenton-like chemistry (Theil *et al.*, 2013).

The 24-subunit ferritins, called maxi-ferritins, self-assemble to form a nanocage with an outer diameter of approximately 120 Å, while the diameter of the internal cavity is around 80 Å (Liu & Theil, 2005). The ferritin nanocage is characterized by having 432 (*O*; octahedral) point symmetry with three fourfold, four threefold and six twofold axes (Crichton & Declercq, 2010). Thousands of Fe atoms can be stored in the inner cavity as an iron mineral obtained by catalytic oxidation of iron(II) by dioxygen or hydrogen peroxide in the protein oxidoreductase sites (OS; Fig. 1), where the substrates are coupled to obtain iron(III) mineral precursors (Theil *et al.*, 2013; Theil, 2011). In vertebrates, ferritin usually functions as a heteropolymer composed of two distinct subunits, the H (heavy, about 21 kDa) chain and the L (light, about 19 kDa) chain, that co-assemble in H:L ratios that are tissue-specific (Arosio *et al.*, 2009). Ferritin rich in L chain, which lacks oxidoreductase activity, is found in tissues involved in long-term storage of iron such as the liver or spleen, while H-chain-rich ferritin, with oxidoreductase activity, is found in tissues with more active iron metabolism such as muscle.

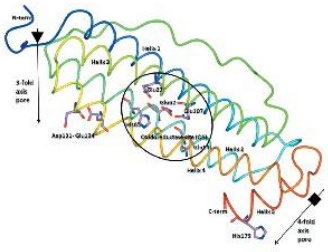

Iron-binding sites in maxi-ferritins have been identified by conventional X-ray crystallography only for those from the extremophilic archaeon *Pyrococcus furiosus* (Tatur *et al.*, 2007), the prokaryote *Escherichia coli* (Stillman *et al.*, 2001) and the eukaryotic pennate diatom *Pseudo-nitzschia* (Marchetti *et al.*, 2009). The identification of iron-binding sites in other ferritins has been more difficult owing to the quite rapid turnover, which also occurs in the crystal and prevents the use of soaking–freezing experiments. Recently, a different approach has successfully revealed iron binding to *Rana catesbeiana* M ferritin (RcMf; Bertini *et al.*, 2012; Pozzi *et al.*, 2015). These studies have identified the existence of several iron-binding sites defining a possible pathway for iron(II) ions from the entry channels to the OS and have highlighted the role of several residues along this path.

There is an intense ongoing debate in the literature about the mechanism(s) by which the different ferritins operate. Recently, a so-called unifying mechanism for all ferritins has been proposed (Honarmand Ebrahimi *et al.*, 2012, 2015), but other views are also supported by the experimental evidence (Bou-Abdallah *et al.*, 2014; Bradley *et al.*, 2014; Pozzi *et al.*, 2015).

The wide ferritin panorama still lacks the identification of the iron-binding sites in a mammalian ferritin. To fill this gap, we report here the results of the crystallographic determination of iron adducts of human H ferritin (HuHf) obtained by applying the same experimental method as used in a previous study of RcMf (Pozzi *et al.*, 2015). Time-lapse anomalous data have allowed us to follow the progressive population of a series of iron-binding sites in a recombinant form of HuHf.

HuHf and RcMf share about 64% identity; the residues identified as active-site ligands in RcMf (*i.e.* Glu103, Glu58, His61 and Glu23) are all conserved in HuHf (the HuHf sequence numbering is shifted by +4 with respect to RcMf, as shown in Supplementary Fig. S1), but there are meaningful differences in the amino-acid composition of the OS residues proposed to be additional transient iron-binding sites in RcMf. The comparative analysis of the X-ray crystal structures and kinetic data for HuHf and RcMf presented here shows changes in the number and positions of these additional iron sites and in reaction rates. The implications for the proposed ferritin mechanism(s) are discussed.

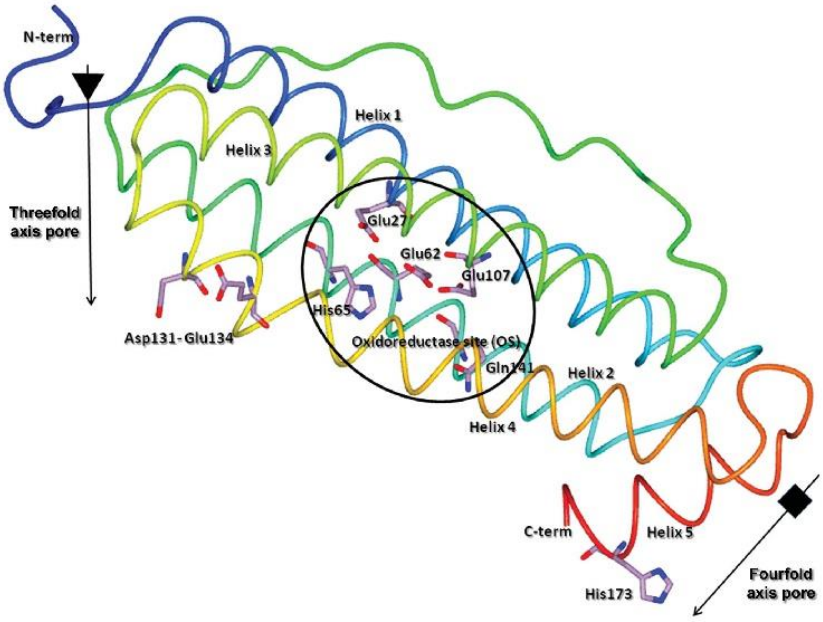

Figure 1
The HuHf subunit represented as a ribbon rainbow-coloured from the N-terminus (blue) to the C-terminus (red). The five α-helices are sequentially numbered starting from the N-terminus. The oxidoreductase site (OS) is circled and the threefold and fourfold pore locations are shown by arrows pointing into the interior of the ferritin cage; the amino-acid residues involved in iron binding are labelled and represented as sticks.

2. Materials and methods

2.1. Protein expression and purification

RcMf was expressed as described previously (Pozzi *et al.*, 2015). The gene-coding sequence for HuHf was custom-synthesized (GenScript, USA) and subcloned into pET-9a expression vector using NdeI and BamHI restriction sites.

The expression plasmid was introduced by thermal shock into *E. coli* strain BL21 (DE3) (Invitrogen). Transformants were selected in LB agar supplemented with 50 mg l^{-1} kanamycin. The bacterial culture was grown at 37°C on LB medium supplemented with 50 mg l^{-1} kanamycin. Protein overexpression was induced with 0.2 m*M* isopropyl β-D-1-thio-galactopyranoside (IPTG) when the cell density reached an A_{600} of 0.6 with incubation at 30°C. The cells were harvested by centrifugation after 16 h of induction and were resuspended in buffer *A* [20 m*M* Tris pH 7.7, 1 m*M* ethylenediaminetetraacetic acid (EDTA), 0.15 *M* NaCl, 0.1 m*M* phenylmethanesulfonyl fluoride hydrochloride (PMSF)]. The intracellular contents were liberated by sonication and the resulting suspension was centrifuged at 18 500*g* for 45 min at 6°C to remove the insoluble fraction. The supernatant of the resulting crude extract was incubated at 60°C for 10 min and the heat-stable fraction was further purified by ammonium sulfate precipitation (50–60% saturated fractions), anion-exchange chromatography and size-exclusion chromatography as described previously for RcMf (Pozzi *et al.*, 2015).

Table 1
Data collection and processing.

Values in parentheses are for the outer shell.

HuHf + iron(II)	1 min	5 min	15 min	30 min
PDB code	4y08	4zjk	4oyn	4ykh
Diffraction source	I04-1, DLS	I04-1, DLS	I04-1, DLS	I04-1, DLS
Wavelength (Å)	0.92	0.92	0.92	0.92
Temperature (K)	100	100	100	100
Detector	Pilatus 2M	Pilatus 2M	Pilatus 2M	Pilatus 2M
Crystal-to-detector distance (mm)	165	170	180	160
Rotation range per image (°)	0.20	0.20	0.20	0.20
Total rotation range (°)	100	100	100	100
Exposure time per image (s)	0.3	0.5	0.5	0.5
Space group, *Z*	*F*432, 4	*F*432, 4	*F*432, 4	*F*432, 4
No. of subunits in asymmetric unit	1	1	1	1
a, *b*, *c* (Å)	184.14	183.80	183.91	184.05
Mosaicity (°)	0.24	1.07	0.29	0.41
Resolution range (Å)	29.11–1.34 (1.41–1.34)	31.07–1.56 (1.64–1.56)	32.51–1.43 (1.51–1.43)	29.10–1.52 (1.60–1.52)
Total No. of reflections	1205847 (172066)	437700 (36197)	990962 (142832)	809546 (102979)
No. of unique reflections	60022 (8623)	38257 (5431)	49578 (7123)	41531 (5956)
Completeness (%)	99.7 (100.0)	99.8 (99.1)	100.0 (100.0)	100.0 (100.0)
Anomalous completeness (%)	99.8 (100.0)	99.0 (95.7)	100.0 (100.0)	100.0 (100.0)
Multiplicity	20.1 (20.0)	11.4 (6.7)	20.0 (20.1)	19.5 (17.3)
Anomalous multiplicity	10.6 (10.3)	5.9 (3.4)	10.5 (10.3)	10.3 (8.8)
$\langle I/\sigma(I)\rangle$	28.2 (8.0)	25.0 (3.6)	27.9 (7.1)	25.8 (7.0)
$R_{\rm meas}$	0.072 (0.414)	0.062 (0.510)	0.072 (0.438)	0.082 (0.434)
Overall *B* factor from Wilson plot (Å^2)	8.5	11.0	9.7	10.3

2.2. Crystallization

Purified HuHf in 20 m*M* Tris pH 7.7, 0.15 *M* NaCl was concentrated to 13.4 mg ml^{-1}. Crystals of native HuHf were grown using the hanging-drop vapour-diffusion technique at 297 K. Drops were prepared by mixing equal volumes (2 µl) of HuHf and a precipitant solution composed of 2.0 *M* $MgCl_2$, 0.1 *M* bicine pH 9.0 to give a final pH value of about 8.0. Octahedrally shaped crystals of 50–100 µm in size grew in 3–6 d. The crystallization of HuHf was also performed under strict anaerobic conditions using the same procedure as previously reported for RcMf (Pozzi *et al.*, 2015). These crystals were used as a control for the oxidation state and coordination environment of iron in the aerobic crystals.

A time-controlled iron-loading study was performed by allowing solid-to-solid iron(II) ion diffusion from grains of $[(NH_4)_2Fe(SO_4)_2]\cdot 6H_2O$ (Mohr's salt) to HuHf crystals of approximately the same size (~100 µm) for monitored exposure times of 1, 5, 15 and 30 min, and for up to 8 min for the anaerobic crystals, followed by flash-cooling in liquid nitrogen, as reported previously for RcMf (Pozzi *et al.*, 2015).

2.3. Data collection, structure solution and refinement

Complete data sets were collected on beamline I04-1 at Diamond Light Source (DLS) using a Pilatus 2M detector at 100 K. Data were integrated using *MOSFLM* v.7.0.4 (Leslie, 2006) and scaled with *SCALA* (Evans, 2006, 2011) from the *CCP*4 suite (Winn *et al.*, 2011). The HuHf crystals belonged to the cubic space group *F*432, with unit-cell parameter $a \simeq 185$ Å, varying slightly among the different crystals. Data-collection and processing statistics are reported in Table 1. Anomalous difference maps were computed from the single-wavelength data exploiting the iron anomalous signal, which was still present at 0.920 Å (13.477 keV; $f' \simeq -0.298$ e$^-$, $f'' \simeq 1.35$ e$^-$) and nevertheless provides very clear anomalous maps owing to the high quality and the redundancy of the data collected. All of the iron-binding sites found in these maps have subsequently been fully confirmed by lower resolution data sets collected in a two-wavelength measurement mode (Fe *K* edge and remote) at Elettra, Trieste, Italy from crystals treated with iron under exactly the same conditions.

Phasing was performed by molecular replacement using *MOLREP* (Vagin & Teplyakov, 2010) from the *CCP*4 suite. A subunit of human H ferritin (PDB entry 3ajo; Masuda *et al.*, 2010) was used as a search model, excluding nonprotein atoms and water molecules. The positions of the iron ions were determined from anomalous difference Fourier maps computed using *FFT* from the *CCP*4 suite. The anomalous signals corresponding to iron ions were between 6σ and 40σ in the anomalous difference maps.

The structures were refined with *REFMAC* v.5.8 (Murshudov *et al.*, 2011). The refinement protocol involved sequential iterative manual rebuilding of the model and maximum-likelihood refinement. Manual rebuilding and modelling of the missing atoms into the electron density was performed with the molecular-graphics software *Coot* (Emsley *et al.*, 2010). Partial occupancies for the iron or magnesium ions, for other ligands and for several amino-acid residues were adjusted in order to obtain atomic displacement parameters that were close to those of neighbouring protein atoms in fully occupied sites. The occupancies of the water molecules or other ligands bound to metal ions were kept the same as those of the parent metal ion. *ARP*/*wARP* was used for the addition of water molecules (Langer *et al.*, 2008). The final models were inspected manually and checked with *Coot* and *PROCHECK* (Laskowski *et al.*, 1993). The final refinement statistics are reported in Table 2. All figures were generated using *CCP*4*mg* (McNicholas *et al.*, 2011).

2.4. Stopped-flow kinetics

The addition of 1–4 iron(II) ions per subunit (Bernacchioni *et al.*, 2014, 2015; Theil *et al.*, 2014) to HuHf and RcMf was monitored by the change in $A_{650\,\rm nm}$ (diferric peroxo; DFP) or $A_{350\,\rm nm}$ [diferric oxo/hydroxo species; DFO(H)] after rapid mixing (less than 10 ms) of equal volumes of 100 µ*M* protein subunits (4.16 µ*M* protein cages) in 200 m*M* 3-(*N*-morpho-

Table 2
Structure solution and refinement.

Values in parentheses are for the outer shell.

HuHf + iron(II)	1 min	5 min	15 min	30 min
PDB code	4y08	4zjk	4oyn	4ykh
Resolution range (Å)	27.76–1.34 (1.38–1.34)	31.07–1.56 (1.60–1.56)	31.09–1.43 (1.47–1.43)	28.07–1.52 (1.56–1.52)
Completeness (%)	99.7 (100.0)	99.7 (98.3)	100.0 (100.0)	99.9 (100.0)
σ Cutoff	2.0	2.0	2.0	2.0
No. of reflections, working set	56945 (4127)	36303 (2592)	47040 (3384)	39434 (2874)
No. of reflections, test set	3037 (230)	1918 (124)	2508 (190)	2086 (139)
Final R_{cryst}	0.163 (0.175)	0.168 (0.202)	0.167 (0.183)	0.165 (0.171)
Final R_{free}	0.173 (0.190)	0.192 (0.237)	0.179 (0.214)	0.187 (0.180)
Cruickshank DPI	0.043	0.068	0.053	0.062
No. of non-H atoms				
Protein	1409	1413	1413	1410
Ion	19	24	23	23
Ligand	4	–	19	11
Water	328	329	320	323
Total	1760	1766	1775	1676
R.m.s. deviations				
Bonds (Å)	0.006	0.007	0.005	0.006
Angles (°)	1.037	1.000	0.981	1.007
Average B factors (Å^2)				
Protein	10.2	13.7	11.7	12.9
Ion	13.9	20.3	16.1	16.4
Ligand	9.2	0.0	22.5	9.5
Water	23.6	29.4	26.2	27.8
Estimate error on coordinates based on R value (Å)	0.043	0.068	0.053	0.062
Ramachandran plot				
Most favoured (%)	98.8	98.8	98.8	98.8
Allowed (%)	1.2	1.2	1.2	1.2

lino)propanesulfonic acid (MOPS), 200 m*M* NaCl pH 7.0 with freshly prepared solutions of 100, 200, 300 or 400 µ*M* ferrous sulfate in 1 m*M* HCl in a UV–visible stopped-flow spectrophotometer (SX.18MV stopped-flow reaction analyzer; Applied Photophysics, Leatherhead, England). Routinely, 4000 data points were collected during the first 5 s. The initial formation rates of DFP and DFO(H) species were determined from linear fitting of the initial phases (0.01–0.03 s) of the change in absorbance at 650 and 350 nm, respectively. The decay rate of the DFP species was fitted with a mono-exponential function of the decrease in intensity at 650 nm (Tosha *et al.*, 2012).

2.5. Transmission electron microscopy (TEM)

Recombinant ferritin protein cages (3 µ*M*) were mineralized with ferrous sulfate [80 iron(II) ions per subunit] in 100 m*M* MOPS, 100 m*M* NaCl pH 7.0. Two different procedures were followed: (i) a total of 80 iron(II) ions per subunit were added in a single step or (ii) three sequential additions were performed [20 iron(II) ions per subunit, 20 iron(II) ions per subunit and 40 iron(II) ions per subunit]. After each addition the solutions were incubated for 2 h at room temperature and then overnight at 4°C to complete the iron-mineralization reaction. For TEM tests, solutions of mineralized HuHf and RcMf cages were dropped onto and dried on a Cu grid covered by a holey carbon film. Bright-field TEM images were collected using a Philips CM12 microscope operating at 80 kV (Bernacchioni *et al.*, 2014).

2.6. PDB codes

The final coordinates and structure factors for HuHf loaded with iron ions for 1, 5, 15 and 30 min have been deposited in the PDB under accession codes 4y08, 4zjk, 4oyn and 4ykh, respectively.

3. Results

3.1. Overall structure of human H ferritin

A series of HuHf structures were obtained at high resolution by following an established protocol that allows us to use time-lapse crystallography to appreciate the sequence of iron-binding events (Pozzi *et al.*, 2015). Crystals of iron-free HuHf were mixed with crystalline ferrous ammonium sulfate powder (Mohr's salt) and frozen after 1, 5, 15 and 30 min of free diffusion of iron(II) ions into the crystallization drop in the presence of the second reaction substrate, dioxygen (see §2).

The structure of iron-free HuHf (not described) was obtained as a reference structure and shows the same quaternary structure as all other maxi-ferritins, consisting of the assembly of 24 identical subunits to form a hollow cage. The asymmetric unit contains a single HuHf subunit which represents the spatial and time average of all subunits of the molecule in the crystal. The HuHf subunit reported in Fig. 1 shows the characteristic four-helix bundle (helices 1–4) tertiary structure completed by a fifth helix (helix 5) (Theil *et al.*, 2013).

Each of the four structures determined in this work contains a variable number of metal ions [magnesium and/or iron(II)/iron(III)]; the chemical nature of the metal was discriminated according to the anomalous signal detected. The oxidation state of the iron ions was more elusive and was derived from comparison with the structure obtained under anaerobic conditions (see below). The refined structures are all nearly complete as according to the electron density, the polypeptide chain has been built starting from residue 5 to residue 176. No significant changes in the fold of the HuHf subunit were observed upon exposure to the iron salt.

3.2. HuHf iron binding to the ferroxidase site at different diffusion times

The structure obtained after free diffusion of iron(II) ions for about 1 min under aerobic conditions has been refined to 1.34 Å resolution. Fig. 2(*a*) shows a view of the OS with the iron ions found from the anomalous difference map computed

from data collected above the Fe K edge. The $2F_o - F_c$ and Fourier difference maps are superimposed on the anomalous map. The largest anomalous signal (28σ) identifies an iron ion bound at iron site 1 (Fe1) defined by Glu27 (monodentate ligand from helix 1), Glu62 (monodentate ligand from helix 2) and His65 (from helix 2). A water molecule (Wat1 in Fig. 2*a*) bound to Fe1 is clearly visible. A much weaker anomalous signal (6.5σ) corresponds to the Fe ion bound to the nearby site 2 (Fe2), where it is held by the Glu62 carboxylate, forming a bridge to Fe1, and by coordination bonds to Glu107 (as a bidentate ligand from helix 3). Fe1 and Fe2 refine to occupancies of about 0.7 and 0.2, respectively, and are located at a distance of 3.48 Å. These two sites are the same as the Fe1 and Fe2 sites found in RcMf. At variance with the RcMf structure obtained under the same experimental conditions (Pozzi *et al.*, 2015), no magnesium ions from the crystallization solution are found bound in the OS. In addition, a large maximum between Fe1 and Fe2 that cannot be accounted for by a bridging water/hydroxide molecule is present in the Fourier difference map (Fig. 2*a*). This maximum indicates that the completion of the coordination spheres of Fe1 and Fe2 might involve other ligands.

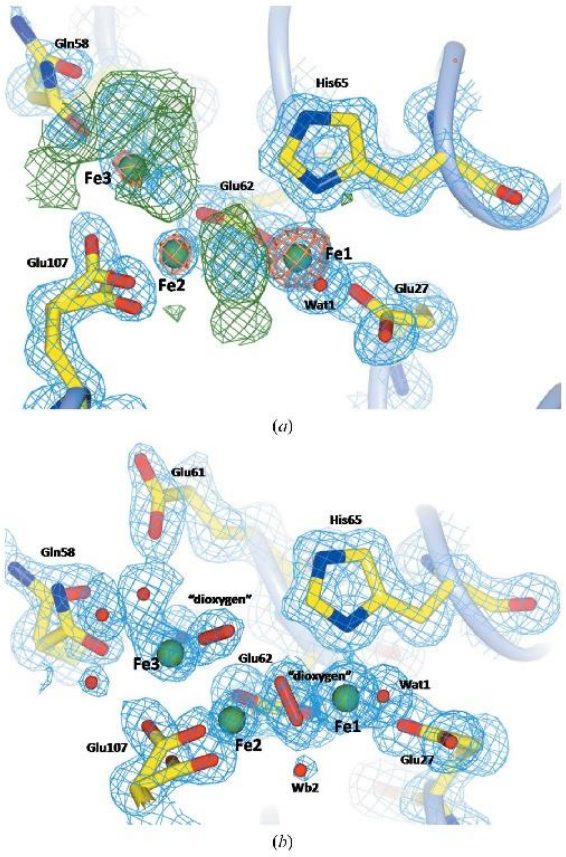

Figure 2
(*a*) Electron density in the HuHf oxidoreductase site after 1 min of free diffusion of iron into the crystals. The $2F_o - F_c$ map is represented as a light blue mesh (1.5σ), while the residual $F_o - F_c$ difference map contoured at 3.0σ is represented as a green mesh. The copper mesh represents the anomalous difference map contoured at 4.0σ. The protein backbone is represented as a light blue cartoon and residues involved in iron coordination are highlighted as yellow sticks. The disorder present in some side chains is visualized as double conformations. Iron ions are represented as green spheres. (*b*) Our interpretation of the electron-density maps shown in (*a*). Two 'dioxygen-like' molecules are represented as sticks. The $2F_o - F_c$ map is contoured at 1.5σ (light blue mesh). The $F_o - F_c$ Fourier difference map is featureless at 3.0σ.

Fig. 2(*b*) shows a view of the ferroxidase site after completing the refinement that reports our best interpretation of the difference Fourier map. The elongated maximum of continuous electron density between Fe1 and Fe2 (Fig. 2*a*) suggests the presence of a diatomic molecule and persists even when two water molecules at partial occupancy (too close to be independent) were inserted. We were then tempted to model this density as a peroxide anion or a dioxygen molecule. Finally, our best model consists of a diatomic 'dioxygen' molecule bound to Fe1 and Fe2 in a μ-η_2:η_2 configuration (bridging side-on) with the same occupancy as Fe2 (0.2) and of a bridging water/hydroxide at the same occupancy as Fe1 (0.7) (hidden by the 'dioxygen' in Fig. 2*b*). A second bridging water/hydroxide at low occupancy (0.3) can account for residual electron density between the iron ions (Wb2 in Fig. 2*b*). As can be seen from Fig. 2(*b*), this model accounts for the maxima of the $F_o - F_c$ map in this part of the cavity.

Inspection of the anomalous difference map (see Fig. 2*a*) reveals the presence of a third Fe ion (Fe3, 5.5σ) bound to the nearby Gln58 residue found disordered over two positions (iron-bound and unbound). Fe3 is close to Fe2 (2.73 Å) and can be refined to an occupancy of 0.3. Here, the $F_o - F_c$ map shows several maxima that are difficult to interpret, revealing disorder in this site (Fig. 2*a*). In addition to the Gln58 side chain, one conformer of Glu107 is within coordination distance of Fe3 and the well ordered side chain of Glu62 lies at about 2.65 Å. Two water molecules and one 'dioxygen' molecule with the same occupancy as the metal ion can be refined as Fe3 ligands to attain hexacoordination. However, after refinement the residual $F_o - F_c$ map still presents very diffuse maxima of positive electron density in the surroundings of Fe3. A fourth iron ion (Fe4) is found bound with 0.3 occupancy to the nearby His57 residue that extends into the cage cavity at about halfway between the threefold pore (22 Å) and the fourfold pore (24 Å) (not shown in Figs. 2*a* and 2*b*).

The 1 min exposure experiment was repeated twice in order to verify the reproducibility of the quite puzzling results obtained, and the Fourier maps obtained displayed the same features.

However, although suggestive, our interpretation of the electron-density maps cannot be claimed as clear evidence for the trapping of the dioxygen substrate in the HuHf OS before reaction (see §4). On the other hand, the interpretation described above leads to the best minimum of the refinement quality indicators and it can be framed as the superposition of different states occurring in HuHf subunits: in about 30% of

them no iron is bound, in about 70% of them the OS Fe1 site is occupied by iron and in about 20% the OS Fe2 site (which is empty in 80% of the cases) also binds iron. In the 50% of the cases where only site 1 is occupied by iron, a water molecule completes the Fe1 coordination, while in the 20% of the cases where both Fe1 and Fe2 sites are occupied by iron, a dioxygen molecule might bind in μ-η_2:η_2 coordination mode to both Fe1 and Fe2. It should be noted that the shape of the electron density interpreted as dioxygen is the same or even better when compared with the electron density of 'dioxygen' molecules bound to enzymes such as naphthalene dioxygenase (PDB entry 1o7m; Karlsson *et al.*, 2003) or cytochrome P450cam (PDB entries 1dz8 and 2a1m; Nagano & Poulos, 2005; Schlichting *et al.*, 2000).

The Fe3 site might represent the 30% of the subunits in which the Fe1 and Fe2 sites are not yet occupied by iron. This is supported by the double conformation of Glu107 that appears to take Fe3 from Gln58 and drive it to the Fe2 site (Figs. 2*a* and 2*b*).

In any case, this crystal structure confirms that Gln58 is involved in iron shuttling into the OS Fe1 and Fe2 iron-binding sites in a dynamic process, as shown by the structural disorder present in this portion of the cavity and as already suggested by our previous experiments on RcMf, where His54 takes the role of Gln58, and on the RcMf His54/Gln54 variant (Pozzi *et al.*, 2015). In other words, the different HuHf subunits of our crystal are trapped in different states related to their interaction, with iron(II) ions providing a superposition of images that show the conformational variability of the residues involved in iron processing.

The anomalous difference map of HuHf measured after 5 min of free diffusion of iron(II) reveals a clearer picture of the ferroxidase site, although some disorder is still present. The map confirms the sites already observed in the previous structure, but the occupancies are now much higher (Fig. 3*a*). Fe1 is fully occupied, while Fe2, Fe3 and Fe4 reach 50% occupancy. The coordination spheres of all iron ions are also better defined, as shown in Fig. 3(*b*). Fe1 displays a 5 + 1 coordination sphere with five ligands (Glu27, Glu62, His65, Wb1 and Wat1) arranged in a square-pyramidal geometry (with His65 at the apex) and a further water molecule (Wb2) at a longer distance that forms an asymmetric second bridge to Fe2. The Fe2 coordination can be described as trigonal bipyramidal, with Glu62, Glu107 (considering the bidentate Glu107 as one ligand) and Wb1 in the basal plane and Wb2 and Wat2 at the apices. The same Fe1 and Fe2 ligands have previously been observed to bind iron ions in RcMf in the same fashion (Pozzi *et al.*, 2015), with the exception of Wb2, which has never been observed in other ferritins. In the 5 min structure, the 'biatomic' molecule bridging Fe1 and Fe2 in the 1 min structure has been replaced by the Wb1 species (water/hydroxide). Both Wb1 and Wb2 have gained full occupancy: Wb1 is hydrogen-bonded to the side chain of Gln141, while Wb2 is at a contact distance to Val110. The Fe1–Fe2 distance is 3.49 Å. A hydrogen-bonding network links Gln141, the bidentate Fe2 ligand Glu107 and Tyr34. Tyr34 and Gln141 together with the other residues involved in Fe1 and Fe2 binding are highly conserved in H/M-type ferritins (Ebrahimi *et al.*, 2012; see Supplementary Fig. S1).

The position of Fe3 has now changed to give a different and better defined coordination environment (see Figs. 3*a* and 3*b*). Fe3 is in a new position located 6.61 Å away from Fe2, being bound at coordination distances to Gln58 (now ordered) and Glu61, the only protein ligands in this site, and surrounded by four water molecules that complete a quite regular octahedral coordination. The involvement of Glu61 in HuHf in the attraction of iron towards the OS is similar to that observed for the corresponding Glu57 in RcMf.

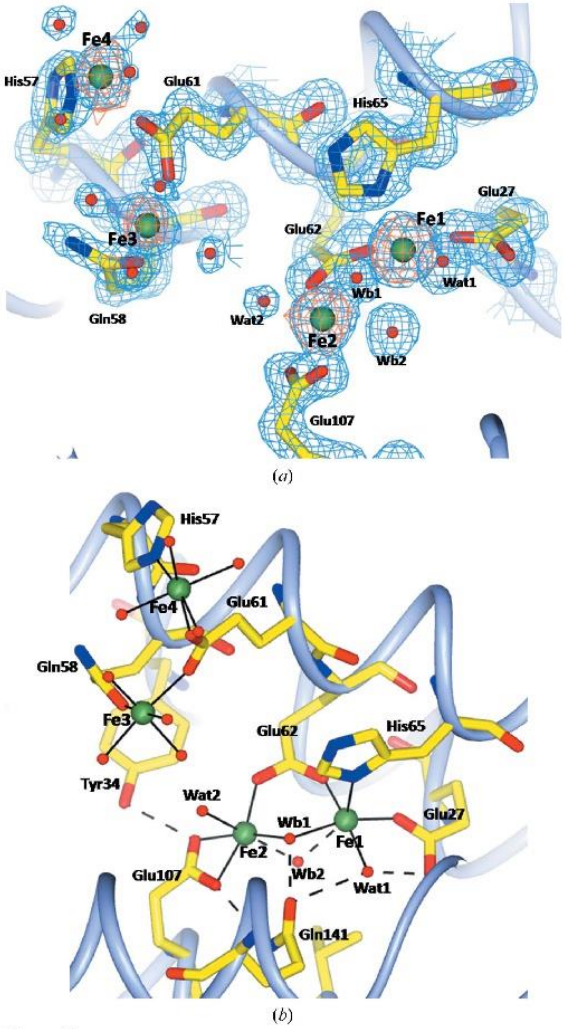

Figure 3
(*a*) Electron density in the HuHf oxidoreductase site after 5 min of exposure to Mohr's salt. The Fourier maps and anomalous difference map contours and colours are the same as in Fig. 2. (*b*) Schematic view of the OS of HuHf. Coordination bonds are shown as black continuous lines; hydrogen bonds are represented by dotted lines. The colour codes are the same as used in Fig. 2.

Fe4 is 5.08 Å from Fe3 and is bound to Glu61, which bridges it to Fe3. His57 and four water molecules are the remaining ligands that also define an octahedral coordination geometry for this site.

Increasing the iron(II) diffusion time (to 15 and 30 min) leads to no further changes in the iron-binding sites in the OS and surroundings. All iron ions, Fe1 to Fe4, maintain the same coordination environments, indicating that after about 5 min a dynamical equilibrium has been reached in the protein crystals.

In summary, the occupancy of Fe1 to Fe4 does not vary after 5 min of exposure to Mohr's salt. The Fe1 site is about 70% occupied after 1 min and is fully occupied from 5 min onwards. On the contrary, the Fe2 occupancy ranges from about 20% in the structures determined after a short diffusion time to a maximum of about 50%. The same occurs for the Fe3 and Fe4 occupancies, which achieve a maximum of 50%. At variance with the observations made for iron-bound RcMf (Pozzi *et al.*, 2015), both the Wb1 and the Wb2 molecules make asymmetric bridges between Fe1 and Fe2, with both being closer to Fe2. There are not evident structural reasons to justify this behaviour. A possible explanation could be that in all HuHf structures (except for the 1 min structure) we are observing a mixed-valence Fe1[iron(II)]–Fe2[iron(III)] cluster instead of the Fe1[iron(II)]–Fe2[iron(II)] cluster suggested by the RcMf crystal structures (Pozzi *et al.*, 2015). The increased positive charge of the site may also explain the presence of Wb2 (possibly a hydroxide anion), which is never observed in RcMf.

The high-resolution structure (1.2 Å) of iron-bound HuHf, which was obtained after 8 min of exposure to Mohr's salt from crystals obtained under strict anaerobic conditions (data not shown), was used as a check for the oxidation state of iron in the aerobically grown crystals. This structure shows iron ions bound only to Fe1 and Fe2 sites, with occupancies of about 80% for Fe1 and of about 30% for Fe2. The Fe1–Fe2 distance is 3.52 Å and, more importantly, only one water/hydroxide molecule is found symmetrically bridging the two irons, at variance with the aerobic crystals. Fe1 and Fe2 adopt the same coordination geometry as observed for RcMf (Pozzi *et al.*, 2015).

3.3. Threefold-symmetry channels

The threefold-symmetry channels have been identified as the main entrance of iron ions into the protein shell (Haldar *et al.*, 2011; Theil, 2011). The structure of iron-free HuHf shows two magnesium hexaaqua ions, arising from the crystallization buffer, inside this negatively charged protein pore defined by the side chains of the three symmetry-related Asp131, Glu134 and Thr135 residues. A third magnesium hexaaqua ion is found just beyond the channel on the internal protein surface. The positions of these magnesium ions in the threefold pore are remarkably consistent with those previously reported for HuHf (Masuda *et al.*, 2010). The same three magnesium hexaaqua ions have also consistently been observed in the structure of HuHf exposed to iron(II) ions for 1 and 5 min. On the contrary, in the structures determined after 15 and 30 min of iron loading two iron(II) hexaaqua ions have replaced the magnesium aqua ions inside the channel, as indicated by the strong anomalous peaks that are present in these sites (Figs. 4*a* and 4*b*). The occupancy for both iron(II) aqua ions inside the channel refines to 0.6. The observation of iron in the threefold channel has previously been reported after a longer exposure time to iron (60 min) for RcMf and its H54Q variant (Pozzi *et al.*, 2015).

3.4. Fourfold-symmetry channels

The fourfold pores of the ferritin cage are defined by four helices 5 (Fig. 1) from symmetry-related subunits which make a four-helix bundle around the fourfold axes. The part of the fourfold channel facing the external surface of the ferritin cage is highly hydrophobic, as in RcMf, being constituted by four symmetry-related Leu165 and Leu169 residues. Like RcMf, the internal portion of the channel has a hydrophilic character, being constituted by four symmetry-related His173 residues.

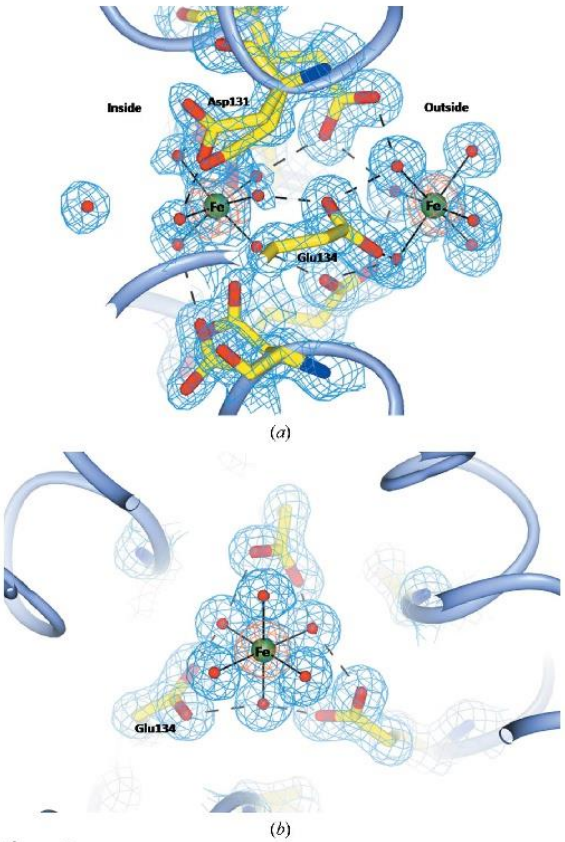

Figure 4
Views perpendicular (*a*) and parallel (*b*) to the threefold-axis pore of HuHf as appearing in the crystal structure obtained after 15 min of free diffusion of iron ions inside the crystal. The $2F_o - F_c$ and the anomalous difference maps are superimposed on the atomic model. The cutoffs and the colour codes are the same as used in the previous figures.

In the iron-free HuHf structure two chloride ions (identified by the anomalous signal) from the crystallization buffer are located above and below the plane of the four His173 residues.

The binding of iron ions in the fourfold channel develops with time. The anomalous difference map of the 1 min HuHf structure shows a very weak trace of the presence of iron ions bound to a tiny fraction (less than 10%) of the His173 residues. However, after 5 min the fourfold pore is fully occupied by an iron(II) ion bound to the four symmetry-related His173 residues defining the plane of a tetragonal bipyramid; at the apices are one chloride anion and one water molecule directed towards the external and the internal surface of the cage, respectively (Fig. 5). This kind of coordination environment for iron bound to the fourfold pore is identical to that previously observed in iron-loaded RcMf (Pozzi *et al.*, 2015), and is consistent with the presence of iron(II) ions in this pore. No iron transport into the inner cage occurs through these types of channels (Theil *et al.*, 2014).

3.5. Reactivity in solution

For both RcMf and HuHf, stopped-flow kinetic measurements reveal that the same intermediate species form during the reaction, although with different kinetics. With a stoichiometry of one iron(II) ion per subunit, the activity at the OS is essentially negligible for both proteins (Figs. 6*a* and 6*b*). With two iron(II) ions per subunit or more, we can clearly observe the formation of the DFP intermediate and its rapid decay through a monoexponential process as well as the formation of the ferric oxo species. The initial rate of formation in RcMf increases essentially linearly when going from two to four iron(II) ions per subunit (Fig. 6*b*); the increase in initial rate is less regular for HuHf. While for the latter protein the formation rate of DFP is slightly faster at a low iron(II) ratio, it levels off with four iron(II) ions per subunit. On the contrary, the exponential decay of DFP is always slower in the HuHf protein, and this difference increases on increasing the number of iron(II) per subunit (Figs. 6*a* and 6*b*). The initial rate of formation of DFO(H) species grows linearly with number of iron(II) per subunit but with different slopes for the two proteins (Fig. 6*b*). In spite of the different rates of the catalytic reactions, the end product of the biomineralization reaction is an iron-oxo core of comparable size with the same iron:protein ratio: 4.74 ± 0.26 nm for HuHf *versus* 5.37 ± 0.29 nm for RcMf, as shown in Fig. 7.

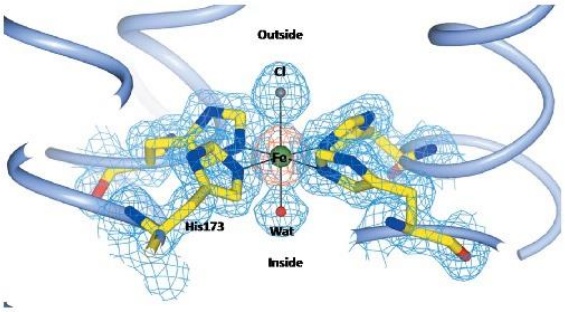

Figure 5
View of the fourfold-axis pore of HuHf as appearing in the crystal structure obtained after 5 min and onwards. The $2F_o - F_c$ and the anomalous difference maps are superimposed on the atomic model. The cutoffs and the colour codes are the same as used in the previous figures.

4. Discussion

Observing iron-binding sites in most vertebrate maxi-ferritins is made difficult by the quite rapid reaction rates measured in solution (<25 ms for RcMf; Hwang *et al.*, 2000) that prevent the use of conventional soaking or co-crystallization approaches. We have thus developed a solid-to-solid free-diffusion technique that allows the trapping of iron ions in their diffusion pathways through ferritin by freezing the protein crystals at different times after exposure to iron (Pozzi *et al.*, 2015).

The sequence of iron-binding events monitored by our experiments reported here starts with the partial occupancy of oxidoreductase sites 1 and 2 by iron; the higher occupancy for Fe1 observed in the 1 min structure, which reaches full occupancy after 5 min, confirms all previous thermodynamic data (Bou-Abdallah, Arosio *et al.*, 2002; Bou-Abdallah *et al.*, 2003; Honarmand Ebrahimi *et al.*, 2012) and structural data (Pozzi *et al.*, 2015) about the higher affinity of this site for metal ions in vertebrate ferritins. This is easily explained by the three protein ligands present in site Fe1 with respect to the two protein ligands present in site Fe2 (Pozzi *et al.*, 2015; Treffry *et al.*, 1997). Selective population of a single site in the OS is also consistent with the kinetic data (Figs. 6*a* and 6*b*) which, at variance with previous Mössbauer data (Bou-Abdallah, Papaefthymiou *et al.*, 2002), show the absence of any ferroxidase activity when one iron(II) ion per subunit is added. Similarly, the observation of a high-affinity iron-binding site corresponding to the HuHf Fe1 site has previously also been reported in the structures of ferritin from other organisms, such as *Pseudo-nitzschia multiseries* (Marchetti *et al.*, 2009; Pfaffen *et al.*, 2013), *E. coli* (Stillman *et al.*, 2001) and *P. furiosus* (Tatur *et al.*, 2007).

The 1 min crystal structure evokes a fascinating hypothesis about a possible binding mode for the substrate dioxygen in the OS and suggests that this substrate binds the dinuclear oxidoreductase centre only when Fe2 site is occupied by iron(II) ions, possibly linked to the movement of iron from the provisional site 3 to site 2. A μ-η_2:η_2 side-on coordination mode to a first-row transition-metal ion has been observed for dioxygen or peroxide only in a copper laccase (PDB entry 3zdw) and in model complexes of dinuclear copper centres (Mirica *et al.*, 2004, 2006). This binding mode of dioxygen might evolve in the peroxo-diferric intermediate structure suggested by vibrational and XAS spectroscopies (structures E or G in Fig. 3 of Hwang *et al.*, 2000).

The observation of a short Fe3–Fe2 distance in the 1 min structure (2.73 Å) that lengthens to 6.61 Å in the 5 min structure suggests that the former structure has trapped the iron(II) ion (Fe3 in Figs. 2*a* and 2*b*) approaching the empty Fe2 site, possibly dragging an already bound dioxygen molecule with it.

The similarity of the 5, 15 and 30 min HuHf structures indicates that after a short time lapse a dynamical equilibrium is reached in the iron diffusion inside the crystals and a steady-state-like situation is established. The incoming iron(II) ions are processed and stored as a ferric mineral inside the ferritin cage, as indicated by the rusty colour that is gained by the crystals with time.

Taken together, the time-lapse pictures from the present study delineate a pathway for the incoming iron(II) ions that starts with the electrostatic attraction and hydrogen-bonding interactions of the iron(II) hexaaqua ions with the Asp131 and Glu134 residues in the threefold pore and continues with Glu140, Glu61, His57 and Gln58 to reach the Fe1 and Fe2 sites.

The coordination of the Fe1 and Fe2 sites observed in HuHf shows relevant differences with respect to the same sites in RcMf determined under the same experimental conditions. While Fe1 and Fe2 in RcMf are linked by a double symmetric bridge (Glu58 and a water/hydroxide molecule), a triple asymmetric bridge is found between Fe1 and Fe2 in HuHf (Glu62 and two water/hydroxide molecules; see Fig. 3*b*). Furthermore, Fe1 in HuHf shows a 5 + 1 type of coordination sphere in contrast to RcMf, where Wb2 (Figs. 3*a* and 3*b*) is absent.

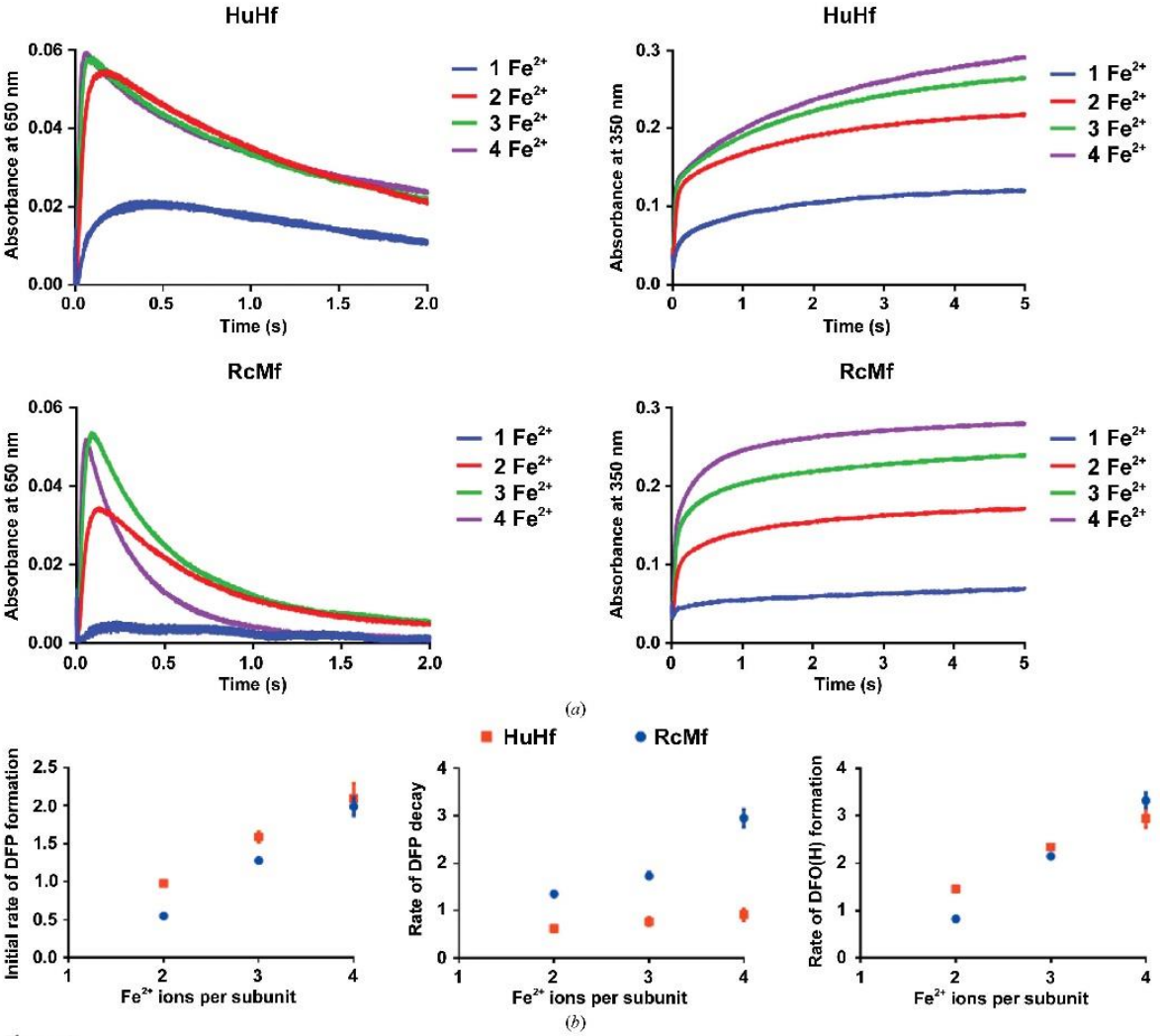

Figure 6
(*a*) The catalytic reaction rates in HuHf and RcMf are differently modulated by the Fe^{2+}:subunit ratio. Comparison of the reaction kinetics of the formation of (left) the intermediate DFP ($A_{650\ nm}$) and (right) the products DFO(H) ($A_{350\ nm}$) after the addition of one, two, three and four Fe^{2+} ions per subunit to HuHf (upper panels) and RcMf (lower panels). (*b*) The panels show the dependency on the Fe^{2+}:subunit ratio of the initial rates of the formation of DFP (left), the decay of DFP (middle) and the formation of DFO(H) (right).

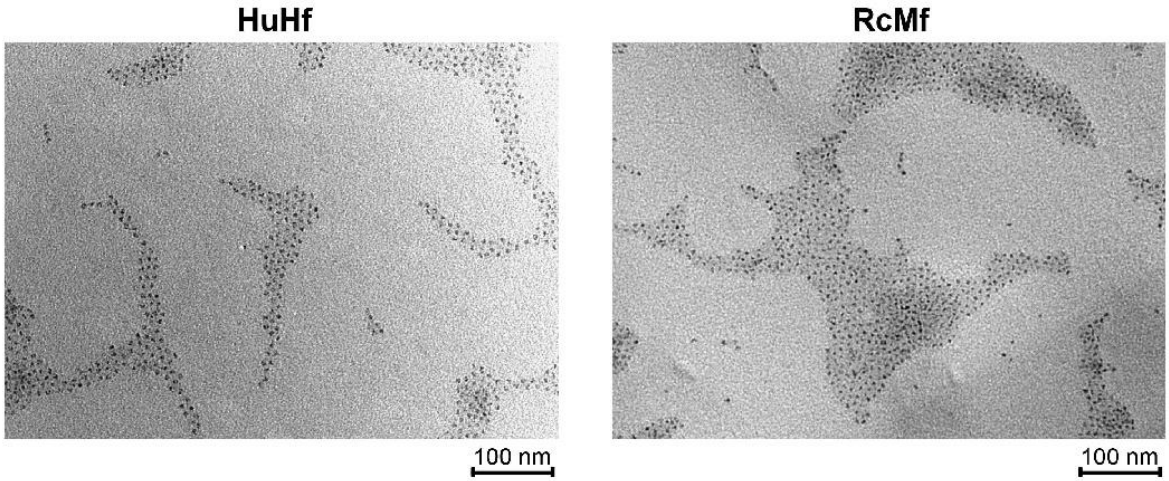

Figure 7
Biomineral core characterization. Representative TEM micrographs of HuHf and RcMf caged biominerals obtained from 3.0 μ*M* solutions of each protein mineralized with ferrous sulfate (80 Fe^{2+} ions per subunit). The samples are not negatively stained; thus, the observed density represents the iron core within ferritin and not the protein.

A possible explanation of such differences can be found by analyzing the only experimental findings that can be correlated with the oxidation state of the iron ions in our structures, namely the coordination distances and the iron-coordination geometry.

The Fe1–Fe2 distance in all HuHf structures remains remarkably constant at a value of 3.49 Å, which is the same (within error) as that found in mixed-valence model compounds (3.53–3.62 Å)[1] (Majumdar *et al.*, 2014) and in the mixed-valence structure of methane monoxygenase, where an iron(II)–iron(III) distance of 3.4 Å has been reported (2.07 Å resolution; Whittington & Lippard, 2001). The Fe1–Fe2 distance observed in HuHf is the same as that observed in the crystal obtained under anaerobic conditions, but differs from the same distances found in RcMf structures at similar resolution, which appear to be longer and to vary between 3.5 and 3.8 Å, suggesting the presence of an iron(II)–iron(II) dinuclear cluster in this case. Despite the similarity of the Fe1–Fe2 distance in aerobic and anaerobic HuHf, their coordination numbers and geometries differ, but in the anaerobic crystal their geometry is the same as that found in RcMf. In summary, our data provide some support for the hypothesis that Fe1 and Fe2 form a mixed-valence dinuclear cluster in aerobic HuHf after 5 min of exposure to iron under aerobic conditions. In other words, the 1 min structure is most probably showing the binding of iron(II) ions, while the 5, 15 and 30 min structures may show the occurrence of a mixed-valence Fe1–Fe2 cluster. Clearly, the distinction of a mixed-valence from a fully reduced iron cluster cannot rest on crystallography alone, but comparison between the HuHf and RcMf structures obtained under the same experimental conditions clearly shows differences in coordination geometry and intermetal distances, indicating a different chemical environment for the iron ions in the two proteins.

The measured differences in the dependence of the reaction rates on iron concentration between RcMf and HuHf most probably reflect the different amino-acid composition of the OS and the different chemical environment of the iron ions. Consequently, the slower rate of DFP decomposition in HuHf

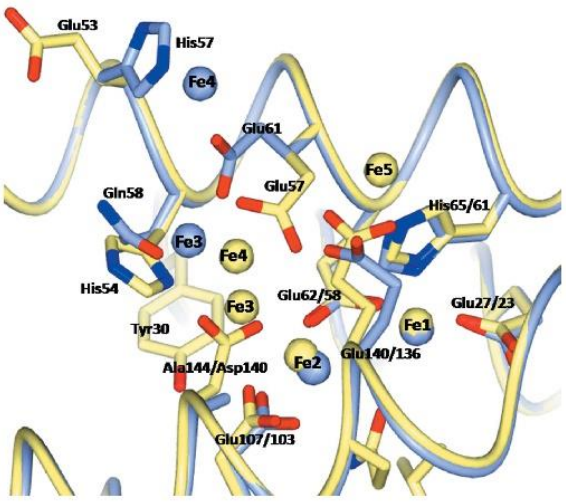

Figure 8
Least-squares superimposition of the OS of HuHf (pale blue ribbon) and RcMf (pale yellow ribbon). The different locations and ligands of the Fe3, Fe4 and Fe5 iron-binding sites are evident. The amino acids are represented as sticks coloured following the colour of the parent protein backbone.

[1] See Cambridge Structural Database codes NIXLIR and NIXLUD for mixed-valence compounds in which the iron(II)–iron(III) distances are 3.53–3.62 Å; for comparison, the iron(III)–iron(III) distances in ferric oxo(hydroxo) bridged compounds are 3.1 Å (codes NIXMAK and VARYOC10).

with respect to RcMf provides support for our hypothesis of having possibly trapped intermediate dioxygen species in our structures.

As can be appreciated from Fig. 8, the replacement of RcMf residues Glu53, His54 and Asp140 with His57, Gln58 and Ala144, respectively, results in the net loss of two negative charges and in different ligand strengths towards iron ions in the HuHf oxidoreductase site. Consequently, it is not surprising that the kinetic data show different profiles for the same iron loading of the two enzymes and markedly different decay rates of the DFP intermediate.

The differences between HuHf and RcMf do not end at the Fe1 and Fe2 sites. Fig. 8 shows the superposition of the 15 min structures of HuHf and RcMf, showing the different number and coordination of iron ions to the OS, which varies following the amino-acid variations of the two ferritins. For example, Fe3 in RcMf is bound only to His54, while in HuHf it is bound to Gln58 and Glu61 and occupies a different location. In RcMf Fe4 is bound to Glu57 (the analogous residue to Glu61 in HuHf) and to Asp140. In HuHf, Asp140 is substituted by the noncoordinating Ala144; hence, the fourth iron ion is bound to His57 in HuHf, which replaces Glu53 in RcMf. In the present structures, Glu61 is found bridging Fe3 and Fe4, supporting the hypothesis that it plays a role in driving iron ions to/from the ferroxidase site (Honarmand Ebrahimi *et al.*, 2012; Lawson *et al.*, 1991).

In summary, both the crystallographic and the stopped-flow data clearly show the existence of relevant structural and kinetic differences between RcMf and HuHf and confirm that beyond the Fe1 and Fe2 sites, which remain structurally constant, the additional iron-binding sites follow the chemical characteristics of the amino acids present in the OS and play a relevant role in the enzymatic reaction. Based on the reported evidence, the postulated third iron-binding site, which is a common characteristic of all ferritins (Honarmand Ebrahimi *et al.*, 2012, 2015), does not exist as a specific, well defined metal-coordination site, but is rather a region extending up to about 10 Å from the Fe1 and Fe2 sites where heterogeneous iron-anchoring points in ferritins of different origin are present.

5. Related literature

The following reference is cited in the Supporting Information for this article: Rice *et al.* (2000).

Acknowledgements

We acknowledge the financial support from MIUR PRIN 2012 (contract No. 2012SK7ASN). CB is the recipient of a post-doctoral fellowship funded by Ente Cassa di Risparmio di Firenze (contract No. 2013.0494). The research leading to these results has received funding from the European Community's Seventh Framework Programme (FP7/2007–2013) under BioStruct-X (grant agreement No. 283570). We thank Diamond Light Source for access to beamline I04-1 (proposal No. BIOSTRUCTX_1358) and Elettra, Trieste, Italy for provision of synchrotron-radiation facilities. We would also like to thank all of the staff of the synchrotron sources for assistance in using the beamlines.

References

Arosio, P., Ingrassia, R. & Cavadini, P. (2009). *Biochim. Biophys. Acta*, **1790**, 589–599.
Bernacchioni, C., Ciambellotti, S., Theil, E. C. & Turano, P. (2015). *Biochim. Biophys. Acta*, **1854**, 1118–1122.
Bernacchioni, C., Ghini, V., Pozzi, C., Di Pisa, F., Theil, E. C. & Turano, P. (2014). *Chem. Biol.* **9**, 2517–2525.
Bertini, I., Lalli, D., Mangani, S., Pozzi, C., Rosa, C., Theil, E. C. & Turano, P. (2012). *J. Am. Chem. Soc.* **134**, 6169–6176.
Bou-Abdallah, F., Arosio, P., Levi, S., Janus-Chandler, C. & Chasteen, N. D. (2003). *J. Biol. Inorg. Chem.* **8**, 489–497.
Bou-Abdallah, F., Arosio, P., Santambrogio, P., Yang, X., Janus-Chandler, C. & Chasteen, N. D. (2002). *Biochemistry*, **41**, 11184–11191.
Bou-Abdallah, F., Papaefthymiou, G. C., Scheswohl, D. M., Stanga, S. D., Arosio, P. & Chasteen, N. D. (2002). *Biochem J.* **364**, 57–63.
Bou-Abdallah, F., Yang, H., Awomolo, A., Cooper, B., Woodhall, M. R., Andrews, S. C. & Chasteen, N. D. (2014). *Biochemistry*, **53**, 483–495.
Bradley, J. M., Moore, G. R. & Le Brun, N. E. (2014). *J. Biol. Inorg. Chem.* **19**, 775–785.
Crichton, R. R. & Declercq, J.-P. (2010). *Biochim. Biophys. Acta*, **1800**, 706–718.
Ebrahimi, K. H., Hagedoorn, P. L., van der Weel, L., Verhaert, P. D. & Hagen, W. R. (2012). *J. Biol. Inorg. Chem.* **17**, 975–985.
Emsley, P., Lohkamp, B., Scott, W. G. & Cowtan, K. (2010). *Acta Cryst.* D**66**, 486–501.
Evans, P. (2006). *Acta Cryst.* D**62**, 72–82.
Evans, P. R. (2011). *Acta Cryst.* D**67**, 282–292.
Haldar, S., Bevers, L. E., Tosha, T. & Theil, E. C. (2011). *J. Biol. Chem.* **286**, 25620–25627.
Honarmand Ebrahimi, K., Bill, E., Hagedoorn, P. L. & Hagen, W. R. (2012). *Nature Chem. Biol.* **8**, 941–948.
Honarmand Ebrahimi, K., Hagedoorn, P. L. & Hagen, W. R. (2015). *Chem. Rev.* **115**, 295–326.
Hwang, J., Krebs, C., Huynh, B. H., Edmondson, D. E., Theil, E. C. & Penner-Hahn, J. E. (2000). *Science*, **287**, 122–125.
Karlsson, A., Parales, J. V., Parales, R. E., Gibson, D. T., Eklund, H. & Ramaswamy, S. (2003). *Science*, **299**, 1039–1042.
Langer, G., Cohen, S. X., Lamzin, V. S. & Perrakis, A. (2008). *Nature Protoc.* **3**, 1171–1179.
Laskowski, R. A., MacArthur, M. W., Moss, D. S. & Thornton, J. M. (1993). *J. Appl. Cryst.* **26**, 283–291.
Lawson, D. M., Artymiuk, P. J., Yewdall, S. J., Smith, J. M., Livingstone, J. C., Treffry, A., Luzzago, A., Levi, S., Arosio, P., Cesareni, G., Thomas, C. D., Shaw, W. V. & Harrison, P. M. (1991). *Nature (London)*, **349**, 541–544.
Leslie, A. G. W. (2006). *Acta Cryst.* D**62**, 48–57.
Liu, X. & Theil, E. C. (2005). *Acc. Chem. Res.* **38**, 167–175.
Majumdar, A., Apfel, U.-P., Jiang, Y., Moënne-Loccoz, P. & Lippard, S. J. (2014). *Inorg. Chem.* **53**, 167–181.
Marchetti, A., Parker, M. S., Moccia, L. P., Lin, E. O., Arrieta, A. L., Ribalet, F., Murphy, M. E. P., Maldonado, M. T. & Armbrust, E. V. (2009). *Nature (London)*, **457**, 467–470.
Masuda, T., Goto, F., Yoshihara, T. & Mikami, B. (2010). *Biochem. Biophys. Res. Commun.* **400**, 94–99.
McNicholas, S., Potterton, E., Wilson, K. S. & Noble, M. E. M. (2011). *Acta Cryst.* D**67**, 386–394.
Mirica, L. M., Ottenwaelder, X. & Stack, T. D. (2004). *Chem. Rev.* **104**, 1013–1046.
Mirica, L. M., Rudd, D. J., Vance, M. A., Solomon, E. I., Hodgson, K. O., Hedman, B. & Stack, T. D. (2006). *J. Am. Chem. Soc.* **128**, 2654–2665.

Murshudov, G. N., Skubák, P., Lebedev, A. A., Pannu, N. S., Steiner, R. A., Nicholls, R. A., Winn, M. D., Long, F. & Vagin, A. A. (2011). *Acta Cryst.* D**67**, 355–367.
Nagano, S. & Poulos, T. L. (2005). *J. Biol. Chem.* **280**, 31659–31663.
Pfaffen, S., Abdulqadir, R., Le Brun, N. E. & Murphy, M. E. P. (2013). *J. Biol. Chem.* **288**, 14917–14925.
Pozzi, C., Di Pisa, F., Lalli, D., Rosa, C., Theil, E., Turano, P. & Mangani, S. (2015). *Acta Cryst.* D**71**, 941–953.
Rice, P., Longden, I. & Bleasby, A. (2000). *Trends Genet.* **16**, 276–277.
Schlichting, I., Berendzen, J., Chu, K., Stock, A. M., Maves, S. A., Benson, D. E., Sweet, R. M., Ringe, D., Petsko, G. A. & Sligar, S. G. (2000). *Science*, **287**, 1615–1622.
Stillman, T. J., Hempstead, P. D., Artymiuk, P. J., Andrews, S. C., Hudson, A. J., Treffry, A., Guest, J. R. & Harrison, P. M. (2001). *J. Mol. Biol.* **307**, 587–603.
Tatur, J., Hagen, W. R. & Matias, P. M. (2007). *J. Biol. Inorg. Chem.* **12**, 615–630.
Theil, E. C. (2011). *Curr. Opin. Chem. Biol.* **15**, 304–311.
Theil, E. C., Behera, R. K. & Tosha, T. (2013). *Coord. Chem. Rev.* **257**, 579–586.
Theil, E. C., Turano, P., Ghini, V., Allegrozzi, M. & Bernacchioni, C. (2014). *J. Biol. Inorg. Chem.* **19**, 615–622.
Tosha, T., Behera, R. K. & Theil, E. C. (2012). *Inorg. Chem.* **51**, 11406–11411.
Treffry, A., Zhao, Z., Quail, M. A., Guest, J. R. & Harrison, P. M. (1997). *Biochemistry*, **36**, 432–441.
Vagin, A. & Teplyakov, A. (2010). *Acta Cryst.* D**66**, 22–25.
Whittington, D. A. & Lippard, S. J. (2001). *J. Am. Chem. Soc.* **123**, 827–838.
Winn, M. D. *et al.* (2011). *Acta Cryst.* D**67**, 235–242.

BIOLOGICAL
CRYSTALLOGRAPHY

Volume 71 (2015)

Supporting information for article:

Iron binding to human heavy-chain ferritin

Cecilia Pozzi, Flavio Di Pisa, Caterina Bernacchioni, Silvia Ciambellotti, Paola Turano and Stefano Mangani

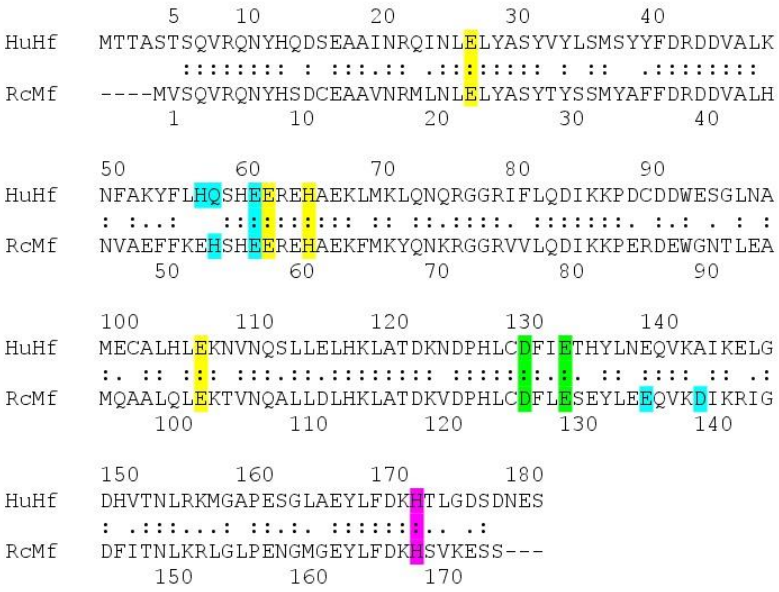

Figure S1 Amino acid sequence alignment prepared with EMBOSS (Rice *et al.*, 2000). The different numbering of the two sequences is maintained. Yellow bars highlight the residues acting as iron ligands of Fe1 and Fe2, the cyan bars the amino acids in additional binding sites in the oxydoreductase cavity, the green and the magenta bars indicate the residues involved in the interactions with Fe-aquaions or Fe binding in the 3-fold and four-fold axis pores, respectively.

Annex III

Submitted Manuscript

"Chemistry at the protein-mineral interface in L-ferritin: assisted assembly of a functional (μ^3-oxo)tris[(μ^2-peroxo)] triiron cluster"

C. Pozzi[a], S. Ciambellotti[b,c], C. Bernacchioni[b,c], F. Di Pisa[a], S. Mangani[a,c] and P. Turano[b,c]

[a] Dipartimento di Biotecnologie, Chimica e Farmacia, Universita` di Siena, Via Aldo Moro 2, 53100 Siena, Italy,
[b] CERM, Universita` di Firenze, Via L. Sacconi 6, Sesto Fiorentino, 50019 Firenze, Italy.
[c] Dipartimento di Chimica, Universita` di Firenze, Via Della Lastruccia 3, Sesto Fiorentino, 50019 Firenze, Italy,

Chemistry at the protein-mineral interface in L-ferritin: assisted assembly of a functional (μ^3-oxo)tris[(μ^2-peroxo)] triiron cluster

Cecilia Pozzi[a], Silvia Ciambellotti[b,c], Caterina Bernacchioni[b,c], Flavio Di Pisa[a], Stefano Mangani[a,b,1], and Paola Turano[b,c,1]

[a]Department of Biotechnology, Chemistry and Pharmacy, University of Siena, Via Aldo Moro 2, Siena, 53100, Italy; [b]CERM, University of Florence, Via Luigi Sacconi 6, Sesto Fiorentino, Florence, 50019, Italy; and [c]Department of Chemistry, University of Florence, Via Della Lastruccia 3, Sesto Fiorentino, Florence, 50019, Italy

[1]To whom correspondence should be addressed:

Paola Turano
CERM, University of Florence
Via Luigi Sacconi, 6
50019 Sesto Fiorentino, Italy
Tel: +39 055 4574266
e-mail: turano@cerm.unifi.it

Stefano Mangani
Dipartimento di Biotecnologie, Chimica e Farmacia
University of Siena
Via Aldo Moro 2
53100 Siena, Italy
Tel: +39 0577 234255
e-mail: stefano.mangani@unisi.it

Keywords: L-ferritin, metallocluster, nucleation site, biomineralization, x-ray, ferritin mutants.

Abstract

X-ray structures of homopolymeric L-ferritin obtained by freezing protein crystals at increasing exposure times to a ferrous solution showed the progressive formation of a triiron cluster on the inner cage surface of each subunit. After 60 minutes exposure, a fully assembled (μ^3-oxo)tris[(μ^2-peroxo)(μ^2-glutamato-κO:$\kappa O'$)](glutamato-κO)(diaquo)triiron(III) anionic cluster appears in human L-ferritin. Glu60, Glu61 and Glu64 provide the anchoring of the cluster to the protein cage. Glu57 shuttles towards the cluster incoming iron ions. We observed a similar metallocluster in horse spleen L-ferritin, indicating that it represents a common feature of mammalian L-ferritins. The structures suggest a mechanism for iron mineral formation at the protein interface. The functional significance of the observed patch of carboxylate side chains and resulting metallocluster for biomineralization emerges from the lower iron oxidation rate measured in the E60AE61AE64A variant of human L-ferritin, leading to the proposal that the observed metallocluster corresponds to the suggested but yet unobserved nucleation site of L-ferritin.

Significance Statement: Iron is an essential element in biology but has limited bioavailability. Ferritins are 24-mer iron-storage nanocage proteins that concentrate iron in their inner compartment as a bioavailable iron oxide biomineral. In L-type subunits, abundant in ferritins from organs involved in long-term iron storage, the biomineralization has been proposed to proceed through nucleation events involving iron(II) oxidation at the inner cage surface. Here we demonstrate the nature and structural features of these nucleation sites. Structures captured during iron uptake show that the formation of the iron biomineral proceeds via the assembly of a tri-nuclear iron cluster, anchored to the protein via glutamic acid side chains, and involving oxo and peroxo ligands that are produced during the iron(II) oxidation by dioxygen.

Twentyfour-mer ferritins are ubiquitous iron-biomineralizing nanocage proteins. In mammals, they are generally heteropolymers composed by two different types of subunits, the heavy H and the light L (183 and 175 amino acids, respectively, in the human chains). The subunits self-assemble to form a hollow structure with a central cavity capable of accommodating thousands of iron atoms in the form of an oxoferric biomineral (1, 2) (Fig. 1*A*). The relative ratios of the two types of subunits in the 24-mers vary in different tissues; ferritins in iron storage organs, such as liver and spleen, are richer in L-subunits, while those with fast iron metabolism such as brain and heart are richer in H-subunits (3). The H-subunit contains a ferroxidase center, composed by the so-called Fe1 and Fe2 sites, capable of rapidly oxidizing Fe^{2+} to Fe^{3+} (4, 5); a relatively low number of amino acid ligands characterizes the two sites. In human H-subunit, Glu62 acts as a bridging ligand between the two metals; the metal at Fe1 is also bound to His65 and monodentate Glu27 while the metal at Fe2 binds bidentate Glu107 (4). Accessories transient metal sites (Fe3, Fe4 and, in some cases, Fe5) have been identified by X-ray crystallography in the proximity of the ferroxidase site and they have been demonstrated to play a key role in the reaction turnover (4, 6). L-subunits lack the ferroxidase site, whereas a number of other residues are conserved with respect to the H-subunit (homology 53% between human L- and H-chains; see Fig. 1*B*) (7). Consequently, iron incorporation in nanocages rich in L-subunits is much slower. Nevertheless, even homopolymeric L-ferritins are able to biomineralize iron. The proposed mechanism involves the presence of a putative nucleation site on the inner cage surface of L-subunits. In several studies, the role of residues Glu57, Glu60, Glu61, and Glu64 (human H-chain aligned numbering, Fig. 1*B*), for an efficient biomineralization was inferred by site directed mutagenesis or chemical modifications (8, 9). Non-physiological metal ions like Cd^{2+} have been observed bound to the corresponding glutamates of the above mentioned human Glu residues in several mammalian L-ferritins (10-14), while the structure with iron of these homopolymeric L-ferritins has not been yet reported.

Here, we describe a structural study of iron binding to human and horse L-ferritins (HuLf and HoLf, respectively), were we observe the ferritin-mediated assembling of a tri-nuclear iron cluster on the inner surface of L-ferritin cages with a scaffold provided by Glu60, Glu61 and Glu64 ligands. The presence of these residues facilitates the biomineralization process, as demonstrated by different kinetics of biomineral formation between recombinant wild type (WT) homopolymeric HuLf and its triple variant E60AE61AE64A. All together, these results provide a direct evidence of the glutamate-bound triiron cluster as the mineral nucleation site in L-ferritins. The cluster structure is unprecedent in biological systems although it shows striking structural similarities to a synthetic hexanuclear iron cluster proposed about 20 years ago as a possible model of ferritin biomineral (15).

Results

Structural Studies on Iron-free HuLf and HoLf. Overall Structures. Crystals of iron-free HuLf were exposed to a concentrated ferrous ammonium sulfate (Mohr's salt) solution and frozen after 15, 30 and 60 minutes of diffusion of Fe^{2+} ions into the crystals. The same experimental approach was used to characterize the iron-loaded state of the HoLf ferritin. The structures of HuLf and HoLf before iron exposure were determined as reference structures. They show the typical quaternary structure of maxi-ferritins, consisting of the 24-subunit assembly to form a hollow cage. The asymmetric unit in both structures contains a single protein chain, representing the spatial and time average of all the molecular subunits found in the crystals. Each ferritin subunit shows the characteristic four-helix bundle tertiary structure completed by a fifth helix (Fig. 1*A*) (13, 16). The protein models are almost complete with the exception of the two initial and the three final residues of HoLf and the two starting residues in the HuLf sequence. The structure of the purified horse spleen ferritin is that of an L-chain homopolymer.

Several cadmium ions have been observed bound to both iron-free HuLf and HoLf, in the 3-fold axis channel, on the 2-fold axis and on the internal surface of the protein shell, but none on the 4-fold axis channel (see SI Channels and Metal Ions Binding Sites) (17, 18). In the iron-free structures of both L-type ferritins two Cd^{2+} ions are coordinated by Glu57 and Glu60, and by Glu61 and Glu64, respectively.

L-ferritin Subunits Provide the Scaffold for a Trinuclear Peroxo-bridged Cluster. Despite several structures of HuLf and HoLf ferritins have been determined in complex with different metal ions (13, 16, 19), no structural observation of iron binding to the mineralization site have been reported in the literature, the only iron(III) ion reported in HoLf being bound to an exogenous ligand (20). To the goal of obtaining insights on the ferritin biomineralization process, we have obtained the crystal structures of the iron-loaded HuLf and HoLf cages. Besides observing the expected iron ions in the access 3-fold channels (SI Channels and Metal Ions Binding Sites), we could monitor iron binding inside the cavity. Iron binding to the inner cage surface is achieved with the involvement of the carboxylic side chains of three glutamic acids, namely Glu60, Glu61, and Glu64 in HuLf and the corresponding residues in HoLf (Fig. 2 and 3). Three iron ions are coordinated to the above carboxylate side chains, generating an oxo-centered trinuclear cluster (Fig. 2). The anomalous difference maps show that the triiron cluster is formed at 30 minutes of iron exposure (the 15 minutes structure does not show any iron atom bound), but the best defined ligand set of the iron ions appears in the structures obtained after 60 minutes (Fig. 3*A*-*D*), which will be described in detail below. Fourier difference maps of both HuLf and HoLf show the presence of an atom in the middle of the iron cluster that has been interpreted as an oxide anion forming a μ^3-oxo bridge (Fig. 3*B*,*D*; see SI Structural Features of the Metal Cluster). In the 60 minutes structure of HuLf (1.98 Å resolution) the

oxide anion is located almost centrally in the plane formed by the three iron ions with coordination distances in the 1.8 – 2.0 Å range, all identical at 2σ significance level (Fig. 2 and 3*B*). The coordination displayed by the iron ions in the cluster is a distorted octahedral geometry. The carboxylate groups of Glu60, Glu61 and Glu64 symmetrically bridge the three Fe couples (Fig. 2) on the same side of the cluster. On the opposite side, each pair of iron ions results connected by an elongated electron density compatible with a diatomic molecule. The observed densities have been interpreted as due to three peroxide anions generating a second series of bridges (Fig. 3*B*). The arrangement of the three carboxylates, the three iron ions and the three peroxides follows an almost regular 3-fold symmetry centered on the oxide anion. A sixth ligand is present in the basal plane of each Fe ion: a water molecule for Fe1 and Fe2, and an oxygen from the carboxylate group of Glu57 (monodentate) for Fe3. Glu57 bridges a nearby fourth iron aqua-ion present at lower occupancy (about 50%). A likely explanation of the described arrangement of the iron ions in this site, is that we have detected a (μ^3-oxo)tris[(μ^2-peroxo)(μ^2-glutamato-κ*O*:κ*O*')](glutamato-κ*O*)(diaquo)triiron(III) anion. Remarkably, the L-ferritin cluster shows the same structure of the analogous portion present in a synthetic hexanuclear iron(III) cluster reported as a model of the ferritin mineral core (a detailed structural comparison is reported in SI Structural Features of the Metal Cluster) (15). The striking similarity to that model compound supports the presence of iron ions in the ferric state resulting in an overall trinegative charge of the assembly in HuLf, which can provide the driving force to attract new iron(II) ions to promote oxidation and biomineralization, as exemplified by the observed fourth iron ion approaching the cluster via Glu57.

The comparison with the iron-free HuLf structure reveals that the formation of the oxo-centered trinuclear iron cluster occurs without modification of the protein fold, but with a rearrangement of the glutamate side chains involved in iron coordination. The Cd^{2+} ions present in the same site in the iron-free structure are displaced by iron. Upon formation of the iron cluster the carboxylate of Glu57 shifts by ca 2.5 Å (and rotates on the β-carbon by 60°) whereas the carboxylate of Glu60 moves by about 1.3 Å (and rotates on the γ-carbon by 50°). The formation of the cluster induces also the rearrangement of the side chains of several surrounding residues. In particular, the hydrophilic side chains of Arg68 and Glu140 contribute to stabilize the cluster through the formation of a network of water-mediated interactions involving Glu61 and the water molecule indicated as WatL in Fig. S2. The structures of HoLf exposed to an iron salt solution for the same time intervals confirm the formation of the oxo-centered trinuclear iron cluster in the mineralization site of L-type ferritins (Fig. 3*C*,*D*). Only two peroxide anions can be modelled bridging the Fe1-Fe2 and Fe2-Fe3 couples (Fig. 3*D*). No density is present in the omit map in correspondence to the third peroxide observed in HuLf. Only an elongated maximum is found close to Fe1 and incoming Fe4 that has been interpreted as a water

molecule. The lower resolution of this structure (2.22 Å) does not provide a satisfying modelling of all aqua-ligands that should complete the iron coordination in the cluster. However, the arrangement of the three iron ions in the cluster and of the incoming fourth iron ion, at lower occupancy, is almost superimposable with that present in HuLf (Fig. 3*A*,*C*). This confirms that the formation of such cluster is a general feature of L-subunits and suggests its functional relevance.

Assessing the Functional Relevance of the Trinuclear Iron Cluster. The crystal structure indicates the key role of Glu60, Glu61 and Glu64 to act as template for the formation of the cluster. Our functional working hypothesis was that substituting these negatively charged glutamate residues with non-polar alanine could alter the biomineralization process. To prove the functional role of the residues linking the triiron cluster to the protein matrix, we designed and produced the triple mutant E60AE61AE64A. The protein yield was 30 mg/L, meaning that these multiple mutations did not affect the expression efficiency. Moreover, the typical quaternary structure was maintained as demonstrated in size exclusion chromatography experiments (Fig. S1). A comparative kinetic analysis of the formation of ferric biomineral between WT HuLf and its variant E60AE61AE64A was performed spectrophotometrically. Temporal spectral changes monitored A_{350nm} (see Materials and Methods) after the addition to protein solutions of different amounts of Fe^{2+} ions (3-18 Fe^{2+} per subunit) in 200 mM MOPS, 200 mM NaCl pH 7 were acquired in parallel (Fig. 4). The same measurements were repeated also in absence of the protein to observe the contribution of spontaneous ferrous ions oxidation. In the absence of ferritin, precipitation of iron-oxo species is clearly observed through a decrease of the A_{350nm}; the effect is stronger at higher concentrations of Fe^{2+} (Fig. 4*C*,*D*, blue curves). Differently, in the presence of HuLf, either WT or E60AE61AE64A variant, the iron is maintained in a soluble form and the A_{350nm} reaches a plateau at incubation times that are dependent upon the number of added Fe^{2+} equivalents (Fig. 4: red and green curves). The initial velocity of Fe^{2+} oxidation is more rapid in the presence of WT HuLF with respect to the E60AE61AE64A variant, thus demonstrating a direct role of the mutated residues in the iron oxidation kinetics and therefore attributing a functional significance to the trinuclear iron cluster that forms at their site. This trend is more evident at lower iron concentration (3 and 6 Fe^{2+} ions per subunit, Fig. 4*A*,*B*), suggesting that the cluster plays a role in the initial steps of biomineralization.

Discussion

It is generally accepted that in ferritin cages lacking or containing a low number of ferroxidase-active subunits, the core biomineral formation proceeds via few key steps. The iron entry into the cage cavity proceeds through the iron channels at the 3-fold symmetry axes (Fig. 5) and is followed by oxidation at specific, yet unobserved, nucleation sites that facilitate the subsequent growth of the mineral (2, 4, 21, 22). Using X-ray crystallography, we detected for the first time iron bound at inner

cage sites of L-subunits of recombinant homopolymeric human ferritin in the form of (μ^3-oxo)tris[(μ^2-peroxo)(μ^2-glutamato-κ*O*:κ*O*')](glutamato-κ*O*)(diaquo)triiron(III) anion; a very similar arrangement was here observed in HoLf. The protein ligands to iron are provided by Glu60, Glu61 and Glu64, while Glu57 appears to be involved in shuttling additional iron ions towards the cluster. The peroxo cluster is fully formed in HuLf after 60 minutes of Fe^{2+} diffusion through the crystals, while in the lower resolution structure of HoLf at the same diffusion time only two fully formed peroxide bridges could be modelled. The functional role to the observed trinuclear iron cluster, emerges from the comparative kinetic analysis of the ferritin-mediated iron oxidation reaction of WT and E60AE61AE64A variant HuLf cages. The three mutated residues have a clear role in accelerating the oxidation reaction at low iron contents. These results allow us to propose the three iron-carboxylate cluster as the site for the iron mineral nucleation site in L-ferritins. Indeed, the observed metallocluster appears to be a general characteristic of animal L-type ferritins, as it is found also in HoLf crystals. The chemical features of the observed triiron cluster partially confirm previous proposals about the nature of biomineral precursors. The observed L-ferritin trinuclear cluster can be considered as a portion of the hexanuclear synthetic cluster discussed in the Results section, which was proposed to represent a ferritin biomineral model (15). Other authors have suggested that an oxo-centered trinuclear iron cluster, which forms spontaneously on the surface of class Ib ribonucleotide reductase R2 protein from *Corynebacterium ammoniagenes* in crystals subjected to iron soaking, could mimic an early stage in the mineralization of iron in ferritins (23). In this case, however, the bridging ligands were provided by six carboxylates whereas no peroxide anions were detected (23).

In analogy with the ribonucleotide reductase case, in L-ferritins, the presence of three adjacent Glu residues at positions 60, 61 and 64 is perfectly suited to provide cooperative binding of iron in a trinuclear center. In H-type subunits, like human H-ferritin (HuHf), this ideal arrangement of carboxylate side chains is disrupted by replacement of Glu60 with a His, with the concomitant increase in the conformational freedom of Glu61 side chain (6). Also Glu57 is replaced by His in HuHf (Fig. 1*B*). Consistently, the biomineralization reaction in H-ferritin cages does not require a nucleation site (24) and His57 and Glu61 are involved in controlling the access of ferrous ions to the ferroxidase site (6). The formation of ferric clusters of high nuclearity in ferroxidase active (H or H') subunits has been inferred from Mössbauer (25-27) and NMR data (28, 29), but they have never been detected by time-lapse anomalous crystallography approaches. This supports the occurrence of a different iron mineralization process in ferroxidase active subunits leading to spatially disordered clusters that escape detection by X-ray crystallography. The observed peroxide ligands in the L-ferritin cluster might result from the initial oxidation of ferrous iron bound to the nucleation site and by the excess reductant (Fe^{2+}) present in solution. The formation of a peroxide-complex in L-ferritins supports a

mechanism for the mineral growth in the absence of the ferroxidase catalytic site, where the reaction between glutamate-bound Fe^{2+} and dioxygen provides the Fe-peroxide anionic catalyst able to attract and oxidize incoming Fe^{2+} aqua-ions. The reaction could be relevant in the contest of the proposed ferritin-mediated detoxification reaction involving both Fe(II) and H_2O_2 (30). *In vivo,* this reaction is important to attenuate harmful Fenton chemistry under conditions of iron overload. *In vitro*, it becomes the dominant one due to the lack of the protective role exerted by catalase that could disproportionate any H_2O_2 produced upon iron oxidation. Time-lapse crystallography shows here once more (4, 6, 31) its merit in capturing reaction intermediates within ferritin cages, thus leading to the identification of functional iron-binding sites and to a dynamic picture of their population by iron ions.

Materials and Methods

Protein Preparation. The plasmid encoding WT HuLf (32) was transformed into *E. coli* BL21(DE3)-pLysS competent cells. The protein was expressed and purified following a home-made protocol developed for HuHf (33) with some modifications (17°C with 0.2 mM isopropyl β-D-1-thiogalactopyranoside (IPTG) for 48 hours in rich medium Luria Bertani, LB). The subunit mass was analyzed by MALDI mass spectrometry. The retention volume obtained in the size exclusion chromatography demonstrated the 24-mer formation (Fig. S1). The E60AE61AE64A HuLf variant was expressed and purified as for WT; mutations were verified by MALDI peptide fingerprint analysis.

HoLf samples were obtained by purification of the commercially available protein.

Details on proteins' preparation, purification, initial characterization and mineralization are provided in the *SI Materials and Methods*.

Kinetic Measurements. The rate of the biomineralization reaction was determined spectrophotometrically upon addition of variable amounts of Fe^{2+} (3-18 Fe^{2+}/subunit), as described in the *SI Materials and Methods*.

Crystallography. A series of L-ferritin structures were determined by soaking HuLF and HoLf ferritin crystals with a freshly prepared $[(NH_4)_2Fe(SO_4)_2]\cdot 6H_2O$ solution for exposure times of 15-60, minutes, followed by flash freezing in liquid nitrogen. The procedure, detailed in the *SI Materials and Methods*, follows with some modifications an established protocol that already allowed us to characterize iron oxidation in the ferroxidase site of human H- and *Rana Catesbeiana* H'- type ferritins (4, 6). Data collection, structure solution and refinement procedures are given in the *SI Materials and Methods* and in Table S1 and S2. The final coordinates and structure factors for 60

minutes iron-loaded HuLf and HoLf have been deposited in the Protein Data Bank under the accession codes 5LG8 and 5LG2, respectively.

Acknowledgments

We acknowledge the financial support of MIUR PRIN 2012 (contract number 2012SK7ASN) and the ESFRI Infrastructure Instruct through its Core Centre CERM, Italy. The research leading to these results has received funding from the European Community Seventh Framework Programme (FP7/2007-2013) under BioStruct-X (grant agreement No. 283570). We thank Diamond Light Source for access to beamline I03 (proposal number: BIOSTRUCTX_1358), Elettra (Trieste, Italy) for provision of synchrotron radiation facilities (beamline XRD-1) and all the staff of the synchrotron sources for assistance in using the beamlines. We would like to thank Prof. S. Torti for providing us the plasmid encoding WT HuLf and Dr. Francesco Vizza for helpful discussion.

Reference List

1. Theil EC, Behera RK, Tosha T (2013) Ferritins for chemistry and for life. *Coord. Chem. Rev.* 257:579-586.

2. Theil EC (2011) Ferritin protein nanocages use ion channels, catalytic sites, and nucleation channels to manage iron/oxygen chemistry. *Current Opinion in Chemical Biology* 15:1-8.

3. Arosio P, Ingrassia R, Cavadini P (2009) Ferritins: a family of molecules for iron storage, antioxidation and more. *Biochim. Biophys. Acta - Gen. Subj.* 1790:589-599.

4. Pozzi C *et al.* (2015) Time lapse, anomalous X-ray diffraction shows how Fe^{2+} substrate ions move throgh ferritin protein nanocages to oxidoreductase sites. *Acta Cryst. D* D71:941-953.

5. Liu X, Theil EC (2005) Ferritins: dynamic management of biological iron and oxygen chemistry. *Acc. Chem. Res.* 38:167-175.

6. Pozzi C *et al.* (2015) Iron bindind to human heavy-chain ferritin. *Acta Crystallogr D Biol Crystallogr* 71:1909-1920.

7. Andrews SC *et al.* (1992) Structure, function, and evolution of ferritins. *J Inorg Biochem* 47:161-174.

8. Granier T *et al.* (1998) Evidence of new cadmium binding sites in recombinant horse L-chain ferritin by anomalous Fourier difference map calculation. *Proteins* 31:477-485.

9. Wade VJ *et al.* (1991) Influence of site-directed modifications on the formation of iron cores in ferritin. *J. Mol. Biol.* 221:1443-1452.

10. Luscieti S *et al.* (2010) Mutant ferritin L-chains that cause neurodegeneration act in a dominant-negative manner to reduce ferritin iron incorporation. *J Biol. Chem.* 285:11948-11957.

11. Wang Z *et al.* (2006) Structure of human ferritin L chain. *Acta Crystallogr. D. Biol. Crystallogr.* 62:800-806.

12. de Val N, Declercq JP, Lim CK, Crichton RR (2012) Structural analysis of haemin demetallation by L-chain apoferritins. *J. Inorg. Biochem.* 112:77-84.

13. Granier T *et al.* (1997) *Comparison of the Structures of the Cubic and Tetragonal Forms of Horse-Spleen Apoferritin*. *Acta Crystallogr D Biol Crystallogr* 53:580-587.

14. Granier T *et al.* (2003) Structural description of the active sites of mouse L-chain ferritin at 1.2 A resolution. *J. Biol. Inorg. Chem.* 8:105-111.

15. Shweky I *et al.* (1997) A Hexairon(III) Complex with Three Non-Planar h2-m4-Peroxo Ligands Bridging
Two Basic Iron Acetate Units. *J. Am. Chem. Soc.* 119:1037-1042.

16. Hempstead PD *et al.* (1997) Comparison of the three-dimensional structures of recombinant human H and horse L ferritins at high resolution. *J. Mol. Biol.* 268:424-448.

17. Bernacchioni C, Ghini V, Theil EC, Turano P (2016) Modulating in permeability of the ferritin channels. *RSC Advances* 6:21219-21227.

18. Bernacchioni C *et al.* (2014) Loop Electrostatics Modulates the Intersubunit and Intercage Interactions in Ferritin. *ACS Chem. Biol.* 9:2517-2525.

19. Suzuki M *et al.* (2009) Preparation and catalytic reaction of Au/Pd bimetallic nanoparticles in apo-ferritin. *Chem Commun. (Camb.)* 32:4871-4873.

20. Nakajima H *et al.* (2015) Construction of an enterobactin analogue with symmetrically arranged monomer subunits of ferritin. *Chem Commun. (Camb.)* 51:16609-16612.

21. Haldar S, Bevers LE, Tosha T, Theil EC (2011) Moving Iron through ferritin protein nanocages depends on residues throughout each four a-helix bundle subunit. *J. Biol. Chem.* 286:25620-25627.

22. Behera RK, Theil EC (2014) Moving Fe^{2+} from ferritin ion channels to catalytic OH centers depends on conserved protein cage carboxylates. *Proc. Natl. Acad. Sci. U. S. A* 11:7925-7930.

23. Hogbom M, Nordlund P (2004) A protein carboxylate coordinated oxo-centered tri-nuclear iron complex with possible implications for ferritin mineralization. *FEBS Lett.* 567:179-182.

24. Bou-Abdallah F, Biasiotto G, Arosio P, Chasteen ND (2004) The putative "nucleation site" in human H-chain ferritin is not required for mineralization of the iron core. *Biochemistry* 43:4332-4337.

25. Bou-Abdallah F *et al.* (2002) mu-1,2-Peroxobridged di-iron(III) dimer formation in human H-chain ferritin. *Biochem. J.* 364:57-63.

26. Bauminger ER *et al.* (1993) Iron (II) oxidation and early intermediates of iron-core formation in recombinant human H-chain ferritin. *Biochem. J.* 296:709-719.

27. Pereira AS *et al.* (1997) Rapid and parallel formation of Fe^{3+} multimers, including a trimer, during H-type subunit ferritin mineralization. *Biochemistry* 36:7917-7927.

28. Lalli D, Turano P (2013) Solution and solid state NMR approaches to draw iron pathways in the ferritin nanocage. *Acc. Chem. Res.* 46:2676-2685.

29. Turano P *et al.* (2010) NMR reveals a pathway for iron mineral precursors to the central cavity of ferritin. *Proc. Natl. Acad. Sci. USA* 107:545-550.

30. Zhao G *et al.* (2003) Multiple pathways for mineral core formation in mammalian apoferritin. The role of hydrogen peroxide. *Biochemistry* 42:3142-3150.

31. Bertini I *et al.* (2012) Structural insights into the ferroxidase site of ferritins from higher eukaryotes. *J. Am. Chem. Soc.* 134:6169-6176.

32. Rucker P, Torti FM, Torti SV (1997) Recombinant ferritin: modulation of subunit stoichiometry in bacterial expression systems. *Protein Eng.* 10:967-973.

33. Ravera E *et al.* (2016) Solid-state NMR of PEGylated proteins. *Angew. Chem. Int. Ed* 55:1-5.

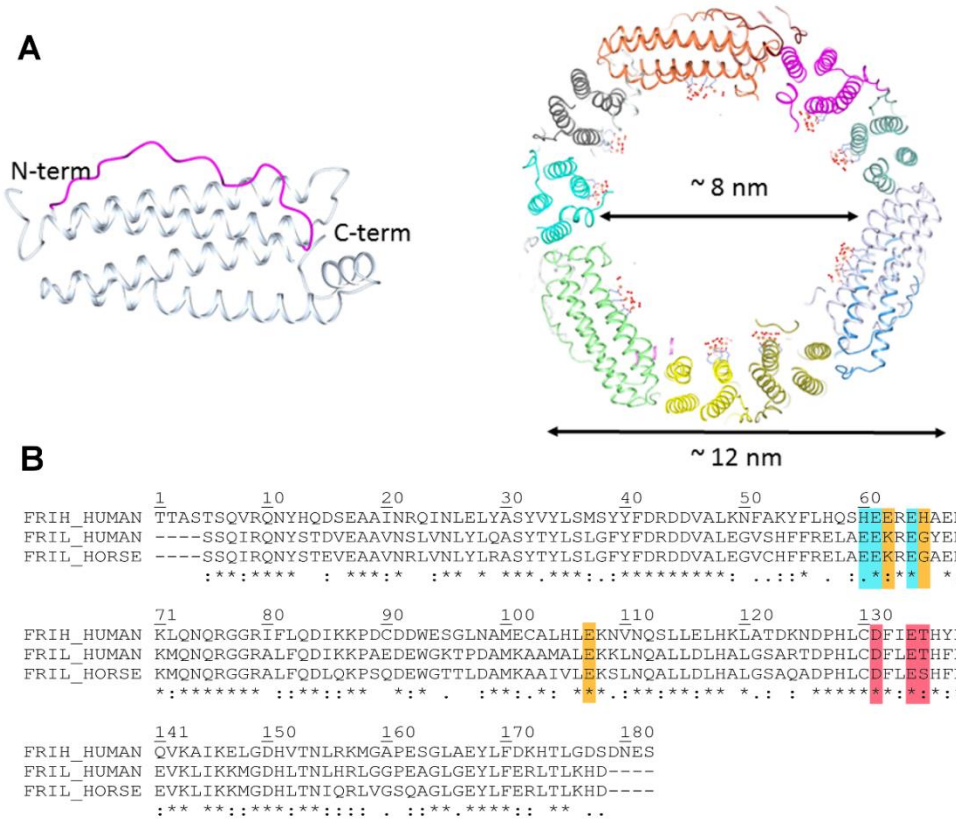

Fig. 1. Ferritin main structural features and sequence alignment. (*A*) *Left*, cartoon representation of the four-helix bundle subunit: helices III and I are solvent-exposed and linked by a long loop (*magenta*), helices II and IV locate on the inner cage surface; a fifth short helix at the C-terminal is tilted of 60° with respect to the bundle axis. *Right*, section of the human L-ferritin (HuLf) cage. The trinuclear iron clusters sprout into the 8 nm cavity, surrounded by the protein shell of 12 nm external diameter. (*B*) Alignment of amino acid sequences of human H-ferritin (HuHf), HuLf and horse spleen L-ferritin (HoLf) (FRIH_HUMAN, FRIL_HUMAN and FRIL_HORSE, respectively), performed by Clustal Omega. All sequences are depleted of the initiator methionine. In light blue, the residues binding the metal cluster in L-ferritin. In orange, the iron-binding amino acids in the ferroxidase site of the catalytically active H-subunit and the corresponding amino acids in the L-chains of HuLf and HoLf (both lacking the ferroxidase site). In magenta, the amino acids in the conserved pore responsible of iron entry.

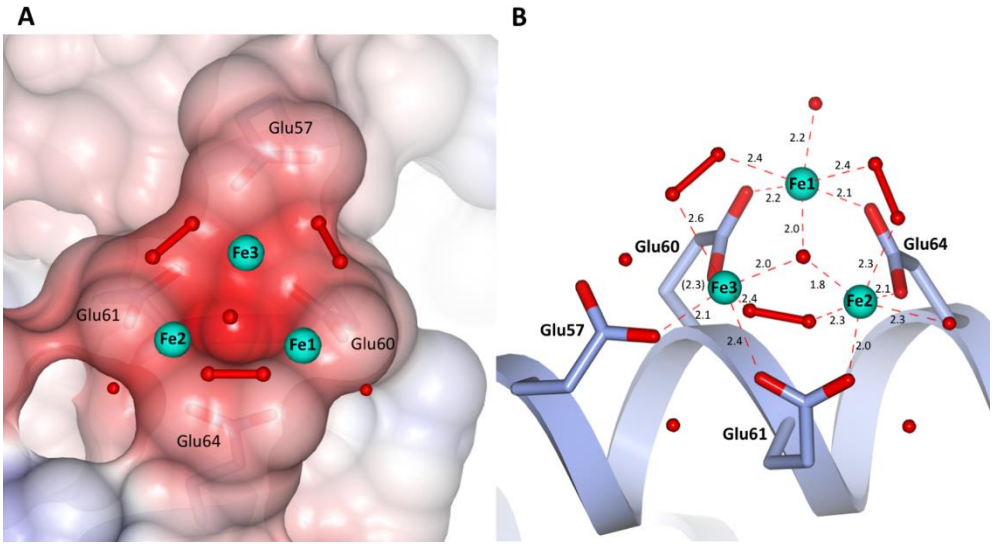

Fig. 2. Different views of the trinuclear iron binding site in HuLf. (*A*) Electrostatic surface representation of the trinuclear cluster binding site. Iron ions and water molecules are represented as cyan and red spheres, respectively. Peroxide molecules are shown as red ball-and-stick models. (*B*) Structure of the oxo-centered trinuclear iron cluster. Coordinating glutamates are highlighted as sticks. Iron ions, water and peroxide molecules are represented as in "*A*". Coordination bonds to iron ions are shown as dashed red lines; coordination distances (Å) are also displayed. Two different orientations are proposed in panels *A* and *B* to better appreciate the structural features of the protein site and metal cluster.

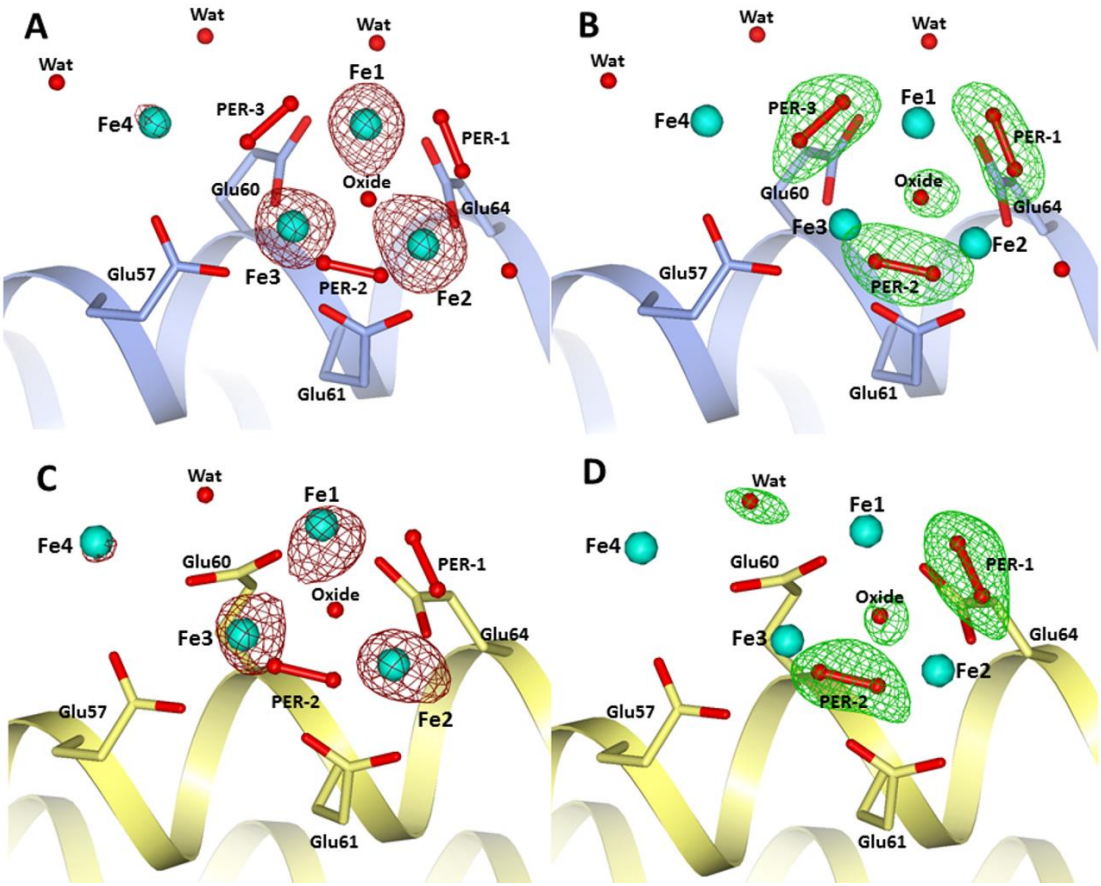

Fig. 3. The iron cluster in HuLf and HoLf. (*A*) Iron ions (*cyan spheres*) in HuLf are surrounded by the anomalous difference map (*dark red mesh*) contoured at 4.0 σ. (*B*) Omit map (*green mesh*) in HuLf contoured at 3.0 σ of peroxide and oxide anions involved in iron coordination. In both HuLf pictures: helix II, light blue cartoon; residues involved in iron coordination, light blue sticks. (*C*) Iron ions (*cyan spheres*) in HoLf are surrounded by the anomalous difference map (*dark red mesh*) contoured at 5.0 σ. d, Omit map (*green mesh*) in HoLf contoured at 3.0 σ of peroxide and oxide anions, and the water molecule involved in iron coordination. In both HoLf pictures: helix II, yellow cartoon; residues involved in iron coordination, yellow sticks.

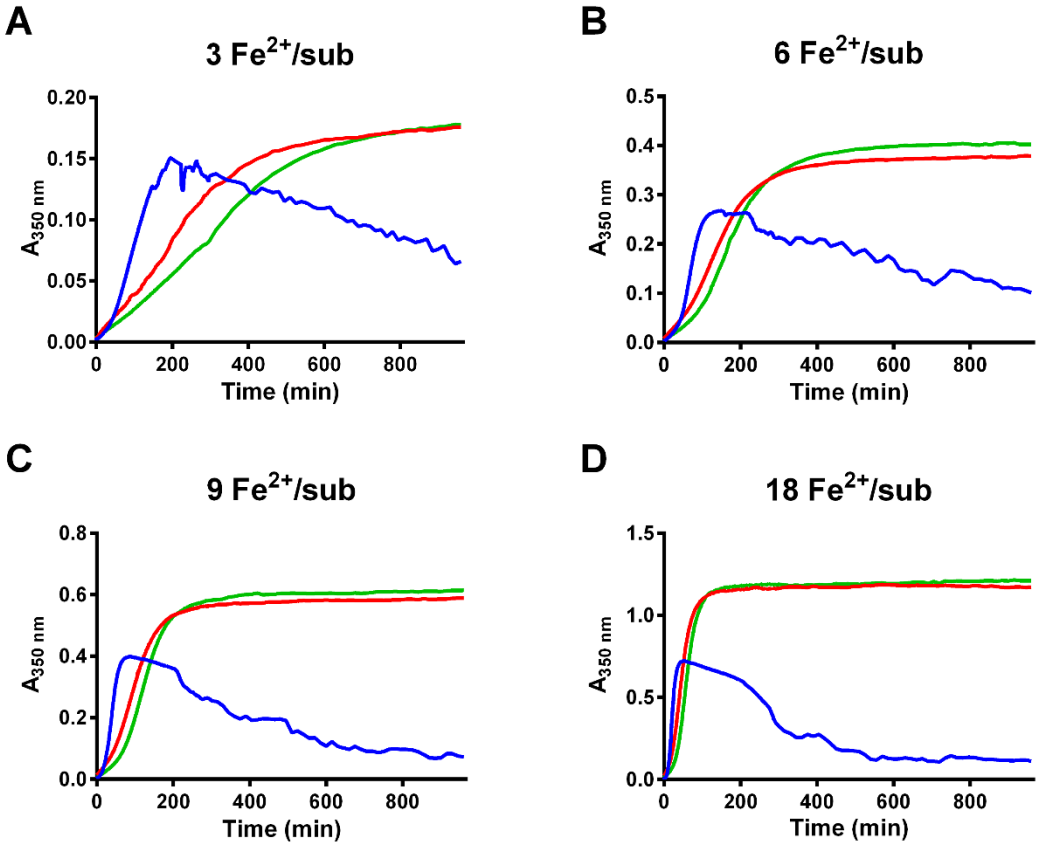

Fig. 4. Kinetic measurements in WT and E60AE61AE64A HuLf variant. Kinetics of oxo-ferric species formation followed spectrophotometrically as the change in absorbance at 350 nm over 16 hours (960'). Different concentrations of Fe^{2+} were incubated, at room temperature, in 200 mM MOPS 200 mM NaCl pH 7 buffer with 25 µM protein subunits of WT HuLf (*red curves*) and triple mutant E60AE61AE64A (*green curves*) or without protein (blank, *blue curves*). Addition of: (*A*) 3 Fe^{2+} ions per subunit; (*B*) 6 Fe^{2+} ions per subunit; (*C*) 9 Fe^{2+} ions per subunit; (*D*) 18 Fe^{2+} ions per subunit.

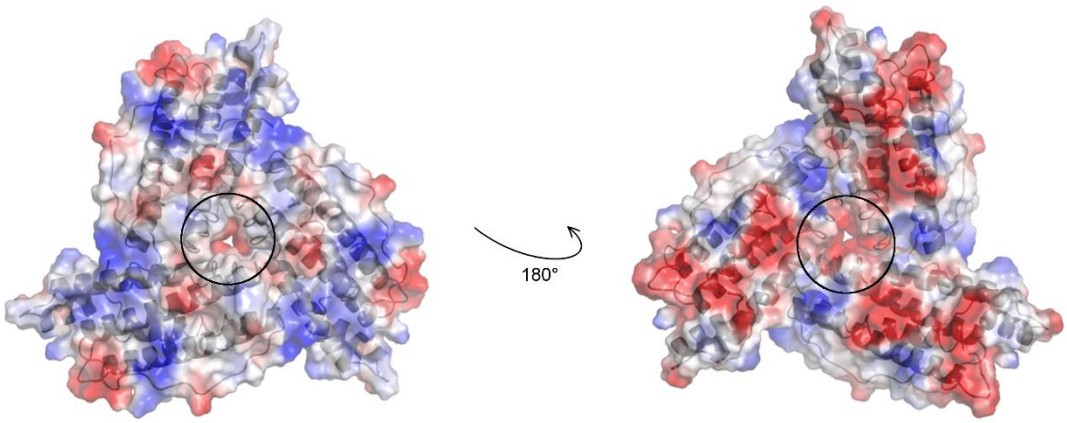

Fig. 5. The properties of the 3-fold ion channel in ferritin. Electrostatic surface representation of a trimer of L-ferritin subunits where three monomers (*gray cartoon*) come in contact generating a 3-fold channel responsible for iron entry. The external (*left*) and the internal (*right*) views of the pore circled with black lines show the negatively charged environment, due to the presence of conserved Asp131, Glu134 and Thr135 side chain residues. In HoLf, in position 135 there is a Ser, which is highly similar to Thr.

Supporting Information

Chemistry at the protein-mineral interface in L-ferritin: assisted assembly of a functional (μ^3-oxo)tris[(μ^2-peroxo)] triiron cluster

Cecilia Pozzi[a], Silvia Ciambellotti[b,c], Caterina Bernacchioni[b,c], Flavio Di Pisa[a], Stefano Mangani[a,b,1], and Paola Turano[b,c,1]

[a]Department of Biotechnology, Chemistry and Pharmacy, University of Siena, Via Aldo Moro 2, Siena, 53100, Italy; [b]CERM, University of Florence, Via Luigi Sacconi 6, Sesto Fiorentino, Florence, 50019, Italy; and [c]Department of Chemistry, University of Florence, Via Della Lastruccia 3, Sesto Fiorentino, Florence, 50019, Italy

[1]e-mail: turano@cerm.unifi.it and stefano.mangani@unisi.it

SI Structural Features of the Metal Cluster

Structural features of the trinuclear iron cluster and similarities to model systems. Figures 3*B* and 3*D* (main text) show the residual electron density present around the iron ions forming the cluster in HuLf and HoLf, respectively. The assignment of the residual electron density present in the center of the three iron ions to an oxide anion is based on the comparison of the coordination distances and on the chemical environment as well as on the similarity to several model compounds. Examples of $Fe_3(\mu^3\text{-O})$ units are abundant in crystal structures of iron(III) complexes synthesized to mimic intermediates in the catalytic cycle of non-heme iron proteins (1-5) Fe^{3+}- (μ^3-O) distances in carboxylate-bridged ferric ions in model compounds are reported between 1.865(2) Å (2) and 2.01(1) (1) while in R2 ribonucleotide reductase example (6) range between 1.7 to 2.2 Å.

Fe^{3+}-peroxide distances in multiple peroxo-bridged models range between 1.997(7) Å and 2.106(5) Å (1, 2). In our HuLf 60 minutes structure we observe Fe-oxo distances between 1.80(15) and 2.03(15) Å and Fe-peroxo distances between 2.27(15) and 2.62(15) Å. The peroxo O-O bond lengths determined in our structure are all identical between experimental error to 1.46(15) Å. This compares well with the canonical 1.48(2) Å found in μ_2-peroxo models (7). The Fe – Fe distances in HuLf range between 3.21(15) and 3.45(15) Å and are comparable to those found in Fe^{3+}- (μ^3-O) models (eg: 3.278(3) - 3.196(2) Å) (2).

The structure of the ferric cluster in the HoLf is somewhat less regular than that of HuLf as the Fe triangle shows one Fe-Fe distance of 3.3(2) Å and two longer Fe-Fe distances (3.8(2) Å and 4.0(2) Å).

Only two μ_2-bridged peroxide anions could be modelled into the residual electron density (Fig. 3*D* main text).

The above structural analysis lead to our interpretation of the cluster as a stable (μ^3-oxo)tris[(μ^2-peroxo)(μ^2-glutamato-κ*O*:κ*O*')](glutamato-κ*O*)(diaquo)triiron(III) anion that constitutes a likely candidate for the nucleation site of the ferric mineral in L-ferritins.

SI Channels and Metal Ions Binding Sites

Twentyfour-mer ferritin cages have a 432 (O, octahedral) point symmetry. In correspondence to the 3-fold and 4-fold symmetry there are eight and six channels respectively, connecting the protein exterior to the inner cavity. The 4-fold channels form at the encounter point of the C-termini of four subunits and the four symmetry-related helices V define the inner wall of the channel. The 3-fold channels occur where three subunits come into contact through the N-terminal ends of helices IV and the C-terminal ends of helices III. The two type of channels differ in their size and hydrophilicity (8).

4-fold symmetry channel. The channel located on the four-fold symmetry axis results not occupied by any metal ion. This can be ascribed to the prevalent hydrophobic nature of the residues present in HuLf and HoLf channels, while Fe-bound His residues are present in both human H-ferritin and *Rana catesbeiana* H'-ferritin (9, 10).

3-fold symmetry channel. It has been largely accepted that the channels present on the 3-fold symmetry in the ferritin protein shell constitute the preferential entry path of iron ions proceeding to the catalytic center. Very recently the transit of iron ions within these channels has been demonstrated through X-ray crystallography in homopolymeric H'-type ferritin from Rana catesbeiana and human H-type ferritin (9, 10). The hydrophilic nature of these channels is strongly conserved among the different ferritin types.

A path of Cd^{2+} ions (discriminated according to the anomalous signal, still strong in the data collected below the Fe K-edge) is present inside this funnel-shaped channel. Three symmetry related Cd^{2+} ions are visible on the external portion of the channel (largest part) at a distance of ca 4.8 Å. Cd^{2+} ions in this sites results coordinated by two protein residues, His118 and Cys130, whereas the other four ligands completing the octahedral coordination geometry have been assigned to water molecules. The partial occupancy of Cd^{2+} ions in this site is also suggested by the two alternative conformation adopted by Cys130. In the first conformation, showing the side chain exposed on the 3-fold channel,

it coordinates a Cd2+ ion (and has been refined with the same occupancy) whereas in the second, the side chain points to the adjacent helix III (and adopts the same conformation observed in HuHf showing magnesium ions inside the channel). Going from the outer to the internal part of the channel three further Cd2+ ions are clearly visible. One of them can be modelled in three symmetry related alternative positions coordinated by the carboxylates of Glu134. A further Cd2+ is placed at the inner end of the channel, located exactly on the 3-fold symmetry axis where it is coordinated by three symmetry related Asp131 and water molecules. A similar cluster of six Cu2+ ions has been previously observed in the 3-fold symmetry channel of Rana catesbeiana H'-ferritin (PDB: 3RE7) (11). In our HoLf structure only one Cd2+ ion is bound to Glu130 in the 3-fold axis channels.

Other Cd2+ binding sites. In HuLf, four Cd2+ ions are bound at partial occupancy, to the cage surface by Asp15, Glu90, His136, Glu49 and Asp178, with their coordination spheres completed by water molecules. In HoLf two Cd2+ ions are bound to the protein surface, one to Asp84 and the other to Glu15 side chains.

SI Materials and Methods

Protein preparation. The WT HuLf homopolymer was expressed and purified according to an in-house developed procedure (reported below), which presents some modifications with respect to that developed for the human H protein (12). The pET-21c plasmid encoding native HuLf was a kind gift of Prof. S. Torti (13). This vector was transformed into *E. coli* BL21(DE3)-pLysS competent cells (already used in our laboratory for ferritin expression). Several expression trials were performed in order to optimize the final protein yield. We tested different incubation temperatures (17°C, 25°C and 37°C), incubation times (4, 8, 16, 24 and 48 hours) and IPTG concentrations (0.2, 0.5 and 1 mM). Our best condition turned out to be 17°C, 0.2 mM IPTG for 48 hours in LB, avoiding the protein to be found in inclusion bodies as it occurred at higher temperatures or higher IPTG concentrations. In details, bacteria were grown in LB rich medium containing 100 mg/L of ampicillin and 34 mg/L of chloramphenicol at 37°C. Once the A_{600nm} reached 0.6-0.8, the over-expression of HuLf was induced with 0.2 mM IPTG, shifting the incubation temperature to 17°C for 48 hours. The cells were harvested (7500 rpm for 15 minutes) and resuspended in 20 mM Tris-HCl pH 7.5. After sonication, the crude lysate was clarified by ultra-centrifugation (40,000 rpm for 40 minutes) and the soluble fraction heated at 65°C for 15 minutes to precipitate undesired proteins (40,000 rpm for 15 minutes). Subsequently, the supernatant was dialyzed against 20 mM Tris-HCl pH 7.5 buffer. Before chromatographic steps, the protein was precipitated with ammonium sulfate at 70% of saturation.

Once the pellet containing protein was resolubilized, it was extensively dialyzed in 20 mM Tris-HCl pH 7.5. Then the protein-containing fractions were recovered through the Q-Sepharose anionic exchange column eluting the sample with a linear NaCl gradient (0-1 M) in 20 mM Tris-HCl pH 7.5. Next, fractions with ferritin (identified with SDS-PAGE analysis) were pooled and further purified by size exclusion chromatography (HiLoad 16/60 Superdex 200 column, GE Healthcare) in 20 mM Tris-HCl, 200 mM NaCl pH 7.5 (Fig. S1).

Maldi-Mass spectrometry (MALDI-MS; Toscana Life Sciences Foundation, Siena) confirmed the calculated mass; the experimental value of 19888 Da corresponds to the mass of the WT HuLf subunit (20019.6 Da from ProtParam tool hrrp://web.expasy.org/protparam/) without the first methionine (131 Da). Trypsin digestion of the protein and the analysis of the fragmentation pattern obtained by MALDI-MS demonstrated the identity of HuLf subunit.

Apoferritin from equine spleen was purchased from Sigma Aldrich (product code A3641) and further purified by size exclusion chromatography (HiLoad 16/600 Superdex 200pg, GE Healthcare). Mass spectra on the purified protein and on the dissolved crystal show the homogeneous presence of HoLf as later confirmed by the crystal structure (*vide infra*).

Design and production of the triple mutant E60AE61AE64A. The proper oligonucleotide primers containing the three point mutations, were designed (QuikChange Primer Design tool) and purchased accordingly (Eurofins Genomics). We used pET-21c vector harboring the native gene as the DNA template, and we set up the site-directed mutagenesis reaction following the QuikChange Site-Directed Mutagenesis kit protocol (Agilent Technologies). The correct introduction of mutations was checked through Next-generation sequencing (Eurofins Genomics). The triple mutant E60AE61AE64A was expressed and purified in the same way as the WT protein. An aliquot of purified E60AE61AE64A was digested with trypsin and subjected to Maldi Peptide Mass Fingerprint analysis confirming the insertion of the desired mutations.

Demineralization and iron-loading procedures. Iron and other metal ions were removed from purified ferritins by four dialysis steps using 4 L each of 20 mM Tris-HCl, 200 mM NaCl, 3 mM ethylenediaminetetraacetic acid (EDTA), ammonium thioglycolate (1:400), pH 7.5 buffer to reduce and chelate the iron, followed by four dialysis steps against 4 L each of 20 mM Tris-HCl, 200 mM NaCl pH 7.5. After removing metal ions from ferritins, known iron equivalents were added to ferritin variants as previously described (14). After removing metal ions from ferritins, for kinetic studies, known iron equivalents were added to ferritin variants preparing fresh ferrous sulfate stock solution in 1 mM HCl to avoid instantaneously oxidation of iron(II) to iron(III).

Kinetic measurements. Kinetics of ferric-oxide species formation in absence and in presence of WT HuLf and E60AE61AE64A HuLf were monitored as the change in A350nm over the time. 25 µM

protein subunits in 200 mM 3-(N-morpholino)propanesulfonic acid (MOPS), 200 mM NaCl pH 7 were incubated at room temperature after addition of 3, 6, 9 and 18 Fe2+ per subunit. Spectra were acquired at Varian Cary 50 Bio UV-vis spectrophotometer collecting one point every 30 seconds in the first 5 hours and every 15 minutes until 16 hours.

Crystallization. Demineralized HuLf in 20 mM Tris pH 7.5 was concentrated to 9 mg/mL. Crystals of HuLf were grown using the hanging-drop vapor-diffusion technique at 281 K (15). Drops were prepared by mixing equal volumes of demineralized HuLf and a precipitant solution composed of 80-100 mM $Cd(NO_3)_2$, 80-100 mM ammonium sulfate, and 200 mM sodium acetate pH 5. Drops were equilibrated over 800 µL reservoir solution. Octahedral shaped crystals appeared in 3-6 days and grew to final dimensions of about 200-400 µm in several days.

HoLf crystals were grown by vapor diffusion hanging drop technique at room temperature. Drops were prepared by mixing 2 µL of HoLf solution (12-24 mg/mL in 0.15 M NaCl.) with 2 µL of precipitant constituted by 80 mM $Cd(NO_3)_2$, 800 mM ammonium sulfate, and 200 mM sodium acetate pH 5. Octahedral crystals, similar to those observed for HuLf, grew in a few days in drops equilibrated over 800 µL reservoir solution.

Iron loading was performed by soaking both L-type ferritin crystals with a freshly prepared $[(NH_4)_2Fe(SO_4)_2]\cdot 6H_2O$ solution (approximately 40 mM) for the monitored exposure times of 15, 30, 60, 90 and 120 minutes. Before flash freezing in liquid nitrogen crystals were washed in cryoprotectant solutions constituted by 40% v/v glycerol added to the precipitant solutions.

Data collection, structure solution and refinement. Complete data sets for iron-free HuLf, HoLf and iron-loaded HuLf and HoLf were collected on the Elettra beamline XRD1 (Trieste, Italy) equipped with a Pilatus 2M detector, and on the DLS beamline I03 (Didcot, UK) equipped with a Pilatus 6M for crystals soaked for 15, 30 and 60 minutes. Crystals frozen after 90 and 120 minutes of exposure to iron appeared to have lost diffraction. The iron-free HuLf, HoLf data were collected for comparison. Data were integrated using either XDS (16) or Mosflm (17) and scaled with Scala (18) from the CCP4 suite (19). The HuLf crystals belonged to the body-centered cubic space group I432, with unit-cell parameter a ~152 Å, varying slightly among the different crystals. On the other hand, the HoLf crystals belonged to the face-centered cubic space group F432, having unit-cell parameter a ~182 Å. Data collection and processing statistics are reported in Table S1. Initial models were obtained by molecular replacement using MOLREP (20) from the CCP4 suite. A subunit of either HuLf or HoLf were used as a search model, excluding non-protein atoms and water molecules.

To unambiguously prove that the observed cluster is formed by iron ions full three-wavelength anomalous data (remote high energy 13500 eV, peak of the Fe K-edge at 7200 eV and immediately below the iron edge at 7050 eV), were collected for HuLf, while for HoLf we collected only the 7200 and 7050 eV data. The positions of metal ions were determined from the anomalous Fourier difference maps calculated at 7200 eV and at 7050 eV, using FFT from the CCP4 suite. Iron can be easily distinguished from cadmium due to the disappearance of its anomalous signal in the 7050 eV map, where the anomalous signal of Cd^{2+} ions is still evident. Anomalous signals indicative of iron placement ranged between 15 σ and 4 σ in the anomalous difference map calculated with data collected at 7200 eV.

The structures were refined with REFMAC5 (21) by using the high energy remote data in case of HuLf or the 7200 eV data in case of HoLf which were those at the highest resolution (Table S2). The refinement protocol involved sequential iterative manual rebuilding of the model and maximum-likelihood refinement. Manual rebuilding and modelling of the missing atoms into the electron density and water molecules addition were performed with the molecular graphic software Coot (22). Partial occupancies for the iron and cadmium ions, for other ligands, and for several amino acid residues were adjusted to keep atomic displacement parameters close to those of the neighbouring protein atoms in fully occupied sites. Metal ions have been refined with anisotropic temperature factors. The occupancies of the water molecules or other ligands bound to the metal ions were kept the same as the parent metal ion. The final models were inspected manually and checked with Coot and PROCHECK (23). The final refinement statistics are reported in Table S2. Figures were generated with CCP4mg (24).

Reference List

1. Micklitz W, Bott SG, Bentsen JG, Lippard SJ (1989) Characterization of a Novel μ4-Peroxide Tetrairon Unit of Possible Relevance to Intermediates in Metal-Catalyzed Oxidations of Water to Dioxygen. *J. Am. Chem. Soc.* 111:372-374.

2. Shweky I *et al.* (1997) A Hexairon(III) Complex with Three Non-Planar h2-m4-Peroxo Ligands Bridging Two Basic Iron Acetate Units. *J. Am. Chem. Soc.* 119:1037-1042.

3. Heath SL, Powell AK (1992) The trapping of iron hydroxide units by the ligand 'heidi': two new hydroxo(oxo)iron clusters containing 19 and 17 iron atoms. *Angew. Chem. , Int. Ed. Engl.* 31:191-193.

4. Taft KL, Papaefthymiou GC, Lippard SJ (1993) A mixed-valent polyiron oxo complex that models the biomineralization of the ferritin core. *Science* 259:1302-1305.

5. Taft KL, Papaefthymiou GC, Lippard SJ (1994) Synthesis, Structure, and Electronic Properties of a Mixed-Valent Dodecairon Oxo Complex, a Model for the Biomineralization of Ferritin. *Inorg. Chem.* 33:1510-1520.

6. Hogbom M, Nordlund P (2004) A protein carboxylate coordinated oxo-centered tri-nuclear iron complex with possible implications for ferritin mineralization. *FEBS Lett.* 567:179-182.

7. Orpen G *et al.* (1989) *J. Chem. Soc. ,Dalton Trans.*S1-S83.

8. Bernacchioni C, Ghini V, Theil EC, Turano P (2016) Modulating in permeability of the ferritin channels. *RSC Advances* 6:21219-21227.

9. Pozzi C *et al.* (2015) Iron bindind to human heavy-chain ferritin. *Acta Crystallogr D Biol Crystallogr* 71:1909-1920.

10. Pozzi C *et al.* (2015) Time lapse, anomalous X-ray diffraction shows how Fe^{2+} substrate ions move throgh ferritin protein nanocages to oxidoreductase sites. *Acta Cryst. D* D71:941-953.

11. Bertini I *et al.* (2012) Structural insights into the ferroxidase site of ferritins from higher eukaryotes. *J. Am. Chem. Soc.* 134:6169-6176.

12. Ravera E *et al.* (2016) Solid-state NMR of PEGylated proteins. *Angew. Chem. Int. Ed* 55:1-5.

13. Rucker P, Torti FM, Torti SV (1997) Recombinant ferritin: modulation of subunit stoichiometry in bacterial expression systems. *Protein Eng.* 10:967-973.

14. Bernacchioni C *et al.* (2014) Loop Electrostatics Modulates the Intersubunit and Intercage Interactions in Ferritin. *ACS Chem. Biol.* 9:2517-2525.

15. Benvenuti M, Mangani S (2007) Crystallization of soluble proteins in vapor diffusion for x-ray crystallography. *Nat. Protoc.* 2:1633-1651.

16. Kabsch W (2010) XDS. *Acta Crystallogr. D. Biol. Crystallogr.* 66:125-132.

17. Leslie AGW (2006) The integration of macromolecular diffraction data. *Acta Crystallogr. D. Biol. Crystallogr.* 62:48-57.

18. Evans PR (2011) An introduction to data reduction: space-group determination, scaling and intensity statistics. *Acta Crystallogr D Biol Crystallogr* 67:282-292.

19. Winn MD *et al.* (2011) Overview of the CCP4 suite and current developments. *Acta Cryst. D* 67:235-242.

20. Vagin A, Teplyakov A (1997) MOLREP: an automated program for molecular replacement. *J. Appl. Crystallogr.* 30:1022-1025.

21. Murshudov GN *et al.* (2011) REFMAC5 for the refinement of macromolecular crystal structures. *Acta Crystallogr D Biol Crystallogr* 67:355-367.

22. Emsley P, Lohkamp B, Scott WG, Cowtan K (2010) Features and development of Coot. *Acta Crystallogr. D Biol. Crystallogr.* 66:486-501.

23. Laskowski RA, MacArthur MW, Moss DS, Thornton JM (1993) PROCHECK: a program to check the stereochemical quality of protein structures. *J. Appl. Crystallogr.* 26:283-291.

24. McNicholas S, Potterton E, Wilson KS, Noble ME (2011) Presenting your structures: the CCP4mg molecular-graphics software. *Acta Crystallogr. D Biol. Crystallogr.* 67:386-394.

Figures

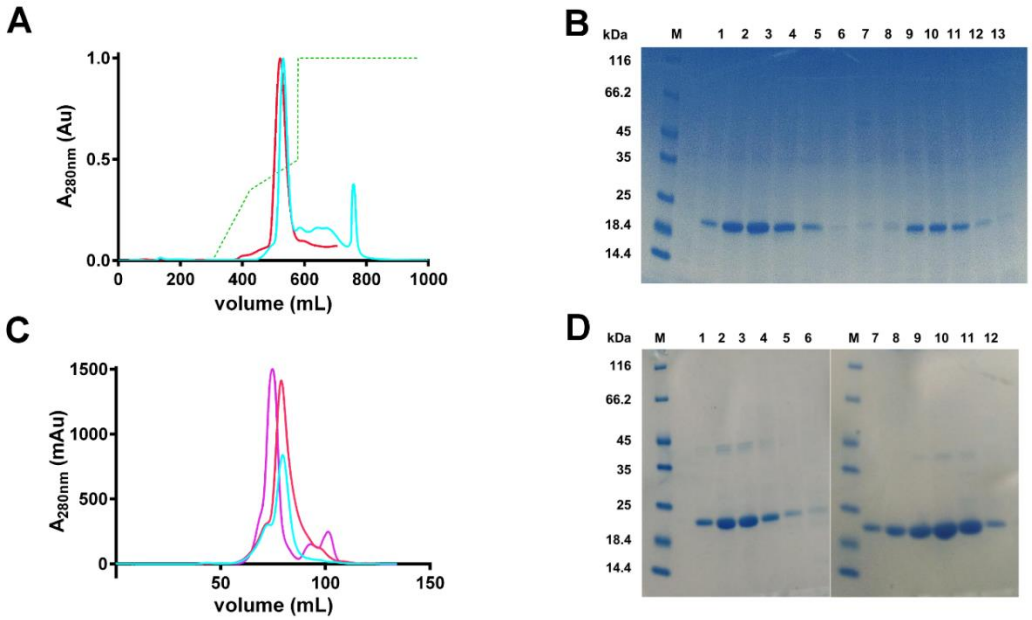

Fig. S1. Purification of WT and E60AE61AE64A HuLf proteins. (*A*) Anionic exchange chromatograms obtained by a Q-Sepharose Fast Flow column with a 0-1 M NaCl gradient (*dashed green line*). In red and cyan, the elution profiles of WT and E60AE61AE64A HuLf respectively, followed by UV detector (FPLC, Akta system). (*B*) SDS-PAGE gel of fractions obtained by anionic exchange chromatography. Lane M: marker, lanes 1-6: main peak of WT HuLf profile, lanes 8-13: main peak of E60AE61AE64A profile (bands around 20 kDa corresponding to the protein monomers). (*C*) Size exclusion elution chromatograms (UV measure) of WT and E60AE61AE64A HuLf superimposed with one of an already-characterized maxiferritin (*violet curve*; human H-ferritin sample) to demonstrate their 24-meric conformation. (*D*) SDS-PAGE analysis of fractions eluted with HiLoad 16/60 Superdex 200 column. Lanes M: marker, lanes 1-6: main peak of WT HuLf profile, lanes 7-12: main peak of E60AE61AE64A profile (bands around 20 kDa corresponding to the protein monomers).

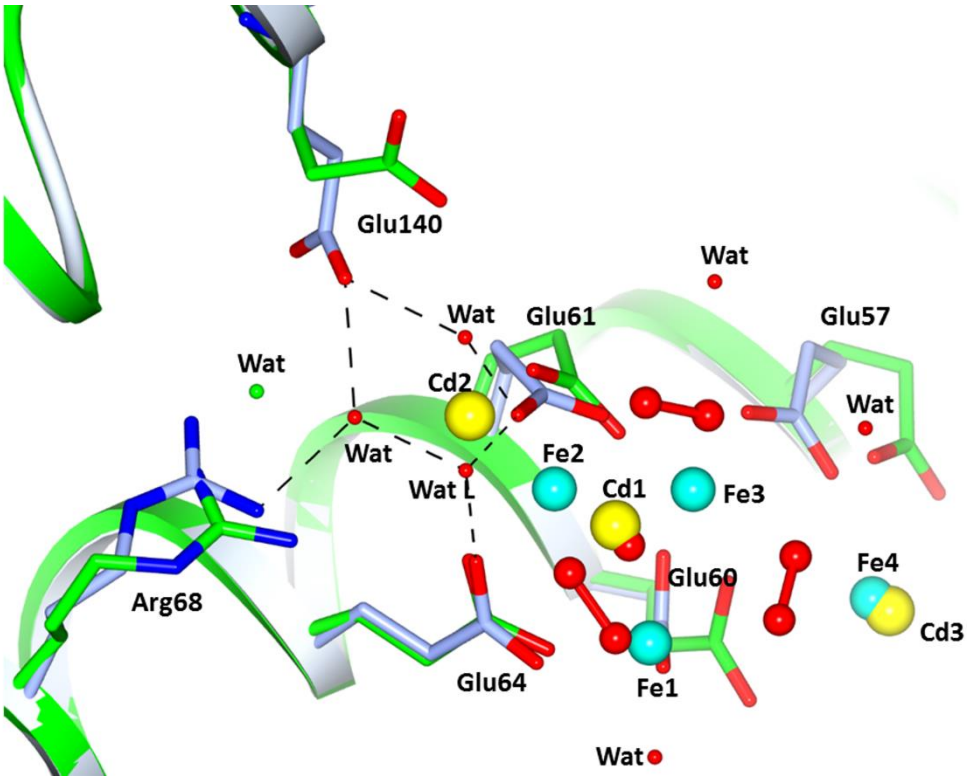

Fig. S2. Least-squares superimposition of iron-loaded HuLf (*light blue*) with iron-free HuLf (*green*). The three Cd^{2+} ions bound in the mineralization site in iron-free HuLf are replaced by Fe^{3+} ions and oxide after 60 minutes of exposure to Fe^{2+}. Upon iron binding the side chains of Glu57, Glu60, Glu61, Arg68 and Glu140 change conformation. The two latter residues are involved in a H-bond network with three water molecules, one of which (WatL) ligates Fe2.

Table S1. Data collection and processing. Values for the outer resolution shell are given in parentheses.

	HuLf + Fe(II) 60’			HoLf + Fe(II) 60’
	High energy remote	Above iron K-edge	Below iron K-edge	Above iron K-edge
PDB codes	**5LG8**			**5LG2**
Diffraction source	I03 (DLS)	XRD-1 (Elettra)	XRD-1 (Elettra)	XRD-1 (Elettra)
Wavelength (Å)	0.9184	1.7220	1.7587	1.7220
Temperature (K)	100	100	100	100
Detector	Pilatus 6M-F	Pilatus 2M	Pilatus 2M	Pilatus 2M
Crystal-detector distance (mm)	342	100	100	90
Rotation range per image (°)	0.15	0.5	0.5	0.5
Total rotation range (°)	75	60	60	60
Exposure time per image (s)	0.25	10	10	15
Space group	I432	I432	I432	F432
a, *b*, *c* (Å)	151.42	151.47	151.64	181.35
Mosaicity (°)	0.73	0.68	0.68	0.54
Resolution range (Å)	29.70-1.98 (2.09-1.98)	25.98-2.25 (2.37-2.25)	26.00-2.28 (2.40-2.28)	23.61-2.22 (2.34-2.22)
Total No. of reflections	241127 (34962)	128079 (19118)	149132 (22337)	138083 (20118)
No. of unique reflections	20846 (2990)	14378 (2052)	13874 (1978)	13146 (1862)
Completeness (%)	99.7 (100.0)	99.9 (100.0)	99.8 (100.0)	99.9 (100.0)
Anomalous completeness (%)	99.7 (100.0)	99.8 (100.0)	99.9 (100.0)	99.9 (100.0)
Redundancy	11.6 (11.7)	8.9 (9.3)	10.7 (11.3)	10.5 (10.8)
Anomalous redundancy	5.9 (5.8)	4.6 (4.8)	5.7 (5.8)	5.6 (5.6)
$\langle I/\sigma(I)\rangle$	16.8 (4.9)	12.6 (4.1)	14.0 (4.9)	12.6 (4.9)

$R_{r.i.m.}$	0.096 (0.481)	0.113 (0.456)	0.113 (0.449)	0.126 (0.401)
Overall *B* factor from Wilson plot ($Å^2$)	15.4	15.9	16.6	14.2

Table S2. Structure solution and refinement. Values for the outer resolution shell are given in parentheses.

	HuLf + Fe(II) 60’	HoLf + Fe(II) 60’
PDB codes	**5LG8**	**5LG2**
Resolution range (Å)	29.70-1.98 (2.03-1.98)	23.61-2.22 (2.28-2.22)
Completeness (%)	99.6 (100.0)	99.8 (100.0)
No. of reflections, working set	19824 (1437)	12489 (905)
No. of reflections, test set	1021 (67)	656 (49)
Final R_{cryst}	14.2 (21.0)	16.5 (19.0)
Final R_{free}	17.7 (23.8)	22.4 (28.0)
Cruickshank DPI	0.103	0.185
No. of non-H atoms		
Protein	1437	1364
Metal Ions (Fe, Cd)	13 (8, 5)	7 (4, 3)
Ions (oxide, peroxide, acetate, chloride, sulfate)	16 (1, 6, 4, 0, 5)	6 (1, 4, 0, 1, 0)
Other	0	6
Water	208	154
Total	1674	1537
R.m.s. deviations		
Bonds (Å)	0.026	0.015
Angles (°)	2.214	1.625
Average *B* factors (Å^2)	25.88	28.35
Ramachandran plot		
Most favoured (%)	98.0	98.0
Allowed (%)	2.0	2.0

Annex IV

Publication

"Solid-State NMR of PEGylated Proteins"

E. Ravera[a], S. Ciambellotti[a], L. Cerofolini[a], T. Martelli[b], T. Kozyreva[b], C. Bernacchioni[a], S. Giuntini[a], M. Fragai[a], P. Turano[a], and C. Luchinat[a,b]

[a]CERM, Universita` di Firenze, Via L. Sacconi 6, Sesto Fiorentino, 50019 Firenze, Italy.
[b]Giotto Biotech S.r.l. Via Madonna del Piano 6, 50019 Sesto Fiorentino, Firenze (Italy)

Protein NMR

International Edition: DOI: 10.1002/anie.201510148
German Edition: DOI: 10.1002/ange.201510148

Solid-State NMR of PEGylated Proteins

*Enrico Ravera, Silvia Ciambellotti, Linda Cerofolini, Tommaso Martelli, Tatiana Kozyreva, Caterina Bernacchioni, Stefano Giuntini, Marco Fragai, Paola Turano, and Claudio Luchinat**

Abstract: *PEGylated proteins are widely used in biomedicine but, in spite of their importance, no atomic-level information is available since they are generally resistant to structural characterization approaches. PEGylated proteins are shown here to yield highly resolved solid-state NMR spectra, which allows assessment of the structural integrity of proteins when PEGylated for therapeutic or diagnostic use.*

Biological drugs (biologics)[1] are the fastest-growing category of approved therapeutics. Most biologics are proteins and, as such, they are the closest proxy of a "natural" help against disease.[2] However, proteins have poor pharmacokinetic and safety profiles. Polyethylene glycol (PEG) coating of biologics provides reduced renal clearance, increased stability to degradation, and a reduced immunogenic response (hence they are often called "stealth drugs").[3] PEGylation is even more important for nanocarriers and liposomes, the lifetimes of which are otherwise shortened by the activity of the reticuloendothelial system. Obviously, preservation of the three-dimensional structure and activity of the PEGylated form is mandatory for human use. While activity can be easily measured in vitro, structural characterization at atomic resolution of PEGylated proteins and protein-based nanocarriers is almost impossible. PEG coating prevents crystallization for X-ray analysis: currently only one crystal structure has been solved, that of the small protein PEG-plastocyanine (PEG-Pc, 11.5 kDa, 4R0O, 4.2 Å resolution). The protein carries a single PEG chain, and protein–protein crystal contacts can still take place owing to the rather large distance between the PEG moieties.[4] Also, PEGylation often pushes protein size beyond the practical limits of solution NMR because of the increase in hydrodynamic volume, which is increased by PEG more than it would be for an equal increase in protein mass.[5] Exceptions are PEG-Interferon$_{2\alpha}$[6] and PEG-Pc,[4] where the protein size remains sufficiently small after PEGylation to permit solution NMR studies. Solid-state NMR (ssNMR) is becoming a better alternative to study proteins[7] because it does not suffer from molecular-weight limitations (although the spectral complexity still increases with protein size), and high resolution spectra can be obtained for multimeric assemblies.[8–11] However, the best resolution is usually obtained for crystalline materials,[12,13] which are precisely what cannot be usually achieved for PEGylated proteins.

Herein, it is shown that highly resolved ssNMR spectra can be obtained for PEGylated proteins in the pelleted state, a densely packed non-crystalline state of a wet macromolecular sample, which can be obtained either by rehydration of freeze-dried material,[14–17] or by ultracentrifugation[18] when allowed by the density and molecular mass of the molecule.[19,20] Such high-quality ssNMR spectra are suitable for extensive resonance assignment and even conventional full structure determination. More importantly, the simple comparison of a standard two-dimensional ssNMR spectrum of the pelleted PEGylated protein with that of the crystalline state of the native protein—for which the X-ray structure is available—can reveal whether the three-dimensional structure is maintained in the PEGylated form. Since preparing a pelleted sample of a PEGylated protein turns out to be particularly simple and fast, and the collection of ssNMR spectra for the comparison is relatively rapid, the approach proposed here can be regarded as the fast-lane to assess at atomic detail whether or not the native conformation is preserved after PEGylation. Assignment of the resonances that experience perturbations, if any, can further push the application of this approach towards tracking where modifications occur in the 3D structure.

The approach is demonstrated on three clinically/preclinically relevant biologics: human Cu^{II}-Zn^{II}-Superoxide Dismutase (SOD), human H Ferritin (hHF), and *E.coli* L-asparaginase II (ANSII). SOD is an enzyme used to scavenge free radicals in radiation therapy and in severe inflammatory diseases.[21] The SOD used here is the popular "AS" C6A, C111S mutant, which is less prone to aggregation than the wild type. SOD is a symmetric homodimer (C_2) of 32 kDa that has been extensively characterized by NMR[22,23] and X-ray crystallography.[24] Ferritins have been proposed as biomineralization scaffolds, MRI contrast agents, and nanocarriers and drug delivery devices.[25] hHF is a homo-24-mer of about 504 kDa (ca. 21 kDa per subunit) that forms a cage of *O* symmetry (snub cube), as characterized by X-ray crystallography.[26] Its ssNMR spectra are here reported for the first time: it has the same architecture as the Bullfrog M ferritin,[27] with which sedimentation for ssNMR was first developed.[18] PEGylation increases the bloodstream circulation of ferritins and reduces specific uptake by cells.[28] ANSII from *E.coli* is in clinical use since 1967 against childhood acute lymphoblastic leukemia.[29] In its therapeutically active form, ANSII consists

[*] Dr. E. Ravera, S. Ciambellotti, Dr. L. Cerofolini, Dr. C. Bernacchioni, S. Giuntini, Prof. M. Fragai, Prof. P. Turano, Prof. C. Luchinat
Magnetic Resonance Center (CERM) and Department of Chemistry "Ugo Schiff", University of Florence, and Magnetic Resonance Consortium (CIRMMP)
Via L. Sacconi 6, 50019 Sesto Fiorentino, FI (Italy)
E-mail: claudioluchinat@cerm.unifi.it
Dr. T. Martelli, Dr. T. Kozyreva, Prof. C. Luchinat
Giotto Biotech S.r.l. Via Madonna del Piano 6, 50019 Sesto Fiorentino, FI (Italy)

Supporting information and ORCID(s) from the author(s) for this article are available on the WWW under http://dx.doi.org/10.1002/anie.201510148.

of a homotetrameric assembly of 144 kDa with D_2 symmetry.[30] For therapeutical applications, more recently, native ANSII has been substituted by the PEGylated form of ANSII, which exhibits longer-lasting activity and lower immunogenicity.[31]

Protein PEGylation was achieved by using a linear amine-reactive methyl-PEG reagent containing 24 ethyleneglycol units. PEGylation increases the molecular weight of dimeric SOD from 32 kDa to above 60 kDa, with all of the lysines and the N-terminal moiety largely functionalized (Figures S1, S2 in the Supporting Information). PEGylation of SOD hinders sedimentation, so the sample for ssNMR was prepared by wetting a freeze-dried sample. In hHF, each monomer binds 3–4 PEG chains, thereby increasing the size of the tetramer from 504 kDa up to 600–650 kDa (Figure S3) without changing its function (Figure S4–6). PEGylated hHF is still able to sediment easily. In ANSII, each monomer binds 4–5 PEG chains, thereby increasing the size of the tetramer from 144 kDa up to about 170 kDa (Figure S7). The ssNMR samples of native and PEGylated ANSII were both produced by freeze-drying and rehydration.

ssNMR spectra were collected for the three native proteins in the crystalline form and for the three PEGylated proteins in the pellet state (See Table S1 for detailed experimental conditions). From the analysis of the spectra (Figure 1 and S8) it clearly appears that line shape and resolution for the pelleted PEGylated proteins are very good, and comparable with those obtained from microcrystalline samples of the corresponding native proteins (Figure S8 and S9). Pelleted SOD and hHF in the native and PEGylated forms show spectra of equally good quality (Figure S10).

In all three cases, the spectra of the pelleted PEGylated protein and the crystalline native protein are largely superimposable, thus demonstrating for the first time a negligible effect of PEG coating on protein structure and assembly. In particular, preservation of chemical-shift patterns of well-resolved isoleucine residues indicates an intact hydrophobic core (Figure 1 and Figure S8). Figure 2 shows a superimposition of the spectra for pelleted PEGylated (blue) and crystalline native (red) SOD, thus demonstrating the remarkable similarity and the outstanding resolution achieved. The availability of the assignment of crystalline SOD also allows evaluation of the efficacy and sequence specificity of PEGylation by monitoring the chemical shift of the protein residues at the reaction sites (Figure 2B and Table S2). The residues experiencing non-negligible chemical-shift perturbations are mapped onto the SOD structure in Figure 2C. Chemical-shift perturbations mainly occur for surface residues, as expected. Some perturbations are observed for residues in close proximity to, or facing, the PEGylated lysines, while some are not obviously related to it.

As an illustration of the suitability of ^{13}C-^{13}C solid-state NMR for this kind of applications, Figure S11 shows the dramatic changes that are observed in the 2D ^{13}C-^{13}C correlation spectra of SOD upon chemical denaturation of the enzyme.[32]

The simplicity of the method should make it attractive for industrial purposes: biologics are expensive drugs, in terms both of design and of manufacturing, and significant savings could be obtained if ssNMR could be used to monitor optimization of the PEGylation procedure.

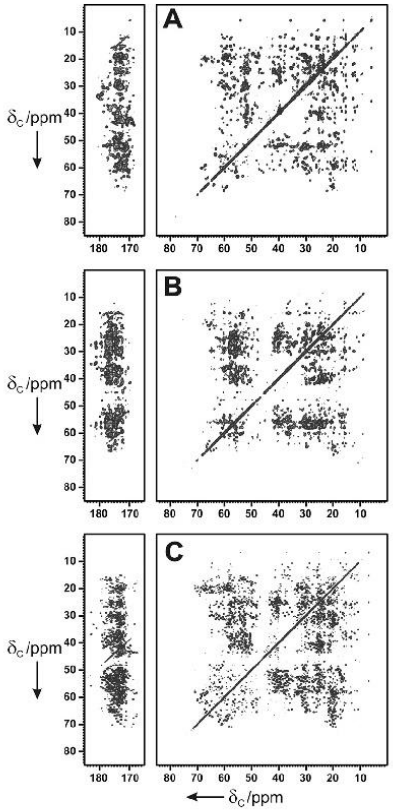

Figure 1. 2D ^{13}C-^{13}C correlation spectra of PEGylated SOD (A), PEGylated hHF (B), and PEGylated ANSII (C). Conditions: A) 16.4 T, 14 kHz MAS, 3.2 mm rotor; B) 16.4 T, 11.5 kHz MAS, 4 mm rotor; C) 20 T, 14 kHz MAS, 3.2 mm rotor (Table S1).

The very good quality of the spectra and the high filling factor intrinsic to protein pellets[33] also make it possible to acquire 3D spectra for assignment (Figure S12). Since almost all carbon atoms can be observed with simple uniform $^{13}C/^{15}N$ labeling, and assignment does not need to rely upon extensive mutagenesis and/or selective labeling, as needed, for example, for methyl-TROSY,[34] for example, ssNMR is expected to lift the limitations for the study of PEGylated biologics.

It is important to remark that the outcome of the analysis does not strictly depend on the type of experiment used:

a) Historically, ^{13}C-^{13}C correlation spectra,[36,37] which are sensitive to changes occurring in the secondary structure, mostly through the Cα–Cβ region, and allow residue-type fingerprinting,[38–40] were used for spectral comparison.
b) With the introduction of robust NC recoupling schemes,[41,42] such comparisons are made even easier.

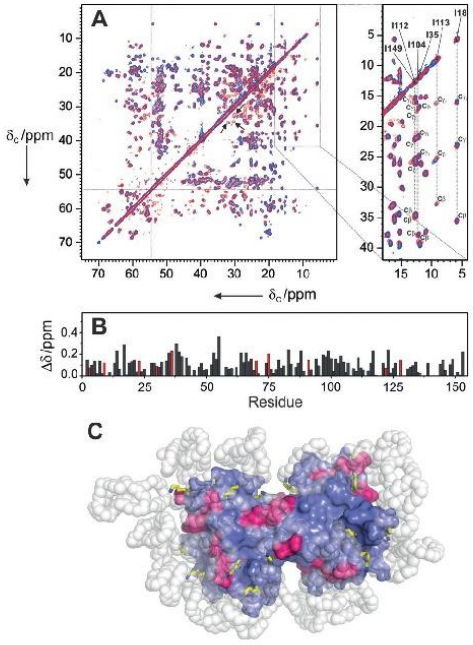

Figure 2. A) Comparison of the aliphatic portion of the ^{13}C-^{13}C correlation spectra for crystalline native SOD (red) and pelleted PEGylated SOD (blue). Off-diagonal regions separated by dashed gray lines in the left panel are plotted with lowered intensities for the PEGylated form to ease comparison between the spectra of the two forms. Resonances marked by arrows belong to glutamate residues neighboring reacted lysine residues. The right panel shows an enlargement of the isoleucine Cδ1 resonances and correlations. B) chemical-shift perturbation between the two species ($\Delta\delta = \frac{1}{2}\sqrt{\Delta\delta^2_{C\alpha} + \Delta\delta^2_{C\beta}}$),[35] where lysine residues are highlighted in red. C) Structure of the PEGylated SOD homodimer (in blue, from the crystal structure) showing the lysine residues as yellow stick models, and the PEG chains (modelled as random chains) as white transparent spheres. The regions with non-negligible chemical shift perturbation of the side chains are shown in magenta.

Indeed, the NC correlation spectrum of ANSII shows remarkably resolved resonances (Figure S14).

c) More recently, ^1H-detection-based ssNMR methods have been proposed,[43–45] and it is possible to foresee that comparison of ^1H-^{13}C or ^1H-^{15}N experiments could become the standard, yielding more sensitive detection on even lower amounts of sample.

Research on biologics is progressing towards the targeting of protein–protein interactions, which requires an even tighter control over the PEGylation processes.[46,47] The possibility of structurally characterizing PEGylated proteins represents a powerful tool for pushing the envelope of structural biology applications to biologics.

Acknowledgements

This work was supported by Ente Cassa di Risparmio di Firenze, MIUR PRIN 2012SK7ASN, EC Contracts pNMR No. 317127, IDPbyNMR No. 264257, the University of Florence CERM-TT, and the ESFRI Infrastructure Instruct through its Core Centre CERM, Italy. E.R. holds a FIRC triennial fellowship "Guglielmina Lucatello e Gino Mazzega" 17941.

Keywords: biopharmaceuticals · PEGylated proteins · protein modification · protein structures · solid-state NMR

How to cite: *Angew. Chem. Int. Ed.* **2016**, *55*, 2446–2449
Angew. Chem. **2016**, *128*, 2492–2495

[1] R. A. Rader, *Nat. Biotechnol.* **2008**, *26*, 743–751.
[2] B. Leader, Q. J. Baca, D. E. Golan, *Nat. Rev. Drug Discovery* **2008**, *7*, 21–39.
[3] J. M. Harris, R. B. Chess, *Nat. Rev. Drug Discovery* **2003**, *2*, 214–221.
[4] G. Cattani, L. Vogeley, P. B. Crowley, *Nat. Chem.* **2015**, *7*, 823–828.
[5] B. Plesner, P. Westh, S. Hvidt, A. D. Nielsen, *J. Pharm. Biomed. Anal.* **2011**, *55*, 597–602.
[6] Y.-S. Wang, S. Youngster, M. Grace, J. Bausch, R. Bordens, D. F. Wyss, *Adv. Drug Delivery Rev.* **2002**, *54*, 547–570.
[7] J.-H. Ardenkjaer-Larsen, G. S. Boebinger, A. Comment, S. Duckett, A. S. Edison, F. Engelke, C. Griesinger, R. G. Griffin, C. Hilty, H. Maeda, et al., *Angew. Chem. Int. Ed.* **2015**, *54*, 9162–9185; *Angew. Chem.* **2015**, *127*, 9292–9317.
[8] A. Loquet, B. Habenstein, A. Lange, *Acc. Chem. Res.* **2013**, *46*, 2070–2079.
[9] A. Loquet, N. G. Sgourakis, R. Gupta, K. Giller, D. Riedel, C. Goosmann, C. Griesinger, M. Kolbe, D. Baker, S. Becker, et al., *Nature* **2012**, *486*, 276–279.
[10] S. Yan, C. L. Suiter, G. Hou, H. Zhang, T. Polenova, *Acc. Chem. Res.* **2013**, *46*, 2047–2058.
[11] Y. Han, G. Hou, C. L. Suiter, J. Ahn, I.-J. L. Byeon, A. S. Lipton, S. Burton, I. Hung, P. L. Gor'kov, Z. Gan, et al., *J. Am. Chem. Soc.* **2013**, *135*, 17793–17803.
[12] F. Castellani, B. van Rossum, A. Diehl, M. Schubert, K. Rehbein, H. Oschkinat, *Nature* **2002**, *420*, 98–102.
[13] E. Ravera, T. Schubeis, T. Martelli, M. Fragai, G. Parigi, C. Luchinat, *J. Magn. Reson.* **2015**, *253*, 60–70.
[14] S. D. Kennedy, R. G. Bryant, *Biopolymers* **1990**, *29*, 1801–1806.
[15] M. Fragai, C. Luchinat, G. Parigi, E. Ravera, *J. Biomol. NMR* **2013**, *57*, 155–166.
[16] I. Bertini, C. Luchinat, G. Parigi, E. Ravera, *Acc. Chem. Res.* **2013**, *46*, 2059–2069.
[17] E. Ravera, *Concepts Magn. Reson. Part A* **2014**, *43*, 209–227.
[18] I. Bertini, C. Luchinat, G. Parigi, E. Ravera, B. Reif, P. Turano, *Proc. Natl. Acad. Sci. USA* **2011**, *108*, 10396–10399.
[19] I. Bertini, F. Engelke, C. Luchinat, G. Parigi, E. Ravera, C. Rosa, P. Turano, *Phys. Chem. Chem. Phys.* **2012**, *14*, 439–447.
[20] Y. R. Gokarn, M. McLean, T. M. Laue, *Mol. Pharmaceutics* **2012**, *9*, 762–773.
[21] R. Esco, J. Valencia, P. Coronel, J. A. Carceller, M. Gimeno, N. Bascón, *Int. J. Radiat. Oncol. Biol. Phys.* **2004**, *60*, 1211–1219.
[22] G. Pintacuda, N. Giraud, R. Pierattelli, A. Böckmann, I. Bertini, L. Emsley, *Angew. Chem. Int. Ed.* **2007**, *46*, 1079–1082; *Angew. Chem.* **2007**, *119*, 1097–1100.
[23] L. Banci, I. Bertini, F. Cramaro, R. Del Conte, M. S. Viezzoli, *Eur. J. Biochem.* **2002**, *269*, 1905–1915.

[24] H. E. Parge, R. A. Hallewell, J. A. Tainer, *Proc. Natl. Acad. Sci. USA* **1992**, *89*, 6109 – 6113.
[25] D. He, J. Marles-Wright, *New Biotechnol.* **2015**, DOI: 10.1016/j.nbt.2014.12.006.
[26] C. Pozzi, F. Di Pisa, C. Bernacchioni, S. Ciambellotti, P. Turano, S. Mangani, *Acta Crystallogr. Sect. D* **2015**, *71*, 1909 – 1920.
[27] C. Pozzi, F. Di Pisa, D. Lalli, C. Rosa, E. Theil, P. Turano, S. Mangani, *Acta Crystallogr. Sect. D* **2015**, *71*, 941 – 953.
[28] R. Tsukamoto, M. Godonoga, R. Matsuyama, M. Igarashi, J. G. Heddle, S. Samukawa, I. Yamashita, *Langmuir* **2013**, *29*, 12737 – 12743.
[29] J. M. Hill, J. Roberts, E. Loeb, A. Khan, A. MacLellan, R. W. Hill, *J. Am. Med. Assoc.* **1967**, *202*, 882 – 888.
[30] A. L. Swain, M. Jaskólski, D. Housset, J. K. Rao, A. Wlodawer, *Proc. Natl. Acad. Sci. USA* **1993**, *90*, 1474 – 1478.
[31] M. L. Graham, *Adv. Drug Delivery Rev.* **2003**, *55*, 1293 – 1302.
[32] M. Assfalg, L. Banci, I. Bertini, P. Turano, P. R. Vasos, *J. Mol. Biol.* **2003**, *330*, 145 – 158.
[33] L. Ferella, C. Luchinat, E. Ravera, A. Rosato, *J. Biomol. NMR* **2013**, *57*, 319 – 326.
[34] R. Rosenzweig, L. E. Kay, *Annu. Rev. Biochem.* **2014**, *83*, 291 – 315.
[35] S. Grzesiek, A. Bax, G. M. Clore, A. M. Gronenborn, J. S. Hu, J. Kaufman, I. Palmer, S. J. Stahl, P. T. Wingfield, *Nat. Struct. Biol.* **1996**, *3*, 340 – 345.
[36] S. Balayssac, I. Bertini, K. Falber, M. Fragai, S. Jehle, M. Lelli, C. Luchinat, H. Oschkinat, K. J. Yeo, *ChemBioChem* **2007**, *8*, 486 – 489.
[37] A. Loquet, L. Bousset, C. Gardiennet, Y. Sourigues, C. Wasmer, B. Habenstein, A. Schütz, B. H. Meier, R. Melki, A. Böckmann, *J. Mol. Biol.* **2009**, *394*, 108 – 118.
[38] D. Marulanda, M. L. Tasayco, A. McDermott, M. Cataldi, V. Arriaran, T. Polenova, *J. Am. Chem. Soc.* **2004**, *126*, 16608 – 16620.
[39] P. Turano, D. Lalli, I. C. Felli, E. C. Theil, I. Bertini, *Proc. Natl. Acad. Sci. USA* **2010**, *107*, 545 – 550.
[40] M. Matzapetakis, P. Turano, E. C. Theil, I. Bertini, *J. Biomol. NMR* **2007**, *38*, 237 – 242.
[41] J. Pauli, M. Baldus, B. van Rossum, H. de Groot, H. Oschkinat, *ChemBioChem* **2001**, *2*, 272 – 281.
[42] J. J. Helmus, K. Surewicz, P. S. Nadaud, W. K. Surewicz, C. P. Jaroniec, *Proc. Natl. Acad. Sci. USA* **2008**, *105*, 6284 – 6289.
[43] D. H. Zhou, G. Shah, C. Mullen, D. Sandoz, C. M. Rienstra, *Angew. Chem.* **2009**, *121*, 1279 – 1282.
[44] M. J. Knight, A. L. Webber, A. J. Pell, P. Guerry, E. Barbet-Massin, I. Bertini, I. C. Felli, L. Gonnelli, R. Pierattelli, L. Emsley, et al., *Angew. Chem. Int. Ed.* **2011**, *50*, 11697 – 11701; *Angew. Chem.* **2011**, *123*, 11901 – 11905.
[45] D. Lalli, P. Turano, *Acc. Chem. Res.* **2013**, *46*, 2676 – 2685.
[46] M. J. Roberts, M. D. Bentley, J. M. Harris, *Adv. Drug Delivery Rev.* **2002**, *54*, 459 – 476.
[47] C. Bello, S. Wang, L. Meng, K. W. Moremen, C. F. W. Becker, *Angew. Chem. Int. Ed.* **2015**, *54*, 7711 – 7715; *Angew. Chem.* **2015**, *127*, 7823 – 7828.

Received: October 31, 2015
Published online: January 12, 2016

Angewandte
Eine Zeitschrift der Gesellschaft Deutscher Chemiker Chemie

Supporting Information

Solid-State NMR of PEGylated Proteins

*Enrico Ravera, Silvia Ciambellotti, Linda Cerofolini, Tommaso Martelli, Tatiana Kozyreva, Caterina Bernacchioni, Stefano Giuntini, Marco Fragai, Paola Turano, and Claudio Luchinat**

anie_201510148_sm_miscellaneous_information.pdf

Human Cu(II)-Zn(II)-Superoxide Dismutase (SOD)

The preservation of the protein folding and the conservation of the structure of the catalytic site is essential to maintain the enzymatic activity of SOD. SOD has been reported to retain its enzymatic activity after PEGylation. However, structural data at atomic resolution were not available so far.[1]

Protein expression. The C6A, C111S mutant of SOD was expressed in the *Escherichia coli* TOPP1 (Stratagene) or BL21(DE3) strain and purified using previously reported protocols.[2] This SOD mutant is structurally and functionally equivalent to the wild type protein.[3,4]

The apo protein was obtained by dialysis against 10 mM EDTA in 50 mM sodium acetate (pH 3.8). The chelating agent was removed by extensive dialysis against 100 mM NaCl in the same buffer and then against acetate buffer alone, gradually increasing the pH from 3.8 to 5.5. The Cu(II)-Zn(II) form of SOD was obtained by addition of stoichiometric amounts of $ZnSO_4$ and $CuSO_4$ at pH 5.5.

PEGylation Reaction. A solution 250 mM of PEGylation reagent $MS(PEG)_{24}$ (Thermo scientific, Rockford, Il) was prepared, according to the manual, dissolving 100 mg of reagent in 230 μL of dry DMF. To obtain an excess of PEGylation reagent of 20 times respect to the protein, 120 μL of the stock solution were added to 5 mL of SOD 4.6 mg/mL in phosphate buffer (150 mM, pH = 7.5). The mixture was left stirring over-night at 277 K.

In the morning, a purification with a PD10 column was performed to remove the non-reacted and the hydrolyzed PEGylation reagent. Products and yield of the reaction were evaluated by SDS-PAGE (Figure S1) and solution NMR spectra (Figure S2).

NMR spectroscopy. The spectra of the crystalline preparation of the protein, recorded at 20 T, obtained from the conditions listed in Table S1, were kindly provided by Prof. Roberta Pierattelli. DARR mixing time was 150 ms, and ^{1}H decoupling was 80 kHz.

Native sedimented SOD was concentrated to 200 mg/mL. 16.4 μL of concentrated protein solution were transferred into a Bruker 3.2 mm rotor and spun on a tabletop spinner to remove air bubbles that easily form at high protein concentration. Bubbles removal is critical for rotation stability and shimming. The rotor was sealed with a DNP silicon plug (Bruker biospin) to avoid leakage, and sedimentation was achieved by MAS spinning at 14 kHz.[5] Experiments were performed on a Bruker Avance II 850 MHz wide-bore spectrometer (20 T, 213.6 MHz ^{13}C Larmor frequency), equipped with a 3.2 mm DVT MAS probe head in triple-resonance mode. ^{13}C -^{13}C recoupling was accomplished by 50 ms Dipolar Assisted Rotary Resonance[6], where ^{1}H-^{13}C dipolar recoupling is achieved by a continuous wave radiofrequency irradiation on the ^{1}H channel at $\omega_H=\omega_r$; during evolution and acquisition, decoupling was applied at 100 kHz (found to be optimal on the basis of the ^{13}C' echo lifetime) using a swTPPM sequence.[7] At both instruments, interscan delay was 1.6 s.

PEGylated SOD was freeze-dried and packed in the rotor, then rehydrated by multiple additions of 1 μL of buffer, until the resolution of the ^{13}C 1D SSNMR spectrum stopped changing.[8] The ^{13}C 1D SSNMR spectra were acquired with 16 scans each with a recycle delay of 0.9 s, after the sample had stably reached the desired temperature (around 280 K). 5 μL of buffer were added in total to the freeze-dried protein before the acquisition of the ^{13}C-^{13}C correlation spectra. Experiments were performed on a Bruker Avance II 700 MHz wide-bore spectrometer (16.4 T, 176.1 MHz ^{13}C Larmor frequency), equipped with a 3.2 mm DVT MAS probe head in triple-resonance mode. ^{13}C - ^{13}C recoupling was accomplished by 50 ms Dipolar Assisted Rotary Resonance[6], where ^{1}H-^{13}C dipolar recoupling is achieved by a continuous wave radiofrequency irradiation on the ^{1}H channel at $\omega_H=\omega_r$, during evolution and acquisition, decoupling was applied at 100 kHz (found to be optimal on the basis of the $^{13}C'$ echo lifetime) using a swTPPM sequence.[7]

Human-H Ferritin (hHF)

The use of ferritin as a carrier to deliver imaging and therapeutic agents relies i) on the intactness of its nanocage architecture that ensures their efficient solubilisation and transport and ii) on the accessibility of the C3 pores to iron or other metal ions able to form inorganic cores directly inside the inner cage.[9]

Here we report a comparative analysis of the native and PEGylated hHF to establish the conservation of the nanocage 24-mer structure via DLS (Figure S6) and of the stability of the subunit secondary structure via CD (Figure S4). Comparative stopped flow kinetics of the catalytic reactions occurring at the ferroxidase site is used as an efficient tool to demonstrate intact accessibility of the C3 ion channels upon PEGylation (Figure S5).[10]

Protein Expression. pET-9a construct encoding hHF was transformed into *Escherichia coli* BL21(DE3) pLysS cells which were subsequently cultured in rich (LB) or ^{13}C,^{15}N-labelled minimal medium (M9) containing kanamycin (0.05 mg mL^{-1}) and chloramphenicol (34 μg mL^{-1}). Cells were grown at 310 K, until A_{600nm} reached 0.6–0.8 and subsequently induced with isopropyl 1-thio-β-D-galactopyranoside (IPTG, 1 mM final concentration) for 4 h. Ferritin was purified from the harvested cells, as described previously for the bullfrog M ferritin[11,12]. Briefly, cells were broken by sonication and the cell free extract obtained after centrifugation (40 min, 40000 rpm, 70Ti Beckman Coulter, at 277 K) was incubated for 15 min at 338 K as the first purification step. After removal of the aggregated proteins by ultracentrifugation (15 min, 40000 rpm, 70Ti Beckman Coulter, at 277 K), the supernatant solution was dialyzed against Tris-HCl 20 mM pH 7.5; applied to a Q-Sepharose column in the same buffer and eluted with a linear NaCl gradient of 0-1 M in Tris 20 mM, pH 7.5. Fractions containing ferritin, identified by Coomassie staining of SDS-PAGE gels, were combined and further purified by size exclusion chromatography using a Superdex 200 16/60

column. Iron and other metal ions were removed by four dialysis steps at room temperature each using 4 L 20 mM Tris, 2.5 mM EDTA, 10 mL ammonium thioglycolate pH 7.5 to reduce and chelate the iron, followed by four dialysis steps at room temperature each using 4 L 20 mM Tris pH 7.5.

PEGylation Reaction. A solution 250 mM of PEGylation Reagent $MS(PEG)_{24}$ (Thermo scientific, Rockford, Il) was prepared, according to the manual, dissolving 100 mg of reagent in 230 μL of dry DMF. To obtain an excess of PEGylation reagent of 10 times respect to the protein, 40 μL of the stock solution were added to 5.5 mL of hHF 3.6 mg/mL in phosphate buffer (150 mM, pH = 7.2). The mixture was left stirring over-night at 277 K.

In the morning, a purification with a PD10 column was performed to remove the non-reacted and the hydrolyzed PEGylation reagent. Products and yield of the reaction were evaluated by SDS-PAGE (Figure S3).

Circular Dichroism Spectroscopy. CD spectra to assess the stability of the protein secondary structure were acquired in the far-UV with a Jasco J-810 spectropolarimeter using a 0.1 cm path length quartz cuvette and 5 μM protein concentration (in subunits) in 150 mM sodium phosphate buffer, pH 7.5. For temperature melting curves in the 298-358 K, a CD spectrum was first measured at 298 K, the protein was then incubated in thermostated cells at the desired temperatures for 5 min and the corresponding CD spectra was acquired in 6 min. The mean of 10 scans between 190 and 250 nm wavelength was calculated by subtraction of the corresponding buffer spectrum. The resulting curves are reported in Figure S4.

Stopped-flow kinetics. Single turnover oxidoreductase kinetics (2 Fe^{2+}/subunit) was monitored in hHF, or PEGylated (PEG-hHF). Changes in A_{650nm}, corresponding to the diferric-peroxo (DFP) intermediate, and A_{350nm}, corresponding to ferric-oxo $(Fe^{3+}O)_x$ species, were measured after rapid mixing (<10 msec) of equal volumes of 100 μM protein subunits in 200 mM MOPS, 200 mM NaCl, at pH 7 with freshly prepared solutions of 200 μM ferrous sulfate in 1 mM HCl, in a UV/visible, stopped-flow spectrophotometer (SX.18MV stopped-flow reaction analyzer, Applied Photophysics). Routinely, 4000 data points were collected during the first 5 seconds. Initial rates of DFP and $(Fe^{3+}O)_x$ species formation were determined using data from three independent analyses through the linear fitting of the initial phases of absorbance changes at 650 nm and 350 nm traces (0.01–0.03 s) (Figure S5).

Dynamic Light Scattering (DLS). DLS measurements at $\theta = 90°$ were performed using a Brookhaven Instrument 90 Plus (Brookhaven, Holtsville, NY). Each measurement was an average of five repetitions of one minute (Figure S6). The normalized electrical field time autocorrelation functions of the normalized intensity time autocorrelation of the scattered light were measured at

90° and analyzed according to the Siegert relation (Eq. (1)), which connects the first order or field normalized autocorrelation function $g_1(q, \tau)$ to the measured normalized time autocorrelation function $g_2(q, \tau)$[13]:

$$g_2(q, \tau) = 1 + \beta|g_1(q, \tau)|^2 \quad (1)$$

with β being the spatial coherence factor which depends on the geometry of the detection system. The functions $(\beta|g_1(q, \tau)|^2)^{1/2})$ were also normalized to vary between 0 and 1 for display purposes. The field autocorrelation functions were analyzed through a cumulant analysis stopped to the second order, allowing an estimate of the hydrodynamic diameter of particles and of the polydispersity index (Figure S6)[14].

NMR Spectroscopy. The crystalline preparation of the protein was obtained from the conditions listed in Table S1. The high-salt crystallization conditions, which sizably affect the radiofrequency characteristics of NMR probeheads, prompt the use of a small-diameter rotor, and experiments were performed in a 1.3 mm rotor, at 60 kHz spinning at 20 T. ^{13}C-^{13}C recoupling was accomplished by 3 ms of Radio-Frequency-Driven Recoupling[15] (number of scans 64), where ^{13}C-^{13}C dipolar recoupling is achieved with a train of rotor-synchronized π-pulses; this approach has the tendency to favor recoupling to the nearest neighbors, lowering the intensity of long-range cross peaks;[15] for this reason, the aliphatic to carbonyl correlation region was acquired at 40 kHz spinning rate with a CORD-xy4 sequence, with 350 ms mixing time (number of scans 128).[16] During evolution and acquisition, decoupling was applied at 13.5 kHz using a using a swTPPM sequence.[7]

Both native and PEGylated hHF pelleted spectra were obtained sealing the proteins into a 4 mm rotor as 100 mg/ml solution, and sedimented by the rotor spinning at 11.5 kHz. For the 1D experiments, 128 scans with 1.5 s interscan delay was used. For the DARR Experiments were performed on a Bruker Avance II 700 MHz wide-bore spectrometer (16.4 T, 176.1 MHz ^{13}C Larmor frequency), equipped with a 4 mm DVT MAS probe head in triple-resonance mode. ^{13}C - ^{13}C recoupling was accomplished by 100 ms Dipolar Assisted Rotary Resonance[6], where ^{1}H-^{13}C dipolar recoupling is achieved by a continuous wave radiofrequency irradiation on the ^{1}H channel at $\omega_H=\omega_r$; during evolution and acquisition, decoupling was applied at 75 kHz (found to be optimal on the basis of the $^{13}C'$ echo lifetime) using a using a swTPPM sequence.[7] Recycle delay was set to 1.5 and the number of scans was 176.

E. coli L-Asparaginase II (ANSII)

L-Asparaginase from *Escherichia coli* and its PEGylated derivative obtained by reacting the enzyme with $MS(PEG)_{24}$ have been prepared and characterized.

Protein expression. The gene encoding ANSII in pET-21a was transformed into *Escherichia coli* BL21(DE3)C41 cells which were subsequently cultured in rich (LB) or ^{13}C,^{15}N-labelled minimal medium (M9) containing ampicillin (0,1 mg mL^{-1}). Cells were grown at 310 K, until A_{600nm} reached 0.6-0.8 and subsequently induced with IPTG (1 mM final concentration). Cells were further grown at 310 K overnight and then harvested by centrifugation at 6500 rpm (JA-10 Beckman Coulter) for 20 min at 277 K. All the purification procedures were carried out at 277 K. The pellet was re-suspended in 10 mM Tris-HCl, pH 8.0, 15 mM EDTA, 20% sucrose buffer (60 mL per liter of culture) and then kept for 20 min under magnetic stirring. Suspension was centrifuged at 10000 rpm (F15-6x100y Thermo Scientific) for 30 min and supernatant discarded. The pellet was re-suspended in H_2O milli-Q (60 mL per liter of culture) and then kept for 20 min under magnetic stirring. Suspension was centrifuged again at 10000 rpm (F15-6x100y Thermo Scientific) for 30 min. The supernatant was treated with ammonium sulfate from 50% to 90% to precipitate the ANSII protein. Then the protein was re-dissolved in minimal amount of 20 mM Tris-HCl pH 8.0 buffer and dialyzed extensively against the same buffer. The ANSII was further purified by Q-Sepharose column using 20 mM Tris-HCl pH 8.6 buffer with a linear NaCl gradient 0-1 M. Fractions containing pure ANSII were identified by Coomassie staining SDS-PAGE gels. The formation of the tetrameric assembly of ANSII was confirmed by gel filtration using a Superdex 200 10/300 IB increase column.

PEGylation Reaction. A solution 250 mM of PEGylation Reagent $MS(PEG)_{24}$ (Thermo scientific, Rockford, Il) was prepared, according to the manual, dissolving 100 mg of reagent in 230 µL of dry DMF. To obtain an excess of PEGylation reagent of 20 times respect to the protein, 120 µL of the stock solution were added to 6.7 mL of ANSII 4.2 mg/mL in phosphate buffer (150 mM, pH = 7.5). The mixture was left stirring over-night at 277 K.

In the morning, a purification with a PD10 column was performed to remove the non-reacted and the hydrolyzed PEGylation reagent. Products and yield of the reaction were evaluated were evaluated by SDS-PAGE (Figure S7).

NMR spectroscopy. The crystalline preparation of the protein was obtained from the conditions listed in Table S1. ^{13}C -^{13}C recoupling was accomplished by 50 ms Dipolar Assisted Rotary Resonance[6], where ^{1}H-^{13}C dipolar recoupling is achieved by a continuous wave radiofrequency irradiation on the ^{1}H channel at $\omega_H=\omega_r$, during evolution and acquisition, decoupling was applied at 100 kHz (found to be optimal on the basis of the $^{13}C'$ echo lifetime) using a swTPPM sequence.[7] The interscan delay was 0.8 s.

PEGylated ANSII was freeze-dried and packed in the rotor, then rehydrated by multiple additions of 1 μL of buffer, until the resolution of the ^{13}C 1D SSNMR spectrum stopped changing.[8] The ^{13}C 1D SSNMR spectra were acquired with 16 scans each with a recycle delay of 1.3 s, after the sample had stably reached the desired temperature (around 280 K). 5 μL of buffer were added in total to the freeze-dried protein before the acquisition of the ^{13}C-^{13}C correlation spectra.

Experiments were performed on a Bruker Avance II 850 MHz wide-bore spectrometer (20 T, 213.6 MHz ^{13}C Larmor frequency), equipped with a 3.2 mm DVT MAS probe head in triple-resonance mode. ^{13}C-^{13}C recoupling was accomplished by 50 ms Dipolar Assisted Rotary Resonance[6], where ^{1}H-^{13}C dipolar recoupling is achieved by a continuous wave radiofrequency irradiation on the ^{1}H channel at $\omega_H=\omega_r$; during evolution and acquisition, decoupling was applied at 100 kHz using a using a swTPPM sequence.[7]

Supplementary Figures

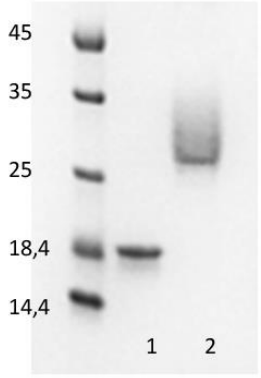

Figure S1. SDS-PAGE gel resulting from PEGylation of SOD. Lane 1: monomeric SOD; lane 2: monomeric PEGylated SOD. Under SDS-denaturing conditions, only the SOD monomer is predicted to be observable.

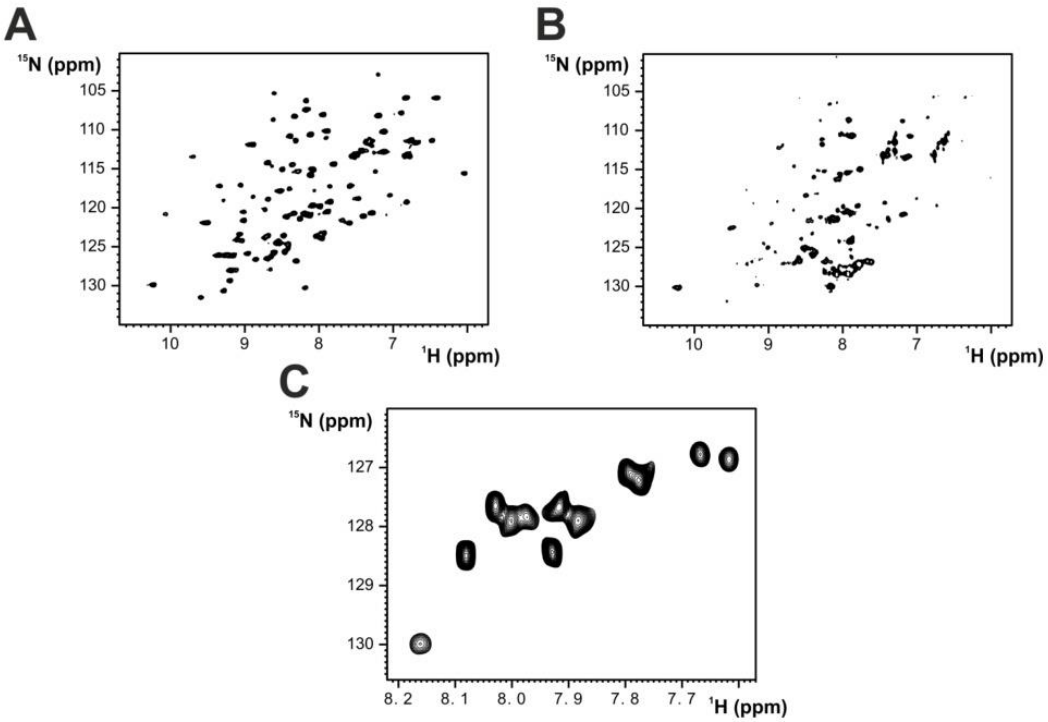

Figure S2. Solution NMR 2D ^{1}H ^{15}N HSQC spectrum of SOD before (A) and 2D ^{1}H ^{15}N TROSY spectrum after (B) PEGylation. In panel C a zoom of the region in the spectrum where are visible the 12 new amide cross-peaks obtained from the PEGylation of the flexible sidechains of the lysines and of the N-terminus.

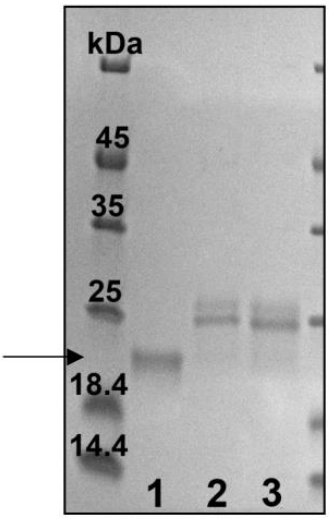

Figure S3. SDS-PAGE gel resulting from PEGylation of hHF. Lane 1: hHF; lanes 2 and 3: PEG-hHF obtained by two independent reactions. Under SDS-denaturing conditions, only the ferritin monomer is predicted to be observable; the arrow indicates the expected molecular weight of hHF monomer.

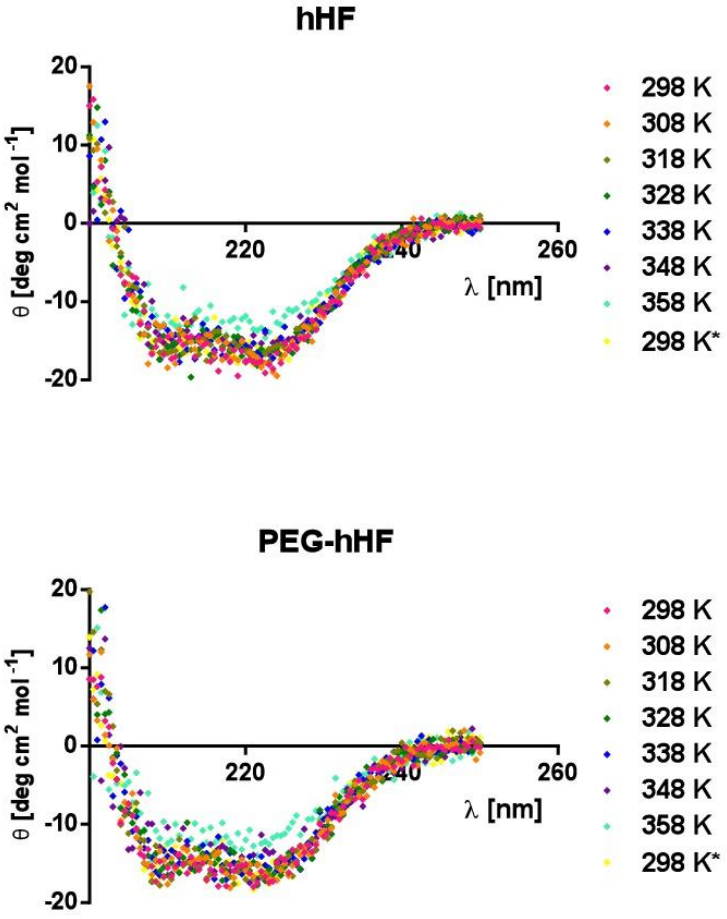

Figure S4. CD melting curves of PEG-hHF and comparison with hHF. Far UV CD spectra of hHF (upper panel) and PEG-hHF (lower panel) apoferritins. Spectra were acquired in the 298–358 K temperature range. The 298 K* traces were recorded after cooling back the samples from 358 to 298 K, to check reversibility

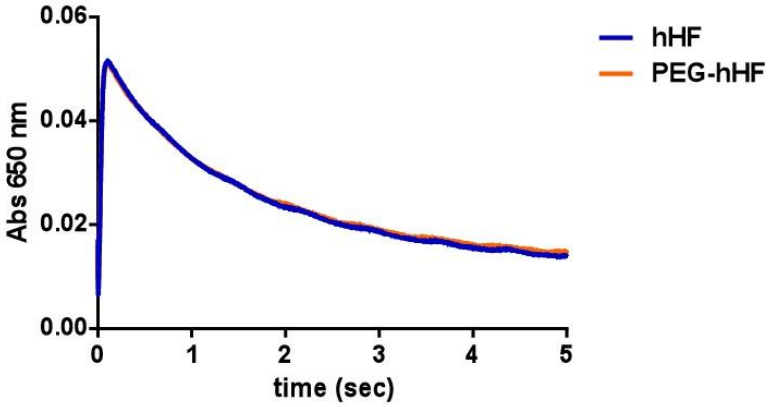

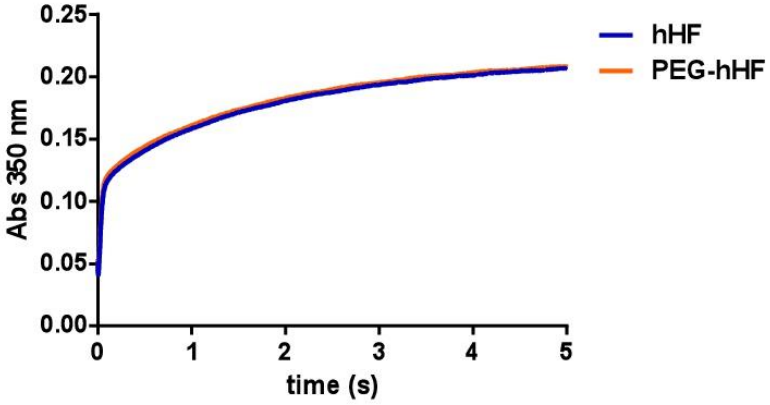

Protein	Initial rate of DFP formation ($\Delta A_{650\ nm}$)	Initial rate of $(Fe^{3+}O)_x$ formation ($\Delta A_{350\ nm}$)
hHF	1.002 ± 0.0139	1.549 ± 0.081
PEG-hHF	0.998 ± 0.022	1.570 ± 0.003

Figure S5. PEG-hHF has the same ferroxidase activity as the hHF. Formation of (upper panel) DFP intermediate ($A_{650\ nm}$) and (lower panel) $(Fe^{3+}O)_x$ products ($A_{350\ nm}$) were measured by rapid-mixing, UV−vis spectroscopy. Shown are a set of representative curves (one of three independent

analyses for each protein). The table shows the rates (mean ±SEM, from data obtained by three independent analyses) calculated as described in the Methods section.

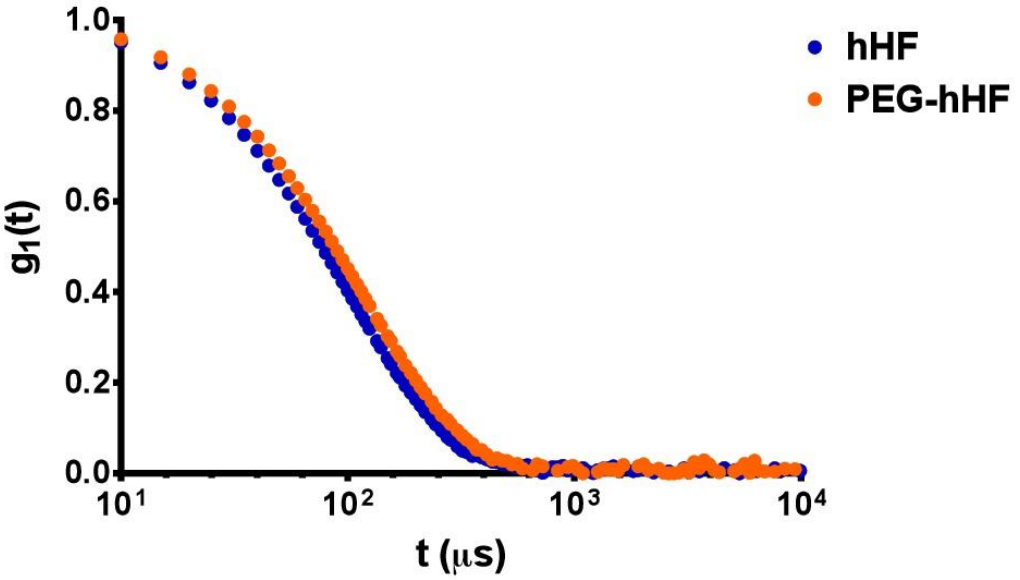

	hHF	PEG-hHF
Dh	**17.6±0.2**	**18.6±0.1**
PDI	**0.094±0.011**	**0.091±0.010**

Figure S6. Representative normalized DLS curves obtained for the hHF and for the PEGylated protein (PEG-hHF). The table summarizes the data (mean ±SD, from data obtained by five independent analyses) for hydrodynamic diameter (Dh) and polydispersity index (PDI) of proteins' dispersions calculated as described in the Methods section.

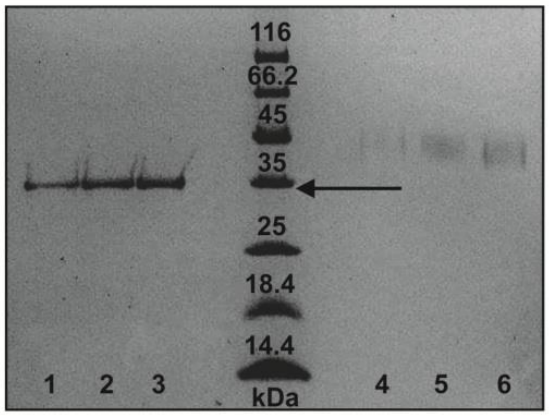

Figure S7. SDS-PAGE gel resulting from PEGylation of L-asparaginase II. Lanes 1, 2 and 3: L-asparaginase II at three different concentrations; lanes 4, 5 and 6: PEGylated L-asparaginase II at three different concentrations. Under SDS-denaturing conditions only the L-asparaginase II monomer is predicted to be observable; the arrow indicates the expected molecular weight of L-asparaginase II monomer.

Table S1. Samples used in the present method and experimental conditions of the presented spectra.

Protein	Crystalline Native	Pelleted Native	Pelleted PEGylated
SOD	Protein solution: SOD 12 mM in unbuffered water Crystallization conditions (diffracting at 8 Å resolution): 20 mM citrate pH = 5, PEG 6k 20%[17] Experimental setup - Magnetic field: 20 T; MAS spinning: 20 kHz, 3.2 mm rotor ; CC recoupling: DARR Figure - S8A, courtesy of Prof. Roberta Pierattelli[18]	Experimental setup - Magnetic field: 20 T; MAS spinning: 21 kHz, 3.2 mm rotor; CC recoupling: DARR Figure – S10A	Experimental setup - Magnetic field: 16.4 T; MAS spinning: 14 kHz, 3.2 mm rotor; CC recoupling: DARR Figure - 1A/S8B/S10B
hHF	Protein solution: hHF 13 mg/mL, 20 mM Tris, pH=7.7, 0.15 M NaCl Crystallization conditions: 2 M $MgCl_2$, 0.1 M Bicine, pH = 8 PDB accession code: 4P03[19] Experimental setup: Magnetic field 20 T; MAS spinning: 60 kHz, 1.3 mm rotor; CC recoupling: RFDR Figure - S8C	Experimental setup - Magnetic field: 16.4 T; MAS spinning: 11.5 kHz, 4 mm rotor; CC recoupling: DARR Figure – S10C	Experimental setup - Magnetic field: 16.4 T; MAS spinning: 11.5 kHz, 4 mm rotor; CC recoupling: DARR Figure – 1B/S8D/S10D
ANSII	Protein solution: ANSII 0.4 mM in 100 mM MES-NaOH pH = 6.5. Crystallization conditions[20]: 100 mM MES-NaOH pH = 6.5, PEG-MME 550 25%, 10 mM $ZnSO_4$. PDB accession code : 3ECA[21]- Experimental setup - Magnetic field: 20 T; MAS spinning: 14 kHz 3.2 mm rotor; CC recoupling: DARR Figure - S8E		Experimental setup - Magnetic field: 20 T; MAS spinning: 14 kHz 3.2 mm rotor; CC recoupling: DARR Figure - 1C/S8F

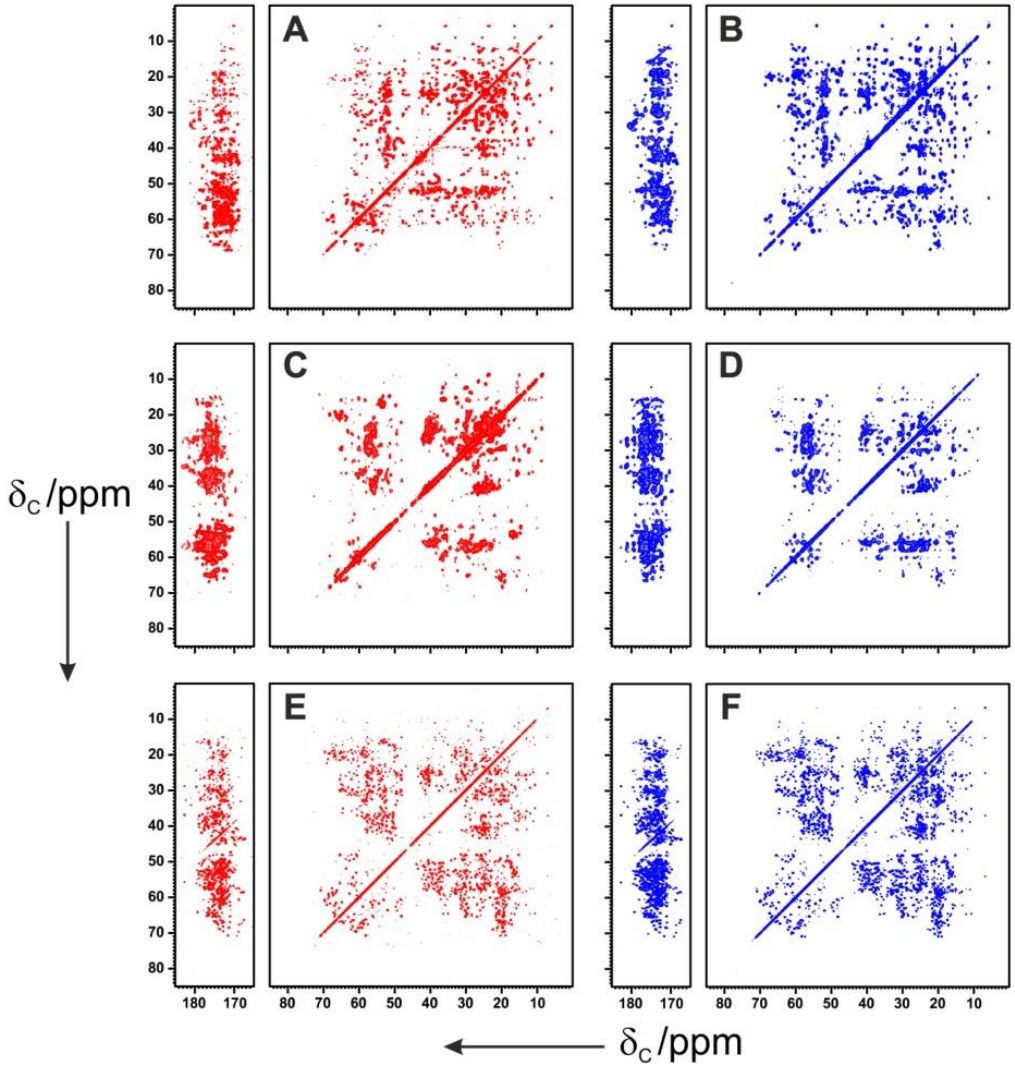

Figure S8. 2D ^{13}C-^{13}C correlation spectra of crystalline (A) and PEGylated (B) SOD; crystalline (C) and PEGylated (D) hHF; crystalline (E) and PEGylated (F) ANSII.

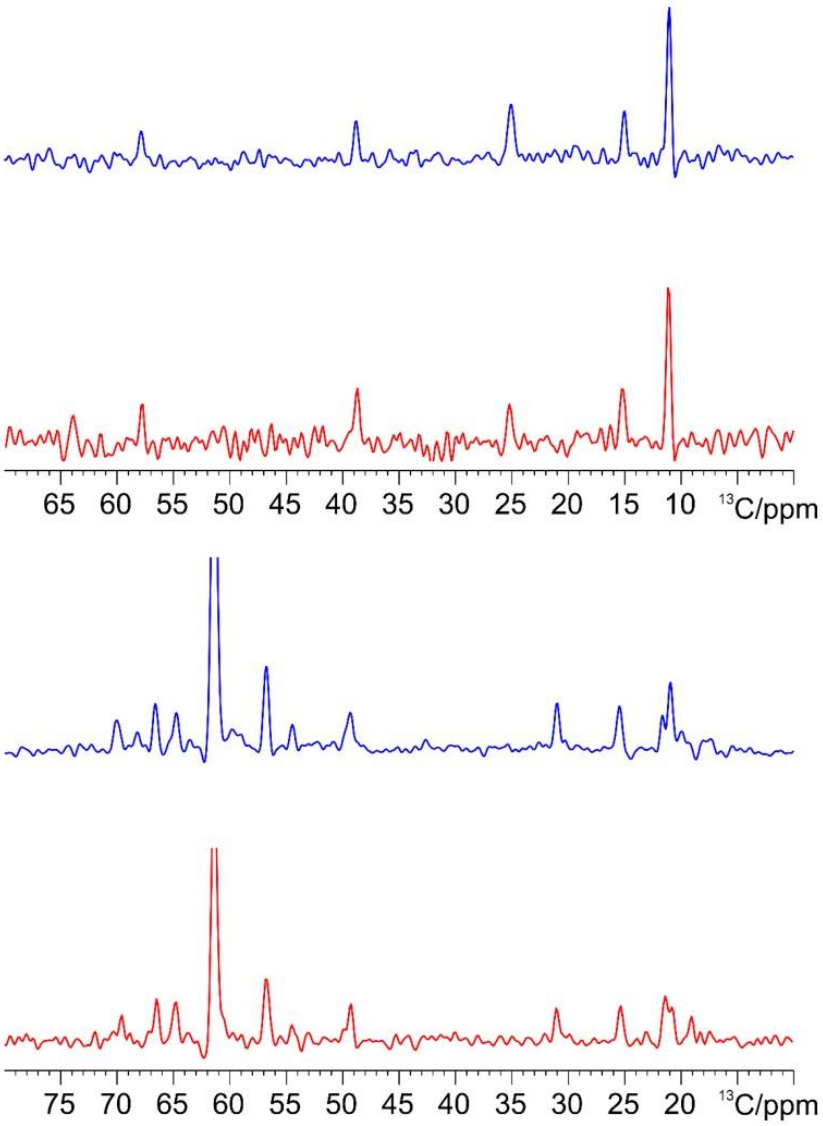

Figure S9. 1D traces of two rows (at 11.0 and 61.4 ppm, respectively) of the 2D ^{13}C-^{13}C correlation spectra of PEGylated (blue) and crystalline (red) ANSII.

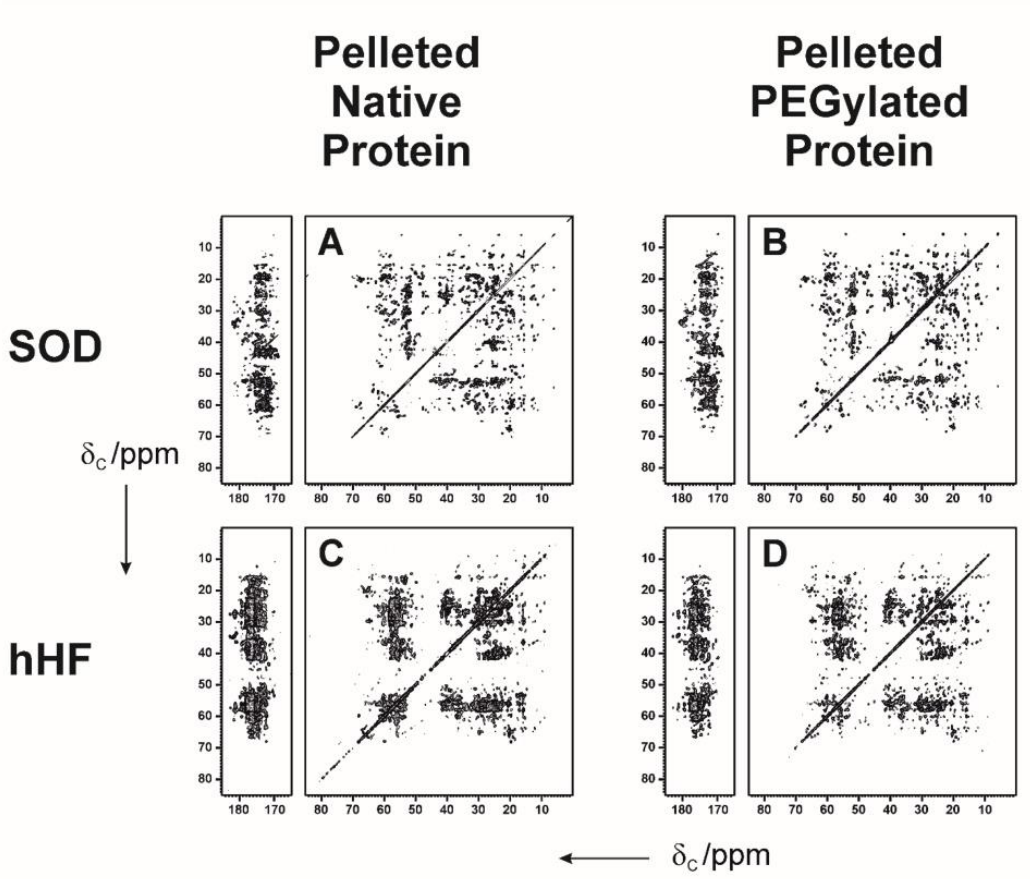

Figure S10. Comparison of the ^{13}C-^{13}C correlation spectra obtained for SOD and hHF as pelleted native proteins (A and C) and as pelleted PEGylated proteins (B and D).

Table S2. Chemical shifts of carbon sidechains of crystalline native[22] and pelleted pegylated SOD.

		Crystalline Native SOD						Pelleted PEGylated SOD					
Num	Res	Cα	Cβ	Cγ		Cδ	Cε	Cα	Cβ	Cγ		Cδ	Cε
1	GLN												
2	THR	60.83	69.21	20.97				60.97	68.94	20.97			
3	LYS	54.06	36.07	24.28		28.22	41.30	53.94	35.97	24.28		28.28	41.13
4	ALA	49.85	22.69					49.66	22.64				
5	VAL	59.09	34.89	20.88	17.91			58.94	34.66	21.05	17.94		
6	ALA	49.64	22.58					49.65	22.63				
7	VAL	60.39	31.89	20.25	20.10			60.12	31.79	20.25	20.10		
8	LEU	53.28	39.50	28.43		23.02		53.28	39.44	28.43		22.94	
9	LYS	54.14	36.35	24.14		28.10		53.91	36.24	24.17		28.02	
10	GLY	44.50						44.50					
11	ASP	53.63	40.08					53.70	40.08				
12	GLY	43.20						43.20					
13	PRO	62.46	31.81	25.07		48.69		62.21	31.78	25.17		48.48	
14	VAL	62.02	29.37	21.47	20.83			61.58	29.52	21.50	20.81		
15	GLN	52.89	30.75	31.98				52.76	30.73	31.98			
16	GLY	45.50						45.50					
17	ILE	60.58	40.41	27.72	16.65	12.82		60.48	40.99	27.58	16.66	13.20	
18	ILE	55.55	36.95	24.93	17.48	7.00		55.57	36.97	24.54	17.55	7.11	
19	ASN	51.34	39.61					51.21	39.81				
20	PHE	53.93	42.13					54.15	42.28				
21	GLU	55.06	33.29	35.95				55.35	33.34	36.28			
22	GLN	53.52	31.21	34.17				53.45	31.24	34.46			
23	LYS	58.14	31.82	24.34		28.04		57.97	32.04	24.22		28.04	
24	GLU	53.24	31.37	34.22				53.31	31.42	34.37			
25	SER	61.06	63.06					61.09	62.93				
26	ASN	51.65	37.38					51.65	37.38				
27	GLY	44.70						44.70					
28	PRO	62.07	31.67	26.14		48.92		61.86	31.80	26.41		48.74	
29	VAL	59.92	32.51	22.39	22.00			59.70	32.40	22.39	22.02		
30	LYS	55.02	32.62	24.39		28.15		55.05	32.79	24.39		28.21	
31	VAL	59.61	32.70	19.86	19.60			59.51	32.57	19.86	19.60		
32	TRP	55.39	31.32					55.28	31.55				
33	GLY	43.60						43.60					
34	SER	55.88	64.62					56.16	64.57				
35	ILE	59.06	40.32	26.48	18.13	13.30		58.86	40.68	26.33	18.13	13.38	
36	LYS	52.67	34.19	23.46		28.43		53.11	34.30	23.49		28.54	
37	GLY	44.50						44.50					
38	LEU	52.56	43.33	25.54		24.98	22.48	51.96	43.32	25.42		25.00	22.43
39	THR	60.16	68.73	21.86				60.46	68.41	21.93			
40	GLU	56.51	28.98					56.40	29.32				
41	GLY	41.20						41.20					
42	LEU	54.23	42.97	26.61		24.41	23.15	54.03	42.71	26.68		24.19	22.83
43	HIS	53.37	30.91					53.23	30.78				
44	GLY	46.20						46.20					
45	PHE	55.52	41.59					55.42	41.63				
46	HIS												
47	VAL	60.77	31.07					60.70	31.22				
48	HIS	54.42	30.22					54.49	30.00				

49	GLU	60.78	30.56	34.26						60.75	30.46	34.40					
50	PHE	55.26	38.62							55.39	38.62						
51	GLY	45.10								45.10							
52	ASP	51.18	41.42							50.97	41.43						
53	ASN	50.61	38.57							50.26	38.33						
54	THR	65.40	67.99	22.10						65.60	68.23	22.58					
55	ALA	48.57	16.77							48.03	17.27						
56	GLY	44.50								44.50							
57	CYS	50.02	41.52							50.02	41.52						
58	THR	65.04	67.83	20.80						65.09	67.67	21.28					
59	SER	57.37	61.13							57.27	61.04						
60	ALA	52.31	18.06							52.18	18.11						
61	GLY	43.20								43.20							
62	PRO	61.88	31.72	25.41		48.73				61.74	31.66	25.46		48.64			
63	HIS																
64	PHE	55.40	36.80							55.48	37.22						
65	ASN	50.19	38.48							49.93	38.47						
66	PRO	63.36	29.64	26.35		47.09				63.26	30.05	26.56		47.08			
67	LEU	53.14	39.66	26.32		23.75	22.19			52.87	39.62	26.41		24.48	22.04		
68	SER	57.84	60.10							58.16	60.12						
69	ARG	53.04	26.61							53.05	26.50						
70	LYS	54.08	29.61	24.22		27.75		40.95		53.84	29.77	24.25		27.75		40.95	
71	HIS	54.29	30.67							54.33	30.71						
72	GLY	43.40								43.40							
73	GLY	43.30								43.30							
74	PRO	62.77	30.45	26.40		47.95				62.54	30.35	26.53		47.75			
75	LYS	53.44	29.85	23.07		25.51		41.65		53.69	29.53	22.36		25.70		41.19	
76	ASP	53.31	40.81							53.20	40.86						
77	GLU	58.09	28.46	35.05						58.03	28.46	35.17					
78	GLU	54.24	28.15	35.51						54.12	28.13	35.50					
79	ARG	54.43	26.62							54.19	26.44						
80	HIS	53.44	28.39							53.29	28.42						
81	VAL	66.27	29.56	22.67	20.87					66.22	29.74	22.17	20.62				
82	GLY	44.60								44.60							
83	ASP	56.16	39.36							56.63	39.48						
84	LEU	52.91	40.60	26.23		25.00	21.48			52.72	40.70	25.96		24.98	21.48		
85	GLY	45.00								45.00							
86	ASN	51.55	43.43							51.52	43.27						
87	VAL	58.17	31.55	20.66	16.23					57.93	31.56	20.74	16.14				
88	THR	60.44	69.01	20.71						60.63	68.58	20.83					
89	ALA	48.58	20.03							48.58	20.13						
90	ASP	51.31	41.04							51.31	41.04						
91	LYS	57.65	30.79	22.72		28.22		41.28		57.44	30.99	22.62		28.32		41.07	
92	ASP	53.39	40.51							53.28	40.45						
93	GLY	45.80								45.80							
94	VAL	60.83	30.85	20.53	19.99					60.53	30.73	20.56	20.06				
95	ALA	49.10	19.26							48.95	19.38						
96	ASP	53.11	40.32							53.11	40.32						
97	VAL	61.41	32.20	20.03	19.64					61.12	32.47	20.06	19.70				
98	SER	57.01	61.83							57.10	62.18						
99	ILE	59.33	43.41	26.87	16.56	14.15				59.12	43.82	26.77	16.58	14.15			
100	GLU	54.36	31.52	36.01						54.22	31.81	36.42					
101	ASP	53.57	46.15							53.48	46.12						
102	SER	57.11	63.22							57.42	63.28						
103	VAL	63.84	31.27	22.26	21.61					63.75	31.06	22.26	21.70				
104	ILE	62.50	39.31	23.20	18.87	13.42				62.15	39.19	23.12	18.58	13.52			
105	SER	54.32	64.62							54.58	64.60						
106	LEU	52.75	39.37	25.92		24.84				52.75	39.30	25.92		24.80			
107	SER	56.81	64.89							56.58	64.79						

108	GLY	44.00							44.00								
109	ASP	55.23	38.27						55.18	38.40							
110	HIS	52.54	26.67						52.45	26.68							
111	SER	56.62	63.04						56.94	62.91							
112	ILE	59.52	35.88	23.64	16.80	13.97			59.37	35.85	23.44	16.79	13.89				
113	ILE	60.44	34.07	26.59	17.38	10.28			60.37	34.16	26.85	17.74	10.66				
114	GLY	44.00							44.00								
115	ARG	53.82	26.04						53.75	26.12							
116	THR	61.60	70.15	23.31					61.61	69.90	23.64						
117	LEU	52.29	43.54	22.60		26.33	22.37		51.84	43.68	22.64		25.85	22.26			
118	VAL	60.37	33.82	21.41	19.67				60.37	33.79	21.42	19.75					
119	VAL	57.27	34.69	21.73	19.54				57.27	34.69	21.44	19.67					
120	HIS																
121	GLU	58.07	31.40	34.61		28.17			57.97	31.61	34.61						
122	LYS	52.67	33.96	23.80		28.14		41.24	52.62	34.10	23.80		28.14		40.97		
123	ALA	51.17	19.07						50.84	19.42							
124	ASP	55.31	41.66						55.28	41.61							
125	ASP	53.17	38.22						53.09	38.34							
126	LEU	54.02	36.83	24.79		24.27	20.71		53.80	36.73	24.79		24.27	20.56			
127	GLY	44.80							44.80								
128	LYS	53.72	32.17	24.53					53.93	32.37	24.54						
129	GLY	44.80							44.80								
130	GLY	45.00							45.00								
131	ASN	49.50	39.05						49.37	39.03							
132	GLU	57.79	28.62	34.86					57.65	28.70	34.93						
133	GLU	58.07	28.26	33.07					58.26	28.30	33.21						
134	SER	59.75	62.03						59.80	61.77							
135	THR	61.91	68.55	20.90					61.98	68.54	20.90						
136	LYS	57.91	34.63	23.75		28.44		41.13	57.85	34.63	24.12		28.44		41.13		
137	THR	59.43	71.40														
138	GLY	43.90							43.90								
139	ASN	55.45	35.89						55.25	36.02							
140	ALA	52.18	16.76						52.18	16.76							
141	GLY	44.70							44.70								
142	SER	59.10	62.88						59.10	62.88							
143	ARG	52.62	26.34						52.62	26.34							
144	LEU	55.68	41.78	25.72		27.42	20.27		55.48	41.70	25.65		27.48	20.65			
145	ALA	50.22	20.43						49.92	20.49							
146	CYS	53.68	46.48						53.66	46.37							
147	GLY	44.60							44.60								
148	VAL	61.86	31.21	20.56	20.22				61.71	31.35	20.56	20.36					
149	ILE	61.58	36.43	27.51	17.40	13.94			61.30	36.30	27.53	17.55	13.94				
150	GLY	42.10							42.10								
151	ILE	62.54	38.90	29.17	12.07	16.43			62.59	38.85	29.17	12.37	16.62				
152	ALA	48.96	20.88						48.94	20.85							
153	GLN	56.73	29.05	33.85					56.51	29.43	34.21						

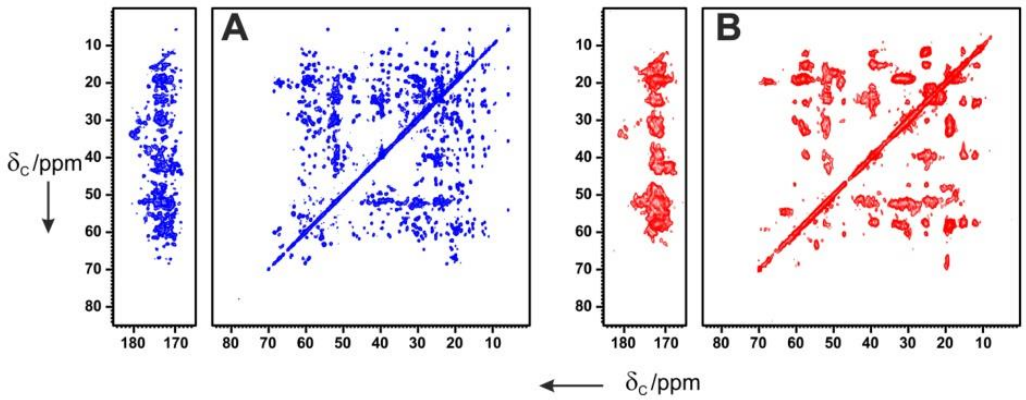

Figure S11. 2D ^{13}C-^{13}C correlation spectrum (DARR) of pelleted PEGylated SOD before (A) and after (B) a drastic treatment with denaturing agents (6 M guanidinium, 100 mM EDTA and 20 mM DTT).[23] The coating of SOD with PEG does not prevent the unfolding of the protein: the ^{13}C-^{13}C correlation spectrum of the guanidinium-treated sample shows the loss of dispersion of resonances typical of the folded structure of SOD. Interestingly, significant changes in ^{13}C chemical shifts are observed especially for the carbons of the side-chains of the Ile residues in the hydrophobic core.

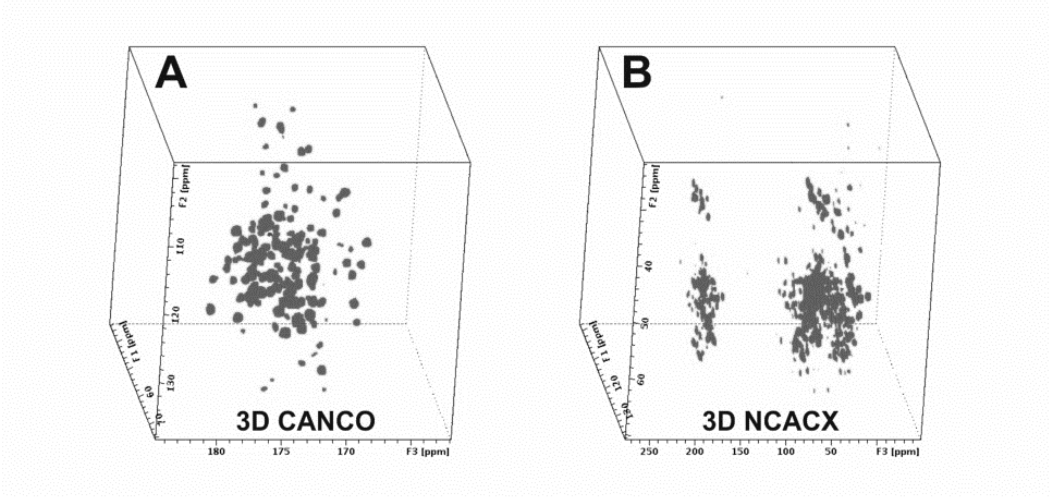

Figure S12. 3D CANCO and NCACX spectra performed on pelleted PEGylated L-asparaginase II. The experiments have been recorded on a Bruker Avance III 850 MHz wide-bore spectrometer (20.0 T, 213.7 MHz ^{13}C Larmor frequency) using a 3.2 mm DVT MAS probe head in triple-resonance mode in both cases. The MAS frequency ($\omega_r/2\pi$) was set to 14.0 kHz. Number of scans were 24 and 16 respectively, with interscan delay set to 2.2 s. From a preliminary peak picking of the 3D spectra 240 resolved spin systems out of 326 residues have been found (74%).

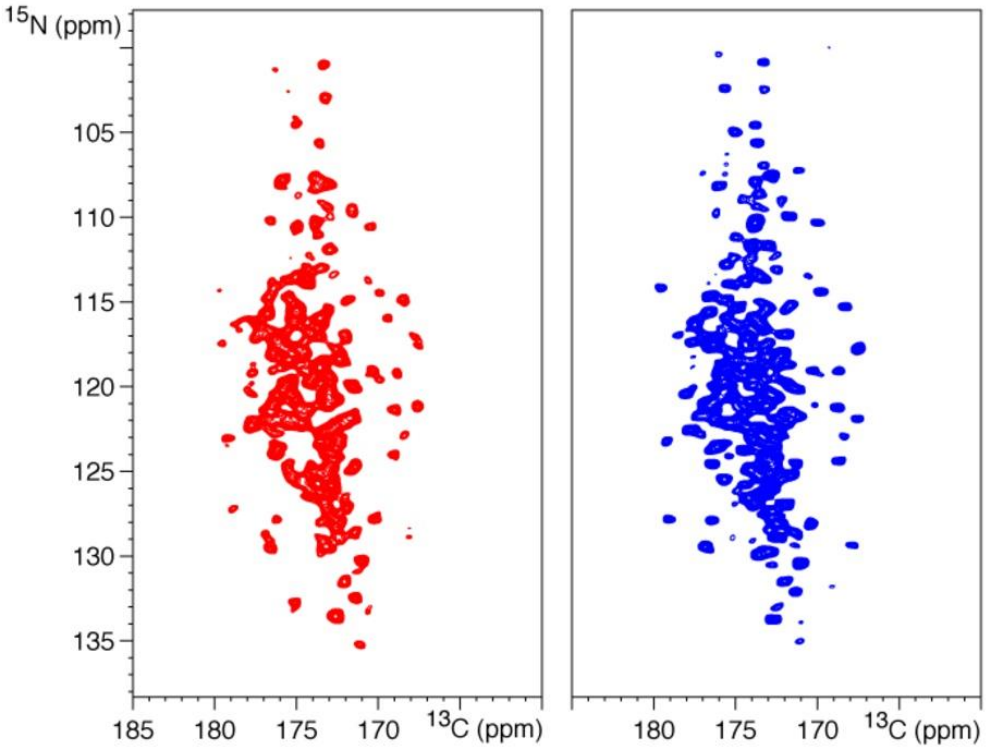

Figure S13. 2D NCO of crystalline native (red) and pelleted PEGylated L-asparaginase II (blue). The experiments have been recorded on a Bruker Avance III 850 MHz wide-bore spectrometer (20.0 T, 213.7 MHz ^{13}C Larmor frequency) using a 3.2 mm DVT MAS probe head in triple-resonance mode in both cases. The MAS frequency ($\omega_r/2\pi$) was set to 14.0 kHz. Number of scans was set to 64, interscan delay was set to 2.2 s.

References

[1] M. Galiñanes, Y. Qiu, A. Ezrin, D. J. Hearse, *Circulation* **1992**, *86*, 672–682.
[2] L. Banci, I. Bertini, F. Cantini, T. Kozyreva, C. Massagni, P. Palumaa, J. T. Rubino, K. Zovo, *Proc. Natl. Acad. Sci. U. S. A.* **2012**, *109*, 13555–13560.
[3] J. R. Lepock, H. E. Frey, R. A. Hallewell, *J. Biol. Chem.* **1990**, *265*, 21612–21618.
[4] H. E. Parge, R. A. Hallewell, J. A. Tainer, *Proc. Natl. Acad. Sci.* **1992**, *89*, 6109–6113.
[5] M. Fragai, C. Luchinat, G. Parigi, E. Ravera, *J. Biomol. NMR* **2013**, *57*, 155–166.
[6] K. Takegoshi, S. Nakamura, T. Terao, *J. Chem. Phys.* **2003**, *118*, 2325–2341.
[7] R. S. Thakur, N. D. Kurur, P. K. Madhu, *Chem. Phys. Lett.* **2006**, *426*, 459–463.
[8] S. D. Kennedy, R. G. Bryant, *Biopolymers* **1990**, *29*, 1801–1806.
[9] G. Jutz, P. van Rijn, B. Santos Miranda, A. Böker, *Chem. Rev.* **2015**, *115*, 1653–1701.
[10] E. C. Theil, P. Turano, V. Ghini, M. Allegrozzi, C. Bernacchioni, *J. Biol. Inorg. Chem. JBIC Publ. Soc. Biol. Inorg. Chem.* **2014**, *19*, 615–622.
[11] C. Bernacchioni, V. Ghini, C. Pozzi, F. Di Pisa, E. C. Theil, P. Turano, *ACS Chem. Biol.* **2014**, *9*, 2517–2525.
[12] E. C. Theil, P. Turano, V. Ghini, M. Allegrozzi, C. Bernacchioni, *J. Biol. Inorg. Chem. JBIC Publ. Soc. Biol. Inorg. Chem.* **2014**, *19*, 615–622.
[13] A. J. F. Siegert, *MIT Rad. Lab. Rep* **1943**.
[14] C. Montis, B. Castroflorio, M. Mendozza, A. Salvatore, D. Berti, P. Baglioni, *J. Colloid Interface Sci.* **2015**, *449*, 317–326.
[15] A. E. Bennett, R. G. Griffin, J. H. Ok, S. Vega, *J Chem Phys* **1992**, *96*, 8624–8627.
[16] X. Lu, C. Guo, G. Hou, T. Polenova, *J. Biomol. NMR* **2015**, *61*, 7–20.
[17] M. J. Knight, A. L. Webber, A. J. Pell, P. Guerry, E. Barbet-Massin, I. Bertini, I. C. Felli, L. Gonnelli, R. Pierattelli, L. Emsley, et al., *Angew. Chem. Int. Ed.* **2011**, *50*, 11697–11701.
[18] S. Laage, A. Lesage, L. Emsley, I. Bertini, I. C. Felli, R. Pierattelli, G. Pintacuda, *J. Am. Chem. Soc.* **2009**, *131*, 10816–10817.
[19] C. Pozzi, F. Di Pisa, S. Mangani, P. Turano, C. Bernacchioni, S. Ciambellotti, *Acta Crystallogr Biol Crystallogr* **n.d.**, *in press*.
[20] M. Kozak, D. Borek, R. Janowski, M. Jaskólski, *Acta Crystallogr. Sect. D* **2002**, *58*, 130–132.
[21] A. L. Swain, M. Jaskólski, D. Housset, J. K. Rao, A. Wlodawer, *Proc. Natl. Acad. Sci. U. S. A.* **1993**, *90*, 1474–1478.
[22] G. Pintacuda, N. Giraud, R. Pierattelli, A. Böckmann, I. Bertini, L. Emsley, *Angew. Chem. Int. Ed.* **2007**, *46*, 1079–1082.
[23] M. Assfalg, L. Banci, I. Bertini, P. Turano, P. R. Vasos, *J. Mol. Biol.* **2003**, *330*, 145–158.

Annex V

Working draft

"Spectral Investigation of the NAMI A - ferritin system"

(Tentative list of authors in alphabetic order)

C. Bernacchioni[a,b], S. Ciambellotti[a,b], A. Pratesi[a], F. Scaletti[a] and P. Turano[a,b]

[a] Department of Chemistry, University of Florence, via della Lastruccia 3, Sesto Fiorentino, (FI) – Italy.
[b] Center for Magnetic Resonance, University of Florence, Via L. Sacconi 6, Sesto Fiorentino, (FI) – Italy

Abstract

The interaction of the antimetastatic ruthenium drug NAMI A with ferritin was investigated to prepare NAMI A/ ferritin adducts with improved pharmacological performances. We observed that the presence of ferritin increases the rate of NAMI A hydrolysis; the resulting Ru species bind the protein at various molar ratios and relatively tight ruthenium/ferritin adducts are formed that may be separated and characterized. Distinct spectral features are observed for NAMI A /HuLF and NAMI A/HuHF adducts; the latter shows a characteristic CD spectrum. We also found that NAMI A produces a large inhibition of ferritin's ferroxidase activity probably due to direct competition with iron ions at the catalytic site. The implications of these results are discussed.

Introduction

NAMI A is a well known ruthenium(III) medicinal compound showing attractive anticancer properties. NAMI A is commonly considered as a scarcely cytotoxic agent but manifests relevant antimetastatic properties both *in vitro* and *in vivo*. The latter properties were described in detail by Gianni Sava and coworkers through a number of research articles (1, 2). Owing to its favorable pharmacological profile NAMI A was eventually admitted to clinical trials (3).

As NAMI A is a quite reactive species that may undergo progressive and relatively rapid transformations, both in the blood and in tissues, before entering cells, we wondered whether it is possible to prepare NAMI A constructs that might protect the drug from transformation reactions for a longer time and/or might improve its uptake and/or pharmacological profile.

To this end, we decided to study the reaction of NAMI A with ferritin. Ferritin is one of the main players in iron metabolism. The biological role of ferritin is the storage of ferric ions within its cavity under the form of a hydrated ferric oxide biomineral, thus preventing the uncontrolled accumulation of toxic iron species inside cells. Ferritins are polymers constituted by 24 subunits that self-assemble giving rise to an almost spherical nanocage. The ferritin cage has 2,3,4-fold symmetry (C2, C3 and C4 symmetry axes). The exterior and interior of the cage are connected via channels along C3 and C4 symmetry axes at subunit junctions. Mammalian ferritins are heteropolymeric twentyfour-mers formed by heavy chain (H) and light chain (L) subunits in a tissue specific ratio according to cell needs. All subunits share a common fold: a bundle of four antiparallel helices H1-H4, a fifth short helix H5 and a long solvent-exposed loop connecting H2 and H3. The H-subunit contains a binuclear ferroxidase center that catalyzes iron(II) oxidation. This antioxidant activity consumes iron(II) and dioxygen or hydrogen peroxide, the reagents that produce toxic free radicals in the Fenton reaction. The ferric products that form at the ferroxidase center are precursors of the

biomineral. On the contrary, the L-subunits lack enzymatic activity; yet they are still able to store iron as a caged biomineral, although biomineralization proceeds at a slower rate. The L subunit contains a high number of carboxyl groups lining the ferritin cavity, which have been identified as iron nucleation sites.

Ferritin has been also exploited as a drug delivery system due to the fact that cells have the natural ability to recognize and incorporate exogenous ferritin by specific receptors recently discovered. In particular, H-ferritin is recognized by the TfR1 (Transferrin receptor 1)(4) while L-ferritin by SCARA5 (Scavenger receptor class A type 5)(5), both overexpressed in specific tumor cells.

In our study NAMI A was incubated with ferritin and the resulting NAMI A/ferritin adducts were characterized and then tested for biological activity. Notably as ruthenium(III) ions originating from NAMI A degradation mimic quite closely iron(III) ions, we decided to explore whether NAMI A inhibits the physiological function of ferritin and elucidate the underlying molecular mechanism of this inhibition.

Materials and methods

Protein expression and purification. Genes encoding HuHf and HuLf subcloned in pET-9a and pET-21c vectors (the latter is a gift by prof. S. Torti) (6) respectively, were transformed into E. coli BL21(DE3) pLysS competent cells. Bacteria were cultured in rich medium (LB) containing 50 mg/L of kanamycin or 100 mg/L of ampicillin and 34 mg/L of chloramphenicol at 37°C. HuHf was produced and purified as previously described (7, 8). Similarly, when A_{600nm} reached 0.6-0.8, the over-expression of HuLf was induced with 0.2 mM IPTG, shifting the incubation temperature to 17°C for 48 hours. The cells were harvested (7500 rpm for 15 minutes) and resuspended in 20 mM Tris-HCl pH 7.5. Lysis of cells was performed by sonication. The crude lysate was clarified by ultra-centrifugation (40,000 rpm for 40 minutes) and the soluble fraction heated at 65°C for 15 minutes to precipitate undesirable proteins (40,000 rpm for 15 minutes). Subsequently, the supernatant was dialyzed against 20 mM Tris-HCl pH 7.5 buffer and loaded into a Q-Sepharose column eluting the containing protein sample with a linear NaCl gradient (0-1 M) in 20 mM Tris-HCl pH 7.5. Next, fractions with ferritin (identified with SDS-PAGE analysis) were pooled and further purified with a size exclusion chromatography (HiLoad 16/60 Superdex 200 column). Iron and other metal ions were removed by four dialysis steps using 4 L each of 20 mM Tris-HCl, 3 mM EDTA, ammonium thioglycolate (1:400), pH 7.5 buffer to reduce and chelate the iron, followed by four dialysis steps against 4 L each of 20 mM Tris-HCl pH 7.5. Differently from HuHf, HuLf required ammonium sulfate precipitation (70% of saturation) followed by extensive dialysis in 20 mM Tris-HCl pH 7.5, before the anionic exchange column.

Spectrophotometric studies. HuHf and HuLf (50 µM in subunits) were incubated with freshly prepared solutions of NAMI A at different molar ratios (1:2, 1:4, 1:8) in phosphate buffer (50 mM sodium phosphate, 100 mM NaCl, pH 7.4). The hydrolysis experiments, both in presence of proteins or with NAMI A alone, were monitored spectrophotometrically at room temperature over 24 hours. The electronic spectra were acquired with a Varian Cary 50 Bio UV-vis spectrophotometer.

Circular dichroism analysis. CD spectra to assess the formation of protein/NAMI A adducts were performed with a Jasco J-810 spectropolarimeter at 25°C. Samples of pre-incubated HuHf (protein concentration: 5 mM in subunits) with 2 equivalents of NAMI A were ultra-filtered before the analysis. The mean of 5 accumulations, in the range of 300 and 700 nm wavelengths were calculated by subtraction of the buffer spectrum. CD data were obtained using a scanning speed set at 200 nm/min, band width and data pitch of 0.5 nm; temperature was maintained constant through the Jasco Peltier apparatus.

Enzymatic activity measurements. After making the ferritin apo, single turnover oxidoreductase kinetic (2 Fe^{2+} ions per subunit) was monitored. Changes in absorbance at 650 nm (diferric-peroxo or DFP) or at 350 nm (diferric oxo/hydroxo species; DFO(H)) were acquired after rapid mixing (< 10 ms) of equal volume of 100 µM HuHf as subunit (native or ruthenated ferritin with 2 NAMI A molecules per protein monomer) in 200 mM MOPS, 200 mM NaCl, pH 7.0, with freshly prepared solutions of 200 µM ferrous sulfate in 1 mM HCl, in a UV/visible, stopped-flow spectrophotometer (SX.18MV stopped-flow reaction analyzer, Applied Photophysics). Routinely, 4000 data points were collected during the first 5 s. Initial rates of DFP and DFO(H) species formation were determined using data from three independent analyses through the linear fitting of the initial phases of absorbance changes at 650 and 350 nm traces (0.01− 0.03 s).

Results

The reaction of NAMI A with ferritin: spectrophotometric profiles.

Due to the characteristic absorption bands in the UV-visible region, the solution behavior of NAMI A can be followed spectrophotometrically (9). In particular, we analyzed the interaction of different amounts of NAMI A with human ferritins in phosphate buffer (50 mM sodium phosphate, 100 mM NaCl, pH 7.4) over 24 hours of incubation at room temperature. The typical spectral profile of NAMI A alone in solution is characterized by the absorption band centered at 390 nm that progressively disappears, meaning that the first chloride group is lost and replaced by a water molecule. At this point, the increase in absorbance at 340 nm is noticed followed by a decrease when the second chloride ligand is released and the second aquation occurs (9) (Fig. 1).

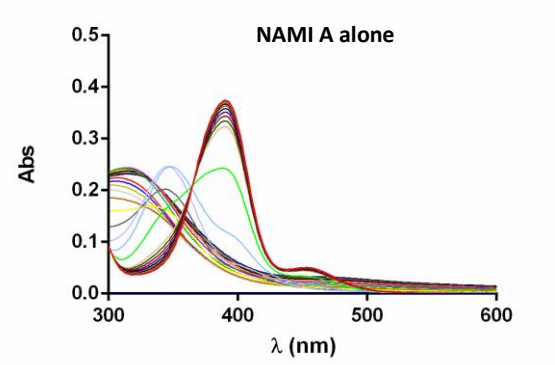

Figure 5. Spectral evolution of NAMI A alone. Time-course UV-vis spectra of the hydrolysis of NAMI A alone (NAMI A concentration: 100 µM) dissolved in 50 mM NaPi and 100 mM NaCl, pH 7.4. Spectra were recorded over 24 hours at room temperature.

The same time dependent profile is still present in the spectra acquired in the presence of ferritins (Fig. 2). The hydrolysis of NAMI A with human H ferritin (HuHf) occurred faster with respect to NAMI A alone even after few minutes of incubation. More interestingly, with 2 equivalents of NAMI-A, we could detect the appearance of a new transition around 500 nm, after the two aquation processes, not referable to NAMI A or protein alone peaks. This change in the spectrum was in agreement with the shifted color of the solution from pale yellow once NAMI A was added to red/brown at the end of the exposure.

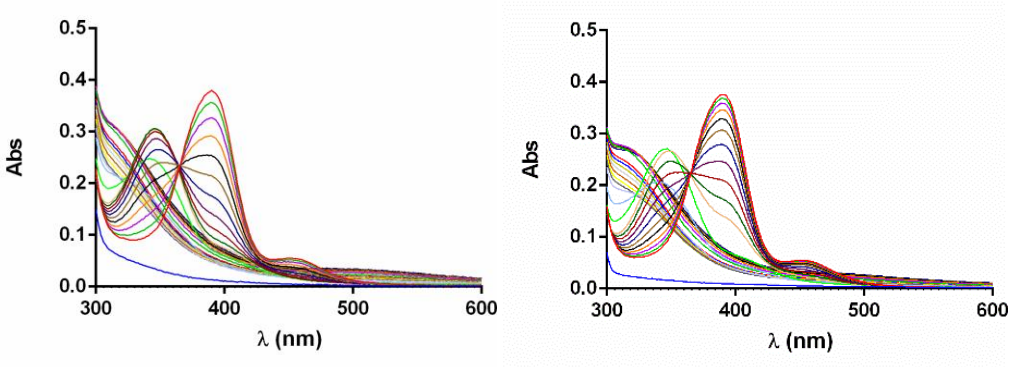

Figure 2. Spectral evolution of NAMI A in presence of ferritins. Time-course UV-vis spectra of the hydrolysis of NAMI A in presence of HuHf (1:2 molar ratio, protein concentration 50 µM in subunits; in the middle) and HuLf incubated with 2 NAMI A per subunits (1:2 molar ratio, protein concentration 50 µM in subunits; on the right) dissolved in 50 mM PB and 100 mM NaCl, pH 7.4. Spectra were recorded over 24 hours at room temperature.

On the contrary, in the reaction with HuLf, the hydrolysis seemed to proceed in the same way as the molecule alone in solution. Moreover, the UV-vis spectra with the L isoform did not evolve in the progressive exhibition of the band around 500 nm.

Recovery of the NAMI A-ferritin adduct, separation and CD characterization.

At the end of the process, samples were extensively ultra-filtered to remove the excess of non-reacted compound. Electronic spectra were repeated on the filtered and on the flow-through fractions confirming that ruthenium was associated to the protein, as shown from the still present transition in the visible region (Fig.3).

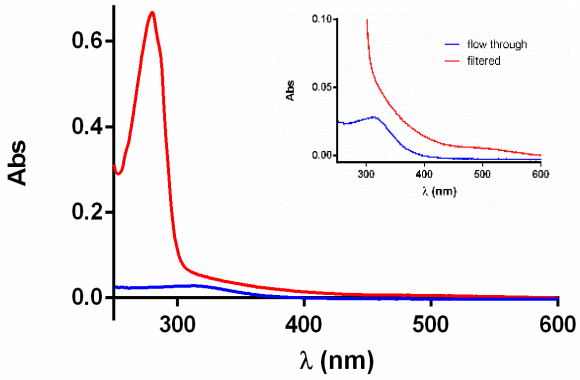

Figure 3. Electronic spectra of ultra-filtered HuHf/NAMI A sample. Analysis of filtered sample (curve in red) and flow-through fraction (curve in blue).

In order to characterize deeply the final NAMI A/H-ferritin complex, we performed also circular dichroism analysis in the range of wavelengths from 300 to 700 nm after 24 hours of treatment. The CD spectrum revealed two bands: the first one is positive and centered at 360 nm and the second one around 500 nm is negative (Fig. 4).

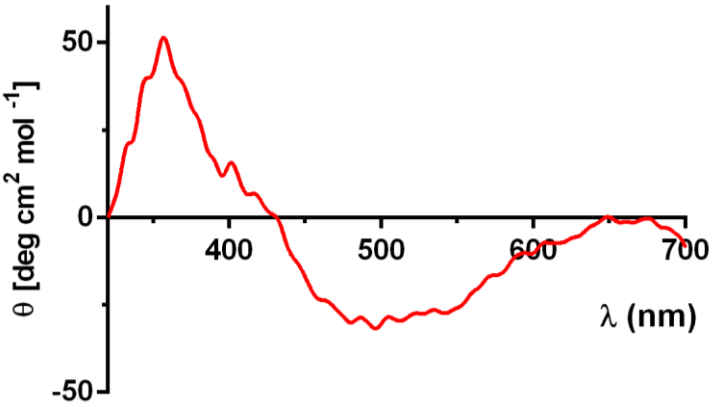

Figure 4. CD analysis of HuHf/NAMI A. CD spectra of HuHf pre-incubated with 2 equivalents of NAMI A for 24 hours. (Protein concentration: 5 mM in subunits). The negative absorption around 500nm confirmed the presence of a NAMI A/HuHf adduct.

ICP-AES analysis on HuHf-NAMI A adducts showed an increased amount of Ru-species linearly proportional to the quantity of NAMI A incubated with the protein. This indicated that HuHf seemed still able to host other Ru-species upon the addition of 8 equivalents per subunits (data not shown).

Inhibition of the ferroxidase activity in HuHf.

Since ruthenium is similar to iron and can use the metabolic routes of iron, we hypothesized that it could enter the cage from the same channels and reach the iron binding sites. Thus, we wondered the possible effect of ruthenation on the enzymatic activity on homopolymers of HuHf, the subunit that contains the catalytic site for iron oxidation. In order to evaluate how Ru-metalation could affect the uptake and oxidation of iron ions, HuHf was incubated with NAMI A at 1:2 molar ratio (HuHf 100 µM in subunits) and the kinetic of iron oxidation of ruthenated ferritin (Ru-HuHf) was monitored by stopped-flow spectrophotometry. In other words, we added two molecule of NAMI A per subunit, since ferritin subunits contain 2 ferroxidase sites each. The initial rates of formation of DFP (A_{650nm}) and DFO(H) (A_{350nm}) species for the native protein and for Ru-HuHf (Table. 1) were calculated as the changes in absorbance in the first milliseconds of traces at 650 nm and 350 nm (Fig. 5). In order to compare wild type HuHf with Ru-HuHf, subtraction of the blank curve with NAMI A alone was applied. We observed a notable inhibition of the ferroxidase activity in the case of Ru-HuHf, both in the formation of ferric oxo species and DFP (Tab. 1).

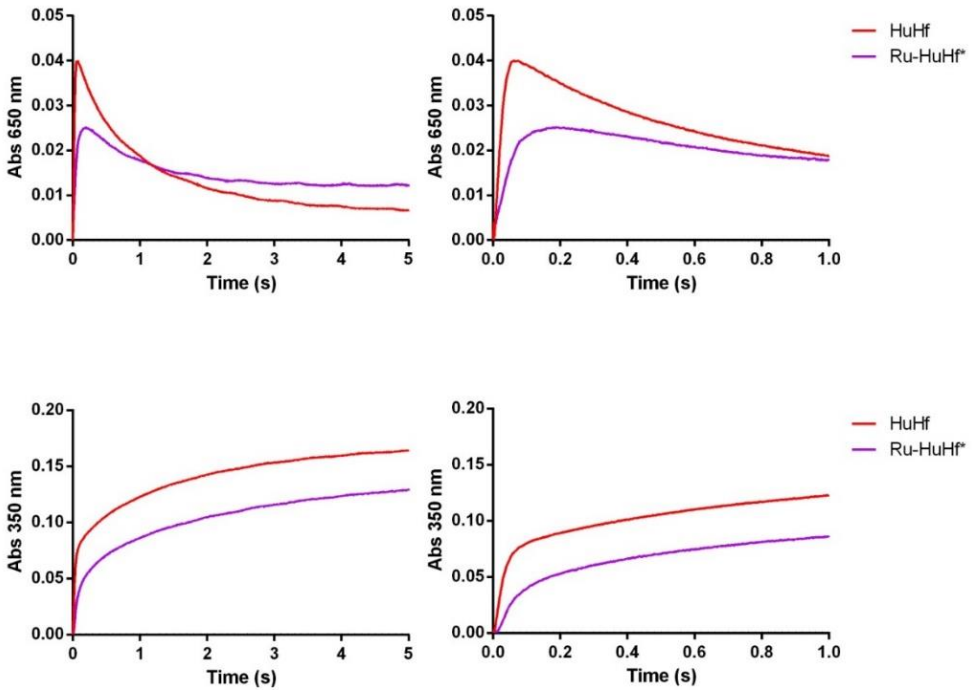

Figure 5. Kinetics of products formation in WT HuHf and Ru-HuHf proteins. Reaction progress of DFP (Abs 650 nm) and DFO(H) (Abs 350 nm) formation measured by stopped-flow spectrophotometer (mean ± SEM). The panels on the left represent plot of the changes in absorbance during 5 seconds, while the panels on the right show an enlargement of the first second of the reaction to highlight the differences in the initial rates. * The NAMI A absorbance values have been subtracted.

	wt HuHf	Ru(III)- HuHf*	% of inhibition
$\Delta A_{650nm}/\Delta t$	1,053 ± 0,061	0,420 ± 0,032*	70
$\Delta A_{350nm}/\Delta t$	1,809 ± 0,008	0,527 ± 0,120*	60

Table 3. Catalytic reaction rates. Initial rates of DFP formation ($\Delta A_{650\ nm}/\Delta t$) and of DFO(H) species ($\Delta A_{350\ nm}/\Delta t$) are showed as mean values from two independent analysis with SEM (standard error of the mean). The percentage of inhibition of the ruthenated protein with respect to wild type are listed. *The NAMI Absorbance values has been subtracted.

Conclusions

Thanks to characteristic time dependent changes of spectral profile in the UV-visible region, we could detect differences in the hydrolysis process of NAMI A attributable to the presence of the protein. In particular the rate of hydrolysis appears to be accelerated by HuHf while the presence of HuLf does not determine significant changes. The formation of a Ru-adduct with HuHf was established by UV-visible and circular dichroism spectroscopies, as well as by kinetic measurements that showed inhibition of the ferroxidase activity of HuHf. Crystallization trials failed till now, preventing to find out the exact localization of ruthenium binding site(s) inside ferritin. Nevertheless, the observed inhibition of the ferroxidase activity in HuHf and the different behavior between HuHf and HuLf strongly supports Ru-binding at the ferroxidase center.

Reference List

1. Bergamo A, Riedel T, Dyson PJ, Sava G (2015) Preclinical combination therapy of the investigational drug NAMI-A(+) with doxorubicin for mammary cancer. *Invest New Drugs* **33**:53-63.

2. Bacac M, Vadori M, Sava G, Pacor S (2004) Cocultures of metastatic and host immune cells: selective effects of NAMI-A for tumor cells. *Cancer Immunol. Immunother.* **53**:1101-1110.

3. Leijen S *et al.* (2015) Phase I/II study with ruthenium compound NAMI-A and gemcitabine in patients with non-small cell lung cancer after first line therapy. *Invest New Drugs* **33**:201-214.

4. Li L *et al.* (2010) Binding and uptake of H-ferritin are mediated by human transferrin receptor-1. *Proc. Natl. Acad. Sci. U. S. A* **107**:3505-3510.

5. Li JY *et al.* (2009) Scara5 is a ferritin receptor mediating non-transferrin iron delivery. *Dev. Cell* **16**:35-46.

6. Rucker P, Torti FM, Torti SV (1997) Recombinant ferritin: modulation of subunit stoichiometry in bacterial expression systems. *Protein Eng.* **10**:967-973.

7. Pozzi C *et al.* (2015) Iron bindind to human heavy-chain ferritin. *Acta Crystallogr D Biol Crystallogr* **71**:1909-1920.

8. Ravera E *et al.* (2016) Solid-state NMR of PEGylated proteins. *Angew. Chem. Int. Ed* **55**:1-5.

9. Sava G, Pacor S, Mestroni G, Alessio E (1992) Na[trans-RuCl4(DMSO)Im], a metal complex of ruthenium with antimetastatic properties. *Clin. Exp. Metastasis* **10**:273-280.

Annex VI

Working draft

"Ferritinoxis: a route to induce cancer cell death by the administration of ferritins"

J.C. Cutrin[a], D. Alberti[a], G. Gonella[a], C. Bernacchioni[b], S. Ciambellotti[b], P. Turano[b], C. Luchinat[b], S. Geninatti Crich[a] and S. Aime[a]

[a]Department of Molecular Biotechnology and Health Sciences, University of Torino, via Nizza 52, Torino, Italy.

[b]Center for Magnetic Resonance, University of Florence, Via L. Sacconi 6, Sesto Fiorentino, (FI) – Italy and Department of Chemistry, University of Florence, via della Lastruccia 3, Sesto Fiorentino, (FI) – Italy.

Abstract

TfR-1 mediated cellular uptake of human H-ferritin loaded with 50 or 350 iron ions, without any additional modifications, results in a high cytotoxicity on HeLa cells. At variance, L-ferritin, which is internalized through the SCARA5 receptor, is significantly less toxic, even when loaded with 1000 iron ions. We propose here that the different cytotoxicity of the two ferritin cages originates from the presence in H-ferritin of a pool of non-biomineralized iron ions bound at the ferroxidase catalytic sites of H-ferritin subunits. This iron pool is readily released during the endosomal-mediated H-ferritin internalization and is more prone to redox reactions with consequent ROS production causing toxicity.

Introduction

Ferritin is a protein highly conserved in all living forms, which stores iron in a bioavailable form. In animals, the 24-meric cage structure is assembled from two subunits, the heavy chain (H-chain) and light chain (L-chain) protein, or a mix thereof. The two distinct subunits share a similar fold and 53 % of sequence identity, but differ in their ability to handle iron. H-subunits contain a catalytic center (ferroxidase or oxidoreductase site) where iron(II) is oxidized to iron(II) by dioxygen on the millisecond time scale. L-subunits lack the ferroxidase site; iron oxidation in L-type cages occurs on a time scale of the order of minutes and the protein mainly provide a shell to maintain the ferric oxide biomineral in a soluble form.

The demineralized form of L-type ferritin (apoferritin) has been used for cellular delivery. More recently the selective ability of cells to internalized L- and H-cages through specific receptors has been demonstrated.

Results

Iron-loaded ferritins are toxic for HeLa cells.

To compare the effect of H- and L-ferritin on tumor cells, we sought a tumor cell model that expresses both TfR1 and SCARA5 receptors, which have been demonstrated to act for the internalization of H- and L- cages, respectively. The choice of HeLa cells allows us to compare the behavior of the two proteins in the same cell line. In literature, a plethora of nanocarriers encapsulating different species within the natural horse spleen cage is available, as recently reviewed in (1). This cage has the advantage of being commercially available and can be considered a model of L-cages, as it contains only about 10% of H subunits. Horse spleen nanocages will be referred to as L-ferritin, hereafter. They have been studied in their apo form (apo L-ferritin) and loaded with an average of 1000 iron ions/cage (L-ferritin1000), as determined by ICP-MS from the commercially available iron-loaded protein.

Recently the human H-ferritin has been proposed as a potentially superior carrier for anticancer drug delivery because, given its human origin, it should not activate inflammatory or immunological response (2). Efficient heterologous expression methods for human H-ferritin ($\geq$100 mg/L of purified protein, in our hands) (3, 4) make it attractive also from the

economical point of view. H-ferritin can be loaded with variable amounts of iron. The first 2 iron ions/subunit localize in the ferroxidase site; addition of more iron ions initiates the biomineralization reaction. Here, we investigated two differently iron-loaded H-ferritin cages:

i) one containing about 50 iron ions per cage (H-ferritin50, hereafter), which corresponds to the complete population of the 24 ferroxidase sites;

ii) the other containing 350 iron ions per cage (H-ferritin350, hereafter), which corresponds to fully populated ferroxidase site plus formation of a biomineral core (expected size of the biomineral 5 nm, according to previous TEM analyses) (3).

The amount of iron internalized by HeLa cells upon 24 h incubation in media containing variable amount of H- and L-ferritin was obtained by ICP-MS determination of the intracellular iron content (Fig. 1A). The relative amount of internalized iron when using H-ferritin350 and L-ferritin1000 roughly correlates with the iron loading of the two cages. The amount of internalized iron after treatment with H-ferritin50 in the 1-8 μM range was too low to be determined with sufficient accuracy.

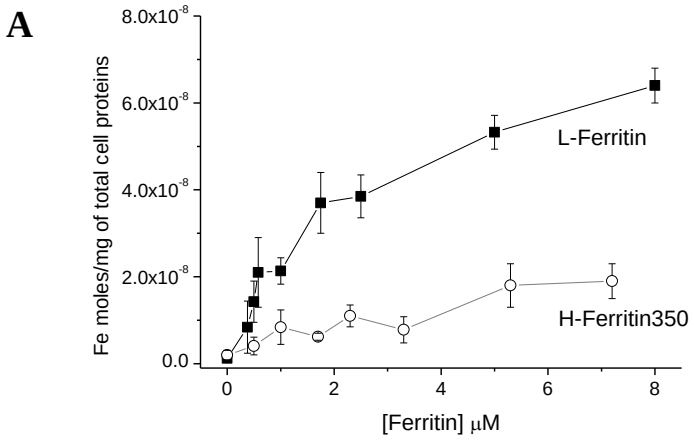

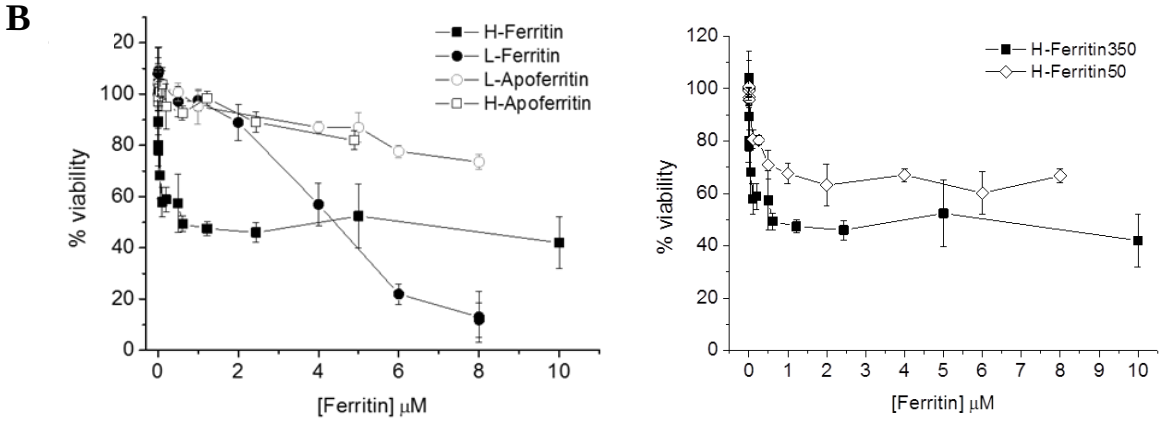

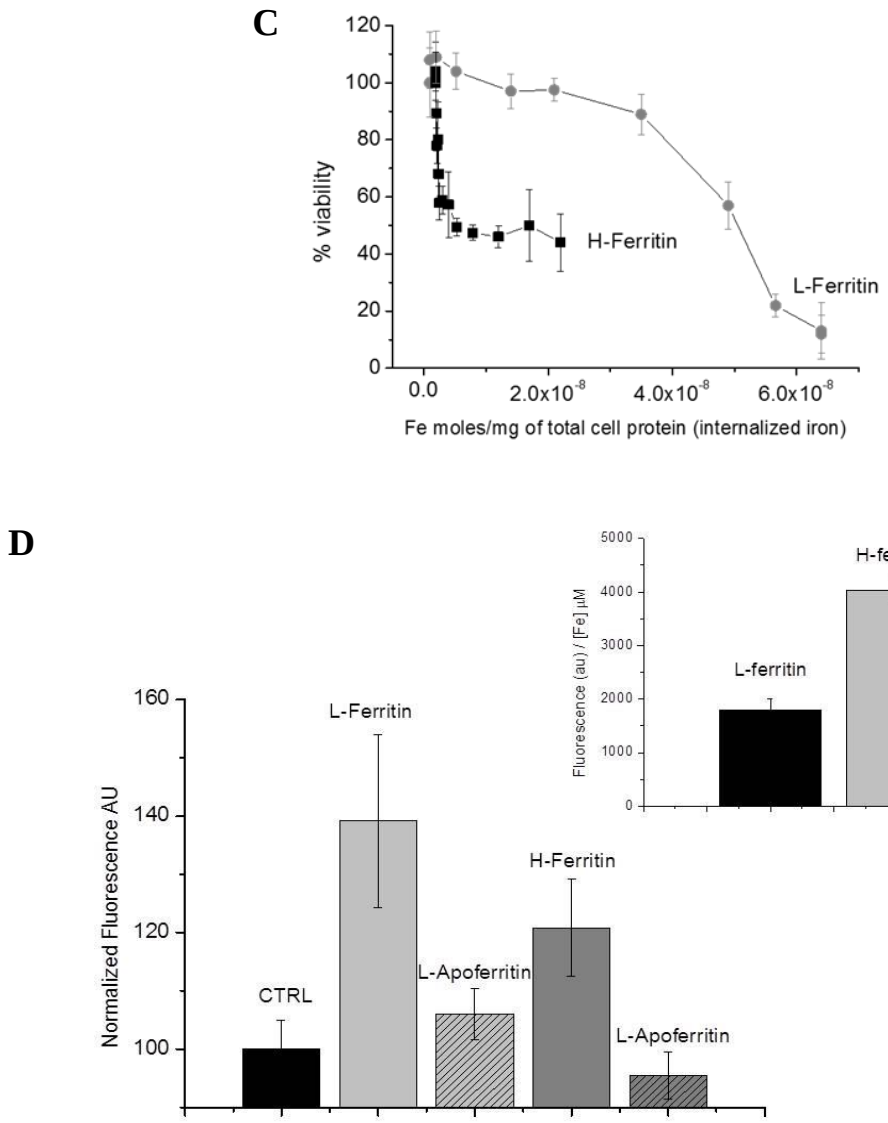

Figure 1. A) Incubation of HeLa cells with increasing amounts of L-Ferritin (■) and H-Ferritin (○) for 24 h. After incubation, cell lysates were analyzed by ICP-MS to measure the amount of internalized iron that was normalized to the total protein cellular content, which in turn, is directly proportional to the cell number. Error bars indicated standard deviation of the data. **B**) On the left, dose-dependent L- and H- Ferritin effects on HeLa cell viability measured by MTT assay; on the right, dose-dependent H-Ferritin50 and H-Ferritin350 effects on HeLa cell viability measured by MTT assay. **C**) HeLa cell viability measured by the MTT assay is reported as a function of the amount of internalized iron measured by ICP-MS normalized on the total protein cellular content (directly proportional to the cell number). In all experiments, cell viability was expressed as percentage relative to untreated cells. Data are presented as mean and SD of at least three independent experiments. **D**) ROS generation measured by DCFDA fluorescence emission (at 529 nm) after the incubation, for 24 h, of HeLa cells with 3µM apo and iron-loaded H- or L- Ferritin, respectively. Fluorescence emission was normalized to the internalized iron concentration (µM).

Cell viability was determined by MTT assay after treatment of HeLa cells for 24 h with apo and iron-loaded H- and L-ferritins. While both apo forms do not show any appreciable toxicity, a clear effect is induced by the iron-loaded cages (Fig. 1B). The profiles of cellular cytotoxicity induced by the H- and L-cages are profoundly different. The L-induced effect is almost linearly dependent on the protein concentration. On the contrary, treatment with H-ferritin50 and H-ferritin350 causes an abrupt decrease in cellular viability, which levels off at about 50% viability for ferritin concentrations $\geq$ 1 μM ferritin. The attainment of a plateau value in cell viability for both iron-loaded H-ferritin nanocages can be interpreted in terms of iron-dependent downregulation of the Trf1 receptor expression; a well-known process in case of incubation of HeLa with an excess of holo-transferrin or Fe-citrate (5, 6). A flow cytometric analysis of the expression of TfR1 showed that the relative expression of this receptor with respect to untreated Hela cells decreases to 59% for cells treated with 1 μM H-ferritin350 and to 74% with 1 μM H-ferritin50, suggesting that also iron-loaded H-ferritins activate a downregulation mechanism. No evidence has yet been reported of an iron-dependent downregulation of SCARA5 expression, consistently with the lack of saturation effects in cytotoxicity when using L-ferritin1000. In spite of the larger intracellular iron internalization induced by L-ferritin-1000 with respect to H-ferritin350, the latter is much more toxic at lower protein concentrations. As illustrated in Fig. 1C, for a given iron concentration H-ferritin350 causes significantly larger reduction in cell viability, suggesting a different mechanism of action for H- and L-cages. Noteworthy, the difference in the cytotoxic effect exerted by treatment with H-ferritin50 and H-ferritin350 is smaller than expected on the basis of the cage iron content (Fig. 1B). This result suggests that the nature of the iron ions within the cage (ferroxidase-bound or biomineralized) might play a role. This aspect is further investigated in the following sections.

Cytoplasmic ROS production was evaluated by measuring 2,7-Dichlorofluorescein diacetate (DCFDA) emission; its fluorescence intensity directly correlates with the steady-state concentration of intracellular ROS. The treatment with iron-loaded ferritins causes a significant increase in ROS production with respect to untreated cells and cells treated with the apo-ferritins (Fig. 1D). ROS generation normalized to the iron intracellular content for L-ferritin1000 and H-ferritin350 was significantly higher for the latter. In conclusion, ROS production requires iron internalization into the cell, but it is not simply proportional to the metal concentration.

The role of the TfR1 receptor and endosomal uptake.

As reported (7), TfR1-imported H-ferritin is mainly localized in endosomes, following a pathway that resembles that of transferrin. We used confocal microscopy to demonstrate the different intracellular localization for rhodamine labeled L- and H-Ferritins. The former, indeed, colocalizes with the lysosomal specific marker Lamp-1, whereas only a small fraction of rhodamine labeled H-Ferritin is localized in the lysosomal compartment (Fig. 2A). Consistently, the cytotoxic effect of L-ferritin1000 is significantly reduced when the MTT assay was conducted in the presence of DFO mesylate, a lysosomal iron chelator, but is not

affected by chloroquine (CHL), an agent that limits endosomal acidification. The opposite behavior is observed for H-ferritin350, where CHL essentially abolishes its cytotoxic effect (Fig. 2B). Mature endosomes are characterized by a low pH value (4.9-6.0) (8). In order to get more insights on the mechanism of iron internalization into HeLa cells, we tested *in vitro* the ability of H- and L-ferritins to release iron as a function of pH. As shown in Fig. 2C, while iron release at neutral pH values requires the presence of reducing agents, in H-ferritin350 (but not in L-ferritin1000) iron release spontaneously occurs at pH 5.0. The amount of released iron corresponds to about 16% of the total iron content in the H-ferritin350 cage i.e. roughly 50 iron ions.

A

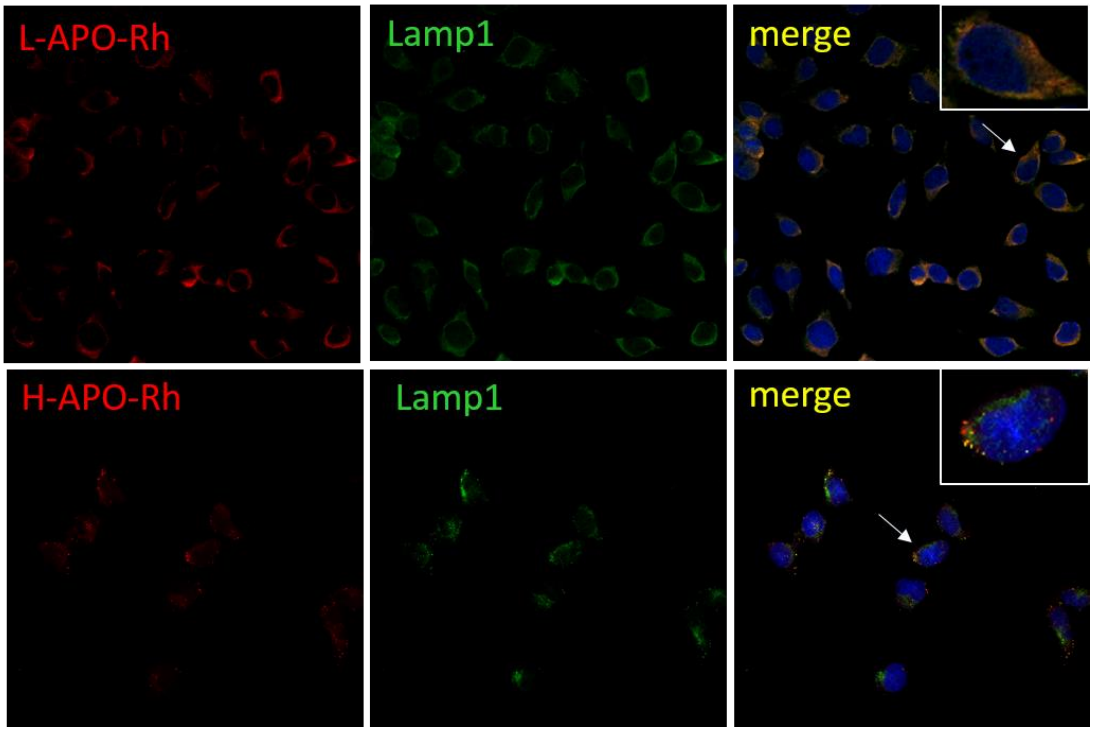

B

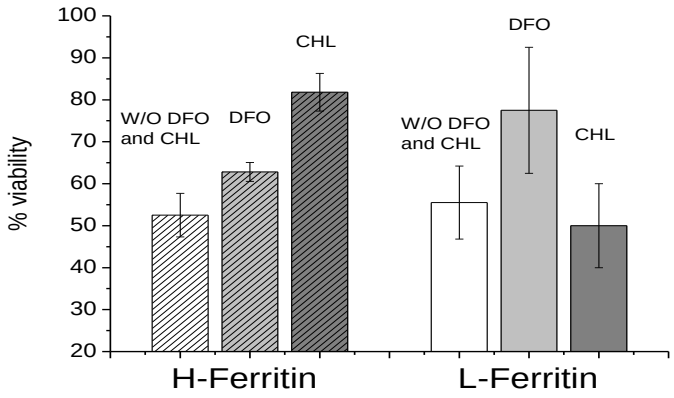

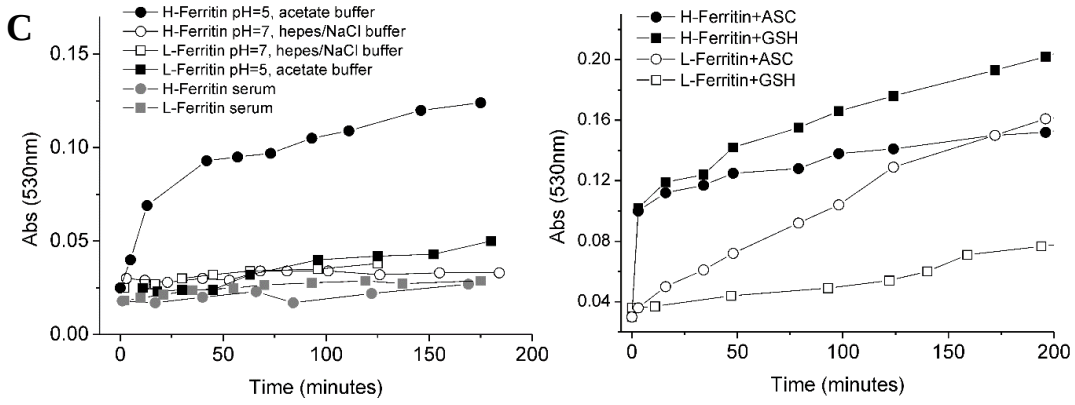

Figure 2. A) Confocal Microscopy Representative images of HeLa cells incubated for 3 h with H- or L-APO-Rhod (red) and stained with an anti-LAMP-1 antibody (green). Nuclei were counterstained with DAPI (blue). Arrows indicates the enlarged cells in the upper right panel. **B**) HeLa cell viability measured by the MTT assay after 24 of incubation with H-Ferritin350 (0.5 μM) or L-Ferritin (2.5 μM) in the absence and in the presence of (DFO mesylate) 150 μM and Chloroquine (100 μM). **C**) Reductive mobilization of iron from 0.2 μM iron loaded H- and L- Ferritin in different media(on the left) and (on the right) in the presence of GSH (0.25 mM, pH=7), ASC (0.25 mM, pH=7) upon incubation in the presence of bipyridyl (1 mM) under aerobic conditions. T=0 corresponds to the instant after the addition of ferritin.

After 3h incubation of HeLa cells in the presence of L- or H-Ferritin 2.5 and 1 μM, respectively, double membrane structures with the morphological features of endosomes enclosing electron-dense amorphous material compatible with hemosiderin bodies were observed only in the cells incubated with L-ferritin (Fig. 3).

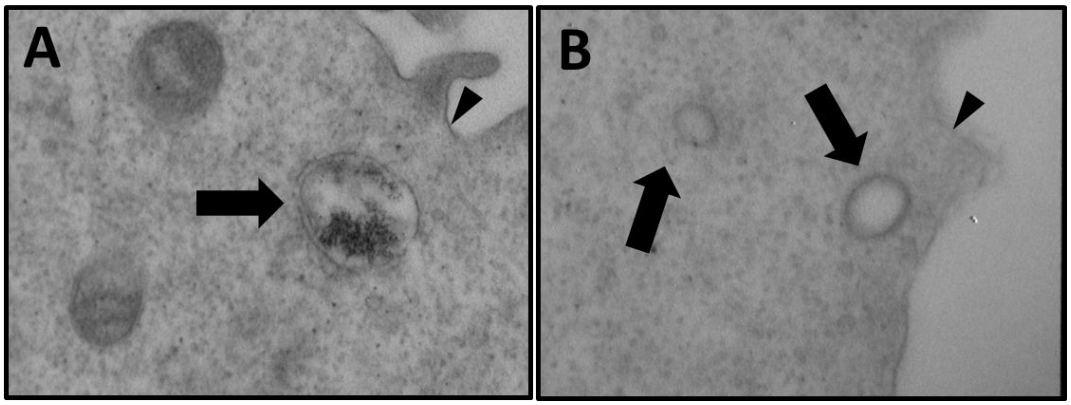

Figure 3. T.E.M. photos of Hela cells treated with L-ferritin (A) and H-ferritin350 (B) (see material and methods for details). Arrows indicate representative endosomes. Only after L-Ferritin incubation (A) endosomes contain hemosiderin bodies. The arrowhead signs correspond to the plasma membrane (x30.000, lead citrate and uranyl acetate stained)

These hemosiderin bodies have been described as the initial product of ferritin degradation by lysosomal enzymes in iron-loaded cells (9, 10). In spite of the lower iron content delivered by H-ferritin, the fact that similar endosomes-lysosomes were not observed after the

treatment of HeLa with H-ferritin could be explained also taking in consideration the following points: a) the endocytic up-take pathway that involves the TfR1 avoids the lysosomal maturation process (see above), b) the rapid iron mobilization in the endosomal compartment due to the lower stability of H- than L-Ferritin at relatively low pH (see below). These results are in line with those obtained with the confocal microscopy (Fig. 2A).

The higher H-ferritin toxicity originates from its peculiar iron cargo.

The peculiar behavior observed for H-ferritin, which shows toxicity effects that are not proportional to the iron-loading suggests a different behavior between the biomineralized caged iron and the "mobile" iron pool constituted by those metal ions that are at the relatively weakly binding ferroxidase sites and low-populated accessory binding sites in the catalytic cavity (3). Indeed, the observed effects can be accounted for as originating by a pool of about 50 iron/cage over a total of 350 iron/cage.

The not-yet biomineralized iron could be easier released upon acidification from the protein sited in the ferroxidase cavity, where the metal ligands are mainly provided by carboxylate and imidazole side chains, as observed in Fig. 2C. It might also be more prone to redox activity leading to a more significant generation of ROS (thus explaining the behavior observed by Fig. 1D). The differences with respect to L-ferritin arise from the fact that non-active cages lack this "mobile iron pool" due to the absence of ferroxidase sites in their subunits.

Human nanocages as MRI probes

Horse spleen ferritin has been largely used as a carrier for MRI contrast agents; here, we investigate the relaxometric properties of H-ferritin with different iron loadings. $1/T_1$ NMRD profiles (at 25 °C, Figure 4A) were recorded for H-ferritin50, H-ferritin350 and L-ferritin1000. The profiles are not affected by addition of deferoxamine (DFO) that selectively binds the iron fraction eventually present on the external surface of the protein. The invariant profiles indicate the absence of weakly, externally coordinated iron ions. The higher millimolar relaxivities shown by H-ferritin50 at any field (Figure 4) arise from the paramagnetic Fe^{3+} ions bound to ferroxidase centers (48 per cage). This contribution is less pronounced in H-ferritin350 and almost absent in L-ferritin1000. As reported (11), the differences in H/L ratio in ferritin cages determine different morphologies of the mineral core and this fact might influence the relaxivity profiles. T_2-weighted MRI experiments were acquired on cells incubated for 24h in the presence of H-ferritin350 and L-ferritin1000. Different protein concentrations were used to obtain the same iron concentration (i.e., 0.38 mM). After incubation, cells were washed, transferred into glass capillaries, and placed in agar phantom to acquire MR images at 7 T. Cells incubated in the same medium without adding ferritin were used as a control. The T_2-weighted RARE (TR/TE/ NEX = 5000/53/4) image confirms

that the internalized amount of both H- and L-ferritins is high enough to induce a detectable contrast that is promising for tracking ferritins in vivo biodistribution (Figure 4B). Cells loaded with L-ferritin are more hypointense than those labeled with H-ferritin. The observed differences could be attributed to the presence of the mobile iron pool in H-ferritin, although the different structure of the biomineral core between H- and L-cages could also contribute.

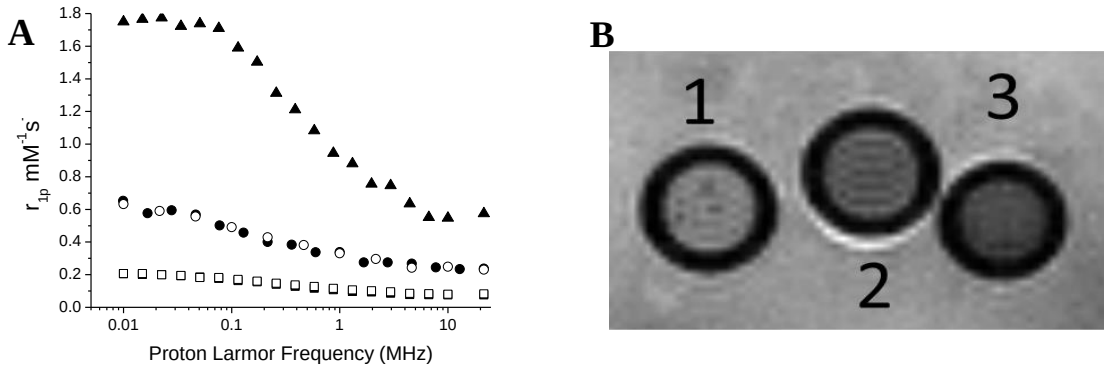

Figure 4. A) Profiles of $1/T_1$ ^{1}H-NMRD (pH 7.4, 25 °C) of H-Ferritin50 (▲),H-Ferritin350 (●) and L-Ferritin (■); open symbols correspond to the same profile recorded in the presence of DFO. The relaxivities (r_{1p} $mM^{-1}s^{-1}$) were normalized to the iron concentration. **B**) A T2-weighted RARE MR image of an agar phantom containing ca. 1 × 106 of (1) HeLa cells unlabeled; (2) Hela incubated for 24 h with H-ferritin and (3) L-Ferritin.

Discussion

A structural biology view of different toxicity of H and L chains.

Recent X-ray crystallography studies have demonstrated that the ferroxidase site of human H-ferritin accommodates two iron ions, named Fe1 and Fe2, that are bound to few protein amino acid side chains: a bridging carboxylate group is provided by Glu62; Fe1 is then bound to His65 and monodentate Glu27; Fe2 to bidentate Glu107; the coordination sphere of each iron ion is completed by water molecules. Nearby, there are other two additional binding sites involving the side chains of His57, Glu58 and Glu62, where hydrated iron ions are bound with low occupancy. The emerging picture is that of a cage that uptakes ferrous hexa-aquaions through the C3 channels and delivers them (as progressively de-hydrated ions) towards the ferroxidase site under the effect of attractive electrostatic gradient created by carboxylate residues. Given the low number of protein residues involved in the binding of the iron at the accessory binding sites and in the ferroxidase site, it' s reasonable to propose that they could be more readily released and react. The Fe1 and Fe2 sites remains always populated during subsequent reaction turnover, while the biomineral growths. Their iron release upon lowering pH can be explained in terms of protonation of the acidic residues

involved in their binding. At variance, in human L-ferritin and horse spleen ferritin, some of us have demonstrated that even the iron ions that react to form the biomineral precursors at the nucleation sites are blocked in a (μ^3-oxo)tris[(μ^2-peroxo)(μ^2-glutamato-κ*O*:κ*O*')](glutamato-κ*O*)(diaquo)triiron(III) cluster that is probably more stable and loses its importance when the biomineral growths.

The apparent H paradox

Our present findings rises an obvious questions. Why a human protein can be toxic for human cells? Here we have to consider a few key aspects:

- **i)** H-ferritin is a cytoplasmic protein; under the cytosolic pH its cargo is stable and is not readily released.
- **ii)** The natural cytoplasmic ferritin never undergoes endosomal-mediated import with consequent iron released induced by the low pH in endosome.
- **iii)** Only ferritin that could be externally administered via the blood stream can be internalized via TfR-1 receptors leading to endosomal internalization.

Therefore, the toxicity of iron-loaded H-ferritin is due to tow main factors: the presence of a mobile iron pool, which has no counterpart in L-ferritins and the lability of this pool at the low pH encountered during the endosomal import.

Materials and Methods.

Horse spleen apoferritin and iron loaded ferritin (15% H chains and 85% L chains, hereafter called L-ferritin), Thiazolyl Blue Tetrazolium Bromide, DCF-DA, deferoxamine mesylate, chloroquine and all other chemicals were purchased from Sigma-Aldrich (St Louis, MO). Commercially available L-apoferritin and L-ferritin were used without any further purification. The number of Fe/cage of L-Ferritin was measured by ICP-MS and the protein concentration by the Bradford assay.

H-Apoferritin production/purification. The gene-coding sequence for human H ferritin was custom-synthesized (GenScript, USA) and subcloned into pET-9a expression vector using NdeI and BamHI restriction sites. The expression plasmid was introduced by thermal shock into *E. coli* strain BL21 (DE3) pLysS cells. Transformants were selected in LB agar supplemented with 50 mg L-1 kanamycin. Cells were grown at 37°C until A600 nm reached 0.6−0.8, and subsequently induced with isopropyl 1-thio-β-D-galactopyranoside (IPTG, 1 mM final concentration) for 4 h. Human H ferritin was purified from the harvested cells, as described previously (3, 4). Briefly, cells were broken by sonication and the cell free extract obtained after centrifugation (40 min, 40,000 rpm, 4 °C) was incubated for 15 min at 65 °C as the first purification step. After removal of the aggregated proteins (15 min, 40,000 rpm, 4 °C), the supernatant solution was dialyzed against Tris-HCl 20 mM pH 7.5; applied to a Q-Sepharose column in the same buffer and eluted with a linear NaCl gradient of 0−1 M in Tris 20 mM, pH 7.5. Fractions containing ferritin, identified by Coomassie staining of SDS-PAGE

gels, were combined and further purified by size exclusion chromatography using a Superdex 200 16/60 column.

Iron loading in H-apoferritin. Iron loading of human recombinant homopolymer H-apoferritin (100% H chain) was carried out by adding a FeSO4 solution (200 mM in HCl) to the protein (9 μM) dissolved in MOPS (100 mM) / NaCl (100mM) at the protein/Fe ratio of 1:500 and 1:50. After the addition the samples were vigorously vortexed for 5' and then left at 25°C for 2 hours and at 4°C overnight. The formed H-ferritins were purified by two cycle of dialysis at 4°C using 1 L of Hepes 4mM/NaCl 150mM as external buffer. Final iron concentration has was measured by ICP-MS. Residual protein concentration was measured by the Bradford assay using Bovine Serum Albumin (BSA) as standard.

Labeling of H- or L-ApoFerritin with Rhodamine B. H- or L-apoFerritin solutions (2 mg/ml) were prepared in 0.1 M sodium carbonate buffer, pH 9. Rhodamine isothiocyanate (Rhod) (Sigma Aldrich) was dissolved in anhydrous DMSO at 1 mg/ml. For 1 mg of protein, 50 μl of Rhod solution were added very slowly in 5 μl aliquots under stirring. Then, the reaction mixture was incubated in the dark for 16 h at 4°C. Afterwards, NH4Cl was added to the reaction to a final concentration of 50 mM and stirred for 2 h at 4°C. The unbound Rhod was separated from the conjugate by dialysis in PBS, pH 7.4, using a 14000 Da cut-off membrane. Finally, the concentration of Rhod and protein were measured by a fluorometer FluoroMax 4 spectrofluorometer (Horiba Jobin Yvon, Edison, USA) and a spectrophotometer (6715 UV/Vis. Spectrophotometer Jenway, Essex, UK) with the Bradford method, respectively.

ICP-MS. Iron concentration was determined by using inductively coupled plasma mass spectrometry (ICP-MS; element-2; Thermo-Finnigan, Rodano (MI), Italy). Sample digestion was performed with concentrated HNO3 (70%) under microwave heating at 160°C for 20 minutes (Milestone MicroSYNTH Microwave labstation).

NMRD profiles. The 1/T1 nuclear magnetic relaxation dispersion profiles (NMRD) of water protons were measured over a continuum of magnetic field strengths from 0.00024 to 0.5 T (corresponding to 0.01–20 MHz proton Larmor frequency) on a Fast Field Cycling relaxometer (Stelar Spinmaster FFC 2000 relaxometer) equipped with a resistive low inductance air cored silver solenoid. The relaxometer operates under complete computer control with an absolute uncertainty in the 1/T1 values of ±1%. The typical field sequences used were the non-polarized (NP) sequence between 20 and 8 MHz and the pre-polarized (PP) sequence between 8 and 0.01 MHz. The observation field was set at 16 MHz. T1 was determined by the saturation recovery method; 16 values of delay (τ) between pulses were used. The number of averaged experiments was 2.

HeLa cell line. Cervical carcinoma (HeLa) cell line was obtained from the American Type Culture Corporation. They were cultured in RPMI 1640 medium (Lonza) containing 10% (v/v) fetal bovine serum (FBS), 2 mM glutamine, 100 U/ml penicillin, and 100 U/ml streptomycin. Cells were incubated at 37 ºC in a humidified atmosphere of 5% CO2. The cell line was

routinely tested to verify the absence of mycoplasma contamination (MycoAlert™ PLUS Mycoplasma Detection Kit, Lonza).

Uptake experiments. For uptake experiments, HeLa cells were seeded at a density of 6 × 105 cells in a 25 cm3 culture flask and placed in a wet (37 °C) 5% CO2 air atmosphere incubator. At 24 h post seeding, cells were incubated with increasing concentrations of the above-mentioned H- or L-ferritins. After 24 h of incubation, cells were washed three times with 10 mL ice-cold PBS, detached with trypsin/EDTA. The Fe content in each cell line was determined by ICP-MS. For MRI analysis (see below) cells were transferred into glass capillaries. The protein concentration (proportional to the cell number) was determined from cell lysates by the Bradford assay, using BSA as a standard.

Fluorescence Activated Cell Sorting (FACS) analysis of Transferrin Receptor expression. In order to perform FACS analysis, $2x10^5$ Hela cells were seeded in 3.5 cm of diameter culture dishes. The day after, cells were treated for 24h with Fe(III) citrate (Sigma Aldrich) 0.34 mM, human holo transferrin (Sigma Aldrich) 10 and 20 µM or H-Ferritin 1µM loaded as previously described. For the experiment, cells were grown in Roswell Park Memorial Institute medium (RPMI) medium (Lonza). At the end of the incubation, the medium was removed and the cells were washed three times with PBS. Then, they were treated with a non enzymatic dissociation solution (Sigma Aldrich) for 15 min at 37°C, transferred in 15 ml falcon tubes and counted in PBS. Cell number was determined using a cell sorting chamber (Burker-Turk chamber). The cells were divided in falcon tubes containing 1x106 cells for each one.
All samples were centrifuged (1100 rpm for 5'), the supernatant was removed, and the cells were further washed with PBS and centrifuged (1100 rpm for 5'). All the samples were then incubated in 10% FBS (0.5 ml) for 30' at 4 °C, then spun down (1100 rpm for 5'), washed with PBS (3 ml), and then this washing step was repeated once more. The PE conjugated antibody (mAb anti human CD71, BD Pharmingen) selective for Transferrin Receptor 1 (TfR1) was added to the samples previously described (20 µl in 100ul of 0.1% BSA/PBS) and to a non-treated sample of Hela cells. As a negative control, a mouse isotype control antibody PE conjugated (Miltenyi Biotec) (5ul in 100ul of 0.1% BSA/PBS) was incubated with a non-treated sample of Hela cells. The incubation was performed at 4 °C for 40'. All samples were then washed with PBS (2 × 3 ml) and centrifuged (1100 rpm for 5'). Finally, cells were diluted in PBS (250µl) and evaluated for their PE fluorescence on a flow cytometer (Becton Dickinson, FACS Calibur). Their PE fluorescence was analyzed using the CELLQUEST PRO program: the mean fluorescence intensity of the treated samples has been calculated as a percentage with respect to the non-treated Hela cells. The experiments were performed in duplicate.

MTT assay. MTT assay is based on the tetrazolium salts reduction to formazan by mitochondrial succinate dehydrogenase (SDH), which is quantified spectrophotometrically. $5×10^3$ Hela cells were seeded in a 96-well microtiter plate at 37 °C and 5% CO_2 air atmosphere. 24 h later, the cells were incubated for 24 h at 37 °C and 5% CO_2 with increasing concentration of iron-loaded H- and L-Ferritin and H- and L-apoFerritin.

Furthermore, H-Ferritin (0.5 μM) and L-Ferritin (2.5 μM) were also incubated in absence or in the presence of DFO mesylate (150 μM) or chloroquine (100 μM) for 24h. After this time, the medium was removed and 100 μl of Thiazolyl Blue Tetrazolium Bromide dissolved in medium at the concentration of 0.45 mg/mL was added into each well and the plate was incubated for 4 h at 37 °C and 5% CO_2. Then, the medium was removed, 150 μl of DMSO were added into each well to solubilize the formazan salt crystals produced by the metabolism of live cells and the microplate was incubated at room temperature for 30 minutes. Finally, absorbance was read at 570 nm with iMark microplate reader (Biorad). Cell viability was reported as percentage of death cells observed in treated samples relative to that observed in control cells. The experiment was performed in triplicate and the data were graphically presented as mean ± SD.

Iron mobilization from H- and L- ferritin. Iron loaded H- and native L- Ferritin (0.2 μM) have been incubated up to 3h at 25°C in different buffers (Hepes/NaCl pH=7.4; 0.1 M acetate buffer pH=5) and in human serum (Seronorm Human, Sero AS, Billingstad, Norway) in the presence of 1 mM 2,2'-bipyridine under aerobic conditions. Incubations of proteins in Hepes/NaCl buffer at pH=7.4 have been repeated in the presence of glutathione (0.25 mM) or ascorbate (0.25 mM) and of 1 mM 2,2'-bipyridine. The concentration of the reductively mobilized iron cations from ferritin was measured by following the absorption of the Fe(II)–bipyridine complex at 530 nm (ε = 8650 M−1 cm−1).

Laser scan microscopy studies. Co-localization determination among H/L-apoferritns and lysosomes were carried on as follow. Cells were seeded in a Ibidi μ-Slide 8 well at a density of 5x104 cells/ml and incubated at 37°C and 5% CO_2 for 24 h, in order to allow them to adhere to the slide surface. Then, cells were incubated with H or L-Apoferritin rhodamine labeled (20 nM) for 3 h. At the end of the incubation cells were washed three times with PBS and fixed in cold methanol at 4°C for ten minutes. Afterwards, cells where rinsed twice with PBS for ten minutes each one. In order to block the non-specific binding sites, cells were treated with 5% normal goat serum during thirty minutes. Then, cells were incubated overnight at 4°C with a mouse monoclonal IgG1 anti-human Lamp-1 (H4A3 from Santa Cruz Biotechnology Inc, Dallas, Texas, USA). After washing twice in PBS for ten minutes, cells were incubated with a goat polyclonal IgG (H+L) fluorescein labeled anti-mouse antibody one hour at room temperature (Molecular Probe, Eugene, Oregon USA). Finally, cells were washed with PBS three times for ten minutes each one and air dried. Nuclei were counterstained with DAPI. Coverslips were mounted with a glycerol/water solution (1/1, v/v). Observations were conducted under a confocal microscopy (Leica TCS SP5 imaging system).

Transmission electron microscopy (TEM) studies. For TEM analysis, HeLa cells were treated for 3 h at 37°C with H-Ferritin 1 μM or L-Ferritin 2.5 μM, respectively. Control cells were incubated under the same conditions without ferritin addition. Then cells were fixed with 2.5 % glutaraldehyde solution in 0.1 M phosphate buffer pH 7.4 and post-fixed in osmium tetroxide solution. Then, samples were dehydrated in 3 x 10 min in 70% ethanol, 2 x 15 min

in 100% ethanol, and 2 x 15 min in 100% propylene oxide, and embedded under vacuum in EMbed 812 resin (Electron Microscopy Sciences, Hatfield, PA, USA). 70 nm slices were sequentially stained with, saturated uranyl acetate, 0.25% lead citrate and 0.04% bismuth subnitrate to enhance ferritin detection 29. Samples were analyzed under a Jeol Jem 1400 transmission electron microscopy (Peabody, MA, USA).

Measurement of reactive oxygen species (ROS) production. Intracellular ROS production was detected using the non-fluorescent cell permeating compound, 2',7'-dichlorodihydro-fluorescein diacetate (DCF-DA). In order to evaluate the effect of H- and L-Ferritin on the ROS production, Hela cells were seeded at a density of 1 x 10^5 cells in a 3.5 cm of diameter dishes and were placed for 24 h in a wet (37 °C) 5% CO_2 air atmosphere incubator. Iron-loaded H- and L-Ferritins and H- and L-apoferritins (without iron content) were incubated at protein concentration of 3 μM for 24 h at 37°C, 5% CO_2. After the incubation, cells were washed two times with PBS and incubated with 5 μM of DCF-DA for 30' at 37°C, 5% CO_2 in pre-warmed EBSS buffer. Cells were then washed two times with PBS and detached using a cell scraper in 100ul of PBS. Cells were then sonicated in ice for 5'' at 30% power and the protein content of cells were determined by the commercial Bradford method. The fluorescence of cells lysates (30000 cells) was measured using a fluorometer microplate reader Promega Glomax-multi detection system (Promega Corporation, 2800 Woods Hollow Road Madison, WI 53711 USA) using a blue module (ex 490 nm, em 510-570 nm) on samples containing 10 μg of cell proteins in 200 μl of PBS. The fluorescence intensity was then normalized to the intracellular iron concentration measured by ICP-MS (2.05 and 0.495 μM for L- and H-ferritin, respectively).

MRI. All the MR images were acquired on a Bruker Avance 300 spectrometer (7 T) equipped with a Micro 2.5 microimaging probe (Bruker BioSpin). Glass capillaries containing 1 × 10^6 cells were placed in an agar phantom and MRI was performed using a T2-Weighted RARE sequence protocol (TR/TE/NEX = 5000/53/4; FOV= 1.2 cm; MTX 128x128).

Reference List

1. Jutz G, van RP, Santos MB, Boker A (2015) Ferritin: a versatile building block for bionanotechnology. *Chem. Rev.* **115**:1653-1701.

2. Liang M *et al.* (2014) H-ferritin-nanocaged doxorubicin nanoparticles specifically target and kill tumors with a single-dose injection. *Proc. Natl. Acad. Sci. U. S. A* **111**:14900-14905.

3. Pozzi C *et al.* (2015) Iron bindind to human heavy-chain ferritin. *Acta Crystallogr D Biol Crystallogr* **71**:1909-1920.

4. Ravera E *et al.* (2016) Solid-state NMR of PEGylated proteins. *Angew. Chem. Int. Ed* **55**:1-5.

5. Ward JH, Kushner JP, Kaplan J (1982) Regulation of HeLa cell transferrin receptors. *The Journal of Biological Chemistry*10317-10323.

6. Zhang DL, Ghosh MC, Rouault TA (2014) The physiological functions of iron regulatory proteins in iron homeostasis - an update. *Front Pharmacol.* **5**:124.

7. Li L *et al.* (2010) Binding and uptake of H-ferritin are mediated by human transferrin receptor-1. *Proc. Natl. Acad. Sci. U. S. A* **107**:3505-3510.

8. Huotari J, Helenius A .

9. Iancu TC (2011) Ultrastructural aspects of iron storage, transport and metabolism. *J. Neural Transm. (Vienna.)* **118**:329-335.

10. RICHTER GW (1957) A study of hemosiderosis with the aid of electron microscopy; with observations on the relationship between hemosiderin and ferritin. *J. Exp. Med.* **106**:203-218.

11. Lopez-Castro JD *et al.* (2012) A new approach to the ferritin iron core growth: influence of the H/L ratio on the core shape. *Dalton Trans.* **41**:1320-1324.

Annex VII

Working draft

"Interaction studies of ferritin with lipids"

Serena Zanzoni [1], Katiuscia Pagano [2], Mariapina D'Onofrio [1], Michael Assfalg [1], Silvia Ciambellotti [3], Caterina Bernacchioni [3], Paola Turano [4], Silvio Aime [5,6], Laura Ragona [2] and Henriette Molinari [2]

[1]Dipartimento di Biotecnologie, Strada Le Grazie 15, Università di Verona, 37134 Verona, Italy; [2]Laboratorio NMR, ISMAC-CNR Via Corti 12, 20121 Milano, Italy; [3] Dipartimento di Chimica, Università di Firenze, Via Della Lastruccia 3, Sesto Fiorentino, 50019 Firenze, Italy; [4] CERM, Università di Firenze, Via L. Sacconi 6, Sesto Fiorentino, 50019 Firenze, Italy; [5]Molecular & Preclinical Imaging Centers, Department of Molecular Biotechnology and Health Sciences, University of Torino, Turin, Italy; [6]IBB-CNR-UOS, University of Torino (IT), Turin, Italy

Introduction

Ferritin-like proteins are a family of well-characterized iron storage proteins with an essentially ubiquitous distribution in all life forms (1-3). They are formed by 12 (in the case of the prokaryotic DNA-binding proteins from starved cells, DPS) or 24 (classical ferritins and bacterioferritins) identical or similar subunits self-assembled into a globular shell containing an iron core consisting of a ferric oxy-hydroxide mineral similar to ferrihydrite (4). In the classical 24-mer ferritins the structure of each subunit is a helix bundle composed of four α-helices, (A, B, C, D) and a fifth C-terminal short α-helix E (Figure 1a). The subunits are assembled into a spherical-shape structure with 4-3-2 symmetry, which form a hollow complex with an approximately 8 nm diameter cavity capable of storing up to 4500 iron atoms (Figure 1b). In eukaryotes, native cytosolic ferritins are the product of self-assembly of two types of highly homologous subunits: "light" (L, 20 kDa), and "heavy" (H, 22.8 kDa) subunits, with up to 53% identity. The H subunit is characterized by the presence of a di-iron binding site embedded inside the 4-helical bundle which is responsible for the interaction with oxygen and confers ferroxidase activity, namely is responsible for the enzymatic oxidation of Fe^{2+} to Fe^{3+}. The L subunit, without a ferroxidase center, still catalyzes Fe^{2+} oxidation but at a much slower rate (5) and plays a role in iron nucleation and mineralization (6, 7), i.e. it can provide a means to control the overall capacity of iron storage improving the overall iron-sequestering process. Ferritins display a dynamic iron-storage function, central to cellular iron homeostasis. Fe^{2+} sequestration prevents spontaneous oxidation to Fe^{3+} and production of toxic free radicals, thus displaying also oxidative stress protection. The nanocage composition in terms of H and L-subunits is tissue specific, with ferritins from liver and spleen, involved in long-term storage of iron, being richer in L-subunits, whereas those from heart and brain, with more active iron metabolism, being richer in H-subunits (6, 8). For example for the horse spleen ferritin (HoSF), here investigated, its average composition is generally stated to be roughly 15% H-subunit and 85% L (H_4L_{20}), (9) corresponding to a mixture with a L-subunit content roughly sixfold greater in abundance than the H-subunit (8, 10).

Crystallographic studies of mammalian ferritins revealed that the pockets at the 2-fold intersubunit are available to bind organic molecules, including protoporphyrin (11), anaesthetics (12) and fatty acids (13). Thus it has been suggested that, besides its iron-storage function, ferritin plays a role in lipid metabolism (13), as also inferred by a series of data on the functional coupling between iron and fatty acid metabolism (14-18). The crystal structure of the HoSF-arachidonate complex (PDB id 4DE6) revealed that the bound ligand has a U-

shaped conformation (characteristic of fatty acids located in the fatty acid binding protein cavity (19)) and is close to residues known to form the nucleation site, which includes E53, E56, E57, E60 and E63 (HoSF numbering, Figure 1c). (13, 20-25). Of interest, the ferritin-bound arachidonate, appeared to contribute to ferrihydrite mineralization by accelerating iron uptake. Intracellular free fatty acid concentration might thus have a signaling role in accelerating iron storage via its incorporation within the ferritin cage. Ferritin may as well protect unsaturated fatty acids from oxidation, limiting their participation in lipid peroxidation chain reaction, thus reducing their inflammatory effects (13, 26).

Intrigued by the possible role of ferritin as a new fatty acid binding protein we have here investigated the interactions of apo horse spleen ferritin (HoSF) with a pool of lipids, employing a series of 1D ^{1}H-NMR, diffusion (DOSY) and saturation transfer (STD) NMR experiments. Unsaturated fatty acids (arachidonate and oleate) exhibited better binding properties with respect to saturated fatty acids (lauric acid), detergents (sodium dodecyl sulphate) and bile acids (chenodeoxycholic acid). These studies have been accompanied by mineralization assays through UV/visible measurements, aimed at clarifying whether functional coupling exists between mineralization and ferritin/lipid interactions. The initial rate of mineralization exhibited the highest increase in the presence of oleate (OLA), with respect to saturated fatty acids and other lipids.

Oleate was also shown to efficiently bind to recombinant homopolymeric human ferritin H (HuFH), although no effect was observed on ferroxidase activity.

Results and Discussion

Interaction of HoSF with lipids. The ^{1}H NMR spectrum of commercial, freshly dialyzed apo HoSF, dissolved in 20mM phosphate buffer in D_2O at pH 7.5, is reported in Figure S1a. The high molecular weight of the 24-mer (approximately 480 kDa), translates into a reduced tumbling rate and a fast nuclear transverse relaxation, giving rise to severely broadened ^{1}H resonances (2). The observable residual broad resonances occurring in the aliphatic region are likely due to superficial mobile ferritin sidechains and/or to the contribution of smaller HoSF oligomer species or to the presence of impurities (vide infra). In order to probe the interactions of ferritin with lipids, we firstly exploited ligand based NMR experiments, which are not limited by the size of the protein. Indeed, small ligand molecules, when reversibly bound to the proteins, retain similar NMR properties as the large macromolecule, leading to a change in their observed parameters, such as chemical shifts, linewidths and/or intensity (28).

At the same time a non-interacting ligand would exhibit unaffected resonances when added to ferritin.

In addition to ^{1}H ligand-observed NMR experiments, a diffusion spectroscopy-based approach (DOSY) (29), which uses gradient pulses to measure translational diffusion, was employed to study the interactions of selected lipids with this "NMR-oversize" system. Small molecules bound to macromolecules diffuse at the slower rate of the macromolecule rather than at their typical rate. The acquisition of DOSY spectra, in the presence and absence of the target protein, can identify binding events from the change of the diffusion properties of the observed ligand partner.

Polyunsaturated, monounsaturated and saturated fatty acids (Figure S2) together with detergents and bile acids were tested for their binding to HoSF. In order to correctly interpret any spectral perturbation in terms of specific binding to the macromolecule, we first selected two small molecules, namely sucrose and tert-butyl alcohol, as control samples for non-interacting ligands. Sucrose density gradient centrifugation is in fact used to purify and analyze recombinant ferritins (9, 30), while tert-butyl alcohol is an inert molecule (31). The ^{1}H NMR (Figure S3), and DOSY spectra (data non shown) of these ligands were unaffected by the presence of HoSF thus confirming the absence of any spurious (viscosity) effect due to the protein.

Polyunsaturated arachidonate (ARA) was tested first. The structure of the complex (PDB 4DE6) (13) has been reported together with an estimate of K_D 60 μM, derived from ITC experiments. ARA is localized at the intersubunit 2-fold pocket (13), thus indicating that twelve equivalents of FA are bound per 24-mer, which was the basis to calculate the protein ligand molar ratio to be employed in the NMR experiments. ^{1}H NMR experiments and DOSY spectra performed on HoSF after progressive addition of ARA showed that the resonances of free ARA started to appear at a ARA:HoSF ratio > 1 (referred to binding sites), as shown in Figure 2, confirming that twelve binding sites are saturated by the lipid. The absence of any chemical shift change of the free ligand (when in stoichiometric excess) indicates that it is in slow exchange with the bound one, suggesting a sub-micromolar affinity. Resonances of the free ARA appear at a diffusion coefficient consistent with the formation of emulsion particles (2-4 mer units; for the assessment of molecular weight see Experimental). It should be further mentioned that the resonances of HoSF occurring at 0.7-0.9 ppm in the spectrum of HoSF, could in principle be due either to impurities of the commercial samples and/or to highly mobile sidechains and/or to the presence of small HoSF oligomeric species. DLS and size exclusion chromatography experiments performed on the commercial HoSF sample

confirmed that the predominant species is the protein 24-mer (Figure S4)

The interaction of HoSF with monounsaturated oleate (OLA), monitored through ^{1}H-NMR and DOSY performed at different OLA:HoSF ratios exhibited a behavior similar to that observed for ARA, with the resonances of the free oleate bulk methylene groups (δ 1.2 ppm) being visible only at L:P ratio of 2 (Figure 2). These methylene resonances display a diffusion coefficient consistent with either a monomeric or a sodium hydrogen dioleate, an insoluble swelling "acid soap" compound (32). CD spectra performed on samples of apo HoSF and HoSF in complex with OLA, confirmed that the native secondary structure of the protein is conserved in the complex (data not shown).

Lauric acid sodium salt (LAU), as an example of saturated fatty acid, was also tested for its interactions with HoSF. At LAU:HoSF ratio of 1, the resonance of LAU at δ 1.2 ppm, corresponding to the bulk methylene groups, was clearly visible at the same chemical shift of the free species, and exhibited linewidth broadening with a substantial attenuation with respect to free LAU at the same concentration (Figure 3a). Diffusion measurements confirmed the presence of free lauric acid already at LAU:HoSF ratio of 1 (Figure S5). These data indicate that LAU binds to HoSF, although with decreased affinity.

Previous crystallographic and ITC data have shown that sodium dodecyl sulphate (SDS) binds specifically to a HoSF internal cavity, at the dimer interface, occupying the same binding site described for ARA and with a K_D of 24±9 μM (33). SDS has a 12-carbon tail, as LAU, but attached to the bigger sulfate polar group, thus allowing an evaluation of the role of the polar head steric hindrance. The NMR data, here acquired, were consistent with a weaker binding of SDS to HoSF with respect to LAU, indicating an unfavorable role of the bulky polar head. Indeed, in the ^{1}H NMR spectra a substantial line broadening (twofold linewidth increase) was observed for SDS methylene resonances (δ 1.2 ppm) in the presence of HoSF (Figure 3b), suggesting that binding occurs on an intermediate exchange regime on the chemical shift time scale, at variance with all the other tested FAs, which exhibit a slow exchange regime. In agreement with this observation, in the DOSY spectra of SDS:HoSF, performed at different molar ratios, the free SDS resonance was already observable at SDS:HoSF ratio of 0.5 (Figure 2). CD spectra on HoSF:SDS samples confirmed that there is no effect of the detergent on the native secondary structure of the protein (Figure S4b).

Finally, we tested the interaction of HoSF with chenodeoxycholate (CDA), a lipid belonging to the bile acid family, a group of amphipathic molecules displaying two different surfaces, the hydrophobic β side with angular methyl groups and the hydrophilic α side characterized by the presence of hydroxyl groups. The angular C18 methyl resonance of CDA occurs at

0.57 ppm, a region free from any HoSF resonance, which can therefore be employed to monitor the appearance of free CDA upon interaction with HoSF, as shown in Figure 4. The observed behavior paralleled that observed for SDS as a substantial linewidth broadening was observed for CDA methyl resonance at all the CDA:HoSF ratios, together with a small chemical shift change, indicating an intermediate exchange regime, typical of a weak binder.

Effect of NaCl addition to ferritin-FA complexes. An increased salt concentration may favor binding when hydrophobic effects dominate protein-ligand interactions (27, 34). Addition of salt may also lead to a drop in the critical micellar concentration (CMC) value of FA molecules, which can possibly further influence the equilibria established in solution (35, 36). The presence of 150 mM NaCl did not alter the observed spectra of HoSF in the presence of oleate, but had significant effects for weaker binders. Figure 3a shows that in the presence of NaCl, the binding of LAU to ferritin is favored, as indicated by a further decrease of the residual resonance of LAU methylene groups, with respect to the same sample solution without NaCl. The addition of NaCl favors as well the binding of SDS with a further linewidth broadening of the bulk methylene resonance at δ 1.2 ppm (Figure 3b).

Competition experiments. NMR competition binding experiments were further performed in order to check whether oleate occupies the same ARA/SDS binding site, at the dimer interface (Figure 1c). Oleate was added to HoSF:SDS complex to obtain a sample with HoSF:SDS:OLA ratio of 1:1:1. The resulting spectrum showed an increase of the free SDS resonance intensities, indicating that oleate could displace SDS. The amount of displaced SDS reached a maximum after 24 hours. The displaced SDS resonances are slightly shifted with respect to those of free SDS, indicating the presence of fast exchange between SDS free and bound to the OLA:HoSF complex (Figure 5). The observed chemical shift changes of SDS cannot be ascribed to the formation of a mixed OLA:SDS micelle, as deduced from NMR control experiments performed by adding incremental amounts of OLA to free SDS in phosphate buffer at the same concentration (data non shown).

STD experiments. Ligand-observed saturation transfer difference (STD) experiments are among the most appealing NMR experiments to monitor weak ligand binding ($K_D \approx$ μM-mM) in the presence of large protein partners (37), via magnetization transfer from the large protein to the smaller ligand. STD spectra were obtained for all the investigated ferritin complexes, using a 50-fold molar excess of ligand (calculated on the basis of the number of binding sites).

Control STD experiments performed in the presence of sucrose, yielded, as expected, no signal. STD spectra of ARA and OLA, in the presence of HoSF, exhibited small signal enhancements (Figures 6b,c). All SDS resonances, at variance, exhibited a substantial enhancement (Figure 6d) in the STD spectra. k_{on}, k_{off} and R_1 rates contribute to determine the observed strengths of the ligand signals. For ARA and OLA, at the employed lipid concentration, equilibrium exists in solution between monomers and micellar aggregates (critical micellar concentration, CMC, are expected to be smaller than 0.1 mM), while higher CMC values (8 mM) are reported for SDS (ref). Thus different k_{off} and R_1 may affect the resulting spectra while k_{on} is expected to be roughly the same for the investigated molecules. The observed lower net saturation transferred to the pool of free ARA and OLA ligands is however consistent with the titration data depicting a tighter binding with respect to SDS. The spectrum of Figure 6d reflects the proximity of all the SDS protons to HoSF, consistent with X-ray data showing the ligand embedded in the protein cavity (33). Competition binding STD experiments were performed by adding OLA to the SDS:HoSF complex, in equimolar amounts, confirming the higher affinity of OLA and its ability to displace SDS, as inferred from the loss of the C_1 methylene resonance (δ 3.96 ppm), the only signal characterizing SDS with respect to OLA (Figure 6e). The other observed resonances (0.8-1.2 ppm) are likely due to the bound OLA methyl and methylene resonances. They appear broader and with a reduced intensity than SDS resonances (Figure 6d), in agreement with the expected lower k_{off}. CDA binds as well to HoSF (Figure 6f), with a lower affinity than OLA. Indeed, in the competition STD experiment with OLA (Figure 6g), CDA resonances disappear with the concomitant appearance of OLA signals.

Iron mineralization. In order to investigate the correlation between the binding abilities of different FAs and the kinetics of mineralization, commercial apo HoSF was first demineralized and then incubated with or without lipids. The kinetics of biomineral formation was followed by UV absorption as the change in absorbance at 350 nm, to monitor the formation of diferric oxo/hydroxo species ($(Fe^{3+}O)_x$) during oxidative deposition of iron (38) in the apo and lipid-bound ferritin forms. A high loading of Fe^{2+} (480 Fe^{2+} per HoSF cage) was here employed, in order to overcome the lack of iron turnover at the ferroxidase centers of the protein (HoSF contains few H chains) and to favor the nucleation and growth of the incipient core, namely to ensure that the mineralization reaction occurs to an appreciable extent (7, 10). The addition of OLA, ARA, and LAU significantly enhances the initial mineralization rate of HoSF. (Figure 7). However, the FAs have different effect on the

mineralization process, with ARA and LAU displaying the same absorbance of apoferritin after 20 minutes and OLA showing an increase of the total amount of ferric oxide species at plateau, and thus possibly favouring the oxidation of Fe^{2+} on the mineral core surface.
A further screening, performed varying the number of insaturation on the C18 alkyl chain (C18:1 oleic, C18:2 linoleic, C18:3 linolenic acids), indicated that the increase of the insaturation number significantly lowered the enhancement of the initial mineralization rate observed with oleate, thus suggesting the relevance of the fatty acid conformation (Figure S5).
An inhibition of iron mineralization was observed in the presence of the weakest binder SDS, albeit reported crystallographic data showed that SDS occupies the same binding site later described for ARA. Thus, the steric hindrance of the polar head plays some structural role in contrasting the flow of iron through the described hydrophilic three-fold channel.
The comparison of the kinetic data translates into an initial rate for the formation of $Fe^{3+}O_x$ species almost 10 times faster in the presence of OLA and ARA (Table 1), thus confirming the hypothesis that FAs enhance iron mineralization, favouring iron uptake, as recently observed in *in vitro* (HepG2 hepatocytes) and *in vivo* (in rats) experimental models (39).
All together these findings suggest that OLA, ARA and LAU influence the mineralization process presumably modelling the environment of the surrounding side-chains, favouring iron storage. (10).

The ensemble of the binding and mineralization experiments clearly shows that oleate is a strong binder displaying the highest effect, among the tested lipids, on HoSF mineralization. In view of the relevance of investigations on functional coupling between lipid transport and iron mineralization, it is important to gain more information on the interactions of oleate with the human protein.

Interaction of recombinant HuHF with oleate. The binding of oleate with recombinant HuHF, displaying a sequence identity of 51% and a similarity of 75% with HoSF, was tested by NMR. ^{1}H NMR spectra of OLA:HuHF, at different ratios, confirmed that resonances of free oleate at δ 0.75 (C18 methyl), 1.2 (bulk methylene groups) and 1.47 ppm (C3 methylene) became clearly visible only at OLA:HuHF ratio of 2 (Figure 8a). DOSY spectra highlight the presence of OLA resonances diffusing as dimeric free species only at OLA:HuHF ratio of 2, (Figure 8b) paralleling the behavior of HoSF .
It was further shown that the OLA complex maintains its secondary structure also upon increasing the temperature (Figure S3).

Materials and Methods

Protein Preparation. Horse spleen apoferritin (HoSF) was purchased from Sigma-Aldrich. For NMR experiments the protein was first dialyzed with 10 mM potassium phosphate buffer (pH 7.4) and then exchanged into D_2O buffer. For mineralization measurements HoSF was further demineralized by extensive dialysis against four changes of at least 20-fold volume excess of 20 mM Tris buffer at pH 7.4 containing 2.5 mM EDTA and 2% ammonium thioglycolate, followed by extensive dialysis against 20 mM Tris buffer pH 7.4. Human H ferritin (HuHF) was expressed and purified as described previously (40).

NMR experiments. NMR experiments were performed at 25°C using a 600 MHz Bruker Avance III spectrometer equipped with a triple resonance TCI cryogenic probe. 1D NMR spectra were recorded with 64 scans and a spectral width of 14026 Hz. Spectra were referenced to the dioxane signal (3.69 ppm) used as internal standard. All spectra were manually phased and baseline corrected using TOPSPIN 3.2 (Bruker, Karlsruhe, Germany).

STD experiments were recorded using a 1D pulse sequence incorporating a T1ρ filter to remove disturbing protein signals (41-44). "On-resonance" irradiation of HoSF (50μM in subunits) was performed in the aromatic region (7.2 ppm), which is free from ligand resonances, while "off resonance" irradiation was set at 35 ppm, a value outside the range of HoSF resonances. The irradiation was performed with a train of selective Seduce-shaped pulses of 50 ms duration, for a total saturation time of 3 s.

2D 1H-DOSY experiments were recorded with a 600 MHz Bruker DMX spectrometer equipped with a triple resonance TXI probe. The convection-compensated two dimensional double stimulated echo bipolar pulse (DSTE-BPP) sequence was employed (45). Matrices of 2048 (t2) by 80 points (t1) were collected. The z axis gradient strength was varied linearly from 2 to 98% of its maximum value (53 G/cm). The gradient pulse duration was 1.8 ms, while the time period between the two gradient pulses was set to 70 ms to allow the detection of free ligand species. DOSY with a longer big delta (200 ms) were also recorded to estimate the diffusion time of larger molecules and evaluate the presence of monomeric and/or oligomeric ferritin. Water suppression in DOSY experiments was achieved with a standar Bruker library DSTE DOSY sequence (46) with the addition of a sculpting module for water suppression. Self-diffusion coefficients were derived by fitting NMR data to Stejskal and Tanner equation (47). Dioxane (45 μM) was added as internal reference to correlate relative diffusion coefficients with MW of molecules and their aggregates in solution. This approach also allows to minimize erroneous D estimates deriving from temperature fluctuations and

changes in sample viscosity and density.

Iron mineralization. The kinetics of biomineral formation were followed monitoring the increasing of absorbance at 350 nm with a Cary 30 UV/visible Spectrophotometer (*Agilent* Technologies). The change of absorbance was monitored after the addition of ferrous sulfate (freshly prepared solution in 1 mM HCl) to HoSF (2.08 μM protein cages) incubated with (700 μM) or without lipids in 200 mM MOPS, 200 mM NaCl, pH 7.0. Initial rates of mineralization were calculated from the linear fitting of the initial phases of the 350-nm traces (0 - 30 s) from three independent measurements.

Size Exclusion Chromatography and Dynamic Light Scattering. 5mg of commercial HoSF were analyzed by SEC using an AKTA Prime (GE Healthcare) equipped with a Sephacryl S-100 HR XK 26/100 column (GE Healthcare) equilibrated in 20 mM Tris, 150 mM NaCl, pH 7.5. Fractions showing an absorbance at 280 nm were analyzed by SDS-PAGE. With the use of SEC calibration standards (GE Healthcare), the peak eluting in the void volume was consistent with the molecular weight of apo HoSF. In order to investigate the size of HoSF, DLS measurements were performed in triplicate at 25°C on apo HoSF before and after SEC using a Zetasizer Nano ZS (Malvern Instruments, Malvern, UK) operating at λ=633 nm and equipped with a back scattering detector (173°). Each measurement was the average of 20 data sets acquired for 10 seconds.

Circular Dichroism Spectroscopy. CD spectra were acquired in the far-UV with a Jasco J-810 spectropolarimeter using a 0.1 cm path length quartz cuvette and 10 μM protein concentration (in subunits) in 20 mM Tris buffer at pH 7.5, in the presence (5μM) or absence of ligands. The CD spectra were first measured at 25 °C, the samples were then incubated in termostated cells at the desired temperatures (in the range 25−85 °C) for 5 min and the corresponding CD spectra were acquired. The final spectrum was calculated as the mean of 10 scans between 200 and 260 nm wavelengths after subtraction of the corresponding buffer spectrum.

Stopped-Flow Kinetics. Single turnover oxidoreductase kinetics (6 Fe^{2+}/subunit) was monitored in apo HuHF and in complex with OLA. Changes in absorbance at 650 nm (diferric-peroxo or DFP) or at 350 nm $(Fe^{3+}O)_x$, were measured in the same conditions of iron mineralization in a UV/visible, stopped flow spectrophotometer (SX.18MV stopped-flow reaction analyzer, Applied Photophysics).

Table 1. Initial rates of biomineral formation at 480 Fe eq. per cage

Sample	Initial rate (ΔA_{350nm}/min)*
HoSF	**0.02873 ± 0.007310**
HoSF-OLA	**0.2621 ± 0.04628**
HoSF-ARA	**0.2486 ± 0.07781**
HoSF-LAU	**0.1607 ± 0.06061**
HuF	***in progress***
HuF-OLA	***in progress***

*calculated from the linear fitting from three independent measurements

Figures

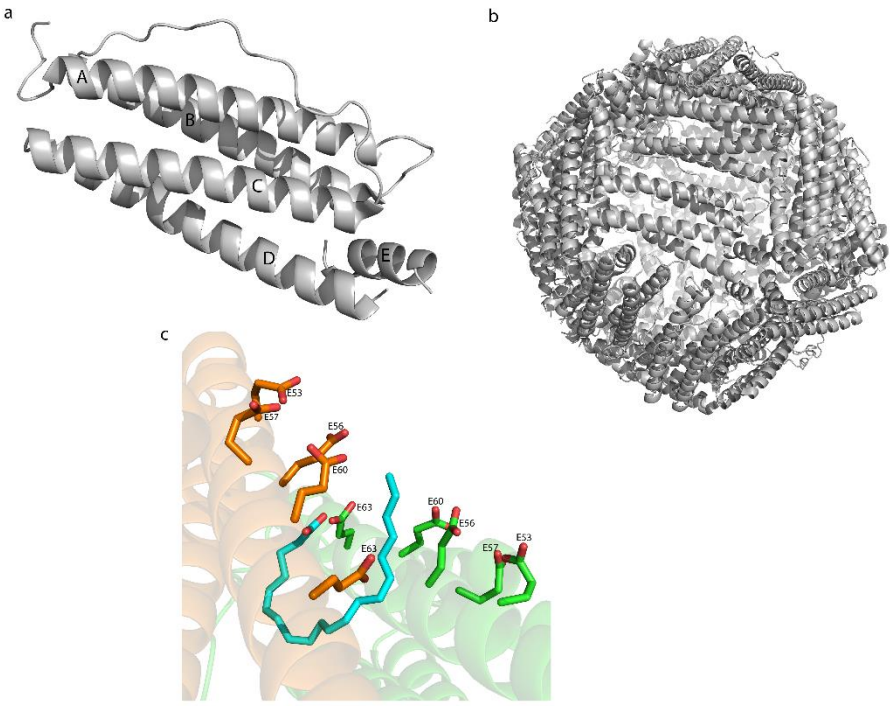

Figure 1

Figure 1. Structure of HoSF (PDB 4DE6). a) Four helix (A,B,C,D) bundle and the fifth short E helix; b) ferritin 24-mer; c) dimer interface hosting the arachidonate lipid.

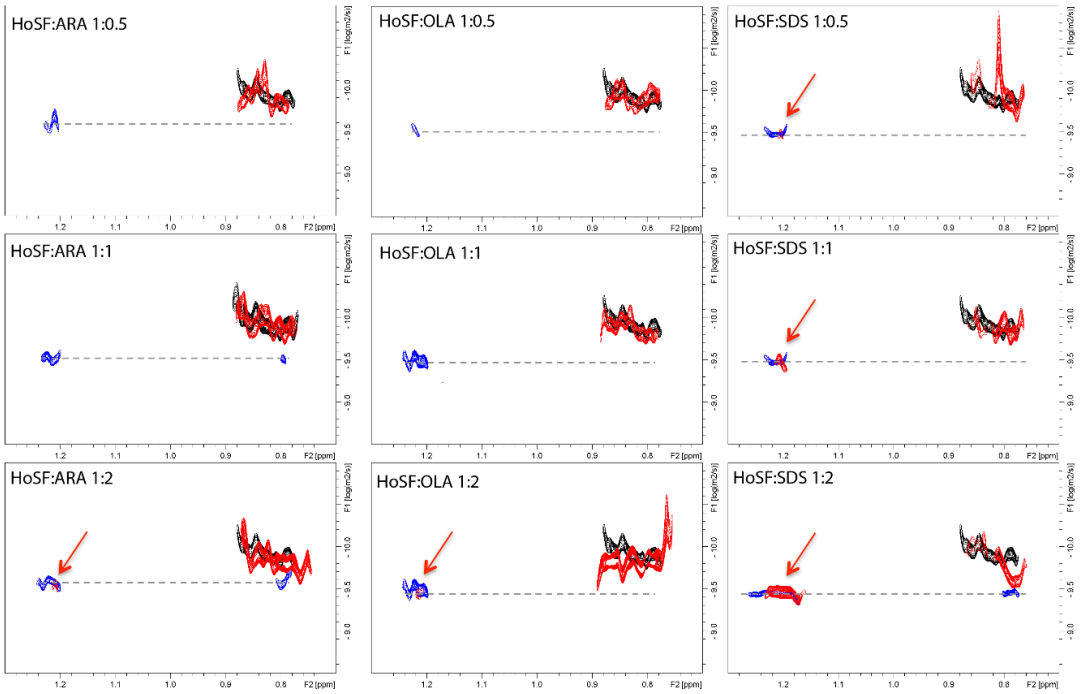

Figure 2

Figure 2. DOSY spectra of the complexes. Left panels: Superposition of DOSY spectra recorded at 600 MHz and 25°C of a sample of 97 μM HoSF in NaPi buffer pH 7.8 (black), ARA:HoSF at different ratios (red), free ARA at the same concentration of each complex (blue). The resonance at 1.2 ppm observed in the ARA:HoSF 2:1 spectrum, corresponding to the C17-C19 methylene resonances of free ligand, is indicated with an arrow. A grey dashed line indicates the diffusion coefficient of free ARA, consistent with the presence of oligomers of 2-4 units. Peaks visible in the aliphatic region of the protein spectra (0.7-0.9 ppm) were characterized by diffusion coefficients consistent with the presence of impurities of the commercial samples and/or to highly mobile sidechains). Central panels: superposition of DOSY spectra recorded at 600 MHz and 25°C of a sample of 90 μM HoSF in NaPi buffer pH 7.8 (black), OLA:HoSF at different ratios (red), free OLA at the same concentration of each complex (blue). The resonance at 1.2 ppm observed in the OLA:HoSF 2:1 spectrum, corresponding to the free ligand, is indicated with an arrow. A grey dashed line indicates the diffusion coefficient of the main species observed for OLA, consistent with the presence of dimers; Right panels: superposition of DOSY spectra recorded at 600 MHz and 25°C of a 84 μM HoSF sample in NaPi buffer pH 7.8 (black), SDS:HoSF at different protein:ligand ratios (red), free SDS at the same concentration of each complex (blue). The resonance at 1.2 ppm observed in all HoSF:SDS spectra, corresponding to the free ligand, is indicated with an arrow. A grey dashed line indicates the diffusion coefficient of the main species observed for SDS, consistent with the presence of dimers.

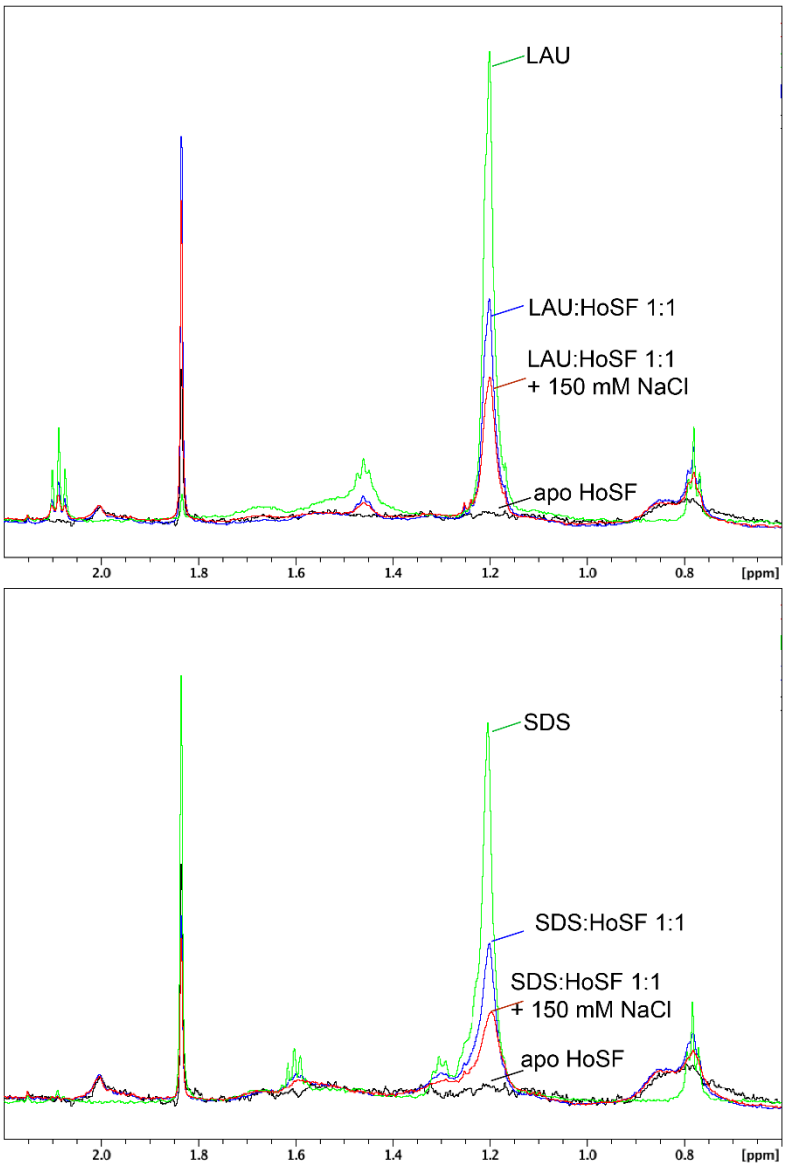

Figure 3

Figure 3. Interaction of HoSF with lauric acid sodium salt (LAU) and SDS. a) superposition of 1D spectra recorded at 600 MHz, 25°C, phosphate buffer, D_2O, pH 7.5 of 85μM apo HoSF (black), LAU:HoSF ratio of 1 (blue), LAU:HoSF ratio of 1 in the presence of 150 mM NaCl (red) and a sample of pure LAU at the same molar concentration of the complex (green). The spectrum of apo HoSF is reported to show that at δ 1.2 ppm only the ligand resonances can be observed. Signal intensities were normalized using dioxane resonance as an internal standard; b) superposition of 1D spectra recorded at 600 MHz, 25°C, phosphate buffer, D_2O, pH 7.5 of 85μM apo HoSF (black), SDS:HoSF ratio of 1 (blue), SDS:HoSF ratio of 1 in the presence of 150 mM NaCl (red) and a sample of pure SDS at the same molar concentration of the complex (green).

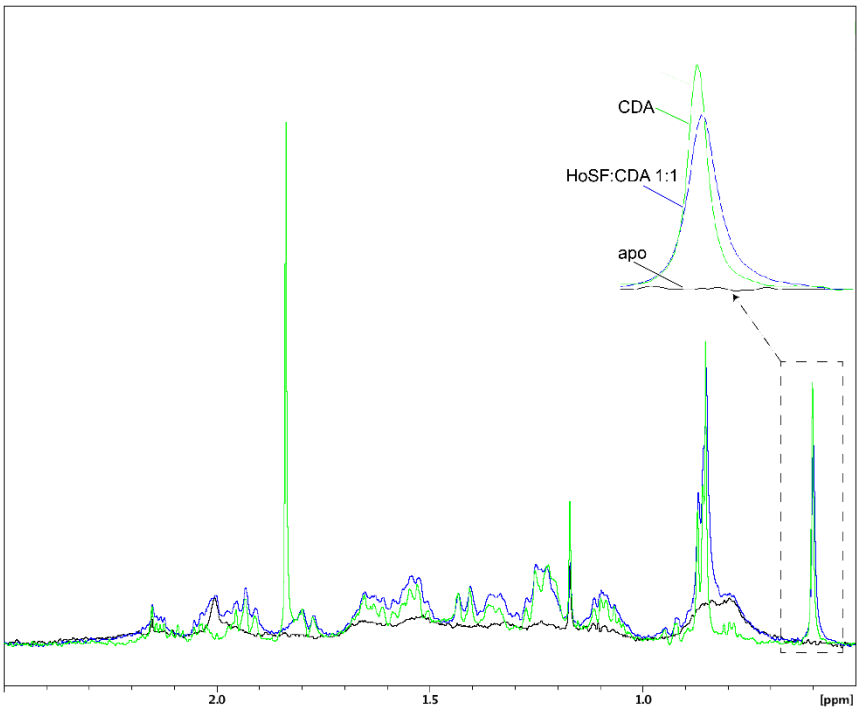

Figure 4. Interaction of HoSF with CDA. Superposition of 1D NMR spectra of a 70 μM HoSF sample in phosphate buffer, pH 7.5, 25°C (black), after addition of CDA at CDA:HoSF ratio of 1 (blue) and free CDA at the same concentrations of the complex (green). A zoom on the C18 methyl resonance occurring at 0,57 ppm where HoSF does not exhibit any resonance, is reported to highlight the observed line broadening.

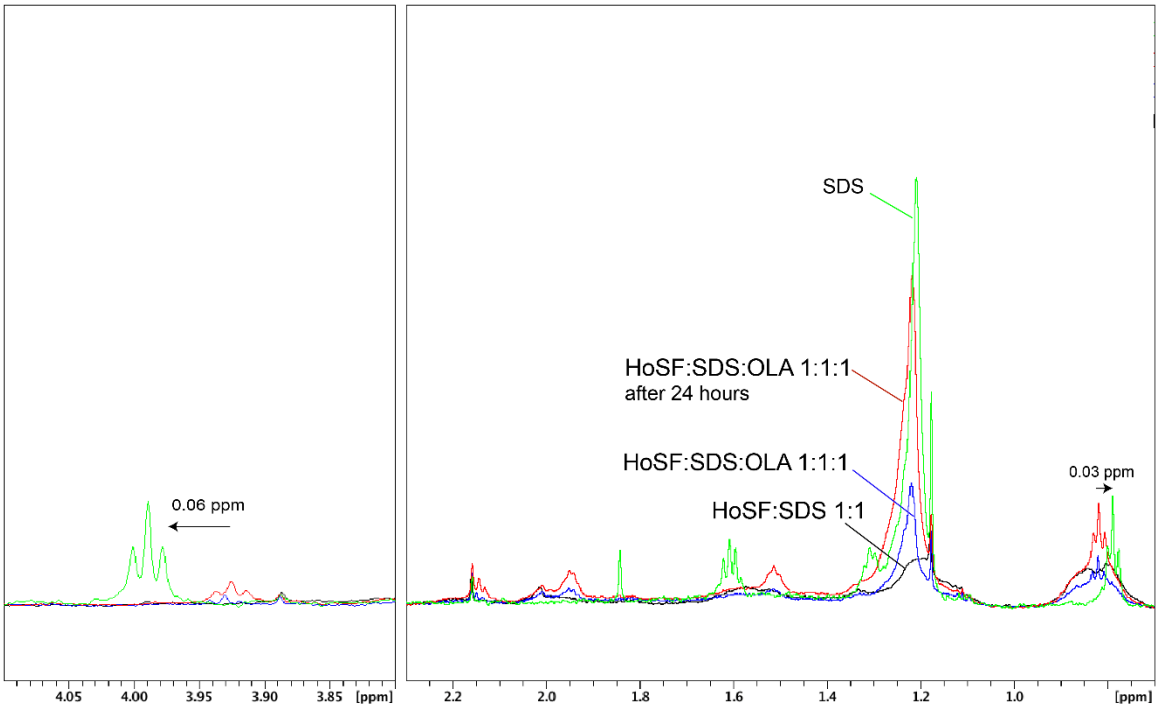

Figure 5

Figure 5. NMR competition experiments. Superposition of 1D spectra recorded at 600 MHz, 25°C, phosphate buffer, D_2O, pH 7.5 of a 85μM HoSF:SDS 1:1 sample (black); HoSF:SDS:OLA mixture at 1:1:1 ratio (blue), the same mixture after 24 hours (red) and, for comparison, pure SDS solution at the same concentration of the previous spectra in the presence of 150mM NaCl (green). The arrows indicate the chemical shift difference between free and SDS displaced by oleate.

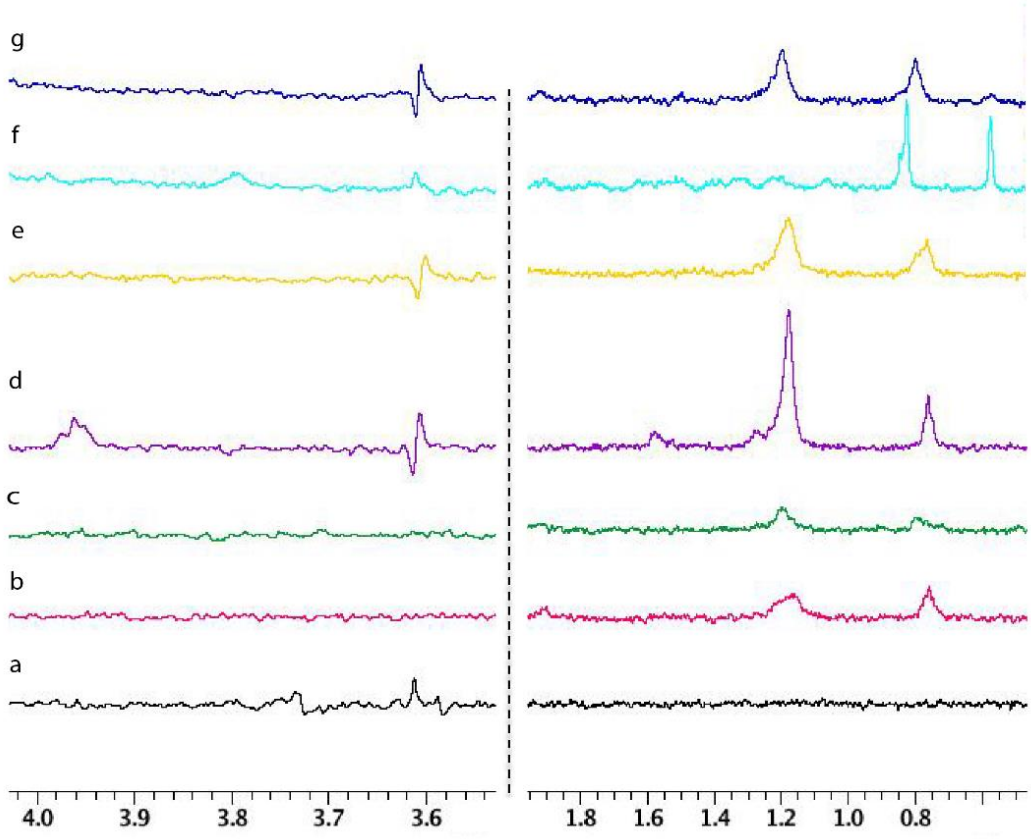

Figure 6. STD NMR experiments. STD spectra of 50 μM HoSF in the presence of 1.25 mM ligands, performed at 600 MHz in phosphate buffer, H_2O, pH 7.2. The ON and OFF resonance spectra were irradiated at 7.2 and -35 ppm, respectively. An irradiation time of 3s was employed. The different ligands employed were: a) sucrose; b) ARA; c) OLA; d) SDS; e) same sample as d) after the addition of the competitor OLA at the same concentration of SDS; f) CDA; g) same sample as f) after the addition of the competitor OLA at the same concentration of CDA.

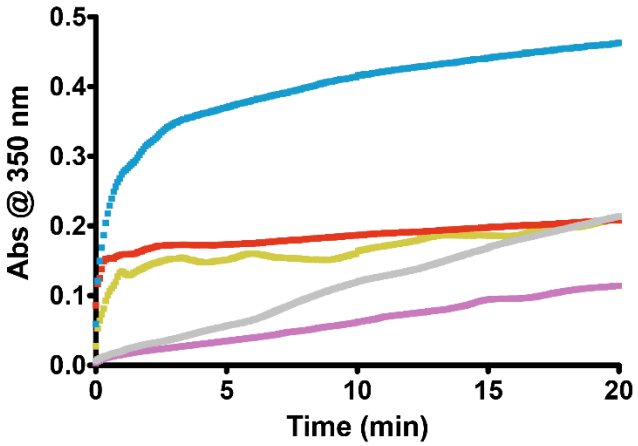

Figure 7. Kinetics of mineralization for HoSF alone (gray trace), incubated with 700 μM of OLA (blu), ARA (red), LAU (gold) and SDS (purple). The kinetics of biomineral formation was followed as the change of $A_{350\ nm}$ after addition of 480 eq of Fe^{2+} per cage.

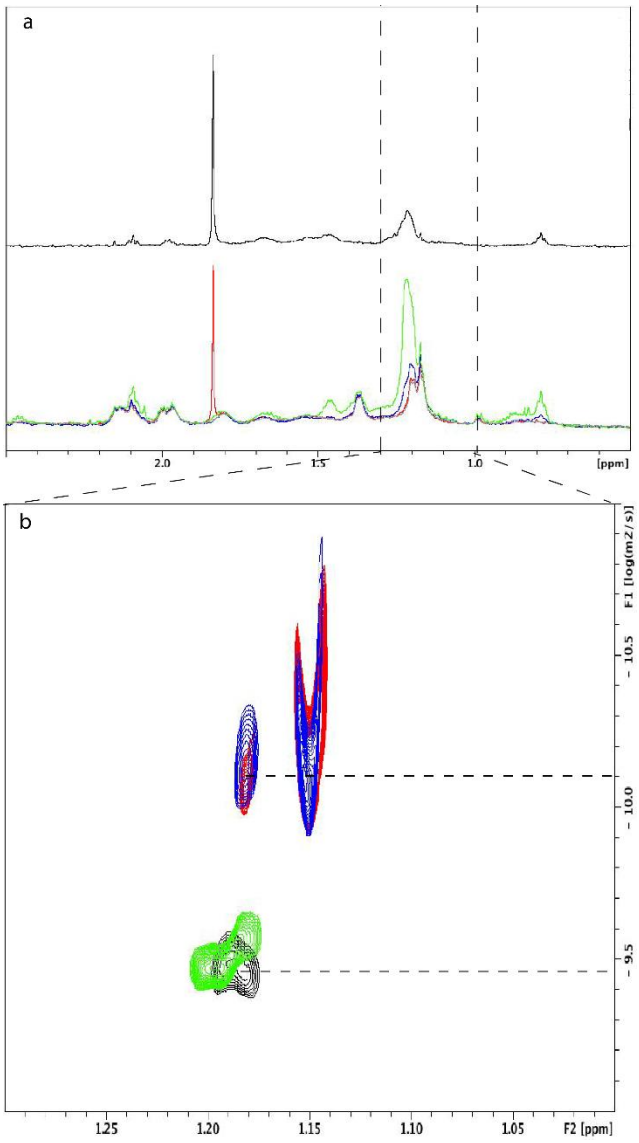

Figure 8. Interactions of HuHF with oleate. a) Superposition of 1D spectra performed at 600 MHz in phosphate buffer, D_2O, pH 7.5 of 95μM apo HuHF (grey), with the different complexes obtained in the presence of oleate at OLA:HuHF ratios of 0.5 (red), 1 (blue) and 2 (green). 1D spectrum of free oleate at the same concentration of the complex with OLA:HuHF ratio of 2 is reported in the upper part of the panel for comparison (black). Dashed lines identify resonances of free oleate which became clearly visible only at OLA:HuHF ratio of 2. b) Superposition of DOSY spectra recorded at 600 MHz and 25°C for samples of free OLA (black), OLA:HuHF at ratios of 0.5 (red), 1 (blue) and 2 (green). A dashed lines is drawn corresponding to the molecular weight of the sodium hydrogen dioleate. Peaks observed at lower diffusion values are due to residual contribution from protein signals.

Supplementary Figures

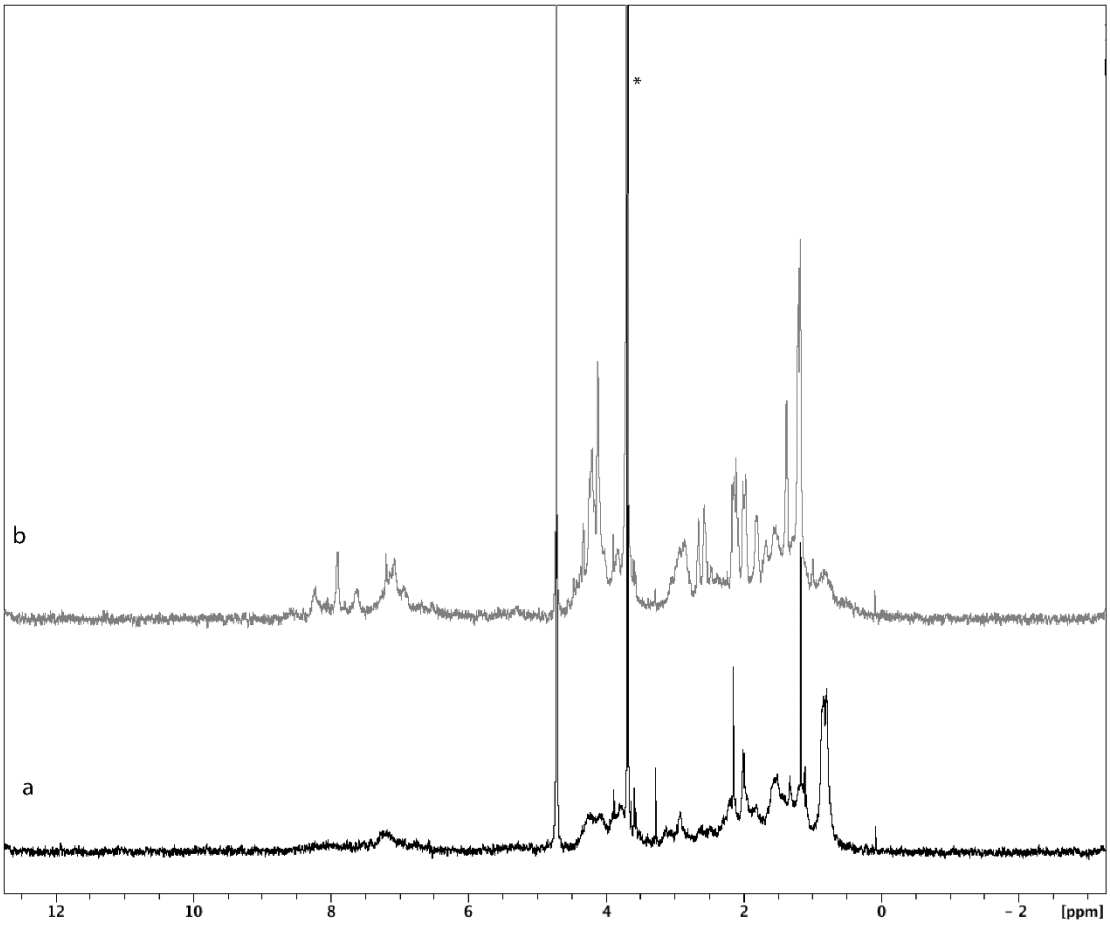

Figure S1. 1D ^{1}H NMR spectra recorded at 600 MHz, 25° C, of ferritin samples in 20 mM phosphate buffer, pH 7.5: a) 85 μM apo HoSF; b) 95 μM recombinant apo HuF. Minor impurities are marked with asterisk.

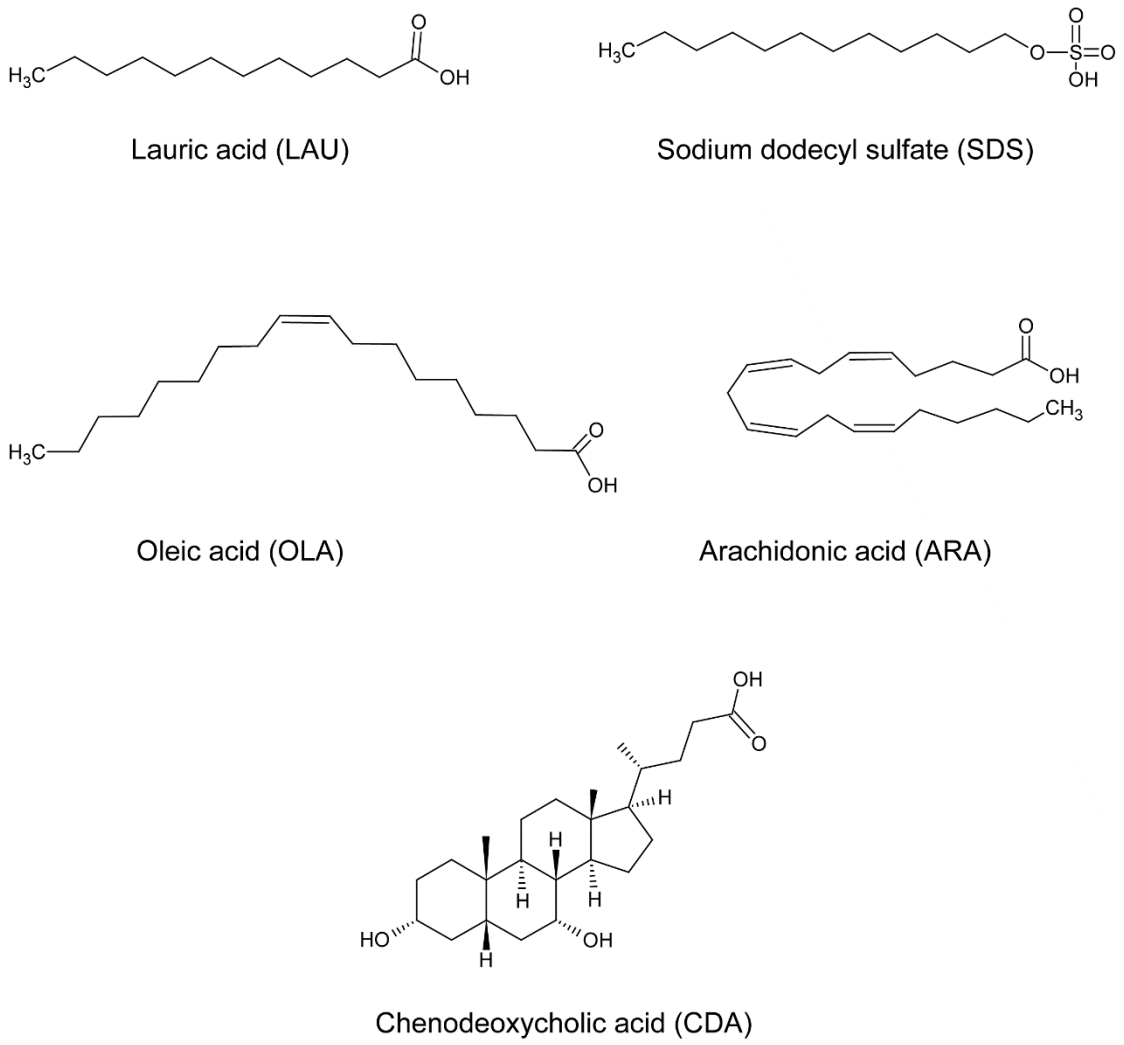

Figure S2. Structures of the polyunsaturated (ARA), monounsaturated (OLA), saturated fatty acids (LAU), detergents (SDS) and bile acids (CDA) analysed. Their sodium salts were employed in the experiments for solubility reasons.

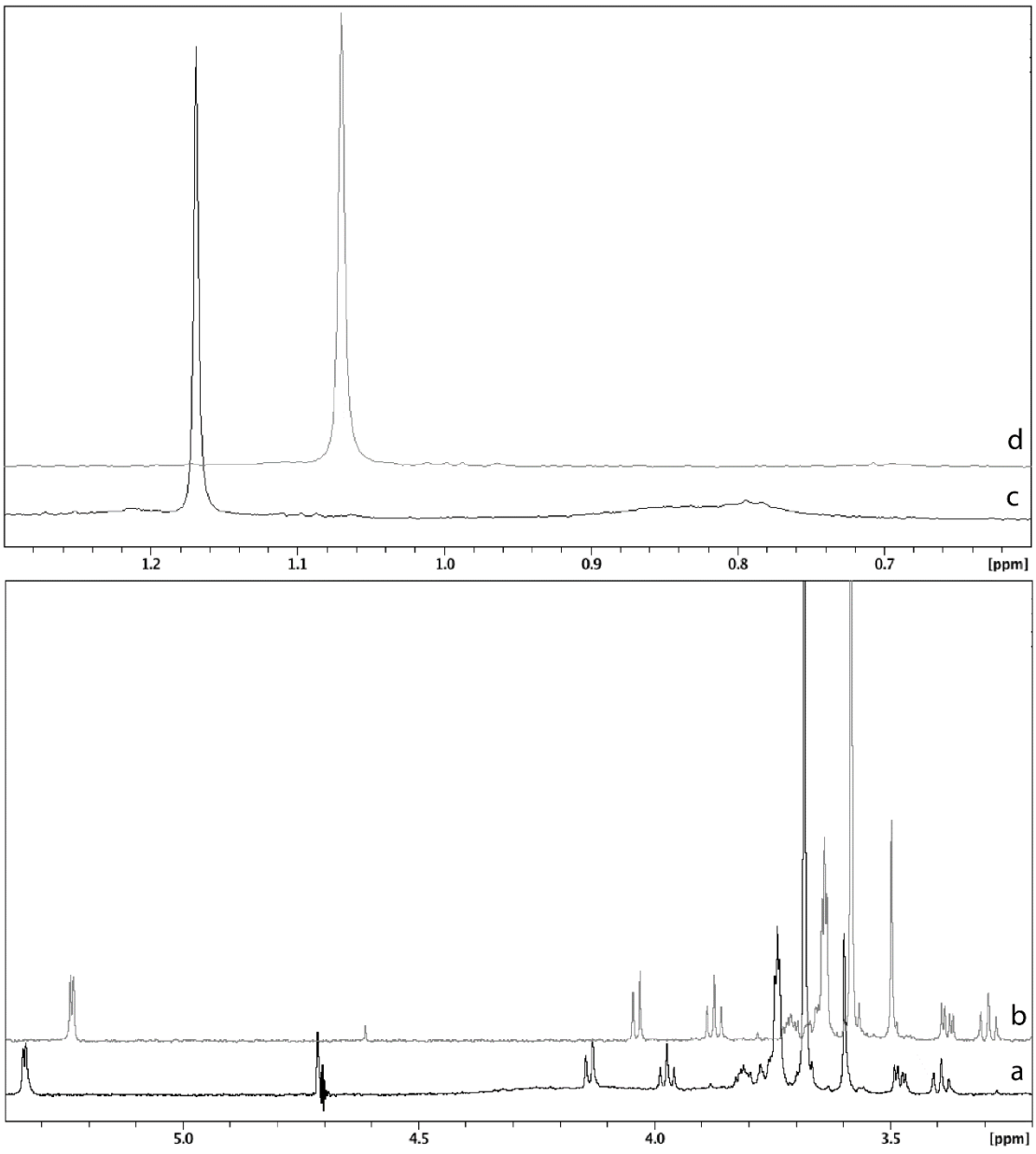

Figure S3. 1D ^{1}H NMR spectra recorded at 600 MHz, 25° C, of ferritin samples in 20 mM phosphate buffer, pH 7.5: a) 85 μM apo HoSF treated with an equimolar amount of sucrose. The region 5.35-3.3 ppm has been selected to highlight the sucrose resonances; b) pure sucrose solution at the same concentration of spectrum a). The comparison of the two spectra evidence the lack of any effect in the presence of HoSF; c) 85 μM apo HoSF treated with an equimolar amount of tert-buthyl alchool; d) pure tert-buthyl alchool solution at the same concentration of spectrum c). In spectra c and d only the highfield region, displaying the single methyl resonance of tert-buthyl alchool, is shown.

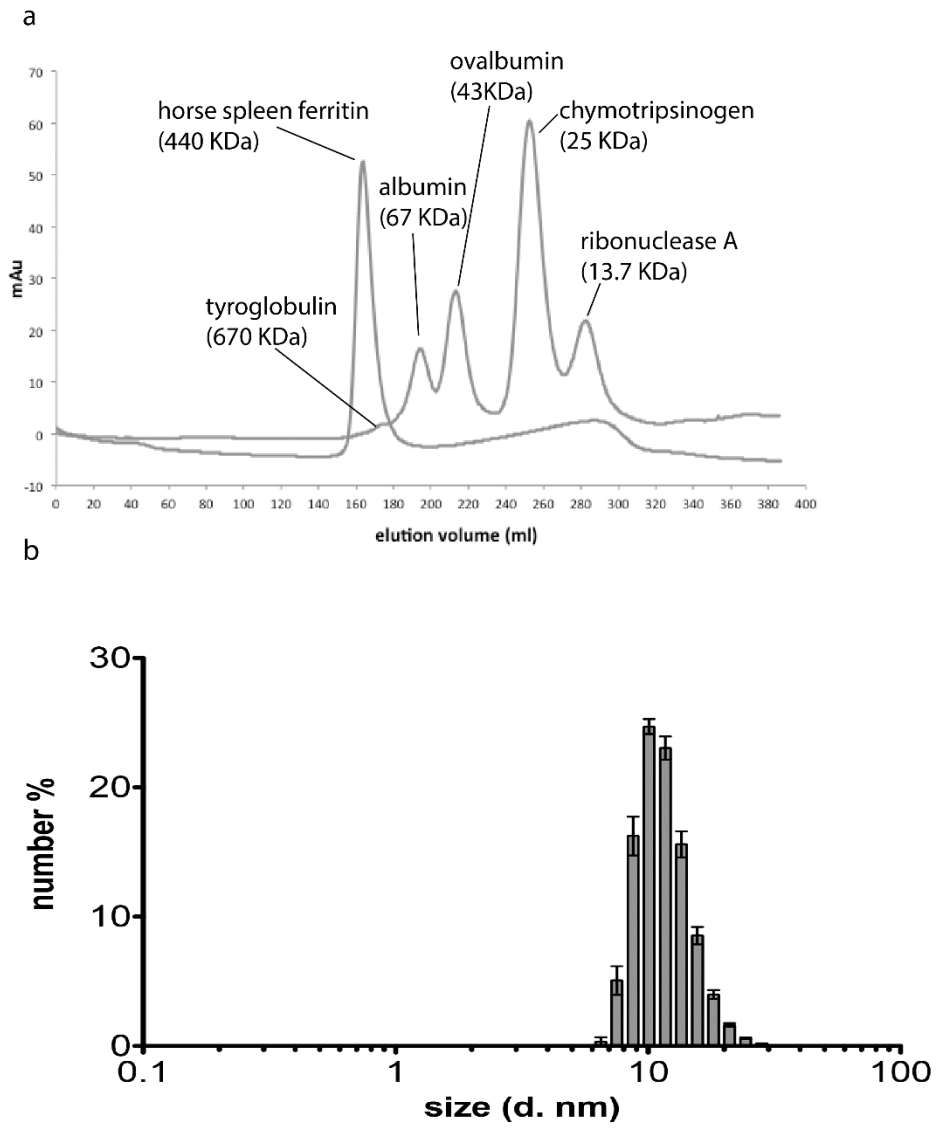

Figure S4. a) Elution profile of size-exclusion chromatography. Size separation was obtained with a Sephacryl S-100 (GE Healthcare) column. The red line corresponds to the elution profile of the proteins used as standards for the calibration; the blue line refers to the chromatogram of the sample containing the horse spleen ferritin; b) Hydrodynamic size of ferritin measured by dynamic light scattering. The distribution curve is the average of three independent measurements.

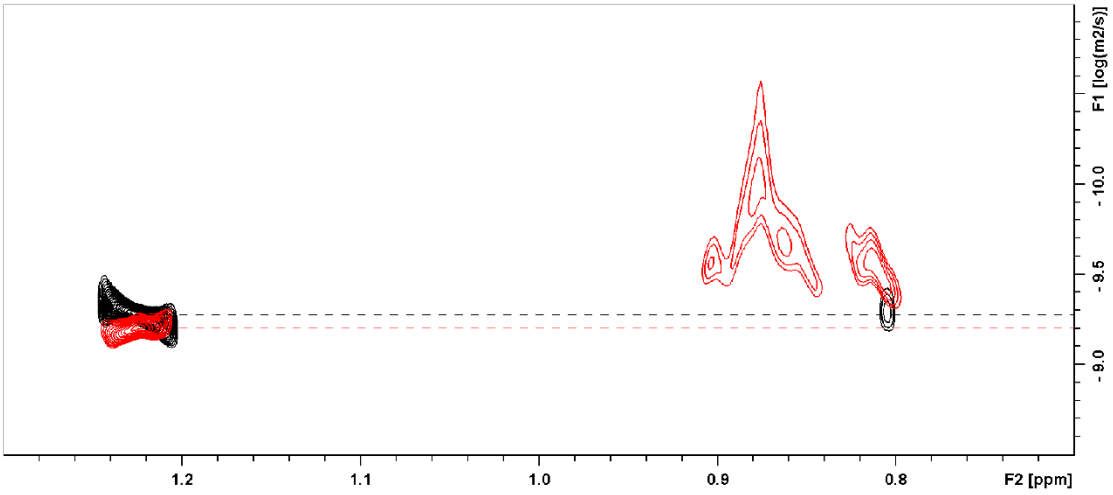

Fig. S5. Superposition of DOSY spectra recorded on a HoSF sample 85μM treated with a stoichiometric amount of LAU, HoSF:LAU at 1:1 ratio (red) and on a sample of free LAU at the same concentration of the complex (black). The DOSY spectra were recorded at 500 MHz and 25°C. The region including the LAU methylene groups (1.2 ppm) and the terminal methyl group (0.8 ppm) is shown. Horizontal lines indicate the logD value, corresponding to a molecular weight consistent with the presence of dimeric (red) and trimeric (black) species, in the presence and absence of ferritin, respectively. The effect of binding of lauric acid is reflected on the observed decrease of the molecular weight of the free LAU species in the presence of ferritin, which decreases LAU concentration in solution by sequestering it. Red peaks at high field and higher D values are due to protein mobile loops. The observed smearing is due to truncation effects as the DOSY spectrum has been optimized for observation of small species (see Material and Methods).

Reference List

1. Jutz, G., van Rijn, P., Santos Miranda, B. & Boker, A. (2015) Ferritin: a versatile building block for bionanotechnology, *Chem Rev.* **115**, 1653-701.

2. Lalli, D. & Turano, P. (2013) Solution and solid state NMR approaches to draw iron pathways in the ferritin nanocage, *Accounts of chemical research.* **46**, 2676-85.

3. Theil, E. C. & Turano, P. (2013) Metalloenzymes: Cage redesign explains assembly, *Nature chemical biology.* **9**, 143-4.

4. Bevers, L. E. & Theil, E. C. (2011) Maxi- and mini-ferritins: minerals and protein nanocages, *Prog Mol Subcell Biol.* **52**, 29-47.

5. Arosio, P. & Levi, S. (2010) Cytosolic and mitochondrial ferritins in the regulation of cellular iron homeostasis and oxidative damage, *Biochimica et biophysica acta.* **1800**, 783-92.

6. Zhao, G., Su, M. & Chasteen, N. D. (2005) mu-1,2-peroxo diferric complex formation in horse spleen ferritin. A mixed H/L-subunit heteropolymer, *Journal of molecular biology.* **352**, 467-77.

7. Zhao, G., Bou-Abdallah, F., Arosio, P., Levi, S., Janus-Chandler, C. & Chasteen, N. D. (2003) Multiple pathways for mineral core formation in mammalian apoferritin. The role of hydrogen peroxide, *Biochemistry.* **42**, 3142-50.

8. Plath, L. D., Ozdemir, A., Aksenov, A. A. & Bier, M. E. (2015) Determination of iron content and dispersity of intact ferritin by superconducting tunnel junction cryodetection mass spectrometry, *Anal Chem.* **87**, 8985-93.

9. May, C. A., Grady, J. K., Laue, T. M., Poli, M., Arosio, P. & Chasteen, N. D. (2010) The sedimentation properties of ferritins. New insights and analysis of methods of nanoparticle preparation, *Biochimica et biophysica acta.* **1800**, 858-70.

10. Bou-Abdallah, F. (2010) Special issue on ferritin, *Biochimica et biophysica acta.* **1800**, 719-31.

11. de Val, N., Declercq, J. P., Lim, C. K. & Crichton, R. R. (2012) Structural analysis of haemin demetallation by L-chain apoferritins, *Journal of inorganic biochemistry.* **112**, 77-84.

12. Liu, R., Loll, P. J. & Eckenhoff, R. G. (2005) Structural basis for high-affinity volatile anesthetic binding in a natural 4-helix bundle protein, *FASEB journal : official publication of the Federation of American Societies for Experimental Biology.* **19**, 567-76.

13. Bu, W., Liu, R., Cheung-Lau, J. C., Dmochowski, I. J., Loll, P. J. & Eckenhoff, R. G. (2012) Ferritin couples iron and fatty acid metabolism, *FASEB journal : official publication of the Federation of American Societies for Experimental Biology.* **26**, 2394-400.

14. Elia, G., Polla, B., Rossi, A. & Santoro, M. G. (1999) Induction of ferritin and heat shock proteins by prostaglandin A1 in human monocytes. Evidence for transcriptional and post-transcriptional regulation, *Eur J Biochem.* **264**, 736-45.

15. Baldi, A., Lombardi, D., Russo, P., Palescandolo, E., De Luca, A., Santini, D., Baldi, F., Rossiello, L., Dell'Anna, M. L., Mastrofrancesco, A., Maresca, V., Flori, E., Natali, P. G., Picardo, M. & Paggi, M. G. (2005) Ferritin contributes to melanoma progression by modulating cell growth and sensitivity to oxidative stress, *Clin Cancer Res.* **11**, 3175-83.

16. Giordani, A., Haigle, J., Leflon, P., Risler, A., Salmon, S., Aubailly, M., Maziere, J. C., Santus, R. & Morliere, P. (2000) Contrasting effects of excess ferritin expression on the iron-mediated oxidative stress induced by tert-butyl hydroperoxide or ultraviolet-A in human fibroblasts and keratinocytes, *J Photochem Photobiol B.* **54**, 43-54.

17. Gillum, R. F. (2001) Association of serum ferritin and indices of body fat distribution and obesity in Mexican American men--the Third National Health and Nutrition Examination Survey, *Int J Obes Relat Metab Disord.* **25**, 639-45.

18. Iwasaki, T., Nakajima, A., Yoneda, M., Yamada, Y., Mukasa, K., Fujita, K., Fujisawa, N., Wada, K. & Terauchi, Y. (2005) Serum ferritin is associated with visceral fat area and subcutaneous fat area, *Diabetes Care.* **28**, 2486-91.

19. Hanhoff, T., Lucke, C. & Spener, F. (2002) Insights into binding of fatty acids by fatty acid binding proteins, *Mol Cell Biochem.* **239**, 45-54.

20. Wang, Z., Li, C., Ellenburg, M., Soistman, E., Ruble, J., Wright, B., Ho, J. X. & Carter, D. C. (2006) Structure of human ferritin L chain, *Acta crystallographica Section D, Biological crystallography.* **62**, 800-6.

21. Levi, S., Yewdall, S. J., Harrison, P. M., Santambrogio, P., Cozzi, A., Rovida, E., Albertini, A. & Arosio, P. (1992) Evidence of H- and L-chains have co-operative roles in the iron-uptake mechanism of human ferritin, *Biochem J.* **288 (Pt 2)**, 591-6.

22. Lopez-Castro, J. D., Delgado, J. J., Perez-Omil, J. A., Galvez, N., Cuesta, R., Watt, R. K. & Dominguez-Vera, J. M. (2012) A new approach to the ferritin iron core growth: influence of the H/L ratio on the core shape, *Dalton Trans.* **41**, 1320-4.

23. Chasteen, N. D. & Harrison, P. M. (1999) Mineralization in ferritin: an efficient means of iron storage, *J Struct Biol.* **126**, 182-94.

24. Toussaint, L., Bertrand, L., Hue, L., Crichton, R. R. & Declercq, J. P. (2007) High-resolution X-ray structures of human apoferritin H-chain mutants correlated with their activity and metal-binding sites, *Journal of molecular biology.* **365**, 440-52.

25. Hempstead, P. D., Yewdall, S. J., Fernie, A. R., Lawson, D. M., Artymiuk, P. J., Rice, D. W., Ford, G. C. & Harrison, P. M. (1997) Comparison of the three-dimensional structures of recombinant human H and horse L ferritins at high resolution, *Journal of molecular biology.* **268**, 424-48.

26. Brash, A. R. (2001) Arachidonic acid as a bioactive molecule, *J Clin Invest.* **107**, 1339-45.

27. Brinkmann, C. R., Thiel, S. & Otzen, D. E. (2013) Protein-fatty acid complexes: biochemistry, biophysics and function, *FEBS J.* **280**, 1733-49.

28. Kleckner, I. R. & Foster, M. P. (2011) An introduction to NMR-based approaches for measuring protein dynamics, *Biochimica et biophysica acta.* **1814**, 942-68.

29. Cohen, Y., Avram, L. & Frish, L. (2005) Diffusion NMR spectroscopy in supramolecular and combinatorial chemistry: an old parameter--new insights, *Angew Chem Int Ed Engl.* **44**, 520-54.

30. Rucker, P., Torti, F. M. & Torti, S. V. (1997) Recombinant ferritin: modulation of subunit stoichiometry in bacterial expression systems, *Protein Eng.* **10**, 967-73.

31. Hilty, S., Webb, B., Frankel, R. B. & Watt, G. D. (1994) Iron core formation in horse spleen ferritin: magnetic susceptibility, pH, and compositional studies, *Journal of inorganic biochemistry.* **56**, 173-85.

32. Staggers, J. E., Hernell, O., Stafford, R. J. & Carey, M. C. (1990) Physical-chemical behavior of dietary and biliary lipids during intestinal digestion and absorption. 1. Phase behavior and aggregation states of model lipid systems patterned after aqueous duodenal contents of healthy adult human beings, *Biochemistry.* **29**, 2028-40.

33. Liu, R., Bu, W., Xi, J., Mortazavi, S. R., Cheung-Lau, J. C., Dmochowski, I. J. & Loll, P. J. (2012) Beyond the detergent effect: a binding site for sodium dodecyl sulfate (SDS) in mammalian apoferritin, *Acta crystallographica Section D, Biological crystallography.* **68**, 497-504.

34. Knyazeva, E. L., Grishchenko, V. M., Fadeev, R. S., Akatov, V. S., Permyakov, S. E. & Permyakov, E. A. (2008) Who is Mr. HAMLET? Interaction of human alpha-lactalbumin with monomeric oleic acid, *Biochemistry.* **47**, 13127-37.

35. Glick, J., Santoyo, G. & Casey, P. J. (1996) Arachidonate and related unsaturated fatty acids selectively inactivate the guanine nucleotide-binding regulatory protein, Gz, *The Journal of biological chemistry.* **271**, 2949-54.

36. Jusufi, A., Hynninen, A. P., Haataja, M. & Panagiotopoulos, A. Z. (2009) Electrostatic screening and charge correlation effects in micellization of ionic surfactants, *J Phys Chem B.* **113**, 6314-20.

37. Rademacher, C., Krishna, N. R., Palcic, M., Parra, F. & Peters, T. (2008) NMR experiments reveal the molecular basis of receptor recognition by a calicivirus, *Journal of the American Chemical Society.* **130**, 3669-75.

38. Bernacchioni, C., Ciambellotti, S., Theil, E. C. & Turano, P. (2015) Is His54 a gating residue for the ferritin ferroxidase site?, *Biochimica et biophysica acta.* **1854**, 1118-22.

39. Dongiovanni, P., Lanti, C., Gatti, S., Rametta, R., Recalcati, S., Maggioni, M., Fracanzani, A. L., Riso, P., Cairo, G., Fargion, S. & Valenti, L. (2015) High fat diet subverts hepatocellular iron uptake determining dysmetabolic iron overload, *PLoS One.* **10**, e0116855.

40. Pozzi, C., Di Pisa, F., Bernacchioni, C., Ciambellotti, S., Turano, P. & Mangani, S. (2015) Iron binding to human heavy-chain ferritin, *Acta crystallographica Section D, Biological crystallography.* **71**, 1909-20.

41. Angulo, J. & Nieto, P. M. (2011) STD-NMR: application to transient interactions between biomolecules-a quantitative approach, *Eur Biophys J.* **40**, 1357-69.

42. Wagstaff, J. L., Taylor, S. L. & Howard, M. J. (2013) Recent developments and applications of saturation transfer difference nuclear magnetic resonance (STD NMR) spectroscopy, *Mol Biosyst.* **9**, 571-7.

43. Bhunia, A., Bhattacharjya, S. & Chatterjee, S. (2012) Applications of saturation transfer difference NMR in biological systems, *Drug Discov Today.* **17**, 505-13.

44. Venkitakrishnan, R. P., Benard, O., Max, M., Markley, J. L. & Assadi-Porter, F. M. (2012) Use of NMR saturation transfer difference spectroscopy to study ligand binding to membrane proteins, *Methods Mol Biol.* **914**, 47-63.

45. Jerschow, A. & Muller, N. (1998) Efficient simulation of coherence transfer pathway selection by phase cycling and pulsed field gradients in NMR, *Journal of magnetic resonance.* **134**, 17-29.

46. Jerschow, A. & Muller, N. (1997) Suppression of Convection Artifacts in Stimulated-Echo Diffusion Experiments. Double-Stimulated-Echo Experiments, *Journal of magnetic resonance.* **125**, 372-375.

47. Stejskal, E. O. & Tanner, J. E. (1965) Spin diffusion measurements: Spin echoes in the presence of a time-dependent field gradient, *The Journal of Chemical Physics.* **42**, 5.

Acknowledgements

Innanzitutto vorrei ringraziare tutte le persone che hanno collaborato con me in questi anni e che hanno contribuito ai risultati raggiunti.

Un grazie enorme a Paola per avermi supportata in questo percorso e soprattutto per la stima, la pazienza e il sostegno al di là del ruolo di tutor.

Dedico questa tesi a tutta la mia famiglia vicina e lontana e soprattutto alla nuova arrivata Virginia, sei la gioia di tutti noi. Alla mia mamma e al mio babbo, per tutto quello che avete fatto e fate per me, vi devo tutto! A Gianlu che mi sopporta da qualche anno, grazie per essere sempre e comunque al mio fianco. Alle mie amiche storiche, Anna Eli Sara Debbi perché il vostro sostegno conta tanto per me.

Vorrei tanto ringraziare la vecchia guardia del CERM che mi manca tanto…gli emigrati all'estero Angelo e Dani, tra le prime persone che ho conosciuto appena arrivata al Cerm. Grazie a tutti i miei compagni di lab, quelli che…si faceva a cazzotti per trovare uno shaker o una cappa libera, ma sempre pronti ad aiutarsi l'uno con l'altro. Ai mattatori dell'ora di pranzo: Diego, Gianlu, Santux e Fuccio. A Melo in particolare grazie per le lezioni di cucina, le motivazioni per il running, le chiacchierate sulle serie tv e l'immancabile espressione "ma che ce ne f..t". A Vince l'uomo del caffè, a cui abbiamo invaso la stanza, ormai diventata un punto di ritrovo…grazie per la pazienza e grazie per i momenti condivisi a casa Panciatichi e nei tour enogastronomici! Un grazie a tutti i frequentatori del bar (room 4) per le risate post pranzo.

A tutte le persone che hanno abitato la mitica stanza 2: da Raquel la spagnola che ti parlava in napoletano, Matteo il Piero Angela della chimica e non solo, Pantelis che è l'unico rimasto a farmi compagnia e che condivide con me gioie e dolori…e per ultima, si fa per dire, alla neomamma Sara, la più figa del CERM, con la risata più contagiosa e silenziosa della storia, appassionata di Ciclone da vent'anni come me che ha ispirato persino il nome di un nuovo elemento chimico (il Sarinio), a te grazie per il bellissimo periodo che abbiamo condiviso insieme a lavoro e per quello che passeremo ancora al di fuori. Alla Berna, compagna di ferritona, grazie per il tuo supporto, i tuoi consigli preziosi e perché mi fai sempre piegare in due dal ridere tra gli aneddoti sulla vecia e le critiche al povero Bagnolesi.

A tutto il gruppo del XXIX ciclo di dottorato Vitek, Azzurra, Alexia, Veronica G. e Veronica N. per avere condiviso con me questi tre anni tra seminari, esami, compleanni e festeggiamenti vari in coffee room.

E poi vorrei aggiungere un grazie a te Vero che…non ci siamo prese da subito, forse perché sono un po' burbera come dici te, ma una volta che ci siamo capite ci siamo trovate. Con te non ci si annoia mai, mi fai "pariare malamente", sei la generosità fatta persona, la mia compagna di merende preferita e la mia roccia nei momenti difficili. Testona e permalosa quasi quanto me, col pericolo di scornarsi, ma con la sicurezza di riderci su dopo cinque minuti, o dieci. E poi fortuna ha voluto che il duo sia diventato un trio. Un grazie a te Debbi, un attrezzo vero, che in poco tempo sei

diventata un punto di riferimento, sei la dolcezza infinita, non molli mai e mi supporti anche dalla mitica S. Marinella. Cerm o non Cerm, sono sicura che noi tre non ci perderemo.

Per chiudere, come di consueto alla fine delle tesi mi faccio sempre un augurio, stavolta citando Liga… spero e voglio credere che "…il meglio deve ancora venire!!…".